SCIAMACHY Product Handbook

Table of Contents

Chapter 1

Introduction
The Road to SCIAMACHY
The Initial Phases of SCIAMACHY
SCIAMACHYs Goals
The Atmospheric Layers
Anthropogenic Impact on the Earth-Atmosphere System
Tropospheric Chemistry
The Tropopause Region
Stratospheric Chemistry and Dynamics
Mesopheric Chemistry and Dynamics

Chapter 2

SCIAMACHY: The Instrument onboard ENVISAT
SCIAMACHY on ENVISAT
Orbit and Attitude
ENVISAT On-board Resources
ENVISAT Ground Segment
Science Requirements and Instrument Concept
Optical Assembly
Scanner Mechanisms and Baffles
Telescope and Spectrometer
Detector Modules
Calibration Unit
Thermal Subsystems
Instrument Operations
Sun and Moon Observation
Moon Occultation
Routine Measurement Orbit
Parameter Tables
Occultation States
Definition
SCIAMACHY Operations Setup

Chapter 3

SCIAMACHY's View of the Earth's Atmosphere
Methane CH_4
Water Vapour H_2O
Heavy Water HDO
Tropospheric Composition Reactive Gases
Sulphur Dioxide SO_2
Formaldehyde (HCHO) and Glyoxal (CHOCHO)
Carbon Monoxide CO
Tropospheric Halogen Oxides BrO and IO
The Stratospheric Ozone Layer
Ozone O_3
Chlorine Dioxide OClO
Bromine Oxide BrO
The Upper Atmosphere and Solar Activity
Mesospheric Ozone and the October November 2003 Solar Storm
Mesopause Temperatures
Observing the Active Sun - The Mg II Index
The Earth Surface and Beneath
Oligotrophic Oceanic Regions

Chapter 4

Calibration Monitoring
Detector Corrections
Channels 6-8 (SWIR)
Wavelength Calibration
Stray Light
Spatial Stray Light
Radiometric Calibration
Optical Throughput Monitoring

Chapter 5

From Radiation Fields to Atmospheric Concentrations
Radiative Transfer in the Earths Atmosphere
Total Column: Nadir Retrieval Schemes of DOAS-type
Cloud and Aerosol Parameter Retrieval
Cloud Parameters
Tropospheric Aerosol Parameters
Profile Retrieval
Application of Inversion Theory to Limb Retrieval
Derivation of Tropospheric Information
Reference Sector Method
Stratospheric O3

Chapter 6

SCIAMACHY Operational Data Products and Algorithms
Relevant calibration parameters
Dark correction
Polarization Correction
Relevant Auxiliary Data
Short-Term Concept
Cloud and Aerosol Parameters
Ozone Total Column
BrO Total Comumn
Content and filling of the database
H2O Total Column
Limb
NO2 Profile
Cloud flagging and top height
Software Tools

Annex

Annex 1
References Chapter 1
References Chapter 2
References Chapter 3
References Chapter 4
References Chapter 5
References Chapter 6

Annex 2
Atmospheric Gases

Annex 3
Abbreviations and Acronyms

Annex 4
Frequently Asked Questions and typical EOHelp replies

CHAPTER 1

1. Introduction

The handbook version 1.0 is based in parts on the SCIAMACHY book *(Gottwald et al. 2006)* and has been updated to cover the Level 1 version 8, and the Level 2 version 6 SCIAMACHY operational processors.

This chapter explains the background of SCIAMACHY.

The recognition, that significant changes in the composition of the Earth's atmosphere are occurring on both short and long timescales and thereby modifying our environment and climate, has resulted in scientific debate as well as public concern, and emphasises the need for global measurements of atmospheric constituents at representative spatial and temporal sampling. Established examples, where change has been identified, are:

- the precipitous loss of Antarctic and Arctic stratospheric ozone (O_3) resulting from the tropospheric emission of chlorofluorocarbon compounds (CFCs, halones, and HFCs) *(WMO 2003)*,
- the global increase of tropospheric O_3 *(WMO 1995)* and its impact on air quality,
- the trans-boundary transport and transformation of pollution resulting for example in acidic deposition and impacting air quality far from pollution sources (*WMO-IGACO 2004)*,
- global dimming attributed to changes in aerosol and clouds *(Wild et al. 2005)*,
- the observed increase of tropospheric greenhouse gases such as CO_2, CH_4, N_2O and O_3 and its impact on climate change *(IPCC 2001)*, and
- the coupling between stratospheric ozone loss and increased greenhouse gas concentrations *(Shindell et al. 1998)*.

In order to assess the significance of such changes a detailed understanding of the physical and chemical processes controlling the global atmosphere is required. The accurate assessment of the impact of current and future anthropogenic activity or natural phenomena on the behaviour of the system, comprising the atmosphere and the Earth's surface, requires quantitative knowledge about the temporal and spatial behaviour of several atmospheric trace constituents (gases, aerosol, clouds) from the local to global scales in the troposphere, stratosphere and mesosphere. These data sets are also needed to test the predictive ability of the theories currently used to model the atmosphere.

The **SCanning Imaging Absorption spectroMeter for Atmospheric CHartographY** (SCIAMACHY, 'SCIAMACHY' is a Greek expression, which means *chasing or hunting shadows* and is equivalent to do the impossible task) as part of the atmospheric chemistry payload on-board the Environmental Satellite (ENVISAT) of the European Space Agency (ESA) was conceived to make a significant contribution to the required data sets and the understanding of climate change.

Prior to the advent of space flight, measurements of atmospheric composition were limited in geographical coverage. The development of satellite platforms in low-Earth and geostationary orbit over the last three decades has provided the opportunity to observe the Earth and its atmosphere in novel viewing geometries. The potential to make near simultaneous observations at the global scale for the first time has facilitated the emergence of *Earth System Science*. In particular the atmospheric sciences have gained from satellite observations. This is because remote regions of the atmosphere over the land and oceans, where ground-based stations or ship-borne measurements are usually rare, can now be probed regularly from space and variations of geophysical parameters on small and large scales, both spatially and temporally, can be studied.

Passive atmospheric sounding from space can be achieved in two ways – either by analysing *absorption* or *emission* spectra, both requiring accurate measurement of radiation leaving the top of the atmosphere. Absorption and emission processes in the atmosphere produce spectra, which are characteristic for the emitting or absorbing atom or molecule.

Emission spectra consist of the signals from atmospheric constituents which radiate mainly in the infrared and microwave spectral range according to their characteristic thermal excitation. They can be regarded as the thermal 'fingerprint' of the atmosphere. From the emission line properties trace gas concentrations are derived.
Measuring *solar absorption spectra* at the top of the atmosphere is the approach utilised in SCIAMACHY. Atoms, molecules and particles absorb, emit and scatter the incoming solar electromagnetic radiation. The incoming solar radiation is described to a good approximation by the emission from a black body having a temperature of about 5800 K, modulated by atomic absorption lines, the solar Fraunhofer lines. The upwelling radiation at the top of the atmosphere from the Ultraviolet (UV) to Short-Wave Infrared (SWIR) comprises – after travelling through the atmosphere – the solar output, modified by scattering, absorption and emission processes along its light path through the atmosphere and reflected as well as scattered at the Earth's surface.

The Road to SCIAMACHY

The SCIAMACHY project has from its outset the aim to utilise all the information contained in the radiation upwelling from the atmosphere to space in order to derive the amounts and distributions of atmospheric constituents, parameters and selected surface phenomena. This task requires – beside high quality measurements – an accurate understanding and knowledge of the absorption spectroscopy and the scattering of electromagnetic radiation in the atmosphere and at the Earth's surface.

1.1 The Road to SCIAMACHY

Recognising the need for global observations of the Earth system, the scientific community has proposed for research and monitoring purposes global observing systems. Over the past three decades pioneering efforts have been made by the scientific community to establish networks of ground based instruments and satellite projects. The overall objectives are:

- to improve our understanding of the physical and chemical processes determining the behaviour of the atmosphere,
- to demonstrate and assess the capability and applicability of remote sensing from space for Earth System and Atmospheric Science, and
- to move towards a global observing system adequate to meet the needs of Earth System Science and to provide the global data needed for policymakers.

The first measurements of atmospheric ozone from space were made by the Soviet space program in the middle of the 1960's. In the early 1970's NASA initiated its efforts to make global measurements of atmospheric ozone with the Backscattered Ultra Violet (BUV) instrument aboard the NASA Nimbus 4 satellite. This instrument was significantly enhanced and extended to both the Solar Backscatter Ultraviolet (SBUV) and Total Ozone Mapping Spectrometer (TOMS), which flew on NASA's Nimbus 7 satellite. Subsequently NOAA was responsible for a series of SBUV-2 instruments on its operational meteorological platforms while NASA operated several TOMS instruments on a variety of satellites (see figure 1-1). Useful solar occultation measurements began in 1978 with the launch of SAM-II (Stratospheric Aerosol Measurement) which was followed by the Stratospheric Aerosol and Gas Experiment (SAGE-I, SAGE-II) and the Russian occultation spectrophotometer SFM-2. The research mission SME (Solar Mesospheric Explorer) was launched in 1983 and made limb scanning measurements of solar backscattered radiation to determine ozone and nitrogen dioxide. Another milestone in the exploration of the atmosphere from space is the Upper Atmosphere Research Satellite (UARS), which carried instruments to sound the upper atmosphere like the Microwave Limb Sounder (MLS) and the Halogen Occultation Experiment (HALOE). UARS was launched in 1991 and the measurements of HALOE were extended into 2005.

The European participation in remote sounding of atmospheric constituents and parameters was focused initially on the development of the geostationary METEOSAT programme. Initiated by ESA and finally transferred to EUMETSAT, it provided measurements of meteorological parameters. While the first polar orbiting European Research Satellite (ERS-1), primarily a platform for microwave and radar sensors, did not address the needs of the atmospheric chemistry community, the second European Remote Sensing satellite (ERS-2), carrying the Global Ozone Monitoring Experiment (GOME), took Europe a large step forward towards ozone and atmospheric composition measurements. GOME on ERS-2 was a smaller scale version of SCIAMACHY derived from the original SCIAMACHY concept, measuring in nadir viewing geometry the upwelling radiation at the top of the atmosphere between 240 and 793 nm. ERS-2 was launched on April 20th, 1995 into a sun-synchronous orbit with an equator crossing time in descending node of 10:30 a.m. The feasibility of the SCIAMACHY instrument and retrieval concepts could be successfully demonstrated for nadir observations with GOME. The absorptions of the trace gases O3, NO2, BrO, OClO, H2O, SO2, and HCHO could be observed as predicted and the retrieval of total and tropospheric column information from GOME measurements was achieved (*Burrows et al. 1999* and references therein). In addition, similarly to SBUV, O3 profiles including some information on tropospheric ozone were retrieved from GOME observations *(Munro et al. 1998)*. ERS-2 has been deorbited on July 4th, 2011.

Recently, several new missions were launched and contribute significantly to research in the fields of atmospheric chemistry and physics: NASA's Earth Observing System (EOS) satellites TERRA, AQUA and AURA, the Japanese Advanced Earth Observing System (ADEOS1/2), the Canadian/Swedish ODIN mission and ESA's ENVISAT.

SCIAMACHY was part of the atmospheric chemistry payload on-board ENVISAT. Following the call for Earth Observation instrumentation in the Announcement of Opportunity for the Polar Platform issued by ESA, the SCIAMACHY proposal was – after peer review – selected as part of the payload for the satellite now known as ENVISAT, which was launched in March 2002 and was in operation until April 2012.

fig. 1-1:

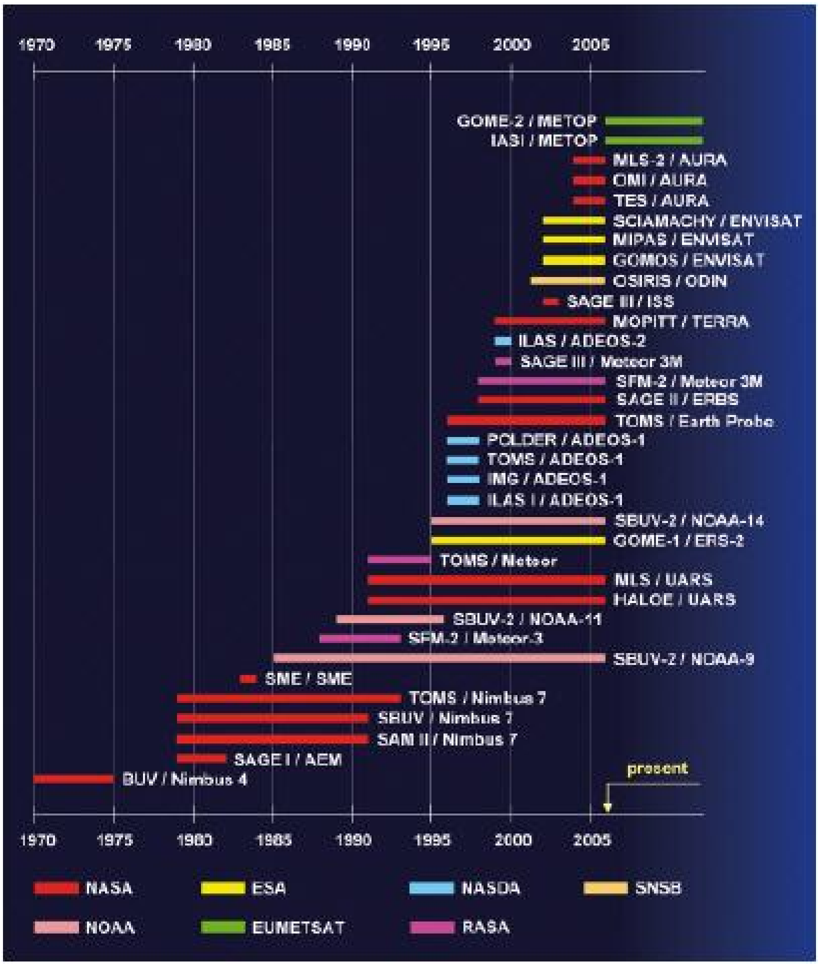

Atmospheric science spaceborne instruments and missions from 1970 to 2006 with relevance for SCIAMACHY. The list of missions is not intended to be complete but to illustrate the progress in space borne instrumentation for atmospheric composition monitoring. (Graphics: DLR-IMF)

The heritage of the SCIAMACHY instrument lies in both, the ground based measurements using Differential Optical Absorption Spectroscopy (DOAS) and previous satellite atmospheric remote sensing missions like SBUV, TOMS, SME, and SAGE. SCIAMACHY combined and extended the measurement principles and observational modes of the nadir scattered sunlight recording instruments SBUV and TOMS, the solar occultation instrument SAGE and the limb scattered sunlight measuring instrument SME within one instrument. SCIAMACHY observed in the wavelength range from 214-2386 nm:

- the scattered and reflected spectral radiance in nadir and limb geometry,
- the spectral radiance transmitted through the atmosphere in solar and lunar occultation geometry,
- the extraterrestrial solar irradiance and the lunar radiance.

Table 1-1:

Instrument	*Name*	*Measurement Altitude*[1]			*Target Species*	*Observation Geometry*[2]				
		TR	*ST*	*ME*		*N*	*L*	*SO*	*LO*	*STO*
BUV	Backscatter Ultraviolet Ozone Experiment		X		O3	X				
GOME-1	Global Ozone Monitoring Experiment	X	X		O3, NO2, H2O, BrO, OClO, SO2, HCHO, CHOCHO, IO, clouds and aerosols	X				
GOME-2	Global Ozone Monitoring Experiment	X	X		O3, NO2, H2O BrO, OClO, SO2, HCHO, CHOCHO, IO, clouds and aerosols	X				
GOMOS	Global Ozone Monitoring by Occultation of Stars	X[3]	X	X	O3, NO2, H2O, NO3, aerosols, T					X
HALOE	Halogen Occultation Experiment				CO2, H2O, O3, NO2, HF, HCl, CH4, NO			X		

IASI	Infrared Atmospheric Sounding Interferometer	X[3]	X		O3, H2O, CO, CH4, N2O, T	X				
ILAS I, II	Improved Limb Atmospheric Spectrometer		X		O3, NO2, N2O, H2O, CFC11, CH4, aerosols			X		
IMG	Interferometric Monitor for Greenhouse Gases	X	X		O3, N2O, H2O, CH4, CO, CO2	X				
MIPAS	Michelson Inferometer for Passive Atmospheric Sounding		X	X	O3, NOx, N2O5 ClONO2, CH4, CFCs, HNO3, and more, T and P		X			
MLS	Microwave Limb Sounder		X	X	ClO, O3, H2O, HNO3, T and P		X			
MLS-2	Microwave Limb Sounder		X	X	CO, HCL, ClO, O3, H2O, BrO, N2O, SO2, HCN, CH3CN		X			
MOPITT	Measurement of Pollution in the Troposphere	X			CO, CH4	X				
OMI	Ozone Monitoring Instrument	X	X		O3, SO2, NO2, BrO, CHOCHO, HCHO, aerosols	X				
OSIRIS	Optical Spectrograph and Infrared Imaging System		X	X	NO, OClO, O3, NO2, aerosols		X			
POLDER	Polarization and Directionality of the Earth's Radiance	X			polarisation, aerosols, clouds	X				
SAM II	Stratospheric Aerosol Measurement II		X		aerosols			X		
SAGE I	Stratospheric Aerosol and Gas Experiment I		X		O3, NO2, aerosols			X		
SAGE II	Stratospheric Aerosol and Gas Experiment II		X		O3, NO2, H2O, aerosols			X		
SAGE III	Stratospheric Aerosol and Gas Experiment III		X		O3, OClO, H2O, BrO, NO2, NO3, aerosols			X	X	
SBUV	Solar Backscatter Ultraviolet Ozone Experiment	X	X		O3, SO2	X				
SBUV-2	Solar Backscatter Ultraviolet Ozone Experiment 2	X	X		O3, SO2	X				
SCIAMACHY	Scanning Imaging Absorption Spectrometer for Atmospheric Chartography	X	X	X	O3, O2, O2(1Δ), O4, NO, NO2, N2O, BrO, OClO, H2O, HDO/H2O, SO2, HCHO, CHOCHO, IO, CO, CO2, CH4, cloud, aerosols	X	X	X	X	
SFM-2	Spectrophotometer		X		O3, aerosols			X		
SME	Solar Mesospheric Experiment		X	X	O3, O2(1Δ), NO2		X			
TES	Tropospheric Emission Spectrometer	X	X		HNO3, O3, NO, H2O, CH4, CO, SO2	X	X			
TOMS	Total Ozone Monitoring Spectrometer	X	X		O3, SO2, aerosols	X				

Table 1-1: The different passive satellite instruments designed to determine trace gas distributions in the atmosphere, coverage of their measurements, species measured and observation geometries. The list of sensors refers to figure 1-1.

- 1) TR = troposphere, ST = stratosphere, ME = mesosphere
- 2) N = nadir, L = limb, SO = solar occultation, LO = lunar occultation, STO = stellar occultation
- 3) upper troposphere

The Initial Phases of SCIAMACHY

Limb, nadir and occultation measurements are made during every orbit. Trace gases, aerosols, clouds and the surface of the Earth modify the light observed by SCIAMACHY via absorption, emission and scattering processes. Inversion of the radiance and irradiance measurements allows retrieval of the amounts and distributions of a significant number of constituents from their spectral signatures.

The Initial Phases of SCIAMACHY

A first attempt to perform DOAS from space, MAP (Measurement of Atmospheric Pollution) was made by J.P. Burrows, D. Perner and P.J. Crutzen at the Max Planck Institut für Chemie in early 1985, in response to an ESA call for research instruments to fly on EURECA, a free-flying platform to be released from the Space Shuttle for making measurements over several months. During the period from 1985 to 1988 the concepts for remote sounding of atmospheric chemical constituents and parameters was refined and developed further. Additional scientists joined a growing scientific team. The concept of SCIAMACHY resulted from these endeavours.

The SCIAMACHY proposal *(Burrows et al. 1988a)* was submitted in July 1988 by the SCIAMACHY Science Team – and supported by the German Space Agency DARA GmbH (now DLR) – in response to ESA's call for experiments to fly on-board the Polar Platform, an element of the Columbus Programme. This mission, the Polar Orbiting Earth Observation Mission (POEM-1), finally evolved into the mission now better known as ENVISAT.
In February 1989 a peer review selected SCIAMACHY to be part of the payload of ENVISAT and a phase A feasibility study was initiated in summer 1989. During Phase A the Dutch Space Agency (NIVR) supported Dutch industry to join the SCIAMACHY consortium. Later in Phase B, the Belgian Federal Science Policy Office decided to also participate in the SCIAMACHY programme by cooperating with the Dutch partner.

In April 1989, SCIAMACHY was also identified to become part of the payload of the German research program ATMOS of the German Ministry of Science and Technology (BMFT). The aim of ATMOS was to investigate the use of instrumentation on a dedicated small satellite platform for Earth System Science. After the decision was made to support ESA's Polar Platform with a full complement of Earth observation instruments, the ATMOS program focused on the development of SCIAMACHY in Germany and providing some additional support to aspects of the ESA developed instruments MIPAS (Michelson Interferometer for Passive Atmospheric Sounding) and MERIS (Medium Resolution Imaging Spectrometer).

After phase A, lasting from 1989 to 1990, SCIAMACHY was selected for flight by ESA as a national contribution to the ENVISAT project. The ESA conference at ministerial level approved the ENVISAT mission in November 1992 and around this time also the German and Dutch governments initiated the development of the SCIAMACHY instrument hardware. These early decisions triggered the development of one of the major national space projects in Germany and The Netherlands in the past decade.

It is interesting to note that under the impression of the observation of the precipitous loss of ozone in austral spring mid of the 1980's, ESA was recommended at the *ESA User Consultation* meeting in Paris, during November 1988, to start measurements of relevance to atmospheric composition earlier than the launch of ENVISAT. In this context ESA announced a call for experiments to measure atmospheric constituents from ERS-2, which was under construction at that time. As a result, J.P. Burrows and P. Crutzen proposed the SCIA-mini experiment (*Burrows et al. 1988b*), being derived from the SCIAMACHY instrument concept. This proposal was selected but subsequently recommended for simplification. After this exercise, including for example descoping of the limb measurement mode, the re-named instrument GOME was accepted for flight on ERS-2. Based on the original SCIAMACHY concept and benefiting from its scientific and industrial development work, it was 'fast tracked' ahead of its much more challenging successor. GOME fitted into redundant platform resources, known to be available aboard ERS-2 and was successfully designed, constructed and made ready for launch in 1995 within only four years. The instrument was flying on the ERS-2 satellite until deorbiting in 2011. Its success has demonstrated the feasibility and capabilities of this new instrument concept. Much of the experience gained with GOME can be used directly for SCIAMACHY.

SCIAMACHYs Goals

1.2 SCIAMACHY's Goals

The main objectives of the SCIAMACHY mission are to improve our knowledge of global atmospheric composition, its change in response to both natural and anthropogenic activity and the processes associated to it as well as the related global issues of importance to the chemistry and physics of our atmosphere such as:

- the impact of anthropogenic activity and natural processes on tropospheric ozone, air quality and global warming,
- exchange processes between the stratosphere and troposphere,
- the interaction of stratospheric chemistry and dynamics,
- natural modulations of atmospheric composition resulting from volcanic eruptions, lightning, solar output variations (e.g. solar cycle), or solar proton events.

To achieve these goals, SCIAMACHY was proposed to deliver a multitude of parameters characterising the system *Earth-Atmosphere-Sun*, especially key trace gases and parameters in the troposphere and stratosphere. The following gases were targeted for measurement: O2, O3, O4, NO, NO2, NO3, CO, CO2, HCHO, CH4, H2O, N2O, SO2, BrO, OClO. The combined use of nadir and limb observations yields tropospheric amounts of the constituents down to the ground or cloud top depending on cloud cover. In addition to the trace gases, information on clouds (cloud top height, cloud optical thickness, ice-water cloud discrimination) and aerosol can be deduced from the SCIAMACHY measurements. Particularly interesting, among these, are Polar Stratospheric Clouds (PSC) and Noctilucent Clouds (NLC), also referred to as Polar Mesospheric Clouds (PMC).

Table 1-2 summarises the parameters to be derived from SCIAMACHY measurements and their application areas. It is expected that the data sets obtained by SCIAMACHY can significantly contribute to the quantification of the complex interactions between natural and human activities, climate, atmospheric composition, and the relevant chemical and physical processes.

Subject	***Parameter from SCIAMACHY Data***	***Application Areas***
Surface	spectral surface albedo, UV A/B, chlorophyll content	Earth radiative budget ocean biology spectral surface characteristics
Troposphere (incl. Boundary Layer[1])	columns of O3, NO2, BrO, SO2, HCHO, CHOCHO, H2O, CO, CO2, CH4, clouds, aerosol, actinic flux	transport and transformation of pollutants including air qualitytropospheric ozone and oxidation potentialcarbon budget quantification of emissionsclimate-chemistry interaction
Tropopause Region	concentrations of O3, NO2, H2O, CO, CH4, Clouds, thermodynamic phase of clouds	transport processes in the tropopause regionwater budget, including ice clouds impact of aviation on climateclimate-chemistry interaction
Stratosphere	profiles of O3, NO2, BrO, OClO, H2O, aerosol, Polar Stratospheric Clouds	development of the ozone layerclimate-chemistry interactions solar-terrestrial interactions
Mesosphere	profiles of O3, NO, OH, metal ions, temperature, Polar Mesospheric Clouds	climate-chemistry interactionssolar-terrestrial interactions
Top of the Atmosphere	Earth spectral reflectance	Earth radiative budget
Sun	spectral solar irradiance, Mg-Index (solar activity)	Earth radiative budgetsolar-terrestrial interactions, solar physics

[1] Sensitivity to boundary layer dependent on surface albedo, cloudiness and aerosol loading

Table 1-2: Summary of parameters to be derived from SCIAMACHY and the relevant application areas.

The Atmospheric Layers

The Atmospheric Layers

The Earth's atmosphere is a complex system comprising a set of layers, which differ in their temperature gradient with respect to altitude. Figure 1-2 shows typical temperature and pressure profiles for mid-latitudes. The rate of temperature change in the atmosphere as a function of height can be used to define regions of positive and negative gradient or lapse rate. Starting at the Earth's surface, the temperature decreases up to the region known as the tropopause. The latter separates the troposphere, which is vertically well mixed, from the stratosphere, which is characterised by slow vertical mixing. In the stratosphere the temperature increases from the tropopause to the stratopause, which separates the stratosphere from the mesosphere. In the thermosphere, above the mesosphere, the temperature increases again.

fig. 1-2:

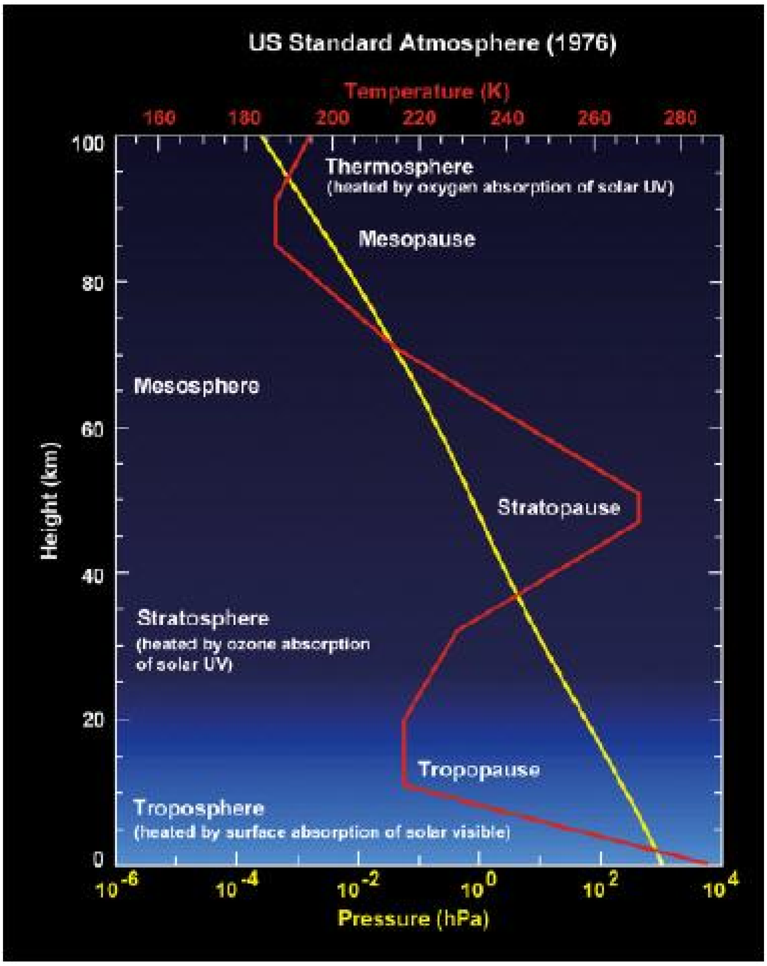

Atmospheric pressure and temperature profiles for mid latitudes (US Standard Atmosphere)

The increase in temperature in the stratosphere results mainly from the absorption of solar radiation between 200-300 nm by the stratospheric ozone layer. In the thermosphere a different but related mechanism results in a temperature increase, caused by the absorption of short wavelength solar radiation typically below 200 nm by molecules, atoms and ions. The temperature of the thermosphere is modulated significantly by the solar cycle.

The pressure of the atmosphere is highest at the Earth's surface and decreases with height according to the barometric formula. The height of the tropopause varies between about 8 km at the poles and 16 km in the tropics. The stratopause occurs at typically about 45-50 km and the mesopause typically at 85-90 km. Between 80 and 90% of the atmospheric mass is contained within the troposphere. The troposphere and stratosphere contain over 95% of the mass of the atmosphere.

Anthropogenic Impact on the Earth-Atmosphere System

Anthropogenic Impact on the Earth-Atmosphere System

The composition of the Earth's atmosphere is different from that of neighbouring planets such as Mars and Venus, which are apparently lifeless. Fossil records indicate that the atmosphere evolved to its present composition as a result of life. The atmospheric increase of the concentration of molecular oxygen since several billion years indicates that it resulted from photosynthesis after the appearance of life *(*e.g. *Wayne 1992)*. With the formation of a sufficiently thick ozone layer harmful short wave radiation became attenuated so that life could spread over the Earth's surface, initially in the oceans still requiring the protecting environment of water, later also on land. According to the *Gaia hypothesis* the biosphere has played an important role in determining the composition of the atmosphere since life on Earth began *(Lovelock 1979)*. This hypothesis also suggests that the biosphere maintains favourable conditions for life on Earth. On geological timescales the impact of anthropogenic activities on the atmosphere has been of minor significance. However, since the onset of the industrial revolution at the end of the 18th century land use, energy and food requirements for the increasing human population have risen dramatically with the consequence of severe impacts on the Earth environment, especially to the Earth's atmosphere. Examples relating to significant modifications of the Earth's atmosphere include (after *Crutzen and Stoermer 2000*):

- Within a few generations fossil fuels that were generated over several hundred million years have been exhausted. The release of SO2, globally about 160 Tg/year into the atmosphere by coal and oil burning, is at least two times higher than the sum of all natural emissions, occurring mainly as marine dimethyl-sulfide from the oceans.
- 30-50% of the land surface has been transformed by human activities; more nitrogen is now fixed synthetically and applied as fertilizer in agriculture than is fixed naturally in all the terrestrial ecosystems.
- The escape into the atmosphere of CO and NOx from fossil fuel and biomass combustion likewise is larger than the natural inputs, giving rise to photochemical ozone (smog) formation and degraded air quality in large regions of the Earth.
- Several climatically important greenhouse gases have substantially increased in the atmosphere: CO2 by more than 30% and CH4 by even more than 100%, accelerating the radiative forcing. CO2 and CH4 are now regulated via the Kyoto Protocol.
- Mankind releases many new and not naturally produced substances into the environment. Some of them, the chlorofluorocarbon gases, have led to the Antarctic *ozone hole* and would have destroyed much of the ozone layer if no international regulatory (Montreal Protocol) measures to end their production had been initiated.

Considering the major and still growing impacts of human activities on the Earth and the atmosphere on global scales, Crutzen and Stoermer proposed to use the term *Anthropocene* for the current geological epoch *(Crutzen and Stoermer 2000)*. (see fig. 1-3)

The behavior and composition of troposphere, stratosphere and mesosphere are coupled through dynamic, radiative and chemical processes as indicated in figure 1-3. Overall, the conditions experienced by the biosphere at the Earth's surface are determined in a complex manner by the physical and chemical processes occurring in all these regions.

Tropospheric Chemistry

fig. 1-3:

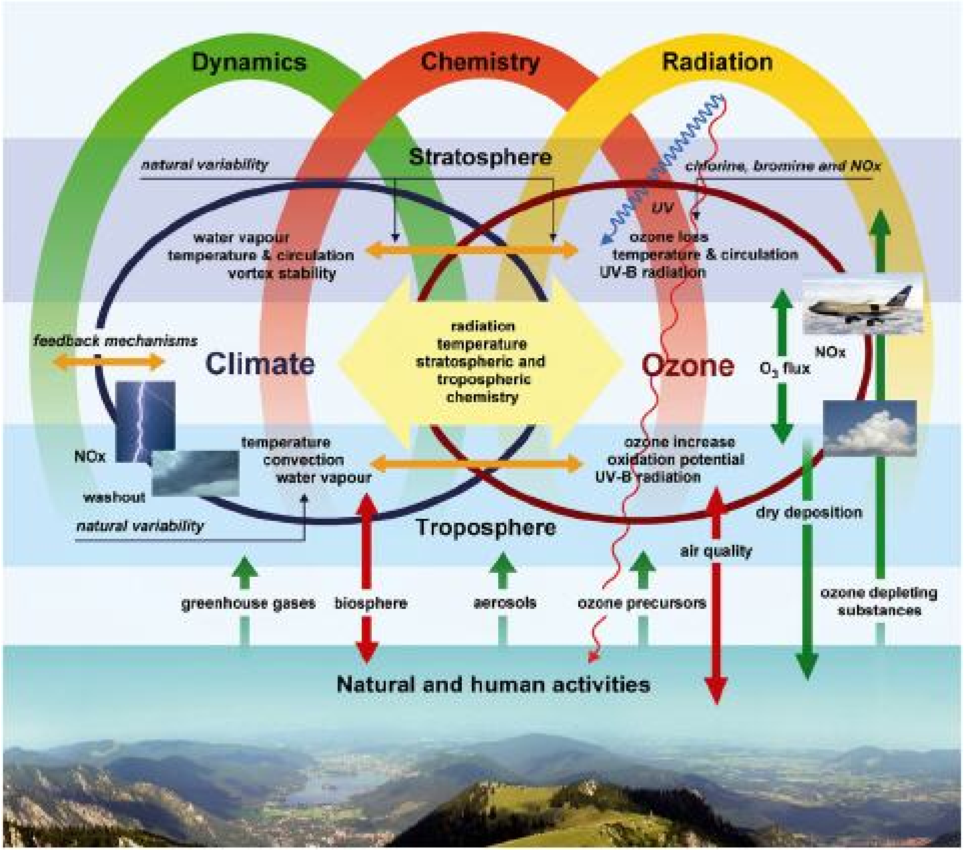

Interactions between human activity, atmospheric composition, chemical and physical processes and climate. (Graphics: DLR-IMF, after WMO-IGACO 2004)

Tropospheric Chemistry

Most gases, like greenhouse gases (CO2, CH4, etc.) or pollutants (NO2, CO, etc.) from natural processes and human activities are emitted into the troposphere. The main source of pollutants in the northern hemisphere is fossil fuel combustion (energy for traffic, industry and domestic heating) coupled with some biomass burning. In the southern hemisphere biomass burning is the dominating source of pollutants. Pollutants are emitted within urban and near-urban areas where they are dispersed over the surrounding countryside and, depending on the atmospheric lifetime of the pollutant or its secondary reaction product(s), are transported around the globe.

Tropospheric processes as sketched in figure 1-4 are well known to exhibit strong variability influenced by meteorology, diurnal variations in the sources of the emissions and solar illumination. Photolysis of O3 initiates the production of OH that determines, to a large extent, the oxidative (or cleansing) capacity of the troposphere. The role of the halogen oxides in the boundary layer as oxidants is currently a research matter. Many of the tropospheric trace gases are transformed into acids and other soluble products which are removed from the atmosphere by precipitation or by uptake on aerosols and subsequent dry deposition on surfaces. The atmospheric oxidation efficiency is vital in the control of radiatively and chemically active pollutants. Therefore, any change in the atmospheric oxidation efficiency directly affects the air quality, atmospheric chemical and radiative budgets and global biogeochemical cycles.

The lack of information on the temporal and spatial distributions of the relevant species, as well as the source strengths of CO, CH4 and NOx (NO and NO2), severely limits the quantitative understanding of the processes involved in tropospheric ozone production and destruction. This is also a prerequisite for quantitative estimates of the hydroxyl radical distribution and thus of the cleansing power of the atmosphere which is expected to be changing as a result of increasing emissions and resulting concentrations of O3, CH4, NOx and CO. One of the major challenges facing atmospheric science is to assess, understand and quantify the impact on air quality of a changing climate and atmospheric composition. (see fig. 1-4)

The Tropopause Region

fig. 1-4:

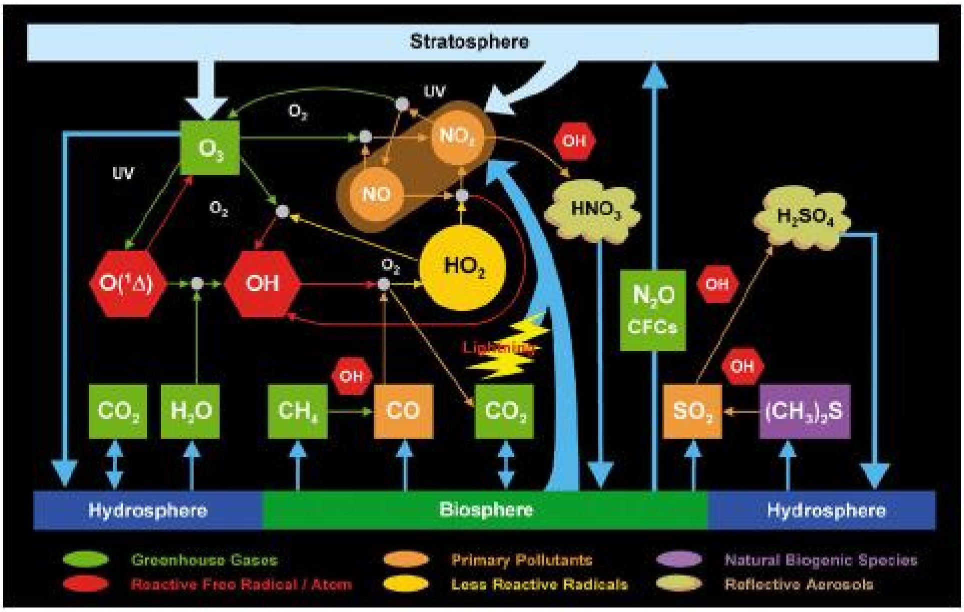

The dominant physical and chemical processes determining the composition of the troposphere. (Graphics: WMO-IGACO 2004)

SCIAMACHY is the atmospheric chemistry sensor on ENVISAT designed to determine the amounts of trace gases and aerosol in the lower troposphere, including the planetary boundary layer. From SCIAMACHY nadir and limb measurements tropospheric columns of O3, CO, NO2, BrO, CH4, H2O, SO2 and HCHO are retrieved. In cloud free regions, the tropospheric measurements of SCIAMACHY include the planetary boundary layer. In addition, surface spectral reflectance, aerosol and cloud parameters – cover and cloud top height – and the tropospheric radiative flux from 280-2380 nm will be retrieved. These data are required for studies of the oxidising capacity of the troposphere, photochemical O3 production and destruction, tropospheric pollution (biomass burning, industrial activities, aircraft), long range transport of pollutants as well as quantification of natural and human emissions.

The Tropopause Region

Exchange of gases and particles between the stratosphere and the troposphere is of importance for the chemical composition of both regions and the atmospheric energy budget in the case of water vapour *(Holton et al. 1995)*. For example downward transport of stratospheric ozone is a source of tropospheric ozone which, as a precursor of OH radicals, to a large extent determines the oxidising power of the troposphere. In the opposite direction upward transport of the precursor molecules (e.g. H2O, CH4, CFCs) originating from the planetary boundary layer provides the feedstock for ozone-destroying HOx, NOx, BrOx and ClOx radicals. For example CH4 is emitted into the planetary boundary layer. Due to their long tropospheric lifetime molecules are transported to the stratosphere, where they are the dominant source of the ozone-destroying HOx radicals. An adequate knowledge of the processes that determine stratosphere-troposphere exchange and the distribution of trace gases, especially in the lower stratosphere, is required. Photo-chemically stable gases in the troposphere are useful as tracers for transport of tropospheric air into the stratosphere and for stratospheric dynamics, e.g. CH4 and H2O. Similarly, gases which have relatively high stratospheric but low tropospheric abundances such as O3, can be used as tracers for downward transport from the stratosphere.

For the investigation of stratosphere-troposphere exchange, SCIAMACHY measurements of the height resolved profiles of O3, H2O, CH4, BrO and NO2 as well as aerosol will be of primary significance. In addition, SCIAMACHY will deliver information on the thermodynamical phase of clouds, which are important for the water and energy budget especially in the tropical tropopause region. With these measurements investigations of the downward transport of stratospheric O3 and upward transport of important species (e.g. aerosol, CH4, H2O) become possible. In the neighbourhood of the tropopause the different measurement modes of SCIAMACHY will have different vertical and horizontal resolutions. The solar and lunar occultation mode yields measurements with a vertical resolution of 2.5 km and a horizontal resolution of 30 km across track and extending roughly 400 km along track. For the limb measurements the spatial resolution is approximately 3 km vertically and typically 240 km horizontally across track and extending roughly 400 km along track. Therefore studies of relatively small scale features such as tropopause folding at mid-latitudes requiring a high spatial resolution are unlikely to be unambiguously observed by SCIAMACHY. However larger scale stratosphere-troposphere exchange will be readily observed.

Stratospheric Chemistry and Dynamics

Stratospheric Chemistry and Dynamics

No part of the global environment has been disturbed by human activity as significantly as the stratosphere. In the upper stratosphere and lower mesosphere ozone is removed by catalytic cycles involving halogen oxides. In addition, a very substantial depletion of stratospheric ozone over Antarctica has been observed during springtime since the end of the 1970's. This depletion is largely due to the emission of industrial chlorofluorocarbon gases (*WMO 2003* and references therein). Also over the Arctic a major depletion of stratospheric ozone by about 100 DU (Dobson Units) has become obvious during springtime in the past decade. Surface reactions on liquid aerosols, nitric acid trihydrate (NAT) particles and ice particles are believed – via the activation of chlorine – to be primarily responsible for these changes. International regulatory measures, in the form of e.g. the Montreal Protocol, having now been taken to eliminate the production of chlorofluorocarbons by the end of the 20th century *(WMO 1995)*. However the amount of stratospheric chlorine will reach its maximum at the beginning of the 21st century. A first recovery of the ozone layer is expected around 2010 *(WMO 2003)*. The loss of ozone in the stratosphere is also affected, in a synergistic manner, by tropospheric emission of greenhouse gases (see figure 1-5). For example, the anthropogenic tropospheric concentrations of nitrous oxide and methane are increasing, leading to additional formation of stratospheric NOx and water vapour (H2O) and potentially enhancing the probability for formation of PSCs. Reactions on these clouds lead to the activation of chlorine radicals that are responsible for the formation of the 'ozone hole'. Thus, even though the stratospheric chlorine content is expected to decline at the beginning of the 21st century, ozone depletion in the lower stratosphere at higher latitudes may not. (see fig. 1-5)

fig. 1-5:

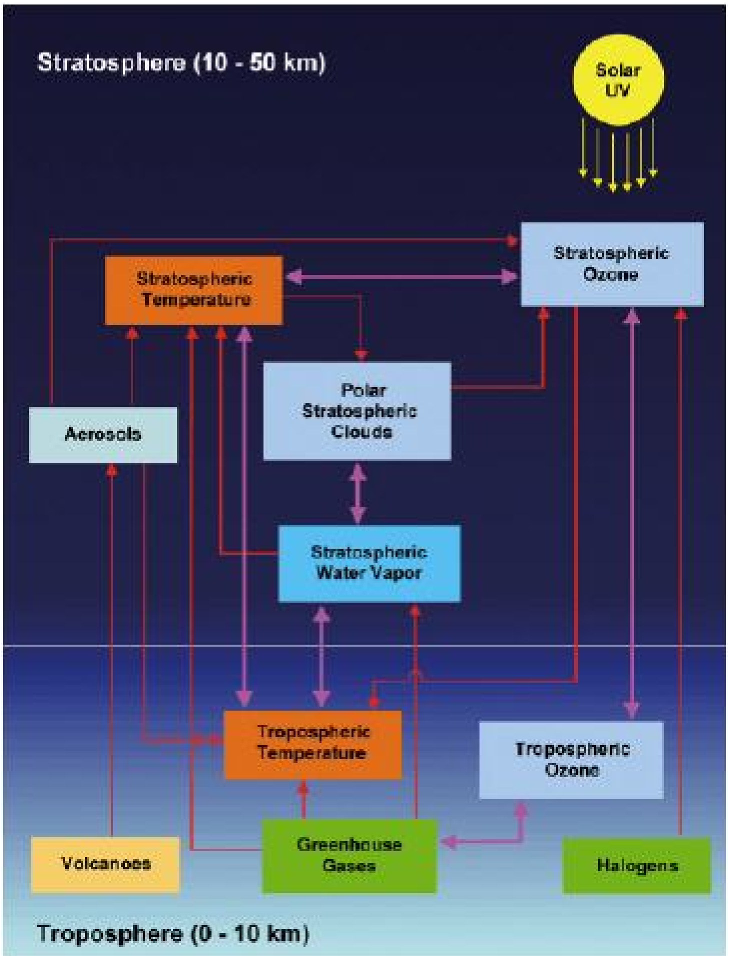

Schematic sketch of the interactions between stratospheric ozone and other atmospheric constituents and processes. Anthropogenic emissions are shown in green while other factors affecting the climate system (e.g., volcanoes) are shown in beige. Red arrows indicate where one species or process affects another. Feedbacks are shown with bold purple lines. For example, decreasing polar stratospheric temperatures increase ozone depletion. Reduced ozone then causes stratospheric cooling, creating a positive feedback. (Graphics after: NIWA)

Mesospheric Chemistry and Dynamics

Future stratospheric aircraft and spacecraft could emit water vapour and nitric oxide into the stratosphere and, as a result of the introduction of advanced supersonic and hypersonic aircraft, environmental issues may ensue. For example the emissions of additional H_2O and NO_x may strongly enhance PSC formation. Improved understanding of stratospheric chemical processes and distributions of trace constituents, including aerosol and PSCs, is essential for environmental assessments of future space and aviation activities.

SCIAMACHY's studies of the stratospheric chemistry and dynamics will utilise the simultaneous retrieval of total columns from nadir measurements and vertical stratospheric profiles from limb and occultation measurements of O_3, NO_2, BrO, H_2O, OClO (under ozone hole conditions), as well as aerosol and stratospheric cloud information. SCIAMACHY is intended to make measurements when halogen loading of the stratosphere maximizes at the beginning of the 21st century. In general, SCIAMACHY observations will yield detailed information about the development of stratospheric O_3 above the Arctic and Antarctica, the global stratospheric active halogen species (BrO, OClO), and the global O_3 budget as a function of the height in the atmosphere. Thus the SCIAMACHY data set may allow testing of the accuracy of current stratospheric models and their predictive capabilities.

Mesospheric Chemistry and Dynamics

The mesosphere extends from the temperature maximum at the stratopause around 50 km altitude to the atmospheric temperature minimum at the mesopause around 85 km. There has been much discussion of upper stratospheric and mesospheric chemistry in the context of the *Ozone Deficit Problem (Crutzen at al. 1995, Summers et al. 1997)*. It has also been suggested that monitoring of H_2O in the lower mesosphere may offer an opportunity for the early detection of climate change *(Chandra et al. 1997)*. Satellites have provided some data about mesospheric temperatures and the temporal and spatial distributions of O_3. In this context, little is known about the global dynamics and chemistry. It is expected that the growth in atmospheric CH_4 will lead to an increase in mesospheric H_2O concentrations which might also result in enhanced PMC formation around 85 km.

In the upper stratosphere and lower mesosphere, SCIAMACHY measurements yield profiles of temperature, O_3, NO, and $O_2(^1D)$ as well as data on PMCs. These measurements can be used to study the distribution of O_3 and the global circulation. The O_3 destruction by mesospheric and upper stratospheric NO will be investigated. In contrast to the retrieval of the majority of trace gases from SCIAMACHY data, NO and $O_2(^1D)$ profiles are to be determined from their emission features rather than their absorptions. The combination of height resolved O_3, $O_2(^1D)$, and UV radiance products from SCIAMACHY provides detailed information about the photolysis of O_3 in the upper stratosphere and mesosphere. This will serve as an excellent opportunity to test our current photochemical knowledge of the mesosphere.

Global Warming and Climate Change

Although already discussed over a century ago by Arrhenius in 1896 *(Arrhenius 1896)*, the issue of global warming caused by the injection of the so-called *greenhouse gases* such as CO_2 and CH_4 into the atmosphere has become prominent in recent years. This is because of the rapid increase in atmospheric CO_2 associated with the combustion of fossil fuels in the second half of the 20th century. The recognition that other species can behave in a similar manner, but often more effectively than CO_2, has resulted in the definition of the *global warming potential* of trace gases. The list of greenhouse gases now comprises many species including H_2O, CO_2, CH_4, nitrous oxide, CFCs and tropospheric ozone. Governments of many nations, concerned with the potential harmful consequences of global warming, have mandated to make evaluations aiming to provide national and international policymakers with an accurate assessment of our current understanding of climate change *(IPCC 2007)*. The increasing evidence that current global warming is to a large extent man-made was documented in the 4th assessment report of the Intergovernmental Panel of Climate Change (IPCC) in 2007. Figure 1-6 summarises the global annual mean radiative forcing of relevant agents contributing to global warming. (see fig. 1-6)

fig. 1-6:

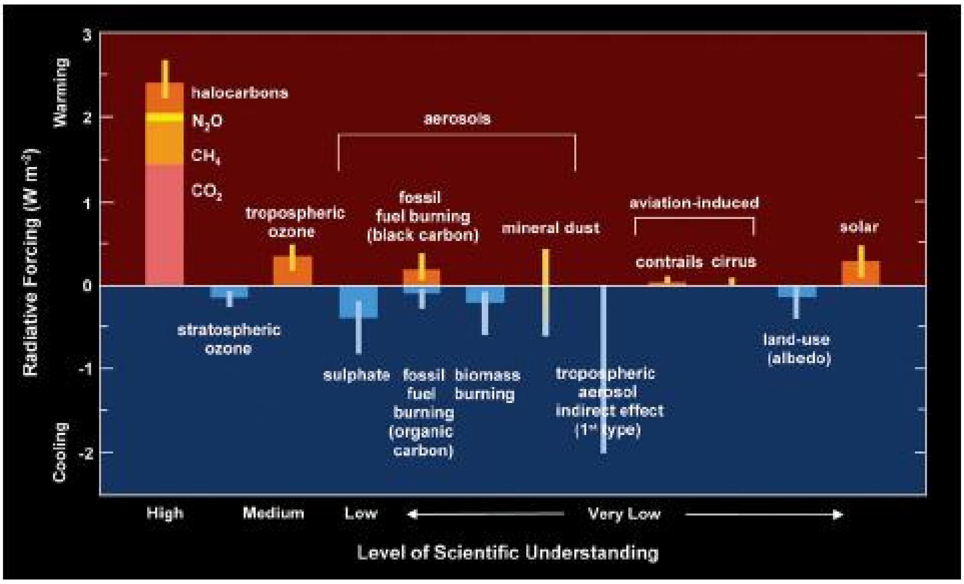

Global, annual mean radiative forcings (Wm-2) due to a number of agents for the period from pre-industrial (1750) to present (late 1990s; about 2000). The height of each box denotes a central or best estimate value while its absence indicates that no best estimate is possible. The vertical bars visualise an estimate of the uncertainty range, for the most part guided by the spread in the published values of the forcing. The uncertainty range specified here has no statistical basis and therefore differs from the use of the term elsewhere in this document. A 'level of scientific understanding' index is associated to each forcing, with high, medium, low and very low levels, respectively. (IPCC 2001)

As the concentrations of atmospheric greenhouse gases and their radiative forcing have continued to increase as a result of human activities, global warming and its impact on the Earth-Atmosphere system will further increase. One of the future challenges is to quantify the complex feedback cycles (see figure 1-3) between climate, atmospheric composition, natural and human activity which are driven by global warming. For example global warming is expected to result in more frequent dry, hot summer periods in Europe – like the summer of 2003 – with degraded air quality in wide parts of Europe.

For use in climate research, SCIAMACHY measurements will provide the distributions of several important greenhouse gases (CH4, CO2, and tropospheric O3), aerosol and cloud data, surface spectral reflectance (280-2386 nm), the incoming solar spectral irradiance and the outgoing spectral radiance (214-2386 nm). The observation of the greenhouse gases CH4 and CO2 will help to better quantify natural emissions globally, thereby improving the scientific basis of the Kyoto Protocol, which was put into force in spring 2005.

As it is intended that SCIAMACHY observations are to be made for many years, this long-term data set will also deliver much unique information useful for the study of the solar-terrestrial interactions and variations of the solar output including its impact on climate change. To maintain continuity with other spectrometers measuring solar spectral irradiance such as SBUV or GOME, SCIAMACHY was calibrated using standard methods which had also been applied to the GOME or SBUV calibration.

CHAPTER 2: What is SCIAMACHY?

2. SCIAMACHY: The Instrument onboard ENVISAT

2.1. Measurement Goals

SCIAMACHY's approach for passive atmospheric sounding from space was to measure *solar absorption spectra* at the top of the atmosphere. Atoms, molecules and particles absorb, emit and scatter the incoming solar electromagnetic radiation. The incoming solar radiation is described to a good approximation by the emission from a black body having a temperature of about 5800 K, modulated by atomic absorption lines, the solar Fraunhofer lines. The upwelling radiation at the top of the atmosphere from the Ultraviolet (UV) to Short-Wave Infrared (SWIR) comprises – after travelling through the atmosphere – the solar output, modified by scattering, absorption and emission processes along its light path through the atmosphere and reflected as well as scattered at the Earth's surface.

SCIAMACHY observed in the wavelength range from 214-2386 nm

- the scattered and reflected spectral radiance in nadir and limb geometry,
- the spectral radiance transmitted through the atmosphere in solar and lunar occultation geometry,
- the extraterrestrial solar irradiance and the lunar radiance.

Trace gases, aerosols, clouds and the surface of the Earth modify the light observed by SCIAMACHY via absorption, emission and scattering processes. Inversion of the radiance and irradiance measurements allows retrieval of the amounts and distributions of a significant number of trace gas constituents from their spectral signatures as well as to obtain information on other atmospheric parameters and even selected surface phenomena. This task requires – beside high quality measurements – an accurate understanding and knowledge of the absorption spectroscopy and the scattering of electromagnetic radiation in the atmosphere and at the Earth's surface.

The targeted atmospheric trace gas species and parameters depend on the main objectives of the SCIAMACHY mission. With the goal to improve our knowledge of:

- global atmospheric composition,
- its change in response to both natural and anthropogenic activity and
- the processes associated to it as well as the related global issues of importance to the chemistry and physics of our atmosphere such as:
  - the impact of anthropogenic activity and natural processes on tropospheric ozone, air quality and global warming,
  - exchange processes between the stratosphere and troposphere,
  - the interaction of stratospheric chemistry and dynamics,
  - natural modulations of atmospheric composition resulting from volcanic eruptions, lightning, solar output variations (e.g. solar cycle), or solar proton events.

SCIAMACHY's list of "deliverables" included tropospheric and stratospheric trace gases, such as e.g. O3, NO2, CO, CO2, HCHO, CH4, H2O, SO2, BrO, OClO. By combining nadir and limb observations tropospheric amounts of the constituents down to the ground or cloud top depending on cloud cover could be determined. In addition to the trace gases, information on clouds (cloud top height, cloud optical thickness, ice-water cloud discrimination) and aerosol were deduced from the SCIAMACHY measurements. Particularly interesting, among these, were Polar Stratospheric Clouds (PSC) and Noctilucent Clouds (NLC), also referred to as Polar Mesospheric Clouds (PMC).

The feasibility of these goals for nadir observations, including measurement principles and retrieval concepts was successfully demonstrated with the Global Ozone Monitoring Experiment (GOME) on ESA's second European Remote Sensing satellite (ERS-2). GOME on ERS-2 was a smaller scale version of SCIAMACHY derived from the original SCIAMACHY concept, measuring in nadir viewing geometry the upwelling radiation at the top of the atmosphere between 240 and 793 nm. ERS-2 had been launched on April 20th, 1995 into a sun-synchronous orbit with an equator crossing time in descending node of 10:30 a.m.. It was deorbited in July 2011, delivering measurements over more than 16 years.

2.2 SCIAMACHY on ENVISAT

SCIAMACHY formed part of the payload of ENVISAT (table 2-1, fig. 2-1). It had, besides AATSR and DORIS, the status of an Announcement of Opportunity Instrument (AOI) contrary to the remaining seven ESA developed instruments (EDIs). As an AOI, SCIAMACHY had been developed and provided by Germany and The Netherlands, including a Belgian contribution. From an operations point of view, however, SCIAMACHY was considered an integral part of ENVISAT's payload following the same guidelines and rules as the EDIs.

ENVISAT Parameters	
Dimensions	26 m x 10 m x 5 m
Total Mass	8140 kg
Payload Mass	2050 kg
Launcher	Ariane-5
Launch	March 1st, 2002

Table 2-1: ENVISAT characteristics

fig. 2-1:

Artist's impression of ENVISAT in orbit. SCIAMACHY was located at the upper right corner of the payload front panel. (photo: ESA)

Together with MIPAS and GOMOS, SCIAMACHY formed ENVISAT's atmospheric mission. The three atmospheric instruments utilized different wavelength ranges and measurement principles. They complement each other such that synergistic views became possible. While SCIAMACHY, as an absorption spectrometer in the UV-SWIR range requed sunlight, MIPAS – operating in the thermal infrared – could measure over the complete orbit. This was also the case for GOMOS, where the UV-VIS component of stars in occultation was used to probe the atmosphere. SCIAMACHY had been viewing in flight direction (limb mode) and towards the sub-satellite point (nadir mode). MIPAS looked along-track into anti-flight and across-track into anti-sun direction. GOMOS could steer its line of sight towards stars which set between anti-flight and across-track anti-sun direction. Additionally, the optical imaging instruments MERIS and AATSR (Advanced Along Track Scanning Radiometer) delivered data for scientific applications in the fields of clouds, aerosols and water vapour. Their nadir views overlapped with SCIAMACHY's nadir geometry thus permitting synergistic analyses.

Orbit and Attitude

ENVISAT operated in a polar, sun-synchronous orbit with a morning descending node crossing (DNX) time (table 2-3). The selected local DNX time of 10 a.m., together with SCIAMACHY's location at the upper right corner on the payload module front panel, was equivalent to the fact that the sun could only be seen when pointing the instrument's line of sight to the left. Orbit perturbations slightly modified the specified reference orbit with time. Once orbit parameters exceeded their limits, an orbit control manoeuvre adjusted the actual orbit. These manoeuvres could either be *In-Plane* (to correct for the effect of air drag on altitude) or *Out-of-Plane* (to adjust the inclination which drifts due to solar and lunar gravity perturbations). SCIAMACHY was one of the instruments which continued with measurements during In-Plane manoeuvres. While executing an Out-of-Plane manoeuvre, SCIAMACHY measurements were interrupted but the thermal status of the Optical Bench Module (OBM) and the detectors remained unchanged.

Orbit and Attitude

During the nominal 5-year mission lifetime from launch to early 2007 both inclination and altitude were maintained within the limits as listed in Table 2-2. This orbit was also applicable in the first part of the ENVISAT mission extension lasting until October 2010. From late October 2010 on, the ENVISAT orbit was lowered by about 17 km for the second part of the mission extension up to at least end of 2013 including a change in the orbit repeat cycle from 35 days / 501 orbits to 30 days / 431 orbits. In order to use the remaining fuel as efficient as possible it had been decided to abandon the fuel-consuming inclination manoeuvres. This causes the inclination and the mean local solar time at DNX to drift as illustrated in Figure 2-2.

Orbital Parameters	
Semi-major axis	7159.50 0.07 km
Inclination	98.55 0.01
Eccentricity	0.001165 (-0.001165/+0.005)
Argument of perigee	90.0 3
Mean altitude	799.8 km
Orbital period	100.6 min
Type	Polar, sun-synchronous
Mean local time at DNX	10:00 a.m. 5 min
Orbits per day	14 11/35
Repeat cycle	35 days (501 orbits)

Table 2-2: Nominal ENVISAT orbit

Fig. 2-2: Nominal and mission extension orbit of ENVISAT (Graphics: DLR-IMF).

ENVISAT's local relative orbital reference coordinate frame forms an orthogonal righthand system with the -Y (roll) axis pointing close to the velocity vector of the platform and the Z (yaw) axis pointing in the direction of the outward local normal of the Earth's reference ellipsoid (Figure 2-3). For the specification of target directions, azimuth and elevation angles are defined. Azimuth is measured clockwise from the -Y axis around the -Z axis to the projection of the target Line-of-Sight (LoS) in the plane perpendicular to the orbital plane containing the velocity vector. Elevation is the angle between that projection and the target line of sight.

ENVISAT On-board Resources

fig. 2-3:

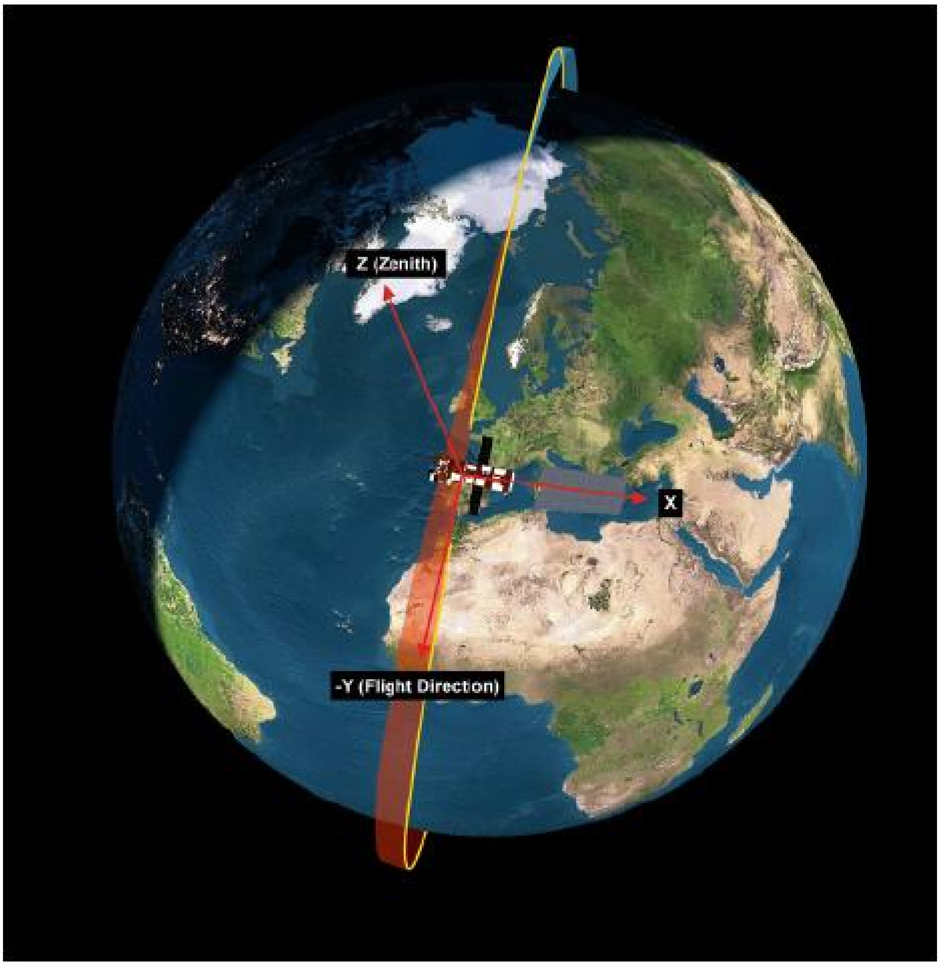

The coordinate system specified in the ENVISAT mission. Platform and instruments use the same definitions. The red/blue areas right and left of the orbit sketch the platform yaw steering. It gradually increases from pole to equator and decreases from equator to pole. The local -Y axis always points to that side, where Earth rotation moves the surface towards the sub-satellite track. (Graphics: DLR-IMF)

The attitude mode of ENVISAT for nominal operations is the *stellar yaw steering mode*. Yaw steering is required by the radar imaging instruments in order to compensate for the rotational velocity of the Earth's surface in the sub-satellite point. This mode is obtained via small rotations about the roll, pitch and yaw axis, with the transformation around yaw being by far the dominant component. Maximum yaw amplitude of ±3.92° occurs when ENVISAT passes the equator at ascending or descending node. Close to the poles it reaches 0°, i.e. yaw steering imposes a sinusoidal 'wobble' of the platform around the flight direction. On the dayside part of the orbit the platform is turned to the right side of the flight direction, in the eclipse part to the left. For measurements with long Line-of-Sights requiring high spatial resolution, particularly when SCIAMACHY is operating in limb mode, the quality of the scientific results, e.g. altitude profiles, is strongly dependent on the precise knowledge of the platform attitude.

ENVISAT On-board Resources

The total ENVISAT payload shares the same on-board resources. Thus instrument operations must be designed such that no interferences occur. For SCIAMACHY this is particularly important in respect of the allocated data rate. Generated data rate depends on an instrument and its measurement mode. The Regional Mission of ASAR (Advanced Synthetic Aperture Radar) and MERIS produces data with high and medium rates whilst the Global Mission, with its lower data rate, is established by all other instruments together with ASAR and MERIS in low rate modes. Global Mission instruments are operated continuously throughout the orbit. Measurement data from the Global Mission instruments are processed on-board via the High Speed Multiplexer (HSM). SCIAMACHY uses HSM resources together with MERIS in Reduced Resolution (RR) mode (fig. 2-3). As long as MERIS runs in RR mode, only the low rate data can be generated by SCIAMACHY. This MERIS mode is operational for solar zenith angles < 80°. Although SCIAMACHY is able to generate data with a data rate of 1.8 Mbit/sec yielding measurements with high spatial resolution, for most parts of the orbit only the low rate of 400 kbit/sec is therefore possible. Only when ENVISAT is close to sunrise during each orbit, the solar zenith angle condition is not fulfilled for MERIS and measurements with the higher rate are possible.

fig. 2-4:

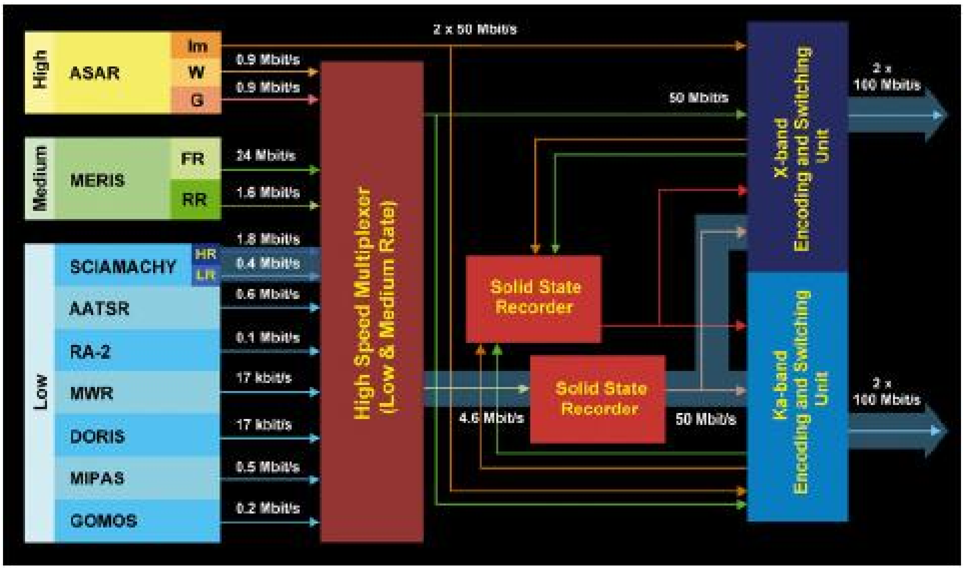

Schematic view of the ENVISAT on-board data handling. SCIAMACHY shares HSM resources with the other instruments generating low rate data. Full orbit data of the Global Mission is stored on one of the solid state recorders and then disseminated to ground via X-band or Ka-band. (Graphics: DLR-IMF)

ENVISAT measurement data can be transmitted to ground stations via the Artemis data relay satellite using the Ka-band. The antenna on the platform is located on the upper payload panel just above SCIAMACHY's sub-solar port, i.e. the instrument window permitting observations of the sun when it has reached highest elevation each orbit. When the antenna dish is deployed in operating position, it vignettes SCIAMACHY's sub-solar window. Sub-solar measurements, necessary to monitor the long-term behaviour of optical components, are therefore only possible when the Ka-band antenna has been moved to its parking position.

ENVISAT Ground Segment

All information generated by the instrument, i.e. recorded housekeeping (HK) telemetry reporting the instrument status over the complete orbit and measurement data, is downlinked either via the X-band or the Ka-band link. The X-band link transmits data to the high latitude receiving ground station at Kiruna while the Ka-band link connects ENVISAT via the Artemis data relay satellite with the receiving station at ESRIN. In the early phase of the mission, when Artemis was not operational, only Kiruna and an additional X-band station at Svalbard were used. In the nominal 'Kiruna-Artemis' scenario, Global Mission data are provided to Kiruna for 8 orbits per day, to ESRIN for 6 orbits per day. HK telemetry is also sent via the command & control (C&C) S-band link of the Kiruna station and its supplementing Svalbard C&C facility. This telemetry stream spans only the coverage interval of Kiruna or Svalbard visible orbits. Of the 14.3 orbits per day, 9-10 are Kiruna visible orbits with coverage intervals amounting up to 12 min (spacecraft elevation > 5°). In addition, low elevation coverages may also be used. Each coverage in a daily cycle occurs at a different time relative to ascending node crossing (ANX) depending on the actual location of the orbital track.

ENVISAT and its instruments are controlled via the Flight Operation Segment (FOS) and the Payload Data Segment (PDS). FOS handles all command & control issues including flight dynamics aspects. In addition, mission planning is performed in cooperation with the PDS. FOS comprises the ENVISAT Flight Operation Control Centre (FOCC) at ESOC and the S-band stations at Kiruna and Svalbard. The PDS is the responsible entity for ENVISAT measurement data. It is an European wide distributed ground segment.

Central control of the PDS occurs at the Payload Data Control Centre (PDCC) at ESRIN. The Payload Data Handling Stations in Kiruna (PDHS-K) and Frascati (PDHS-E) not only receive X-band or Ka-band data but also process and disseminate data in near-realtime (NRT). For data products in offline (OL) mode processing, archiving and distribution is shared among several facilities. At the Low Rate Reference Archive Centre (LRAC), located at Kiruna, level 0 data are consolidated and archived. From these consolidated products, the Processing and Archiving Centres (PAC) generate, archive and disseminate consolidated level 1b and level 2 products. Also NRT products from the two PDHS are collected at the PACs. Although implemented at national remote sensing facilities, PACs are an integral part of the PDS.

2.3 Instrument Description

2.3.1 Science Requirements and Instrument Concept

To detect all species listed in table 2-1, it is essential that SCIAMACHY continuously observes the wavelength ranges 214-1773 nm, 1934-2044 nm and 2259-2386 nm. The retrieval of the amount of constituents depends on the ability to measure their absorptions precisely. Retrieving total column concentrations of minor trace gases with an accuracy of 1-5 % – or 5-10% for their profiles – requires observing intensity changes of 10-3-10-4 with respect to the optical depth. This can only be achieved with an instrument providing measurements with a high signal-to-noise ratio and a good radiometric calibration.

To fulfil the mission objectives with respect to spatial resolution and coverage, it is necessary to observe the scattered and reflected solar photons in nadir and limb direction as well as the light transmitted through the atmosphere in solar and lunar occultation geometry *(Burrows and Chance 1991, Bovensmann et al. 1999)*. For calibration and monitoring purposes the extraterrestrial solar and lunar irradiance above the atmosphere has to be determined. As total column amounts and height resolved profiles are required, SCIAMACHY alternately observes the atmosphere in limb and nadir viewing. Combining both geometries of a single orbit for the same volume of air allows the study of tropospheric properties. Global coverage has to be obtained within 3 days in limb or nadir mode.

These requirements, together with the accommodation on the ENVISAT platform, were translated into an instrument concept providing spectroscopy capabilities from the UV via VIS and Near Infrared (NIR) to SWIR with

- moderately high spectral resolution
- high radiometric accuracy
- high spectral stability
- high dynamic range
- high signal-to-noise

Viewing geometries must account for field of views in nadir, limb (in flight direction), sunrise and moonrise direction. Additional access to the sun around occurrence of the sub-solar condition, i.e. the sun reaches highest elevation above the instrument, is needed. Maintaining thermal stability at several temperature levels is a prerequisite for achieving high radiometric and spectral accuracy. This is ensured by thermal control systems. Finally, instrument control must be executed continuously in a highly autonomous manner with the ability to react to a wide variety of operations conditions. This includes not only measurement data relevant parameters as e.g. line-of-sight, signal-to-noise levels and spectral sampling but also the tasks of overall instrument command & control. All SCIAMACHY instrument requirements were finally documented in the *SCIAMACHY Instrument Requirements Document* (SIRD, *DARA 1998*) (table 2-3).

Instrument Dimensions	
Optical Assembly	109 cm 65 cm 101 cm
Electronic Assembly	82 cm 90 cm 28 cm
Radiant Cooler Assembly	51 cm 91 cm 62 cm
Total Mass	215 kg
Power Consumption	140 W

Table 2-3: SCIAMACHY instrument physical characteristics

Conceptually, SCIAMACHY is a passive imaging spectrometer, comprising a mirror system, a telescope, a spectrometer, and thermal and electronic subsystems. Functionally, three main blocks, the Optical Assembly (OA), the Radiant Cooler Assembly (SRC) and the Electronic Assembly (EA) can be identified. The instrument is located on the upper right (i.e. starboard, referring to nominal flight direction) corner of the ENVISAT platform with the OA mounted onto the front and the EA mounted onto the top panel. The Radiant Reflectance Unit (RRU) of the SRC points sideways into open space away from any heat source. Interfaces with the ENVISAT platform exist for the provision of on-board resources. These include power and command interfaces in one direction. In the other direction measurement data and HK telemetry from SCIAMACHY are routed into the overall ENVISAT data stream for downlinking.

2.3.2 Optical Assembly

The Optical Assembly is the part of the instrument which collects solar radiation as input and generates the spectral information as output. This occurs in the Optical Unit (OU). For maintaining the specified thermal conditions, the OA includes Radiator A and the Thermal Bus Unit. The Optical Unit is organised into two levels. Entrance optics, pre-disperser prism, calibration unit and channels 1 & 2 are contained in level 1 facing in the flight direction (fig. 2-5). Channels 3-8 are located in level 2 (fig. 2-6). All components are mounted onto the OBM which serves as the structural platform and maintains overall alignment between modules. By combining optical components described below, various optical paths (‘trains’) from external and internal light sources to detectors can be established (fig. 2-7).

fig. 2-5:

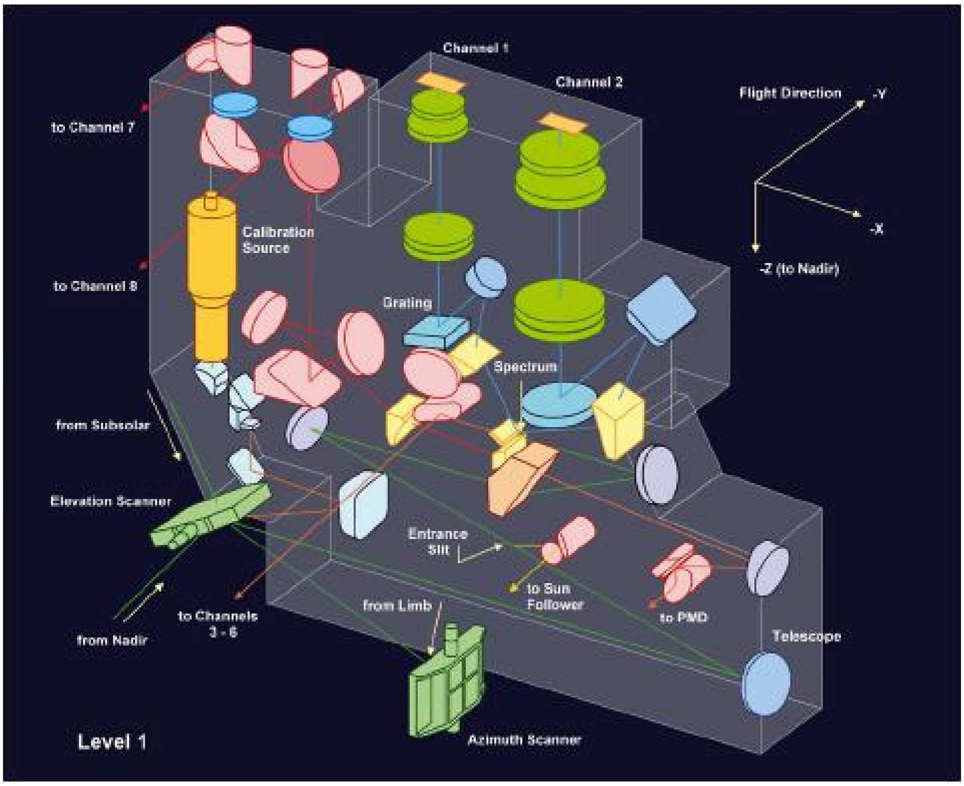

Optical configuration level 1. (graphics: DLR-IMF, modified after SJT 1996)

fig. 2-6:

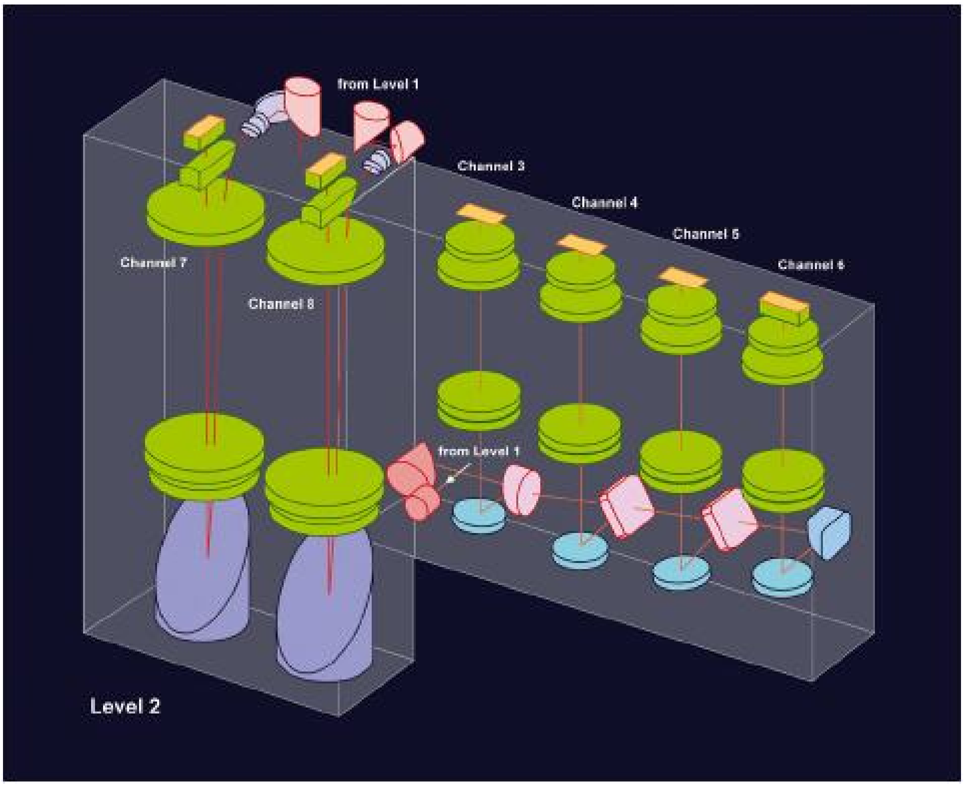

Optical configuration level 2. (graphics: DLR-IMF, modified after SJT 1996)

fig. 2-7:

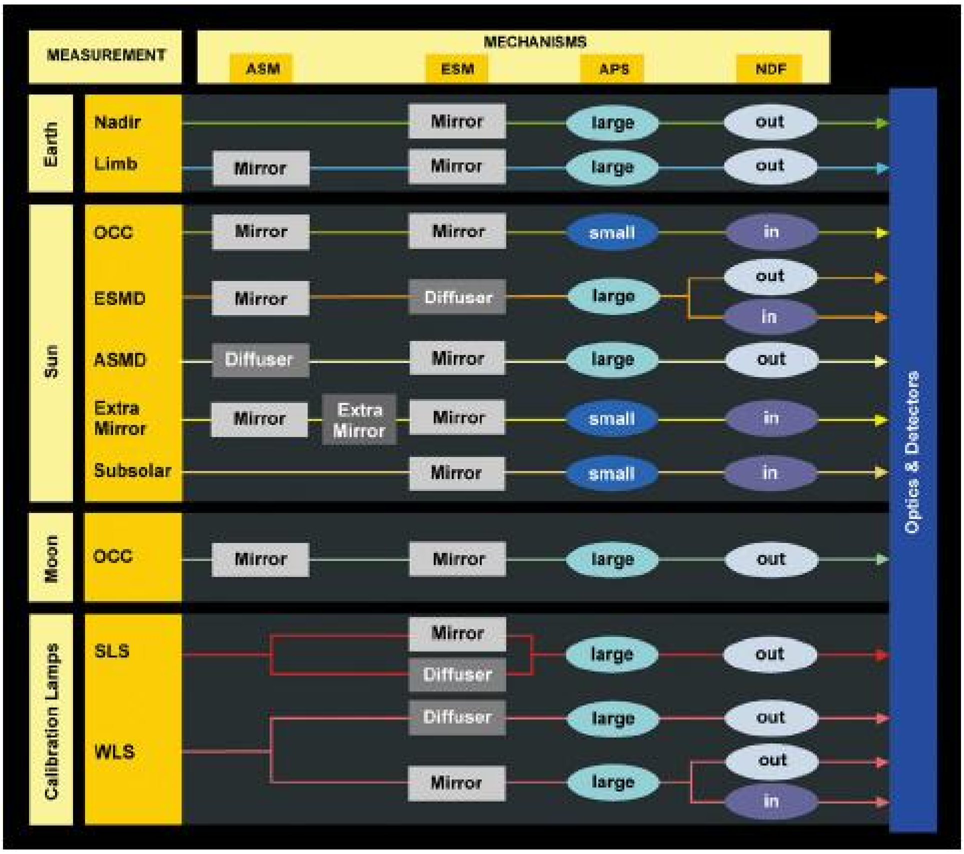

SCIAMACHY optical 'trains'. Each 'train' defines a path for the measured light through the instrument to the detectors. Light sources can be external or internal. (graphics: DLR-IMF and SRON)

Scanner Mechanisms and Baffles

Scanner Mechanisms and Baffles

During nominal measurements light enters the instrument via the azimuth (ASM) or elevation (ESM) scan mechanisms. Both are located below the lower part of the level 1 of the OU. Mechanically, each scanner comprises a mirror block, bearings, a drive motor and encoders. Bearings use a special lubrication reducing life limitation risks in the scanner’s quasi-continuous in-orbit operations. The scanning mirrors have uncoated, polished aluminium surfaces with a size of 90 mm × 60 mm for the ESM and 125 mm × 110 mm for the ASM. Whilst the ASM captures radiation coming from regions ahead of the spacecraft, the ESM either views the ASM or the region directly underneath the spacecraft. In the first case (limb observation), the light collected from the ASM is reflected into the spectrometer, in the second case (nadir observation) the ASM is not involved in the optical path.

Scanning is required in order to steer the Line-of-Sight both for executing particular observation geometries and for collecting light not only from the limited size of the ground projection of the Instantaneous Field of View (IFoV, see below) but from a wider ground scene. Although both scan devices can be rotated by 360°, baffles limit the effective field of view. This results in the Total Clear Field of View (TCFoV) which depends on the observation mode as listed in (table 2-4) and sketched in (fig. 2-8)

Observing Geometry	***Total Clear Field of View (TCFoV)***
Nadir	32 / 31 (ESM, across track left / right)
Limb, Occultation	88 (ASM, azimuth 316 - 44) 8 (ESM, elevation 19.5 - 27.5 from X-Y plane downwards)
Sub-solar	1.7 (azimuth) 14.8 (ESM, elevation 53.7 - 68.5 from X-Y plane upwards)

Tab. 2-4: SCIAMACHY Total Clear Field of View

fig. 2-8:

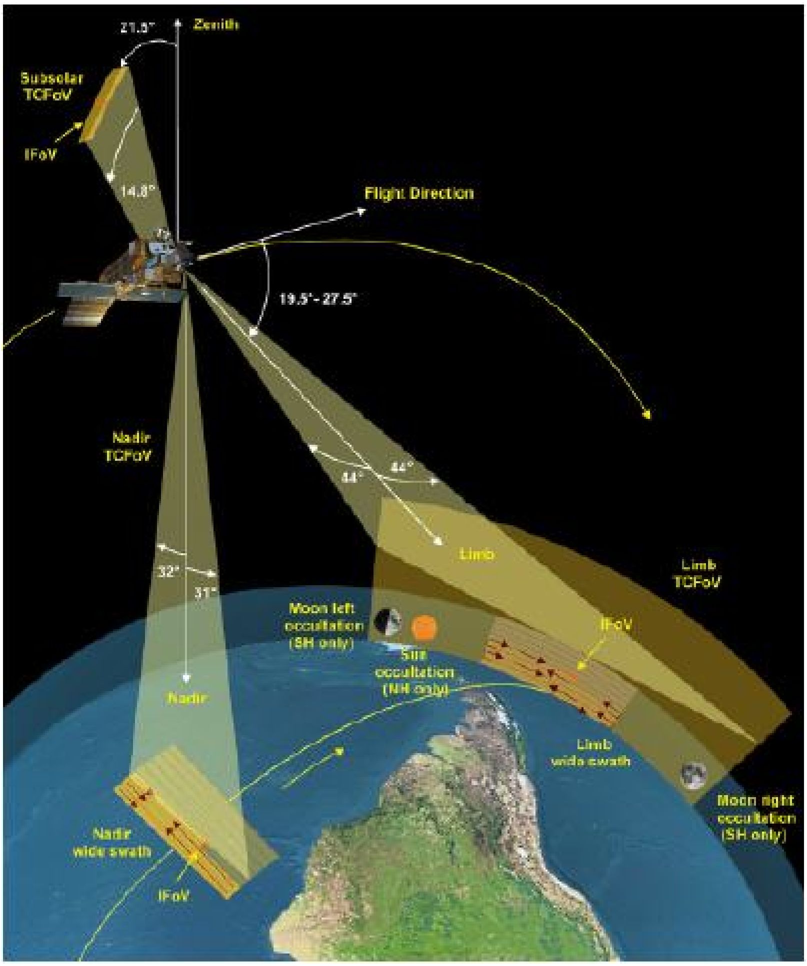

Sketch of SCIAMACHY's TCFoV and observation geometries. (Graphics: DLR-IMF)

For the limb and occultation LoS, the baffles provide a symmetric range on either side of the flight direction while vertically they restrict viewing from slightly below the horizon to an altitude of about 380 km, i.e. well above the top of the atmosphere at 100 km.

The nadir LoS is limited to an area of about +31° (right) to -32° (left) across track. For a special type of measurement, the rectangularly shaped Nadir Calibration Window (NCW) can be opened temporarily allowing light incident from above to enter the instrument via the ESM mirror. Its elongated TCFoV of 1.7°´14.8° is designed to view the sun at high elevation when the spacecraft crosses the orbital sub-solar point.

Telescope and Spectrometer

Executing various LoS trajectories and pointing to the sun or moon requires elaborated scanner control functions, particularly when the movement of both mechanisms has to be synchronized. The scanner control tasks are programmed in on-board software with supporting information being generated by the Sun Follower (SF) in the case of solar and lunar observations. Each scanner is operated separately in feedback control using readings of the rotation angle by an incremental optical encoder. Angular scan trajectories are assembled from pre-programmed basic and relative scan profiles for offset and motion generation. Since precise LoS steering to the Earth's limb or celestial targets depends on the in-orbit platform attitude and state vector, the selected trajectory can be corrected accordingly. In limb measurements the horizontal scans through the atmosphere maintain a constant altitude by applying a correction which takes into account the varying curvature of the Earth (WGS84 model) along the orbit. Further corrections provide for the yaw steering attitude mode of the ENVISAT platform and the known misalignment of the instrument reference frame relative to the spacecraft frame. Sun and moon observations require one or both axes to be centred onto the target. Analytical control algorithms cannot always ensure this. Therefore, information derived from the readout of the four quadrants of the SF is fed into the control loop to steer the scanner motors such that the mirrors lock onto the weighted centre of the intensity distribution and follow the trajectory of sun or moon after successful acquisition. The SF receives light which is reflected from the blades of the spectrometer entrance slit. It has a 2.2° × 2.2° wide Field-of-View (FoV) which is reduced for sun tracking to 0.72° × 2.2° by the small aperture stop (see below).

For obtaining the solar irradiance, the sun has to be measured via a diffuser. Two aluminium diffusers are mounted on SCIAMACHY: one on the backside of the ESM mirror, one on the backside of the ASM mirror. Originally the ESM diffuser was the only one in the instrument. During calibration it turned out that this type of diffuser exhibits spectral features which would have endangered successful retrieval of some trace gas species. Thus very late in the development of phase C/D, when SCIAMACHY was already mounted on the spacecraft, an ASM fitted with the additional diffuser was integrated. Its surface was ground in a different way to yield optimized diffuser properties.

Telescope and Spectrometer

The ESM reflects light towards the telescope mirror, which has a diameter of 32 mm. From the telescope mirror the light path continues to the spectrometer entrance slit. With linear dimensions of 7.7 mm × 0.19 mm (cross-dispersion × dispersion) the entrance slit defines an Instantaneous Field of View of 1.8° × 0.045°. This corresponds to a ground pixel size of 25 km × 0.6 km at the sub-satellite point (nadir) and of 105 km × 2.5 km at the Earth's horizon (limb). For solar observations, the IFoV can be reduced to 0.72° × 0.045° by operating the Aperture Stop Mechanism (APSM) which is located between the ESM and telescope mirror. The APSM reduces the aperture area and thus the intensity level. Channel dependent effects lead to a reduction by a factor of more than 5000 for channels 1-5 and about 2500 for channels 6-8.

The overall spectrometer design is based on a two stage dispersion concept: First, the incoming light is pre-dispersed and projected onto a spectral image. Subsequently, this spectral image is dissected into eight spectral intervals that are diverted into eight spectral channels for further dispersion. The selected approach has the advantage of reducing stray light in the channels covering low light intensity in the UV and NIR-SWIR part of the spectrum. It also effectively prevents the various spectral orders from one grating overlapping with the other parts of the spectrum (*Goede et al. 1991*).

The pre-disperser prism, located behind the entrance slit, serves two purposes. It weakly disperses the light and directs fully polarized light for further processing to the Polarization Measurement Device (PMD). Small pick-off prisms and subsequent dichroic mirrors direct the intermediate spectrum to the 8 science channels where the light is further dispersed by individual gratings. In the light path routed to channels 3-6 the Neutral Density Filter Mechanism (NDFM) can move a filter into the beam. With a filter transmission of 25% it can be used, in conjunction with the APSM, to even further reduce light levels during solar measurements.

Channel	*Spectral Range (nm)*	*Resolution (nm)*	*Stability (nm)*	*Temperature Range (K)*
1	214 - 334	0.24	0.003	204.5 - 210.5
2	300 - 412	0.26	0.003	204.0 - 210.0
3	383 - 628	0.44	0.004	221.8 - 227.8
4	595 - 812	0.48	0.005	222.9 - 224.3
5	773 - 1063	0.54	0.005	221.4 - 222.4
6	971 - 1773	1.48	0.015	197.0 - 203.8
7	1934 - 2044	0.22	0.003	145.9 - 155.9
8	2259 - 2386	0.26	0.003	143.5 - 150.0

Table 2-5: SCIAMACHY science channels (1 & 2 = UV, 3 & 4 = VIS, 5 = NIR, 6-8 = SWIR)

Detector Modules

Detector Modules

The full resolution spectral information is generated in 8 science channels (table 2-6). These employ two types of detectors. For the UV-VIS-NIR range covered by channels 1-5, standard Silicon photodiodes (RL 1024 SR, EG&G RETICON, California) with 1024 pixels are used which are sequentially read out. Additionally, UV channels 1 and 2 are electronically divided into two virtual bands 1a/1b and 2a/2b, which can be configured separately. The SWIR channels 6-8 employ Indium Gallium Arsenide detectors (InGaAs by EPITAXX, New Jersey) specifically developed and qualified for SCIAMACHY (*Hoogeveen et al. 2001*). In the SWIR channels all pixels are read out in parallel. In order to be sensitive to wavelengths beyond 1700 nm, the detector material in the upper part of channel 6 above pixel number 794 (named channel 6+) and channels 7 & 8 were doted with higher amounts of Indium. All channels have to be cooled to achieve the specified signal-to-noise performance. The operational temperature range is channel dependent and lowest for the SWIR channels 7 & 8 (fig. 2-9).

fig. 2-9:

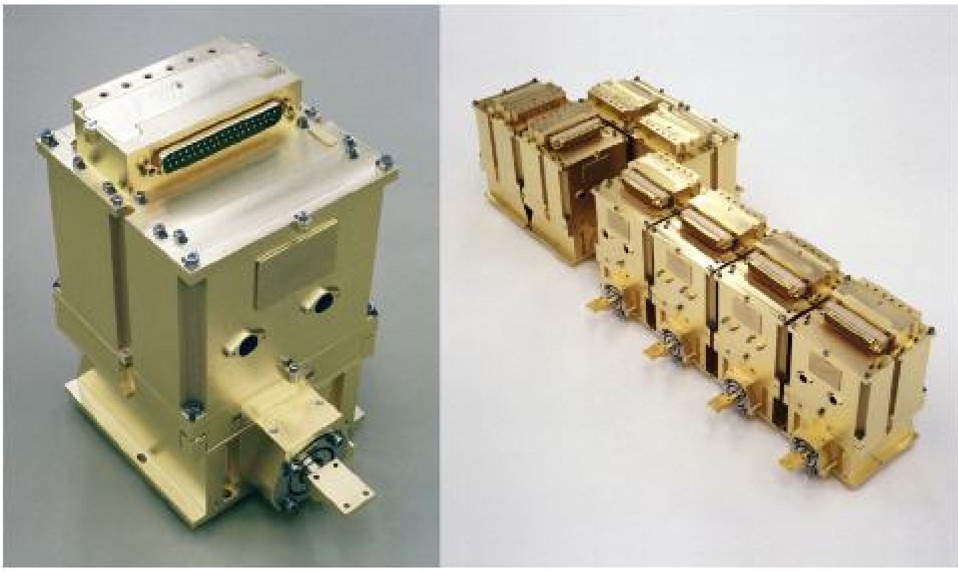

Single SCIAMACHY detector module (left) and the full complement of 8 detector modules (right). (photo: SRON)

Trace gas features are distributed non-uniformly over the spectrum. The limited total data rate would therefore prohibit the detailed sampling of those ranges of interest if the full spectrum had to be downlinked as one block. SCIAMACHY avoids this situation by using spectral clusters and co-adding. The 1024 pixels per channel can be sub-divided into a number of *Clusters* identifying regions where trace gas retrieval will take place. Each cluster can be sampled by on-board data processing applying *Co-adding* factors to the readout of the pixels of this cluster. This results in an integration time (= pixel exposure time × co-adding factor) which defines how many subsequent readouts of each pixel of a cluster are added to generate one measurement data readout. By appropriately setting the integration time, high or low temporal resolution – equivalent to high or low spatial resolution – can be selected. Thus, depending on the executed measurement states, variable ground pixel sizes as a function of spectral region, i.e. trace gas features, are achieved. Efficient setting of co-adding factors is also required ensuring that the volume of the generated data does not violate the assigned nominal data rate limit of 400 kbit/sec. The measurement data stream finally consists of cluster sequences representing different wavelength regions read out at different rates.

Calibration Unit

The requirements to maintain high spectral stability and relative radiometric accuracy over the mission's lifetime are verified via an on-board calibration unit. It consists of two calibration lamps, one for white light and one for spectral lines. The White Light Source (WLS) is a 5 Watt UV-optimized Tungsten-Halogen lamp with an equivalent blackbody temperature of about 3000 K. Its signal is used to verify the pixel-to-pixel signal stability and to monitor the Etalon effect. The Spectral Line Source (SLS) is a Neon filled hollow Pt/Cr cathode lamp. Its operation allows the determination of the pixel-to-wavelength relation. The calibration unit is located close to the ESM. By rotating the ESM mirror into specific positions it is possible to reflect light from the WLS respectively the SLS towards the telescope mirror and thus onto the entrance slit.

An extra calibration mirror near the ESM can be used to provide for an additional reflection of the incoming light on the ESM mirror. Due to its protected position well within the instrument it is assumed that this extra mirror will not degrade throughout the mission. Thus it can be used as a further means of monitoring optical performance.

Channel	***Spectral Range (nm)***	***Detector Temperature (C)***
A	310- 365	-18
B	455 - 515	-18
C	610 -690	-18
D	800 - 900	-18
E	1500 - 1635	-18
F	2280 - 2400	-18
45	800 - 900	-18

Table 2-6: SCIAMACHY PMD. The wavelength ranges are defined so that they contain 80% of the total signal given in the PMD channels.

Polarization Measurement Device

The measurement sensitivity of the spectrometer depends on the polarization state of the incoming light. Therefore SCIAMACHY is equipped with a Polarization Measurement Device. Six of its channels (PMD A-F) measure light polarized perpendicular to the SCIAMACHY optical plane, generated by a Brewster angle reflection at the second face of the pre-dispersing prism. This polarized beam is split into six different spectral bands. The spectral bands are quite broad and overlap with spectral regions of channels 2, 3, 4, 5, 6, and 8 (table 2-6).

The PMD and the light path to the array detectors, including the detectors, have different polarization responses. Consequently, with the appropriate combination of PMD data, array detector data and on-ground polarization calibration data the polarization of the incoming light from the nadir measurements can be determined. For atmospheric limb measurements, where both limb and nadir mirrors are used, the light is outside the optical plane of the spectrometer. This requires measurements of additional polarization information of the incoming light. A seventh PMD channel measures the 45° component of the light extracted from the channels 3-6 light path. All PMD channels are non-integrating and read out every 1/40 sec. They observe the same atmospheric volume as science channels 1-8.

2.3.3 Thermal Subsystems

Radiator A and Active Thermal Control

The OBM needs to be operated in orbit at a constant temperature to preserve validity and accuracy of the on-ground calibration & characterization. Additionally, a low temperature level is required to keep the thermal radiation of the instrument itself at a minimum in order not to enhance the background in the SWIR channels 7 & 8. Therefore a dedicated radiator, RAD A, is used to cool the OBM and the detector module electronics to between -17.6 and -18.2 °C. Its location on the -X side of the instrument avoids direct solar illumination. Heat pipes are used to transfer heat from the OBM and the detector module electronics to the radiator.

While the RAD A provides cooling capacity, thermal stability of the OBM needs to be established via a closed loop Active Thermal Control (ATC) system. It consists of three control loops with heater circuits and thermistors. The heating is controlled by the Power Mechanism & Thermal Control Unit (PMTC) based on measurements by the thermistors. Once ATC settings have been selected, the system maintains the OBM temperature to high precision at the specified temperature.

Thermal Bus and Radiant Cooler Assembly

In-orbit operating temperatures of the detectors lie well below ambient. The detectors are cooled via the Radiant Reflector Unit of the Radiant Cooler Assembly. It is the task of the Thermal Bus to connect the detector modules thermally with the reflector. Heat from detectors 1-6 is transported via an aluminium thermal conductor, from detectors 7 & 8 via two methane filled cryogenic heat pipes. The heat pipes provide an efficient heat transfer in the temperature range 100-160 K. Since the cooling efficiency of the Radiant Cooler is designed to be adequate until the end of the mission, a Thermal Control (TC) system is part of the Thermal Bus. It prevents the detector modules from becoming too cold by counter heating using three trim heaters. The TC system uses open loop heater control. Whenever drifting temperatures of the detectors reach their limits, the power settings of the trim heaters are adjusted by ground command so that the thermal response brings temperatures back within the specified range.

SCIAMACHY’s SRC dissipates heat generated in the detector modules to deep space to permit cooling of the detector arrays to in-orbit operating temperatures.. As for RAD A, the RRU points in the -X direction away from the sun. Earthshine and sunshine are blocked from the radiating surface of the SRC to gain maximum cooling efficiency. Cold temperatures are obtained using a two stage process. An intermediate stage in the Radiator Unit lowers temperatures of detectors 1-6, while the cold stage, fitted with a parabolic reflector, yields temperatures around 150 K for detectors 7 & 8. Due to its low temperature, the RRU surface is expected to attract contaminants from the in-orbit environment, particularly from ENVISAT itself. This would degrade the performance of the Radiant Cooler leading to reduced cooling efficiency. In order to clean the Radiant Cooler, the cold stage and the reflector are equipped with decontamination heaters. Turning the decontamination heaters on raises the temperatures of the RRU, contaminating substances are removed through evaporation and the cooling performance is re-established. Whether contaminants begin to degrade the SRC performance can be determined from the power settings of the TC trim heaters. Degraded cooling efficiency is equivalent to higher radiator temperatures, i.e. higher detector temperatures. Consequently the trim heaters require less power when the SRC efficiency degrades because of contamination.

Because of the necessity to heat up the detectors as much as possible to effectively get rid of the ice layers deposited on channels 7 & 8, the original decontamination procedure was re-defined to form a Non-Nominal Decontamination (NNDEC) to be used during routine operations. During a NNDEC not only the SRC decontamination heaters provide energy to the optical subsystem but also ATC and TC heaters are switched to their maximum power. In the warm-up phase of NNDEC, channels 7 & 8 reach temperatures of 267 K and the OBM approaches a temperature of -3 °C. Also the duration of the warm-up phase was extended by up to 15 days. Measurements continue throughout warm-up and cool-down. Data analysis still permits retrieval of – somewhat degraded – information from the UV-VIS channels even at elevated temperatures such that no long data gaps occur.

2.4 Instrument Operations

fig. 2-10:

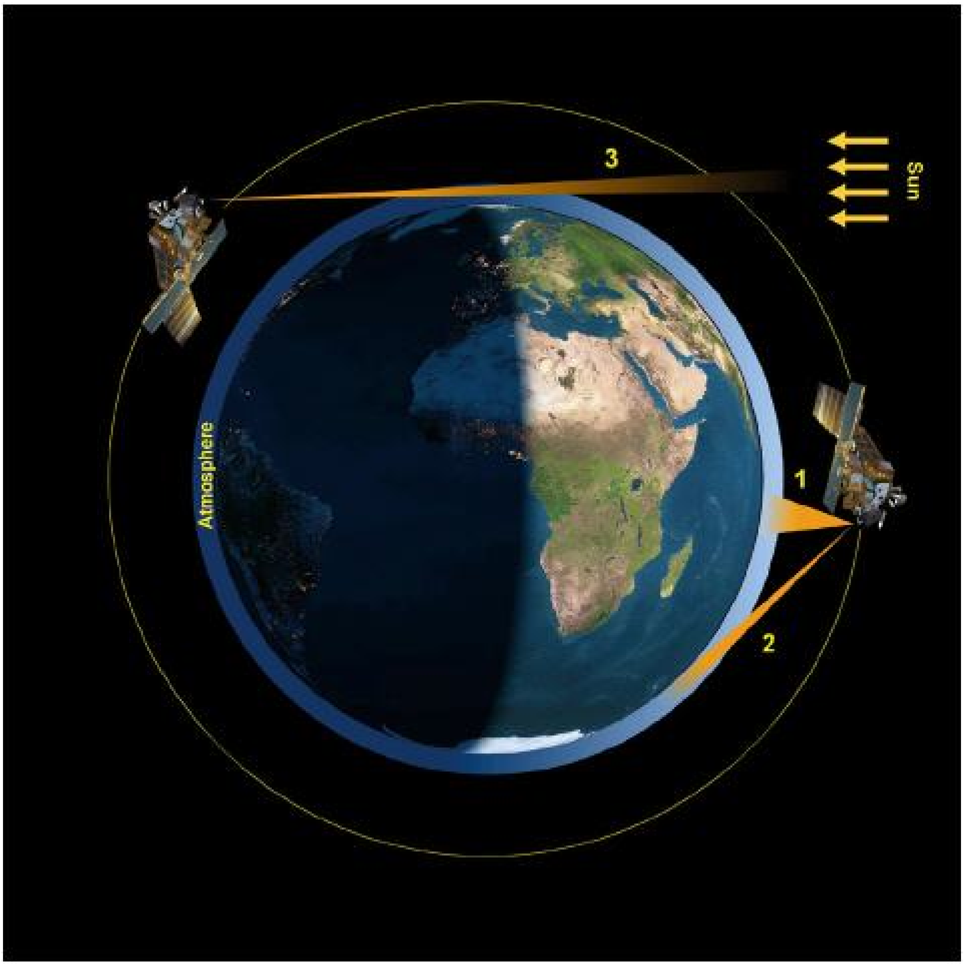

SCIAMACHY's scientific observation modes: 1 = nadir, 2 = limb, 3 = occultation. (graphics: DLR-IMF)

The characteristics of a polar orbiting platform with short telemetry coverage at the high latitude stations Kiruna or Svalbard demanded highly autonomous on-board operations. This comprises not only on-board anomaly detection and initiating corrective actions as part of the instrument control but also the ability to configure the instrument status and to execute measurements without direct manual intervention from ground. Thus the preplanned measurement schedule must be executed on-board in a time tagged manner.

Scientific requirements include viewing geometries for atmospheric measurements of nadir, limb, sun occultation and moon occultation (fig. 2-10). In addition, external (e.g. dark current, sun reference) and internal (calibration lamps) observations supplement the measurement schedule. One of SCIAMACHY’s main objectives is to measure the same atmospheric volume both in nadir and limb within one orbit, i.e. limb/nadir matching.

This can be achieved by first observing an atmospheric volume at the horizon by looking slightly off the flight direction towards Earth’s rotation. Later in orbit, after a time interval Dt = 430 sec, the same volume of air crosses the sub-satellite point and can be observed under nadir conditions (fig. 2-11). The interval of Dt = 430 sec is the result of the angular velocities of Earth and spacecraft platform. In limb mode, SCIAMACHY observes the horizon 3280 km ahead of the instrument close to flight direction. Because the spacecraft’s steering law is determined by the Earth’s angular velocity at the instantaneous sub-satellite point, the line of sight does not intercept the horizon at a point where the Earth’s and spacecraft’s angular velocities lead to limb/nadir matching. Therefore, an instrument yaw steering correction is implemented in SCIAMACHY’s on-board software to compensate for the phase shift between local yaw steering and instrument line of sight in limb observations. It reflects the angular difference of approx. 27° between local sub-satellite point during limb measurement and line of sight interception at the Earth’s horizon (fig. 2-12).

fig. 2-11:

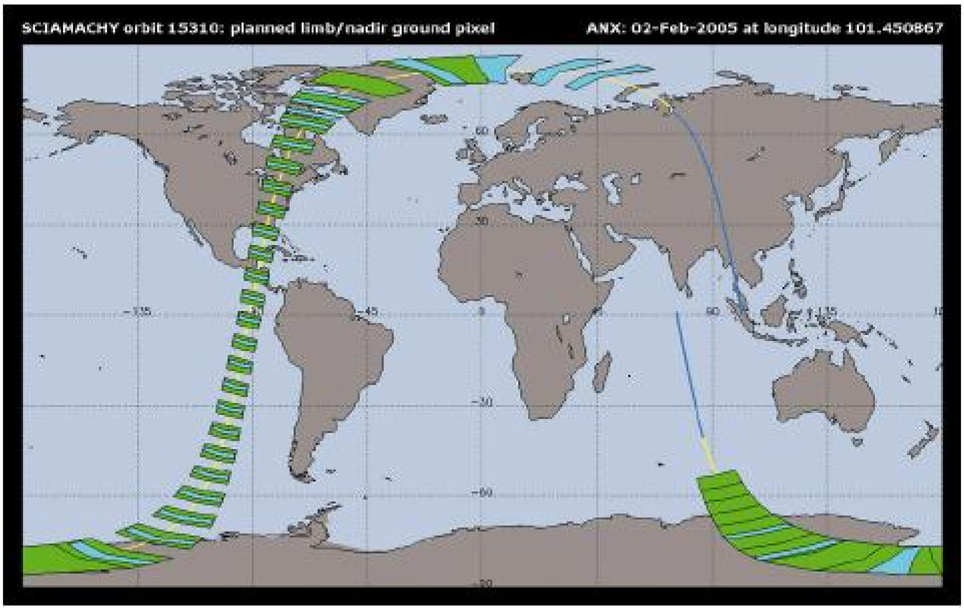

An orbit with planned limb/nadir matching on the dayside of the orbit. The sequence of nadir and limb states in a timeline is arranged so that limb ground pixels (blue), defined by the line-of-sight tangent point, fall right into a nadir ground pixel (green). At the beginning and end only limb or only nadir measurements are executed. (graphics: DLR-IMF)

fig. 2-12:

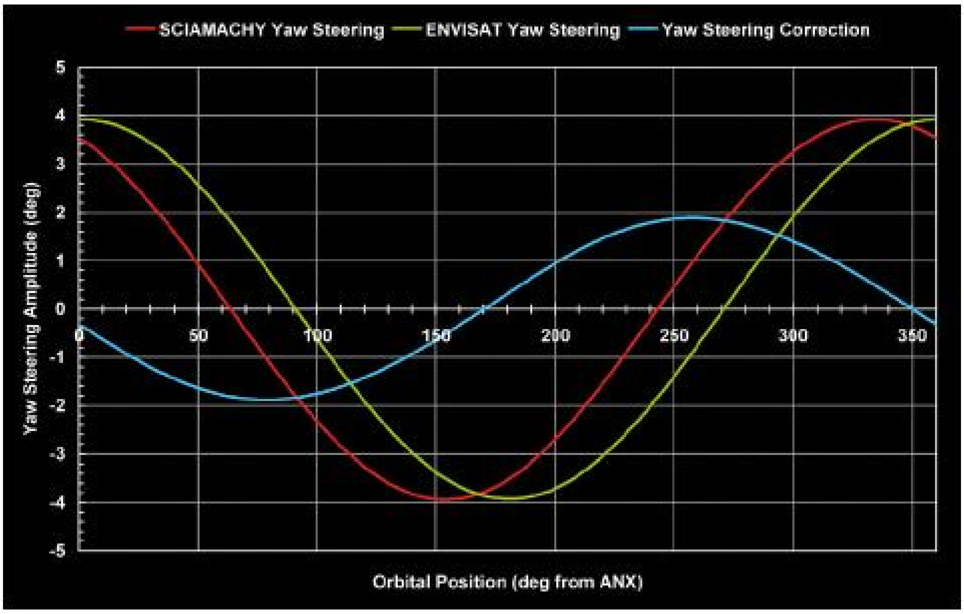

ENVISAT's yaw steering, the yaw steering correction of limb states and the resulting SCIAMACHY yaw steering. Between ENVISAT and SCIAMACHY yaw steering an orbital shift of 27? exists which reflects the observation geometry when looking to the horizon in flight direction. (graphics: DLR-IMF)

2.4.1 Sun and Moon Observation

All measurement activities are planned relative to solar and lunar constellations. SCIAMACHY operations are either sun or moon fixed, but not Earth fixed. Since solar and lunar constellations, as viewed from ENVISAT's orbit, are determined by the orbital motion of the platform, the orientation of the orbital plane, the lunar motion around Earth and the Earth's movement around the sun, the observing conditions can be completely predicted by orbit analysis. These predicted conditions are then translated into configurable instrument states and timelines.

Sun Occultation

The mean local time of 10 a.m. during descending node crossing leaves the sun always to the left of the flight direction, i.e. at azimuth angles > 180°. The elevation of the sun varies between approx. -70° and +70°. Sunrise occurs after ascending node crossing when ENVISAT moves towards the North Pole on the eclipse side of the orbit. The sun becomes visible at the Earth's limb left of the flight direction at middle to high geographic latitudes. The exact latitude is dependent on the actual position of the *true* sun relativeto the Earth (*true* sun reflects the actual annual orbital motion of the Earth contrary to the *mean* sun which is characterized by assuming a constant Earth orbital velocity). In summer, sun occultation measurements start when the spacecraft has reached geographic latitudes of about 27° north while in winter the sub-satellite point moves up to about 75° North. At sunrise the solar elevation is identical to the elevation of the Earth's limb, i.e. approx. 27.2°. The azimuth angle at sunrise has a mean value of 330°, corresponding to the mean local time at descending node crossing of 10 a.m. and changes over a year due to the apparent motion of the true sun. Caused by the orbital motion of ENVISAT, the sun rises almost vertically through SCIAMACHY's limb TCFoV. In an occultation measurement, the ASM has to acquire the sun at an angle of about 330° and to follow the slightly changing azimuth as the sun moves higher. In the elevation direction the sun must be tracked by the ESM up to the maximum elevation angle of 19.5°, limited by the TCFoV. From the Earth's limb up to an elevation angle of 25.2°, corresponding to an altitude of 100 km, the sunlight is absorbed by the Earth's atmosphere. Thus the sun serves both as a target for probing the atmospheric trace gas constituents (altitude < 100 km) and for calibration and monitoring measurements (altitude > 100 km). Therefore the total time of the sunrise in the limb TCFoV is referred to as *Sun Occultation & Calibration (SO&C)* window.

Observation of sunrise from a spacecraft is affected by the refractive properties of the Earth's atmosphere. The refraction angle depends on the Earth's radius, the scale height of the exponentially decreasing refractivity profile, the refractivity and the height of the tangent point of the incident rays. For visible light the refraction angle amounts to approx. 70 arcmin at the horizon (h = 0 km), i.e. SCIAMACHY can observe the first solar photons when the sun/moon is still well below the geometric horizon. As the unrefracted sun rises, the refracted image of the disk is distorted by differential refraction. At an altitude of h » 17 km refraction has become so small that refracted image and solar disk overlap. Below this height the angular rate of the rising sun/moon as defined by the moving spacecraft is larger than the variable rate of their refracted images. At low altitudes, measuring the sun can become difficult due to obscuration by or reflected radiation from clouds. On-board control of the scan mirrors during occultation uses the Sun Follower with its relatively wide field of view of 0.72° × 2.2°.

Sub-solar Observations

The sub-solar port above the ESM provides additional access to the sun above the atmosphere. Because sun viewing in this configuration does not involve the ASM, measurements of this kind can be used to monitor the behaviour of the ASM mirror. The sun is visible through the sub-solar port when the sun has reached its highest elevation. This occurs at an azimuth angle of 270°. The sub-solar elevation angle changes continuously with season. Therefore the sun moves up and down over a year along the elongated dimension of the sub-solar TCFoV when passing through the window. The duration of a sub-solar measurement is defined by the time it takes the sun to pass through the azimuth dimension of the sub-solar port, reduced by the small aperture stop to only 0.72°. This interval amounts to 21 sec, with the sun being fully visible for a short period of only 3.5 sec.

Moon Occultation

Moon Occultation

Individual observations of the moon follow the same principles as described for the sun. The lunar disk is acquired by the ASM and ESM and tracked as the moon rises through the limb TCFoV. The moon acts both as a target for scientific and for calibration & monitoring measurements, as in case for the sun. The corresponding time interval is named *Moon Occultation & Calibration (MO&C)* window. Predicting lunar occultation measurements requires analyses of the viewing conditions as a function of the monthly lunar motion. For a full orbit the moon moves, inclined by 5.1° to the ecliptic, in about 29.5 days around the Earth. Whenever the lunar orbit crosses the limb TCFoV of SCIAMACHY, moonrise can be observed. With a total azimuth size of 2 ´ 44° for the limb TCFoV, the mean monthly time interval when lunar measurements can be executed amounts to 7.2 days, displaying a seasonal variation of between 5.5-8 days. Due to the lunar orbital motion, the first moonrise in a monthly period occurs on the left side of the limb TCFoV (azimuth = -44°). Each orbit moonrise progresses with an azimuth rate of about 1°/orbit to the right side of the limb TCFoV. At the end of the monthly visibility, the moon has reached the right edge of the TCFoV (azimuth = +44°). The lunar phase changes continuously within each monthly period. At the beginning of the visibility, the phase amounts to about 0.6-0.7.

Full moon can be observed close to the end of the monthly cycle because the 10 a.m. descending node crossing time criterion of ENVISAT's sun-synchronous orbit only allows full illumination of the lunar disk when the moon lies at an azimuth of about 30° (fig. 2-13). Moonrise at lunar phases > 0.5 occurs over a large range of geographic latitudes in the southern hemisphere. Different to sunrise, where the geographic latitude of the sub-satellite point (and thus also the geolocation of the tangent point at which the atmosphere is probed) changes slowly over a year, the latitude of the sub-satellite point at moonrise varies significantly within a monthly period. Since the brightness of the lunar disk can be insufficient to exceed that of an illuminated cloudy atmosphere, moon occultation measurements are only possible when the moon rises on the night side beyond the terminator. In addition refraction has to be taken into account. Its impact is similar as in the case of sunrise due to the same apparent size of 31.5 arcmin for both solar and lunar disk (fig. 2-14).

fig. 2-13:

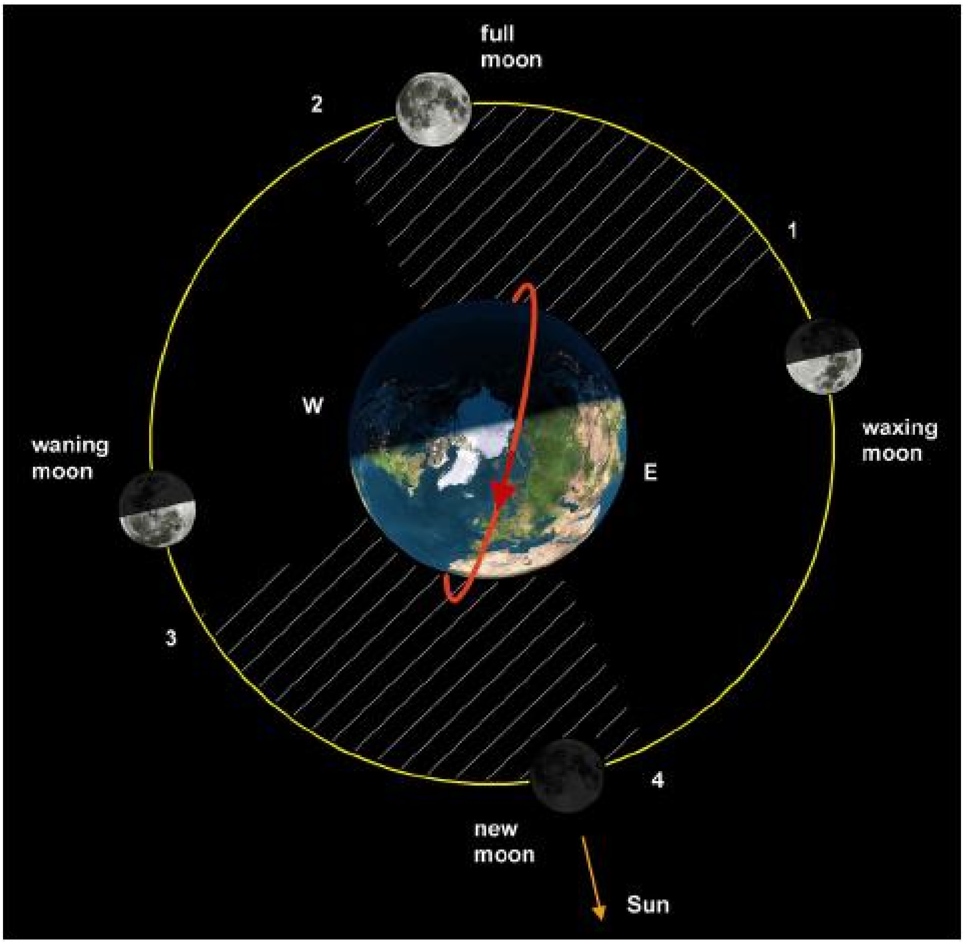

SCIAMACHY's monthly lunar visibility occurs between 1 and 2 over the southern hemisphere (lunar phase > 0.5). The hatched area illustrates the limb TCFoV of 88?. Visibility at smaller lunar phases over the northern hemisphere between 3 and 4 is not used because it coincides with solar occultation. (graphics: DLR-IMF)

fig. 2-14:

The rising moon seen from a spacecraft in a low-Earth orbit. Differential refraction distorts the lunar disk. (photo: NASA)

Routine Measurement Orbit

2.4.2 Routine Measurement Orbit

A routine SCIAMACHY orbit starts above the northern hemisphere with an observation of the rising sun. In order to acquire also light from the sparsely illuminated atmosphere at the limb in the direction of the rising sun, a sequence of limb measurements precedes each sun occultation measurement. Once the sun has risen, it is tracked by the ESM for the complete pass through the SO&C window. After about 175 sec the sun leaves the limb TCFoV at the upper edge. In order to fully exploit the high spatial resolution during occultation, measurement data readout with a high rate is required in the SO&C window.

Until the passage of the sub-solar point, a series of matching limb/nadir observations are executed. At the sub-solar point the sun, generally close to descending node crossing, has reached its highest elevation relative to ENVISAT. Whether a sub-solar measurement is actually executed depends on whether a sub-solar calibration opportunity has been assigned by ENVISAT. Because of the vignetting of the sub-solar TCFoV by the Ka-band antenna in operational position, only 3 orbits per day with sub-solar opportunities are possible, of which nominally one has to be selected. Another sequence of matching limb/nadir measurements follows. Above the southern hemisphere, the moon becomes visible during the monthly moon visibility period, otherwise matching limb/nadir observations continue. The rising moon is observed similarly to the rising sun from bottom to top of the limb TCFoV. A series of limb/nadir observations concludes the illuminated part of the SCIAMACHY orbit. Because the instrument is still viewing sunlight in nadir direction while the projected ground-track in the flight direction will already have seen sunset, the final measurements in this phase are only of the nadir type. When ENVISAT enters the eclipsed part of the orbit, dedicated eclipse observations can be executed until SCIAMACHY moves towards another sunrise and the orbit sequence starts again (fig. 2-15).

fig. 2-15:

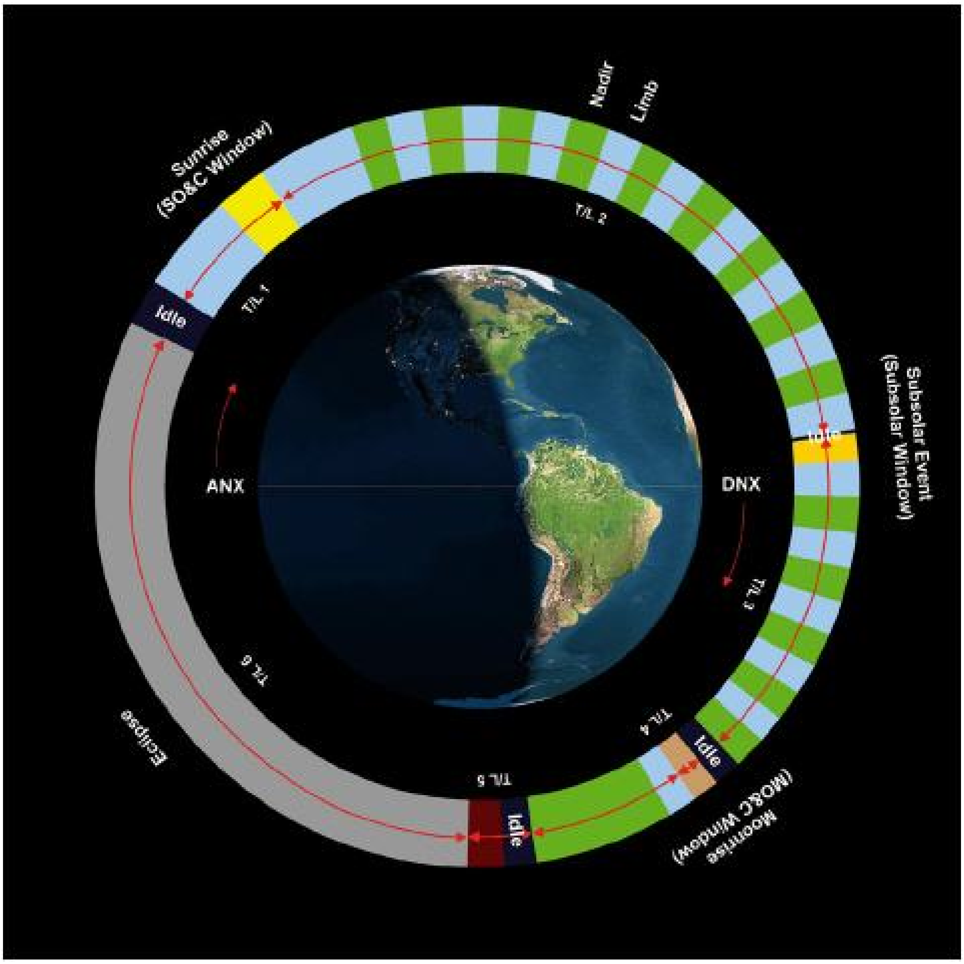

SCIAMACHY reference orbit with sun/moon fixed events along the orbit. The events define orbital segments which are filled with timelines. State duration is not to scale. (Graphics: DLR-IMF)

In summary routine operations can be described by mission scenarios including:

- swath width of ± 480 km relative to ground track in nadir and limb scans for global coverage within 6 days (taking the alternating limb/nadir measurements into account)

- matching limb/nadir measurements in the illuminated part of the orbit
- sun occultation measurements each orbit
- moon occultation measurements whenever possible (moonrise on nightside of Earth)
- calibration & monitoring measurements on a daily (every 14th orbit), weekly (every 98th orbit) and monthly basis

The simplest orbital mission scenario is executed whenever the moon is not visible and no regular calibration & monitoring tasks have to be performed. This scenario occurs about 90% of the time during a month and can be accommodated by 4 timelines (see below). The most complex scenario is defined when implementing monthly calibration & monitoring requirements. This consists of a series of 5 consecutive orbits filled with calibration & monitoring activities.

2.4.3 Parameter Tables

Utilising the high degree of flexibility in the instrument design can only be accomplished through parameterisation of on-board operations. For the execution of scientific and calibration & monitoring measurements this means that associated functions must be predefined and stored on-board with ground control having the capabilities to modify the instrument configuration by commanding. Changing the instrument status includes software updates via patching as well as parameter settings via commanding. Those sets of parameters which are associated with basic instrument properties, e.g. scanner, thermal and mechanism control definitions are termed *engineering* parameters. Parameters relating to the configuration of the spectrometer while measuring are the so-called *measurement* parameters. Engineering and measurement parameters are organized in a series of parameter tables defining common functional tasks.

Measurement tables in most cases relate to individual measurement states (see below) but so-called ‘common’ tables serve all states (table 2-7). Particularly, the values of the pixel exposure times and the co-adding factors ensure, in conjunction with the definition of wavelength clusters, optimised signal-to-noise ratios over the complete orbit. The product of PET and co-adding factor yields the integration time, which defines the read-out frequency. In the case where SWIR channels run into saturation, the so-called *Hot Mode* parameters allow decreasing the exposure times in channels 6-8 below the minimum PET of 31.25 msec. The characteristics of the ASM/ESM rotations are defined via the Scanner State, Basic Scan Profile and Relative Scan Profile parameters. The Basic Scan Profile specifies the underlying standard motion of the respective mirror whereas the Relative Scan Profile is a mirror movement superimposed onto the Basic Scan Profile, e.g. fast upward/downward scans in elevation while the ESM is basically slowly moving in elevation.

Type	***Table***
State	Scanner State
	Pixel Exposure Time
	Hot Mode
	State Index
	State Duration
	Co-Adding
	Detector Cmd Words
	DME Enable
Common	Basic Scan Profile
	Relative Scan Profile
	Cluster per Channel
	Cluster Definition

Table 2-7: Measurement parameter tables

2.4.4 Measurement States

The individual functions to operate SCIAMACHY in measurement modes are defined as *states*. A state is a sequence of activities for a particular measurement task, e.g. nadir observations with certain pixel exposure times, sun occultation with certain scan geometry, etc. SCIAMACHY’s scientific measurement objectives and requirements have led to the definition of the 70 individual states as listed in (table 2-8). 34 states implement scientific requirements, 26 are for the purpose of in-flight calibration, 4 for in-flight monitoring and the data from 6 states can be used for scientific and calibration analyses. The high number of calibration & monitoring states is the result of the thorough and complex in-flight calibration & monitoring concept.

State ID	*State*	***Measurement Type***	***Remark***
1 - 7	nadir 960 km swath	science	all orbital positions
8, 26, 46, 63, 67	dark current	calibration	pointing at 250 km
9 - 15	nadir 120 km swath	science	all orbital positions
16	NDF monitoring, NDF out	monitoring	
17 - 21	sun ASM diffuser	calibration	sun above atmosphere
22	sun ASM diffuser atmosphere	monitoring	various azimuth angles

23 - 25, 42 - 45	nadir pointing	science	all orbital positions
27	limb mesosphere	science	scanning 150 - 80 km
28 - 33	limb 960 km swath	science	all orbital positions
34 - 37, 40, 41	limb no swath	science	all orbital positions
38	nadir pointing left	monitoring	
39	dark current Hot Mode	calibration	
47	SO&C scanning/pointing	science, calibration	sun through and above atmosphere
48	NDF monitoring, NDF in	monitoring	
49	SO&C nominal scanning, long duration	science, calibration	sun through and above atmosphere
50	SO&C fast sweep scanning	calibration	
51	SO&C pointing	science, calibration	sun through and above atmosphere
52	sun ESM diffuser, NDF out	calibration	sun above atmosphere
53	sub-solar pointing	calibration	
54	moon nominal scanning	calibration	moon above atmosphere
55	limb mesosphere_thermosphere	science	scanning 150-60 km
56	moon pointing	science, calibration	moon through atmosphere
57	moon pointing, long duration	science, calibration	moon through and above atmosphere
58	sub-solar pointing/nominal scanning	calibration	
59	SLS	calibration	
60	sub-solar fast sweep scanning	calibration	
61	WLS	calibration	
62	sun ESM diffuser, NDF in	calibration	sun above atmosphere
64	sun extra mirror pointing	calibration	sun above atmosphere
65	ADC, scanner maintenance	calibration	
66	sun extra mirror nominal scanning	calibration	sun above atmosphere
68	sun extra mirror fast sweep scanning	calibration	sun above atmosphere
69	SLS ESM diffuser	calibration	
70	WLS ESM diffuser	calibration	

Table 2-8: Measurement state definition as of early 2009

- ***Occultation States*:**

  The states observing sun or moon require dynamic control of the scanners. They implement a dedicated sun/moon occultation procedure. At an altitude of about 17 km, refracted and geometrical images overlap significantly and rise with an almost constant rate. The ESM is rotated to this elevation and performs continuous vertical scans of 2 sec each with a vertical range of ±0.33°. The ASM is rotated to an azimuth angle which ensures that the sun or moon is within the field of view of the Sun Follower when their refracted disk appears at the limb. Once the sun/moon has reached an altitude of 17 km above the horizon the ESM tracks the upward motion of the sun/moon in pointing or one of the scanning modes. Nominal scanning moves the ESM in 2 sec ±0.33° around the centre of sun or moon. Because the integration times are shorter than 2 sec, the light can be analysed in horizontal slices of the disk. The fast sweep is a 2.1° wide scan over the solar disk in 0.125 sec. The sweep is centred on the sun. The spectrometer records the integrated intensity at one sweep over the full disk.

- ***Calibration & Monitoring States*:**

  Usually, calibration and monitoring states operate either the internal calibration lamps SLS and WLS, measure the dark signal from deep space or observe sun and moon. As long as the line of sight during solar or lunar sunrise traverses the atmosphere, i.e. below an altitude of 100 km, the data serve scientific requirements. Above 100 km, they support calibration & monitoring. Sun measurements above the atmosphere can either observe the solar disk via the scan mirrors or reflect the light via one of the two diffusers. By selecting different light paths – e.g. using the extra mirror – and scanning properties, analysis of solar and lunar states is not only able of providing sun reference spectra for data processing but also information about the status of various optical components.

  Knowledge of the dark current signal is a prerequisite for successful interpretation of data from all measurement states. Therefore 5 dark current states are specified which cover all relevant integration times. Dark states are executed on the eclipse side during measurement orbits and along the whole orbit during monthly calibration orbits. In a dark current state, the line of sight is directed to and maintained at an altitude of 250 km. It corresponds to pointing into deep space well above the atmosphere. No Earthshine light is expected at this altitude and only the detector dark signal should be recorded.

  SLS and WLS states are required to derive further pixel-dependent detector properties and to monitor the instrument's stability. Whenever one of these states is operated, the ESM is rotated to the position where its mirror reflects light from the lamps onto the entrance slit of the spectrometer. Orbital variations may be detected by running SLS or WLS states several times during an orbit. Since each lamp dissipates heat when operated, thermal perturbations have to be kept to a minimum.

2.4.5 Timelines

Concept

SCIAMACHY's measurement schedule is implemented by executing predefined sequences of measurement states. These sequences are called *timelines*. A total of 63 timelines can be stored on-board in the TIMELINE table. Each timeline is characterized by the chronological sequence of states and its total duration. Once the timelines are stored in the TIMELINE table, they can be started via a single Macrocommand (MCMD). This MCMD provides the scheduled timeline start time. If the timeline includes a state executing a sun or moon measurement, e.g. sunrise at a given altitude, sub-solar event or moonrise at a given altitude, additional position parameters specifying the solar or lunar celestial positions, are uploaded with the MCMD. They are used by the instrument to correctly position the scan mirrors at the beginning of the particular state to initially acquire the target. Execution of the timeline is a complex interaction between various parameter tables. From triggering the first timeline related instrument internal commands until the sequence of states has finally run to completion, information is extracted from tables and used to control instrument measurement activities. The timeline definition ensures that sun or moon states in the timeline observe their target at the right time and location to meet the scientific requirements. Since the start timeline MCMD can provide only one set of position parameters for one solar or lunar event, there can only exist one sun or moon related state in a timeline. Thus timelines including a sun or moon state are fixed in time and are called *sun fixed* or *moon fixed*. All other timelines without a sun or moon state are scheduled relative to sun or moon fixed timelines.

Definition

Definition

Based on the objectives of each orbital mission scenario and the occurrence of sun and moon fixed events along the orbit, timelines can be built from the set of 70 states. Each timeline corresponds to an orbit interval with start/stop being related to a sun or moon fixed event. Timelines can be assigned to the following orbit intervals:

- SO&C window
- MO&C window
- eclipse
- end of SO&C window to start of eclipse
- end of SO&C window to start of sub-solar window
- end of sub-solar window to start of eclipse
- end of SO&C window to start of MO&C window
- end of sub-solar window to start of MO&C window
- end of MO&C window to start of eclipse

A complete orbital mission scenario is implemented by assembling a sequence of timelines which covers the full orbit and executes those states required in the scenario. This is an efficient building block approach which reduces the command load drastically. The most frequent scenario executes 4 timelines only – a SO&C timeline, followed by a long limb/nadir sequence and two calibration timelines in eclipse. Because the sequence of limb/nadir states generates a ring-like pattern of nadir and limb ground pixels, it has been decided to switch between two limb/nadir sequences in consecutive orbits. At latitudes where nadir ground pixels exist in one orbit, limb ground pixels are thus generated in the following orbit. The result is a chessboard type pattern better suited for global value added data processing.

All timelines starting or ending with the MO&C window have to accommodate the strong temporal variability of lunar events within a monthly visibility period. Therefore several versions of moon related timelines with different lengths do exist for the same segment. Triggered by mission planning, they are exchanged on-board whenever required by lunar position. This is different from timelines allocated to sun related orbit segments which require only single instances due to the moderate seasonal changes. (fig. 2-17)

fig. 2-17:

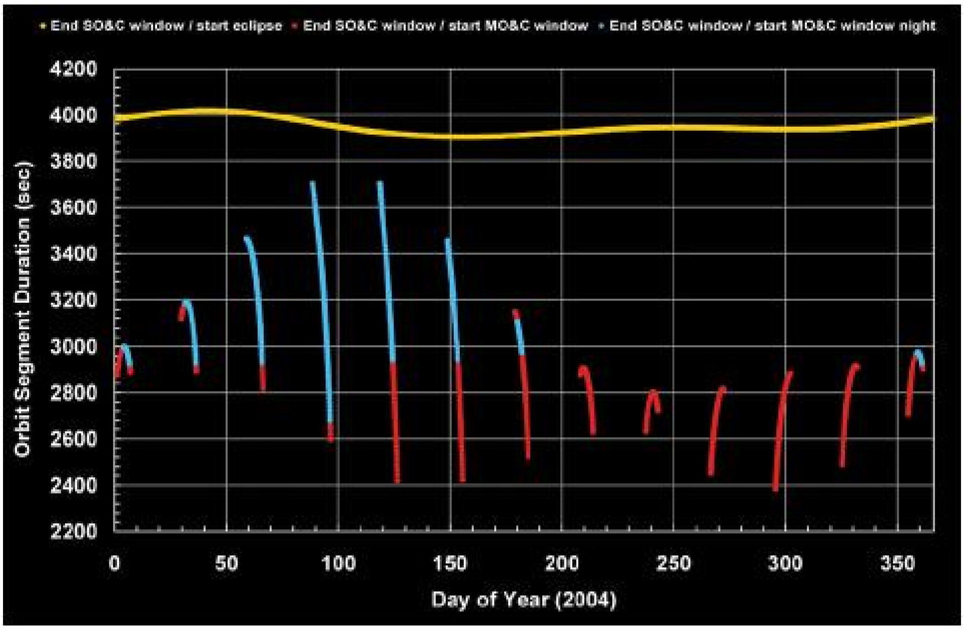

Example of the seasonal temporal variability of orbital segments. The time interval between end of SO&C window and start of eclipse varies only slightly over a year (yellow). In the monthly moon visibility periods, the time between end of MO&C window and start of eclipse shows a much higher variation (red curves). The blue segments indicate lunar visibility phases where moonrise occurs on the nightside, i.e. those which can be used for occultation. (Graphics: DLR-IMF)

As in the case of states, a final flight configuration exists that reflects the currently agreed and verified set of 63 timelines. Its configuration controlled status can be modified via the OCR procedure.

2.4.6 SCIAMACHY Operations Setup

Operations of the instrument include mission planning, configuration control of the on-board measurement status and instrument monitoring. Due to its status as an AO instrument, operational responsibilities for SCIAMACHY were split between ESA and DLR/NIVR. Agreements define that FOCC executes daily SCIAMACHY flight operations as for all other ENVISAT instruments but based on input from the AOP, whereas operational offline tasks are assigned to DLR/NIVR. On the AOP side, the SCIAMACHY Operations Support Team (SOST) interfaces with ESA, particularly FOCC, to fulfil these functions in order to accomplish safe operations and generation of high quality measurement data.

SOST has established a dedicated website at http://atmos.caf.dlr.de/projects/scops/ to report about the past, present and planned status of SCIAMACHY mission planning, instrument configuration and long-term monitoring results. This site includes not only dynamic information but informs also about orbit properties and the overall operations and mission planning concept. A comprehensive description of the final flight states, the corresponding valid parameter settings and a list of timelines supplement the website.

CHAPTER 3

3. SCIAMACHY’s View of the Changing Earth’s Environment

During the years since SCIAMACHY’s launch in 2002, numerous scientific results from the SCIAMACHY mission have been derived, clearly demonstrating the high ‘return on investment’ of this mission. New and exciting insights into the Earth-atmosphere system are obtained. They contribute significantly to atmospheric physics and chemistry, as well as to global climate change research. Many scientific groups at various institutes in Europe and abroad were and are actively involved in the analysis of the data. The following chapter highlights some of the most exciting findings based on operational and scientific data analysis. The chapter is based on material collected for the book "SCIAMACHY - Exploring the Changing Earth’s Atmosphere" *(Gottwald and Bovensmann 2011, published by Springer, ISBN 978-90-481-9895-5)*, where the interested reader will find even more highlights of the SCIAMACHY mission.

The interested reader is further referred to the internet resources:

http://envisat.esa.int/
http://www.sciamachy.de/
http://www.sciamachy.org/
http://wdc.dlr.de/
http://www.iup.physik.uni-bremen.de/
http://www.mpic.de/Satellitenfernerkundung.2050.0.html
http://www.temis.nl/

where SCIAMACHY data products, scientific results and related detailed information about our atmosphere can be found.

3.1 Tropospheric Composition – Greenhouse Gases

SCIAMACHY measurements provide information on tropospheric constituents as solar radiation penetrates the atmosphere down to the surface. Our civilisation imposes a significant stress upon the troposphere. Concentrations of greenhouse gases are increasing and have been identified as the source of global warming. SCIAMACHY permits not only the monitoring of the global status of the major greenhouse gases but also the retrieval of knowledge about the distribution of their sources such as e.g. densely populated regions or wetlands.

Carbon Dioxide – CO2

CO2, the most important anthropogenic greenhouse gas, is regulated by the Kyoto Protocol and can be considered as a synonym for the impact of industrialisation on our environment. In pre-industrial times, CO2 mixing ratios dating back several thousands of years were about 300 ppm at maximum. Present values are around 390 ppm, i.e., 30% higher, with the increase mainly attributed to the past 50 years – a clear indication of an anthropogenic effect. Carbon dumped into natural sinks over millions of years is now being released into the atmosphere by fossil fuel burning (oil, coal, gas). In addition, other anthropogenic activities such as deforestation destroy important CO2 sinks and reduce nature’s ability to recycle atmospheric CO2 efficiently. A thorough study of carbon dioxide is therefore necessary to understand the global carbon cycle and to predict how greenhouse gas concentrations evolve with time. Currently, about 50% of the emitted CO2 remains in the atmosphere, the other half is taken up by the oceans and in the biosphere. Photosynthesis extracts carbon dioxide from the troposphere over land. Thus, large forest areas act as a CO2 sink. The North American and Siberian boreal forests in summer are examples for such extended CO2 sinks. These sink regions can be observed by SCIAMACHY, as illustrated in Fig. 3-1 displaying atmospheric CO2 levels from April to June compared to July to September, where CO2 concentrations are lower due to uptake by the terrestrial biosphere. This seasonal ‘CO2 breathing’ is superimposed on the steady increase of atmospheric CO2 with much higher concentrations in 2009 than in 2003. Both phenomena can be clearly observed by SCIAMACHY.

Methane CH4

fig. 3-1

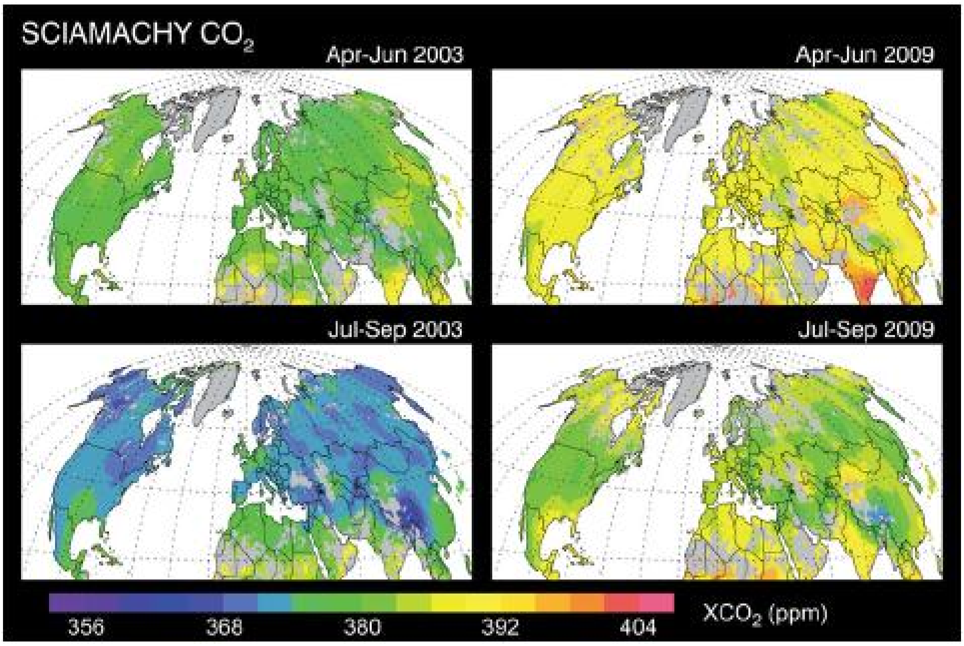

Northern hemispheric CO2 distribution as observed by SCIAMACHY. The differences between spring and summer are due to the CO2 'breathing' of the vegetation. (Graphics: M. Buchwitz, IUP-IFE, University of Bremen)

SCIAMACHY nadir observations in the SWIR spectral region formed the basis for the retrieved CO2 information (*Buchwitz et al. 2005a, 2007a, Bösch et al. 2006, Barkley et al. 2007, Reuter et al. 2010, Schneising et al. 2008*). The CO2 mixing ratio is obtained by normalising the CO2 column with the simultaneously retrieved airmass from oxygen measurements (*Schneising et al. 2008*) or by using meteorological surface pressure (*Barkley et al. 2007*). (fig. 3-1)

Methane – CH4

CH4 is the second most important anthropogenic greenhouse gas next to CO2. It is regulated by the Kyoto Protocol, as well. Compared to pre-industrial times, CH4 concentrations have more than doubled due to anthropogenic activities. Although the total sum of all CH4 sources, about 550 Tg/year, is relatively well known, the distribution among different source categories is highly uncertain and impedes our capability to reliably predict CH4 source strengths in a warming climate. First results from SCIAMACHY showed substantially higher tropical CH4 abundances than previously estimated (*Frankenberg et al. 2005*). Even though these results were recently partially revised (*Frankenberg et al. 2008*), the fact that tropical emissions are very high, constituting about a third of all CH4 emissions, remains true. In general, SCIAMACHY CH4 retrievals have substantially matured and results from several independent studies (see also *Buchwitz et al. 2005b, Schneising et al. 2009*) draw a consistent picture of the global distribution of this greenhouse gas.

fig. 3-2

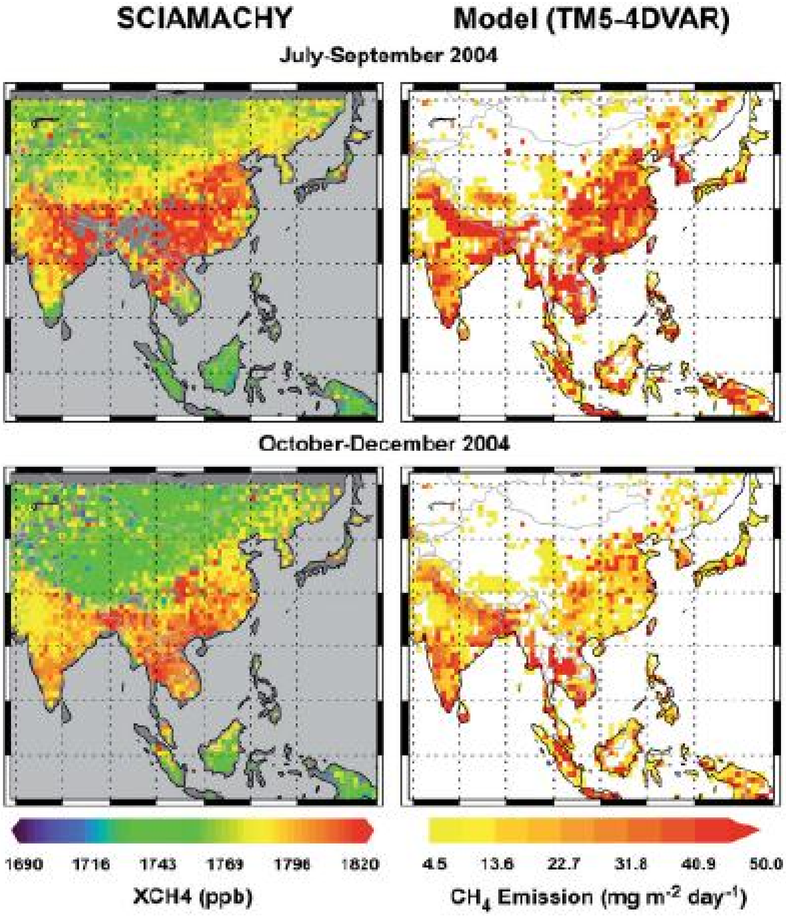

Methane emission derived from SCIAMACHY data. Left column: Column-averaged CH4 mixing ratios (XCH4) over South-East Asia from SCIAMACHY for summer and autumn 2004. Right column: Modelled emissions per 1? ? 1? grid cell. (Graphics: adapted from Bergamaschi et al. 2009, reproduced by permission of American Geophysical Union)

For CH_4, already improved emission estimates have been obtained on the basis of SCIAMACHY data. An atmospheric general circulation model, in which the current knowledge of global sources is implemented, is used to model the worldwide CH_4 distribution. The source terms in this model can be adjusted in magnitude, region and timing until the modelled distribution provides the best match with SCIAMACHY observations, thus obtaining *inverted* source estimates using satellite data (*Meirink et al. 2008*). Recent inversion studies (*Bergamaschi et al. 2009*) result in significant changes in the spatial patterns of emissions and their seasonality compared to the bottom-up inventories. Large CH_4 emissions are attributed to various wetland regions in tropical South America and Africa, seasonally varying and opposite in phase with CH_4 emissions from biomass burning. As obvious in fig. 3-2, India, China and South East Asia are characterised by pronounced emissions from rice paddies peaking in the third quarter of the year, in addition to further anthropogenic emissions throughout the year.

Water Vapour – H2O

Water is the key to the Earth's climate system. As vapour, it is the strongest greenhouse gas and as precipitation, it is the essential ingredient for making our planet habitable. Water vapour is a highly variable component of the atmosphere with direct anthropogenic impact on its amount being usually negligible. Its contribution may reach up to 4% of the atmospheric volume in the tropics and amounts to less than 1% in dry air conditions. Due to the relation between temperature and humidity, water vapour acts as a positive feedback to anthropogenic radiative forcing and is thereby indirectly affected by human activity.
In contrast to microwave instruments, SCIAMACHY water vapour data is available over both land and ocean down to the surface for at least partly cloud-free scenes. Because of their independence from other *in situ* or remote sensing measurements, SCIAMACHY water vapour columns provide a new important global dataset (*Noël et al. 2004, Schrijver et al. 2009*). A combination of SCIAMACHY water vapour with corresponding data derived from GOME and follow-on instruments allows the study of water vapour long-term trends now already spanning more than 15 years, with the potential of extension until 2020 when GOME-2 data on METOP is considered.

Fig. 3-3

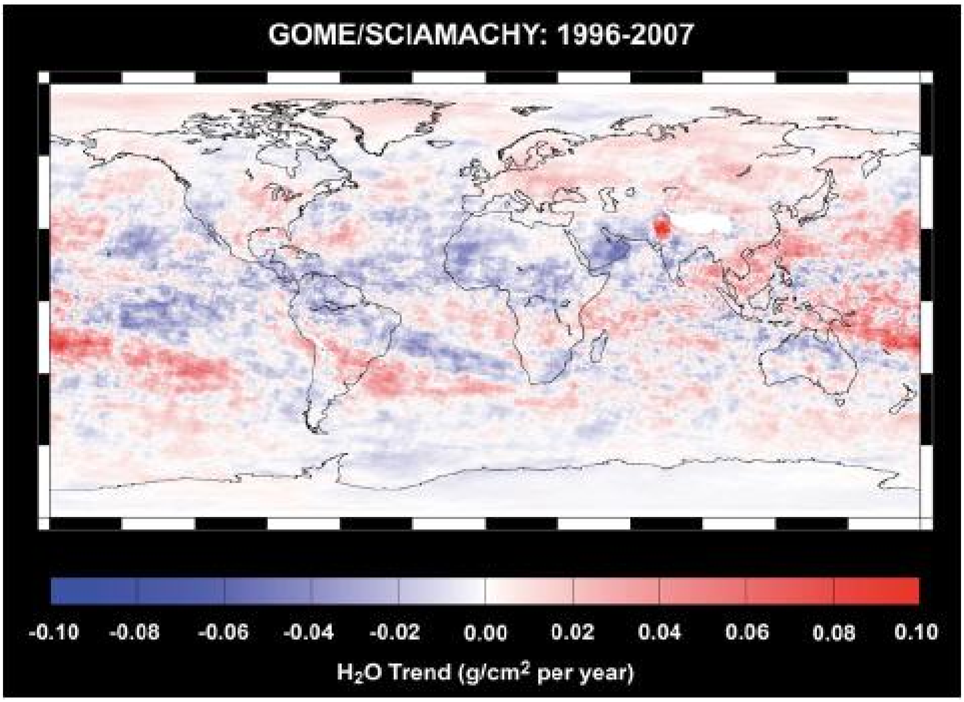

Water vapour trends for 1996 to 2007 as derived from GOME and SCIAMACHY. (Graphics: S. Mieruch, IUP-IFE, University of Bremen)

Using linear and non-linear methods from time series analysis and standard statistics, the trends of H_2O columns and their errors have been derived from GOME and SCIAMACHY for the years 1996 to 2007 (*Mieruch et al. 2008*). The trends clearly show elevated water vapour levels in years of strong El-Nino activity. How these trends are distributed on a global scale is further demonstrated in Fig. 3-3. Increasing long-term trends in water vapour have been observed for Greenland, Eastern Europe, Siberia and Oceania, whereas decreasing trends occur for the northwest US, Central America, Amazonia, Central Africa and the Arabian Peninsula. (fig. 3-3)

Heavy Water HDO

Heavy Water – HDO

When water evaporates from the Earth's oceans and surface, moves through the atmosphere and falls back as rain, evaporation and condensation processes change the content of heavy water (HDO). Therefore, the isotopic composition contains information about the history of water. SCIAMACHY's measurements permit obtaining a global view on the water vapour isotopic composition in the atmosphere (*Frankenberg et al. 2009*). These are the first global isotope measurements with high sensitivity towards the lowest layers of the atmosphere down to the surface, where most of the water vapour resides. By exploiting the capability of SCIAMACHY to retrieve H2O and its heavier isotopologue HDO, new insights into the hydrological cycle are provided.

Fig. 3-4 presents the global distribution of the water isotope HDO shown as relative abundance of water vapour. High fractions of HDO are found in the tropics and sub-tropics where water evaporates from the oceans and is then transported towards the poles. The relative amount of heavy water in the remaining water vapour will be reduced as the heavy isotope rains out preferentially resulting in lower abundances at higher latitudes. The same occurs when moist air from the oceans travels over the continents as e.g. clearly seen in North America. The satellite data bear the potential to rigorously test and subsequently improve the description of such cycles in climate models. This will eventually even result in better predictions of the changes in the hydrological processes, e.g. drought and precipitation in a future climate.

fig. 3-4

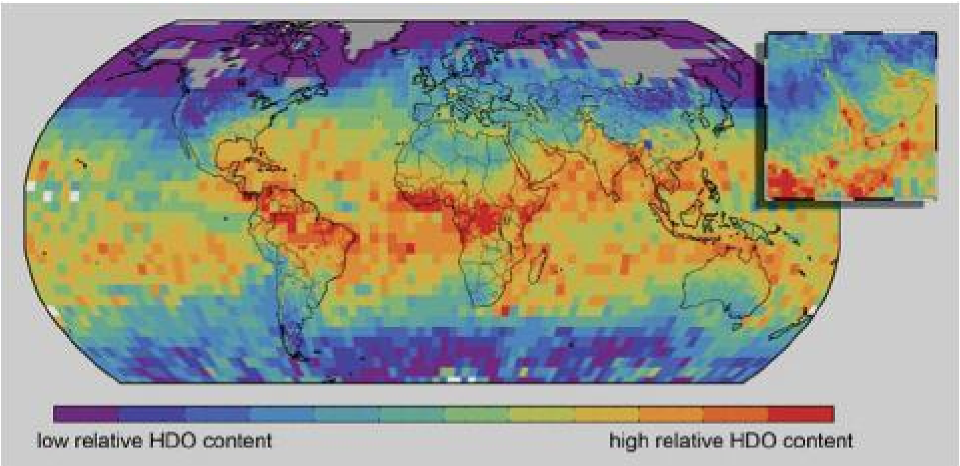

Global distribution of the water isotope HDO shown as relative abundance of water vapour averaged between 2003 and 2005. The inset displays enhanced HDO fractions due to strong evaporation over the Red Sea (Graphics: C. Frankenberg, SRON - now JPL)

Absorbing Aerosol Index and Precipitation

Water in the form of precipitation plays a dominant role in local climate and weather. This is particularly the case in Africa where the monsoon is the driving mechanism for the climate and therefore, also for the social and economic development. The northern part of Africa hosts large dry areas such as the Sahara and the Sahel. Dust storms arise frequently from the dry areas and have a profound impact on the weather conditions and lives of the local people. A linkage between the African monsoon systems and aerosol loading in Africa is suggested by the analysis of GOME and SCIAMACHY measurements. De Graaf et al. (*2010*) investigated multi-year satellite observations of UV-absorbing aerosols and compared these with precipitation data.

fig. 3-5

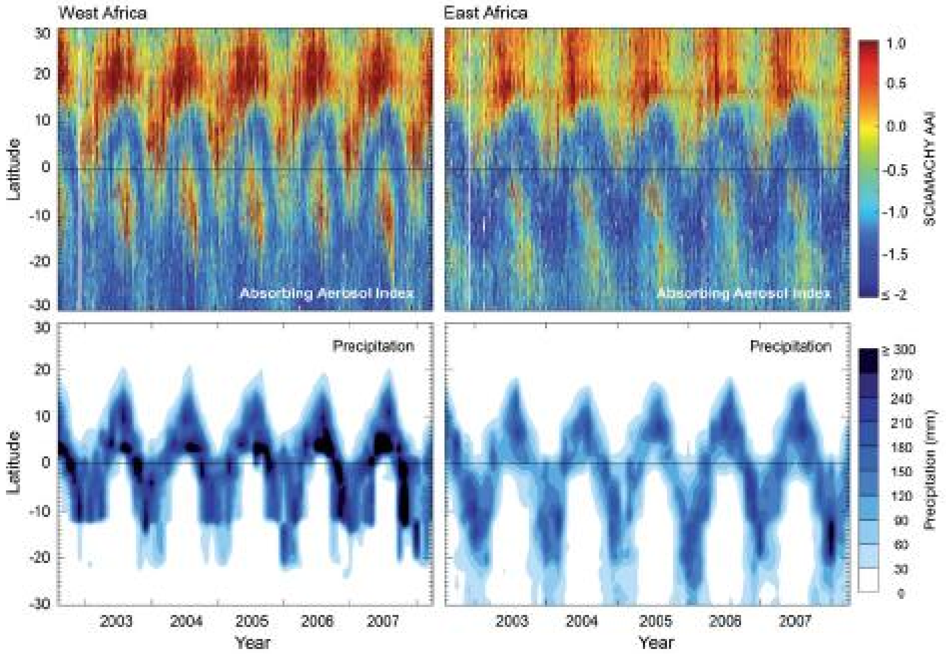

Zonally averaged AAI from SCIAMACHY for each day between August 2002 and April 2008 as a function of latitude in Western and Eastern Africa (upper panels). The bottom panels display the monthly and zonally averaged precipitation for the same areas and the same period. (Graphics: M. de Graaf, KNMI)

Tropospheric Composition Reactive Gases

The main UV-absorbing aerosol types occurring over Africa are desert dust and biomass burning aerosols. Their abundances can be characterised by using Absorbing Aerosol Index (AAI) data from GOME and SCIAMACHY. Time series of regionally averaged AAI from 1995 to 2008 show the seasonal variations of aerosols in Africa. When relating the zonally averaged daily AAI to monthly mean precipitation data, they indicate monsoon-controlled atmospheric aerosol loadings, which are different for the West African and East African monsoons owing to their different dynamics caused by the asymmetric distribution of land masses around the equator. Fig. 3-5 clearly shows that the seasonal variation of the aerosol distribution is linked to the seasonal cycle of the monsoonal wet and dry periods in both areas. During dry periods, the AAI varies freely, driven by emissions from deserts and biomass burning events. During wet periods the AAI depends linearly on the amount of precipitation due to scavenging of aerosols and the prevention of aerosol emissions from wet surfaces. (see fig. 3-5)

3.2 Tropospheric Composition – Reactive Gases

Emissions of greenhouse gases are not the only anthropogenic impact onto the lowest layer of the Earth's atmosphere. Pollution and air quality have become a major concern in an ever increasing industrialised world. SCIAMACHY is able to detect and monitor the global, regional and local signatures of trace gases contributing to air pollution and to follow how emissions evolve with time.

Nitrogen Dioxide – NO2

NO2 is an important indicator of air pollution and a cause of summer smog. NO2 catalyses ozone production contributes to acidification and also adds to radiative forcing. The main sources of NO2 are anthropogenic in origin, e.g. power plants, vehicular traffic, forced biomass burning and both heavy and agricultural industry. Other but slightly less important sources comprise natural biomass burning, lightning and microbiological soil activity. NO2 emissions have increased by more than a factor of 6 since pre-industrial times, with concentrations being highest in large urban areas.Global monitoring of tropospheric NO2 emissions is a crucial task. SCIAMACHY's predecessor GOME has already demonstrated the unique ability to monitor tropospheric air pollution. Fig. 3-6 shows a global survey of tropospheric NO2 as seen by SCIAMACHY. The inset in Fig. 3-6 presents a time series of these concentrations over China. The periodic trend in NO2 columns each year can mainly be explained by seasonal variations in energy consumption while the overall increase in tropospheric NO2 over China is a result of the increase in industrial activity (*Richter et al. 2005a*). The inset also demonstrates how well SCIAMACHY matches with GOME and GOME-2. NO2 vertical columns of both instruments perfectly overlap around the turn of the year 2002 and from 2007 onwards.

fig. 3-6

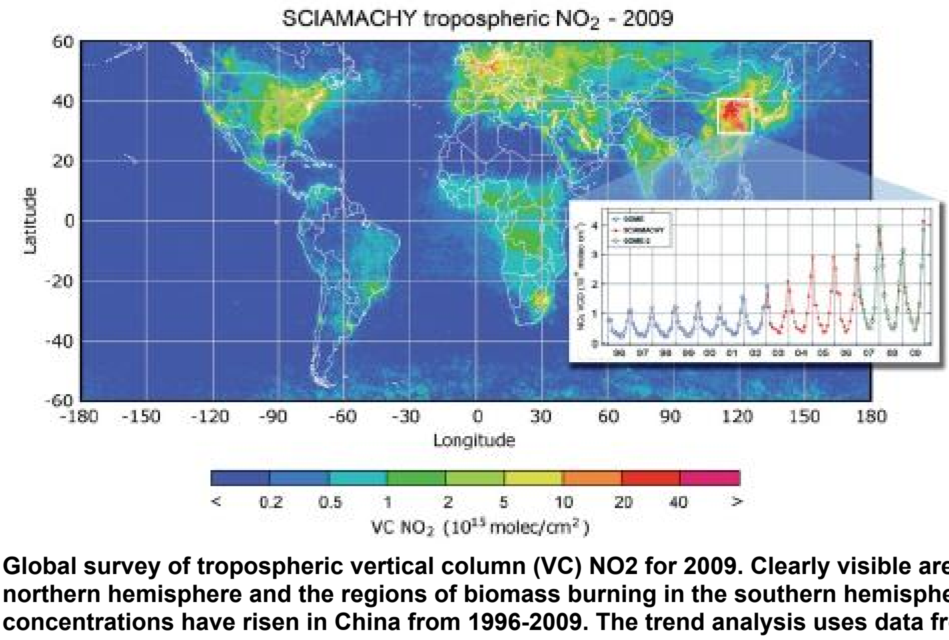

Global survey of tropospheric vertical column (VC) NO2 for 2009. Clearly visible are the industrialised regions in the northern hemisphere and the regions of biomass burning in the southern hemisphere. The inset illustrates how NO2 concentrations have risen in China from 1996-2009. The trend analysis uses data from GOME (1996-2002) and SCIAMACHY (2003-2009). While 'old' industrialised countries were able to stop the increase of NO2 emissions, the economical growth in China turns out to be a strong motor for pollution. (Graphics: A. Richter, IUP-IFE, University of Bremen)

Due to its higher spatial resolution (60 km ´ 30 km as compared to 320 km ´ 40 km for GOME), SCIAMACHY enables very detailed observations of polluted regions. As a result of these new datasets, individual cities (*Beirle et al. 2004*) and even large power plants (*Kim et al. 2009*) can be identified. Similar small scale structure in NO2 emissions can also be detected over the oceans. The high sensitivity and spatial resolution of the SCIAMACHY measurements permits localising frequently used ship routes (Richter et al. 2004). Using data from GOME, SCIAMACHY and GOME-2, *Franke et al.* (2009) could even derive temporal changes in these 'tiny' signatures of anthropogenic activity.

Particularly interesting are studies concerning the global trend in NO2 concentrations (*Richter et al. 2005a, Stavrakou et al. 2008, van der A et al. 2008*). By combining SCIAMACHY results with those of previous missions, e.g. GOME, it is possible to investigate how the tropospheric NO2 load has changed over the past decade. A strong increase in nitrogen dioxide is observed by SCIAMACHY in countries and areas with a booming economy, particularly in China (see inset Fig. 3-6), while in Europe, SCIAMACHY has observed a stabilisation of NO2 levels which is attributed partly to slightly increased traffic emissions after a period of reducing nitrogen dioxide levels in the 1990's as a result of EU regulations. For the US, SCIAMACHY results indicate a decrease in NO2 emissions related to the recent implementation of pollution controls for power plants (*Kim et al. 2006*).

The spatial and temporal characteristics of a multi-year dataset provide much improved constraints for attempts to identify main emission sources and to quantify emission strengths by inverse modelling. It also facilitates the derivation of independent top-down estimates of emissions not only on a country-by-country basis but even on regional scales. Konovalov et al. (*2008, 2010*) investigated such trends within Europe for a 10 year time period showing that while emissions are decreasing in many countries, emissions have increased especially in the Mediterranean area, along the coastlines, as well as in Eastern Europe. Van der A et al. (*2008*) analysed the spatial and temporal patterns in a multi-year dataset of GOME and SCIAMACHY tropospheric NO2 and identified the most dominating emission sources (fig. 3-7) from this data. Whereas in the northern hemisphere, the NO2 mainly stems from anthropogenic sources and from soils, biomass burning is the dominating origin of tropospheric NO2 in the southern hemisphere.

fig. 3-7

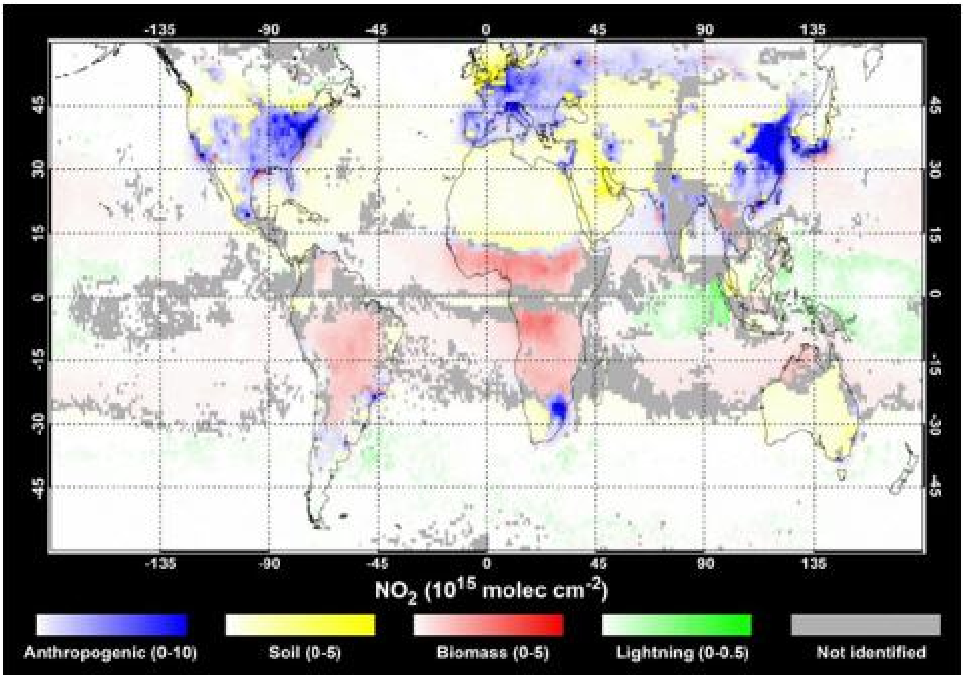

Dominant NOx source identification based on analyses of the time series of measured tropospheric NO2 from GOME and SCIAMACHY satellite observations (1996-2006). (Graphics: van der A et al. 2008, reproduced by permission of the American Geophysical Union)

By combining SCIAMACHY NO2 observations at 10:00 local time with NO2 observations from OMI at 13:30 local time, it even becomes possible to get a first glimpse on the diurnal variations of tropospheric chemistry and emissions from space. These measurements suggest a decrease in tropospheric NO2 between 10:00 and 13:30 over fossil fuel source regions due to photochemical loss. Over tropical biomass burning regions, the opposite effect – an increase due to a midday peak in emissions - is obvious (*Boersma et al. 2008*).

Sulphur Dioxide SO2

Sulphur Dioxide – SO2

SO2 is another pollutant leaving a clear absorption signature in SCIAMACHY spectra. Sources of SO2 are combustion of sulphur rich coal and other fossil fuels or volcanic eruptions including degassing. Although SO2 emissions have been reduced significantly over the last decades, clear signals can be detected over the Eastern US and, in particular, the polluted areas of China (fig. 3-8). As in the case of NO2, the high spatial resolution facilitates source identification and makes the dataset an interesting new data source for air pollution research. By combining GOME and SCIAMACHY results, the long-term trend of SO2 emissions in heavily polluted areas can be inferred and compared with similar analyses for NO2 (see inset of fig. 3-8).

fig. 3-8

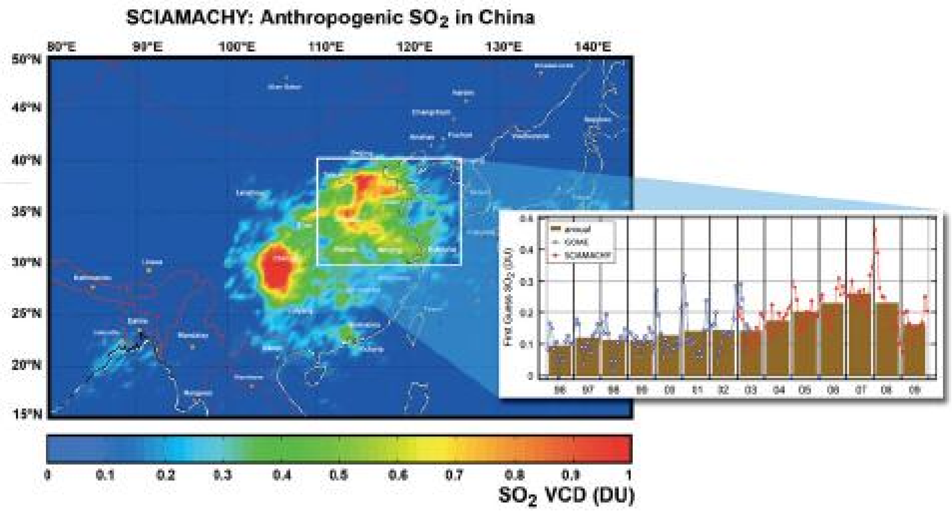

Average SO2 vertical column densities (VCD) over eastern China during the year 2003. SCIAMACHY's improved spatial resolution permits to identify localised emissions due to anthropogenic activities. The trend analysis uses data from GOME (1996-2002) and SCIAMACHY (2003-2009). (Graphics: map - M. Van Roozendael, BIRA-IASB; trend - A. Richter, IUP-IFE, University of Bremen)

Volcanoes are a natural source of SO2. Since the start of SCIAMACHY's routine observations, a few of the several hundred existing active volcanoes have been erupting and were overpassed by ENVISAT. In October 2002, Mt. Etna on the island of Sicily entered an explosive phase. The rectangular overlay in fig. 3-9 represents a SCIAMACHY nadir measurement displaying SO2 emissions which match well with the ash plume visible on an image simultaneously obtained by MERIS on ENVISAT. The SO2 emissions of volcanic eruptions are usually associated with such volcanic ash plumes. These could be a major threat for air traffic. Therefore, SCIAMACHY SO2 retrievals are used in early warning services in support of aviation control. Whenever elevated SO2 densities are obtained in regions with known volcanoes, an alert is issued indicating a potential volcanic ash cloud.

fig. 3-9

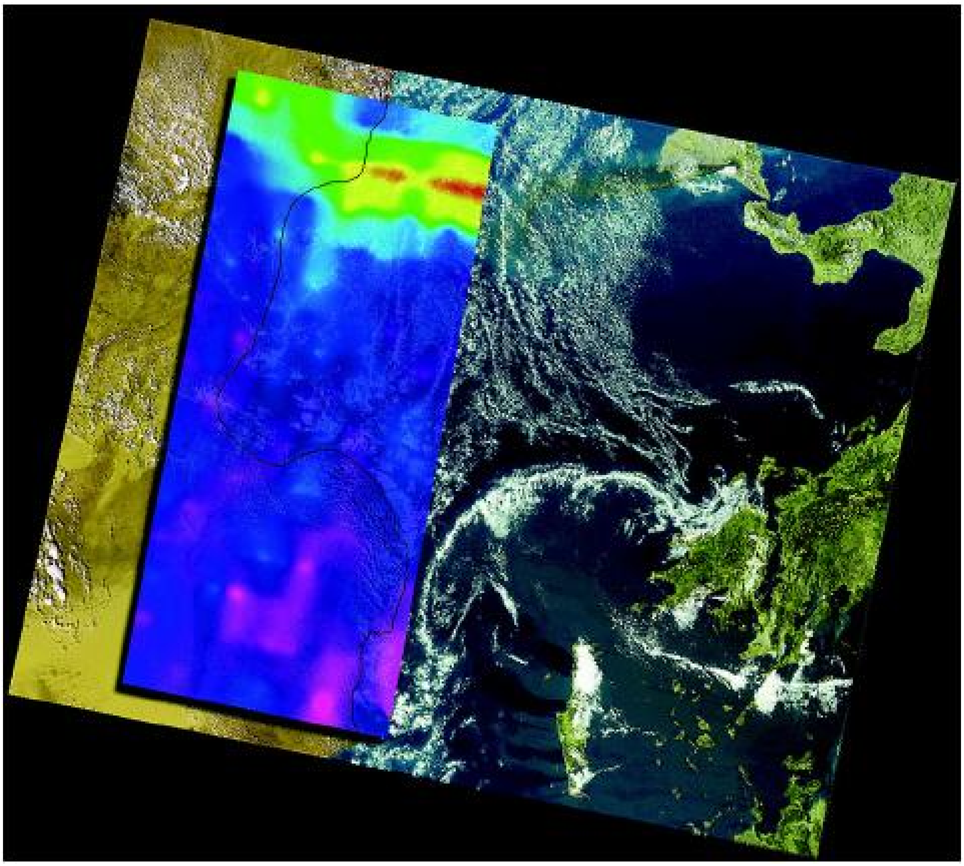

The Mt. Etna volcanic eruption in 2002 with obvious SO2 emissions (reddish plume). The SCIAMACHY nadir measurement is overlayed on a MERIS image showing that the plume of SO2 and the visible ash cloud match well. (Graphics: ESA and Brockmann Consult)

Formaldehyde (HCHO) and Glyoxal (CHOCHO)

Formaldehyde (HCHO) and Glyoxal (CHOCHO)

In the presence of nitrogen oxides, the photochemical degradation of volatile organic compounds (VOC) leads to secondary gaseous and particulate products, such as ozone and secondary organic aerosols (SOA). Both are important contributors to air pollution with severe impacts on human health, ecosystems, and regional climate. Two important intermediate products in the oxidation of volatile organic compounds are HCHO and CHOCHO. Since both trace gases have short lifetimes, their distribution mainly resembles the source areas and can be used as indicators of tropospheric VOC emissions. SCIAMACHY's capability to measure HCHO and CHOCHO from space on a global scale was demonstrated by Wittrock et al. (*2006*). Since then, several studies have been carried out using these data to compare directly with the output from chemical transport models (CTM) and thereby substantially improving the models' accuracy and reliability. In addition, VOC emission strengths have been derived for biospheric, pyrogenic and anthropogenic sources, respectively.

A consistent dataset of global tropospheric HCHO (fig. 3-10) has been created by De Smedt et al. (*2008*) using GOME and SCIAMACHY data covering more than a decade. This dataset has been utilised by Stavrakou et al. (2009) to evaluate the performance of pyrogenic and biogenic emission inventories and to investigate trends in HCHO over Asia and large cities worldwide (*De Smedt et al. 2010*). More regional aspects on the different emissions strengths of VOC based on HCHO data were investigated for Europe (*Dufour et al. 2009*) and Amazonia (*Barkley et al. 2009*). In general, for regions with high biogenic emissions like tropical rainforests, a reasonable agreement was found between modelled and measured HCHO columns. Other areas having more variable or less emissions of VOC reveal higher discrepancies. Recently, Marbach et al. (*2009*) even succeeded in determining HCHO emissions from ships in the Indian Ocean.

fig. 3-10

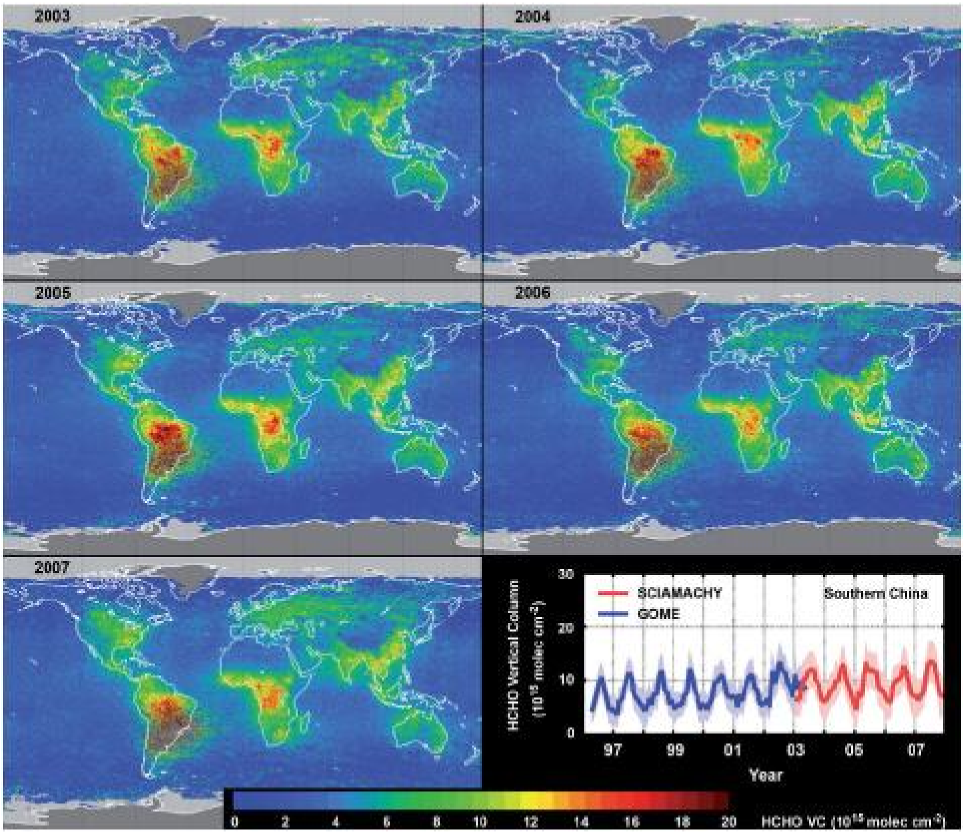

Yearly averaged SCIAMACHY HCHO vertical columns from 2003-2007. The HCHO trend over China is indicated in the bottom right panel. (Graphics: adapted from De Smedt et al. 2008)

Myriokefalitakis et al. (*2008*) adapted a global chemistry-transport model to simulate the temporal and spatial distribution of CHOCHO columns in the global troposphere focussing on the anthropogenic contribution. They found indication for a missing CHOCHO source of about 20 Tg/ year or an overestimate of its sinks by the model. In addition, Fu et al. (*2008*) examined the potential of CHOCHO as a source of secondary organic aerosol. Apparently, irreversible uptake of CHOCHO by aqueous aerosols and clouds could make a significant contribution to the global SOA production. The long SCIAMACHY time series also revealed seasonal and year-to-year variability above several photo-chemical hot spots. This has been studied by Vrekoussis et al. (*2009*) for CHOCHO (fig. 3-11). For the period 2002-2007, a significant annual increase in CHOCHO in addition to a seasonal cycle was reported over north-eastern Asia. In general, the regions influenced by anthropogenic pollution encounter enhanced amounts of CHOCHO.

Carbon Monoxide CO

fig. 3-11

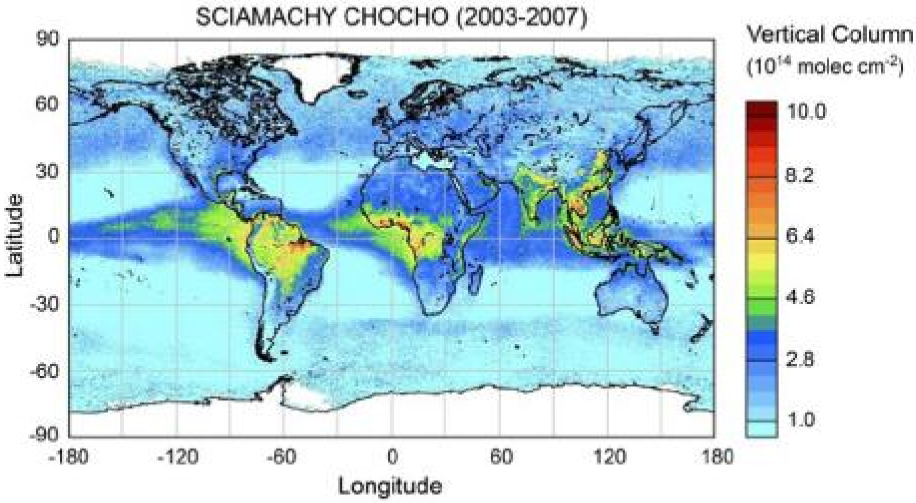

Multiannual (2003-2007) SCIAMACHY CHOCHO vertical columns. The largest amounts are found over the tropics and sub-tropics where vegetation and biomass burning is abundant. (Graphics: Vrekoussis et al. 2009)

Carbon Monoxide – CO

CO plays a central role in tropospheric chemistry because it is the leading sink of the hydroxyl radical, which itself determines the oxidising capacity of the troposphere to a large extent. Therefore, CO is of prime importance for the troposphere's self-cleansing efficiency and for the concentration of greenhouse gases such as CH4. CO also has a large impact on air quality because it is toxic and is a precursor of tropospheric ozone, a secondary pollutant which is associated with respiratory problems and decreased crop yields.

CO detection with SCIAMACHY is an ambitious task. Carbon monoxide vertical columns can be retrieved from a number of CO absorption lines located around 2.3 mm in the SWIR range. The retrieval is not straightforward because these lines are relatively weak, much weaker than the absorption structures of the overlapping absorbers water vapour and CH4. In addition, CO retrieval is hampered by a number of calibration issues that are mainly related to large variable dark signals and changing instrument characteristics as a result of the growth of an ice layer on the channel 8 detector (e.g. *Gloudemans et al. 2005*). Nevertheless, a first survey of global CO over land had been performed which shows elevated CO in the case of fires due to biomass burning. These results are consistent with MOPITT and model predictions to a large degree (*de Laat et al. 2006, Buchwitz et al. 2007b*). Gloudemans et al. (*2009*) also succeeded in deriving CO over the ocean, when using scenes with low maritime clouds. This yielded a five-year CO dataset over both land and clouded ocean scenes between 2003 and 2007 (fig. 3-12).

fig. 3-12

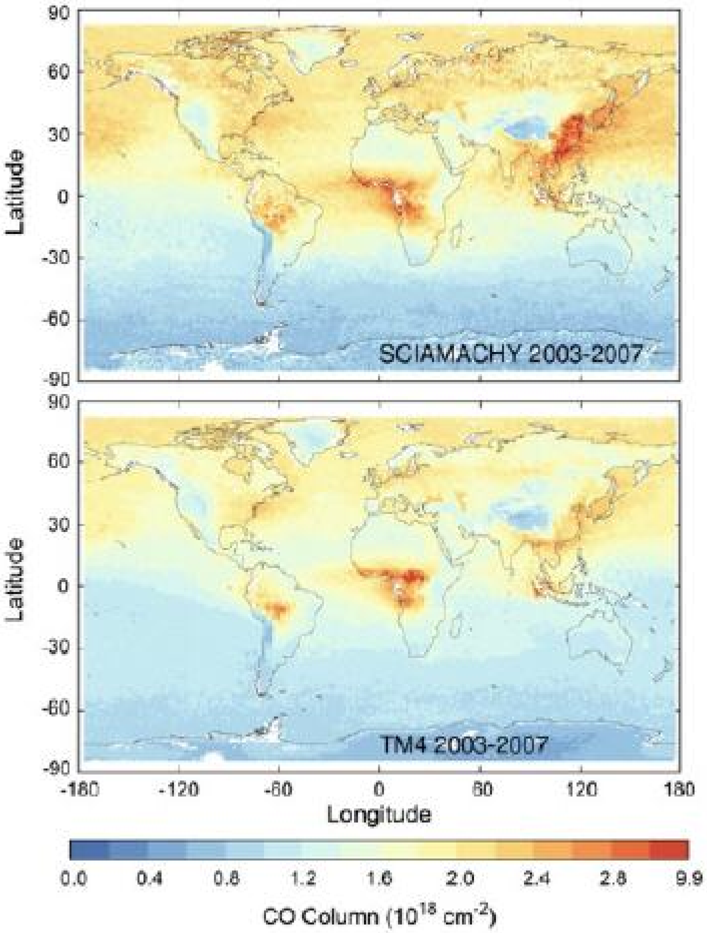

Five year (2003-2007) average CO total columns on a 1? ? 1? grid as retrieved by SCIAMACHY (top) and the TM4 chemistry-transport model (bottom). The SCIAMACHY CO columns above low clouds over sea are filled up with TM4 CO densities below the cloud to obtain total columns (Graphics: Gloudemans et al. 2009)

The CO measurements over clouded ocean scenes have been compared with co-located modelled CO columns over the same clouds and agree well. Using clouded ocean scenes quadruples the number of useful CO measurements compared to land-only measurements. The five-year dataset shows significant inter-annual variability over land and over clouded ocean areas, like Asian outflow of pollution over the northern Pacific, biomass-burning outflow over the Indian Ocean originating from Indonesia, and biomass burning in Brazil. In general, there is good agreement between observed and modelled seasonal cycles and inter-annual variability.
Assimilation of SCIAMACHY CO data was also used to improve CO emission estimates in the Middle East (*Tangborn et al. 2009*). One remarkable result is the finding that CO emissions over Dubai have more than doubled in 2004 compared to those in the available emissions inventory based on data from 1998.

Tropospheric Halogen Oxides – BrO and IO

BrO and IO are reactive halogen radicals which have gained growing interest in recent years (*Simpson et al. 2007*). Both compounds impact on tropospheric chemistry. They react with ozone and change the oxidation pathways of several atmospheric species. Bromine compounds have been identified as initiator of strong boundary layer ozone depletion events in polar spring (*Barrie et al. 1988*). The IO molecule constitutes the starting point for iodine nucleation and the formation of fine aerosol particles, which affect the atmospheric radiation balance and which may potentially grow to cloud condensation nuclei (*O'Dowd et al. 2002*). Widespread plumes of enhanced BrO are regularly observed in the Arctic, as well as in the Antarctic, shortly after polar sunrise where they persist for several months. The spatial distributions and locations of these plumes move rapidly on a daily basis (*Begoin et al. 2010*), with the BrO probably not only being situated in the boundary layer but also at higher altitudes. A strong link exists between the BrO patterns and sea ice cover. Sources of BrO are most likely of inorganic nature. Current discussions consider young sea ice, frost flowers, aerosols and brine (*Kaleschke et al. 2004; Piot and von Glasow, 2008*).

Recent analyses of SCIAMACHY nadir observations using spectral data around 420 nm have enabled the detection of tropospheric IO columns (*Saiz-Lopez et al. 2007, Schönhardt et al. 2008*). IO amounts are small and close to the instrument's detection limit, but through efficient reaction cycles, even these small amounts still have a considerable impact on the polar tropospheric chemistry. A variety of details in the temporal and spatial distribution of both IO and BrO over the Antarctic polar region is revealed in fig. 3-17. Monthly means from October through austral summer until March are shown, in each case data is averaged over four subsequent years. As for BrO, largest amounts of IO appear in Antarctic spring time. Besides this general similarity, spatial distributions are quite different. BrO is observed predominantly above sea ice regions during spring, and furthermore along coast lines and on shelf ice regions in summer. Abundances vanish towards autumn. IO, however, shows larger variability throughout the time series. Regions with enhanced IO include the sea ice, ice shelves, coast lines, but also the continent (in October). Enhanced IO above the sea ice in the characteristic ring-like pattern only occurs much later in spring (November) in contrast to BrO, where enhancements can already be observed in August well before the time period illustrated in fig. 3-13. When southern autumn approaches, IO concentrations begin to increase again. While BrO behaves similarly on both hemispheres, no widespread enhanced IO abundances are observed in the Arctic spring time.

Fig. 3-13

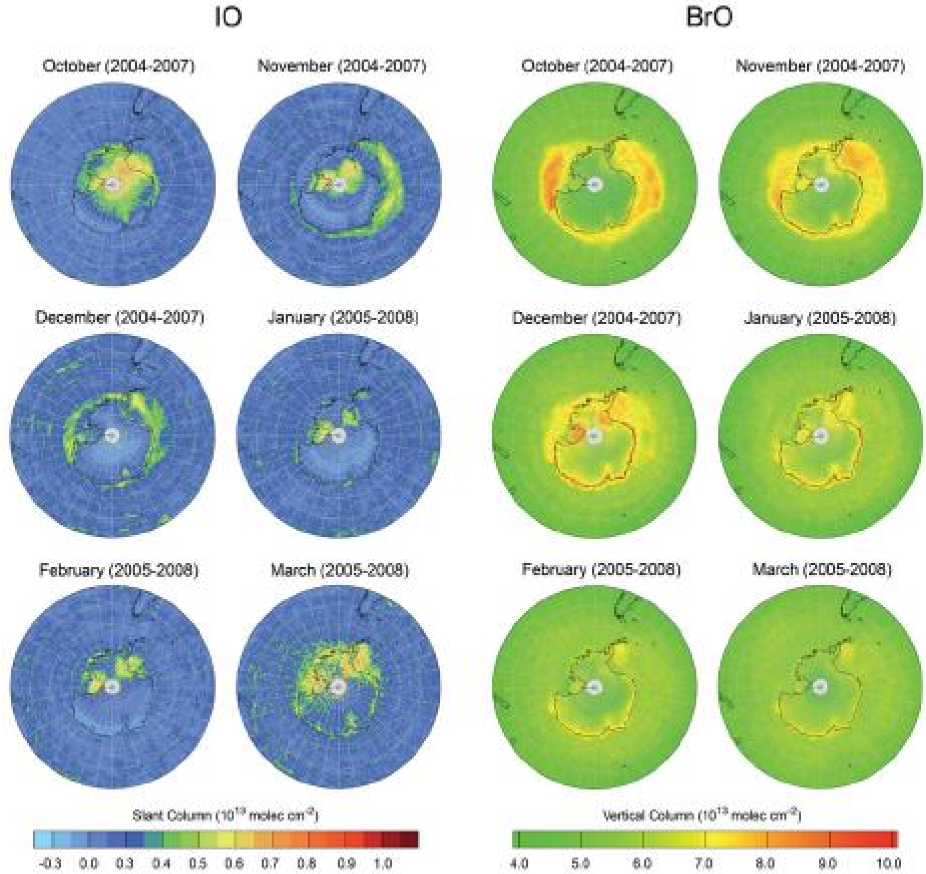

Monthly maps of SCIAMACHY observations of IO (left) and BrO (right), averaged over four subsequent years from 2004-2008. A stratospheric air mass factor (AMF) is applied to the BrO columns only, leaving the patterns of IO and BrO still comparable. (Graphics: A. Schönhardt, IUP-IFE, University of Bremen)

The details of the spatial and temporal patterns of IO in comparison to BrO are not well understood yet. However, the observed differences in the distributions suggest that the two halogen oxides are released by different processes. While the BrO is produced by inorganic emissions and the bromine explosion cycle, it is an open question whether the majority of IO is of biological origin. The cold Antarctic waters show high biological activity, and cold water diatoms may produce organic iodine species. Considerable differences between the South and North Polar regions might be linked to the fact that the biospheres are distinct and are emitting iodine compounds in different amounts and speciation.

3.3 The Stratospheric Ozone Layer

As early as the second half of the 20th century, the stratosphere was seen as fragile to human perturbation. Public interest grew even more with the detection of the Antarctic ozone hole in the mid-1980's. Until the mid-1990s, a steady decrease of up to 3-6% per decade in the ozone abundance has been observed over the South Pole, North Pole and the mid-latitudes. The most striking feature is the massive loss of stratospheric ozone over Antarctica every southern spring. This ozone loss is so large because very low stratospheric temperatures over Antarctica in wintertime foster the underlying depletion processes. The polar vortex isolates the air during the polar night and allows the cold conditions to remain stable and Polar Stratospheric Clouds (PSC) to grow. In this environment the chemistry of ozone depletion begins with the conversion of reservoir species to chemically active molecules on the surface of the PSC. These react with ozone in catalytical reaction cycles resulting in the effective destruction of the O3 molecules. In addition, ozone loss was also observed in the tropics and mid-latitudes. Today, there is broad agreement that a continuous monitoring of stratospheric ozone, the ozone hole and of those species impacting the ozone chemistry is necessary in order to detect possible signs of recovery, and to find out how far the cooling of the stratosphere and the strengthening of the Brewer-Dobson circulation as a consequence of climate change will delay or accelerate the recovery of the ozone layer (*Rex et al. 2006, Newman et al. 2007*).
SCIAMACHY allows exploitation of new opportunities using the limb backscatter, as well as solar or lunar occultation measurement modes, to determine PSC and vertically resolved concentration profiles of trace gases in the stratosphere, in addition to the established column measurements from the nadir mode.

Ozone O3

Ozone – O3

The important role of ozone in the Earth's atmosphere is attributed to the fact that it absorbs solar UV radiation which would otherwise reach the surface where it can cause damage to the biosphere. In the wavelength range below 290 nm, UV photons are almost completely blocked. Radiation from 290 nm to 320 nm is strongly attenuated so that dose levels on ground become harmless. Ozone does not only impact conditions at the bottom of the troposphere but also in the upper atmosphere through the effects of absorption of UV to IR radiation and subsequent heating. The heating produces a temperature profile which makes the stratosphere vertically stable. Even transport mechanisms in the layers above – the mesosphere and thermosphere – were found to be influenced by the energy content of the stratosphere.

fig. 3-14

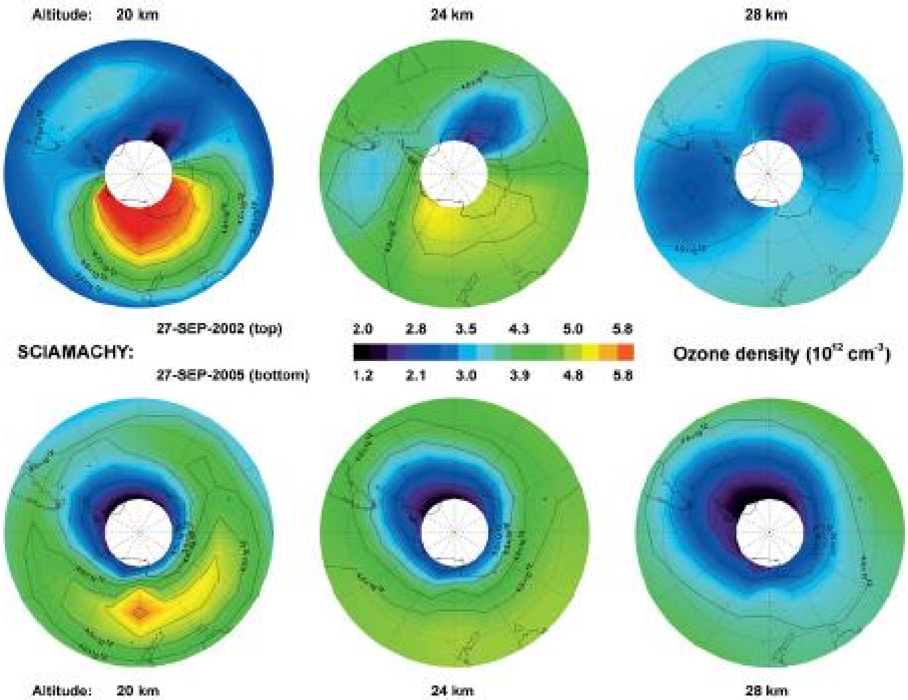

Slices of the polar southern hemisphere ozone field at altitudes of approximately 20, 24 and 28 km on 27 September 2002 and 27 September 2005 as measured by SCIAMACHY. The observed split of the ozone hole in 2002 is not so obvious in the lower stratosphere around 20 km, but clearly visible at 24 and 28 km. In 2005, an ozone hole of 'normal shape' existed at all altitudes. (Graphics: C. von Savigny, IUP-IFE, University of Bremen)

In the year of ENVISAT's launch, the ozone hole over Antarctica differed significantly from what had been observed before and after. Its extent was reduced in 2002 by 40% as compared to previous years. However, this did not indicate a recovery of the ozone layer but was actually caused by peculiar meteorological conditions where an unprecedented major stratospheric warming led to a split-up of the polar vortex, thereby interrupting the heterogeneous processes that usually lead to massive ozone destruction. A more detailed view of this September 2002 event was obtained by retrieving stratospheric profiles over Antarctica (*von Savigny et al. 2005a*). The vertically resolved SCIAMACHY limb measurements showed that the ozone hole split did not occur throughout the entire stratosphere but only above about 24 km. At 20 km there was still a single elongated area with low O3 values (fig. 3-14).

In normal cold Antarctic winters, however, the O3 profiles display a more regularly shaped ozone hole throughout the altitude range. The anomalous ozone hole in 2002 also developed quickly in time. This ozone hole split-up was already predicted in the 9-day ozone forecast at KNMI (see *Eskes et al. 2005*). The following years displayed again an ozone hole similar in size to those observed by SCIAMACHY's predecessor GOME (fig. 3-15).

fig. 3-15

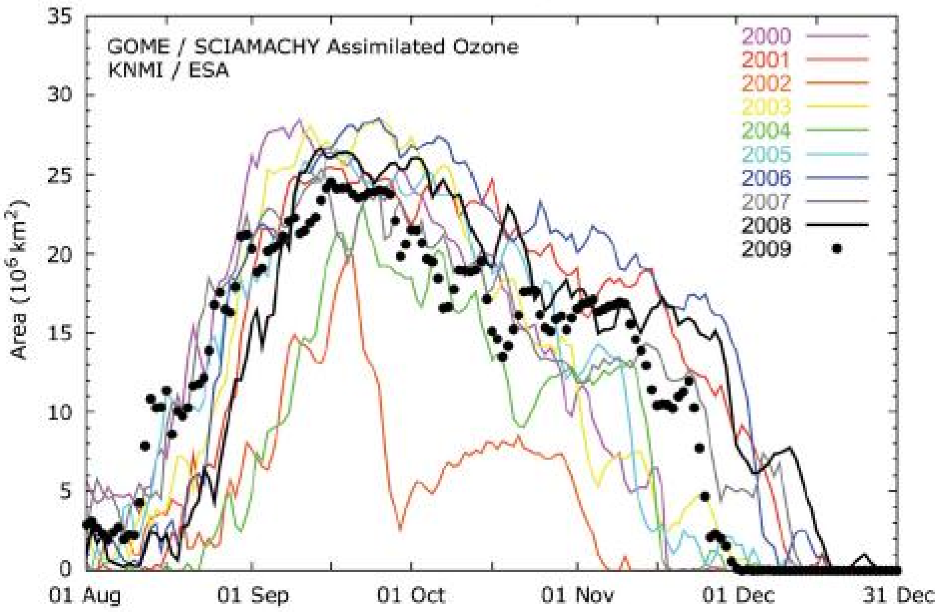

Time series of the size of the Antarctic ozone hole from 2000-2009 based on observations of GOME and SCIAMACHY. The area includes ozone column values below 30?S lower than 220 Dobson Units. (Graphics: TEMIS KNMI/ESA)

Over the Arctic, stratospheric temperatures are usually higher than over Antarctica, i.e. the polar vortex is less stable and PSC are a rare phenomenon. Thus, ozone depletion is not observed as regularly as in high southern latitudes at the end of the winter. However, unexpected cold northern winters change the situation, as was the case in 2005 (e.g. *Bracher et al. 2005*).

While most studies of the chemical ozone loss inside the polar vortices focused mainly on the northern hemisphere because of the strong inter-annual variability in the stability of the vortex and the following ozone loss, Sonkaew et al. (*2010*) also analysed ozone depletion inside the Antarctic polar vortex by using limb ozone profiles. They determined the chemical ozone loss via the difference between the observed vortex-average ozone abundance and the abundance modelled without considering chemical processes, but with including dynamically induced ozone changes.

fig. 3-16

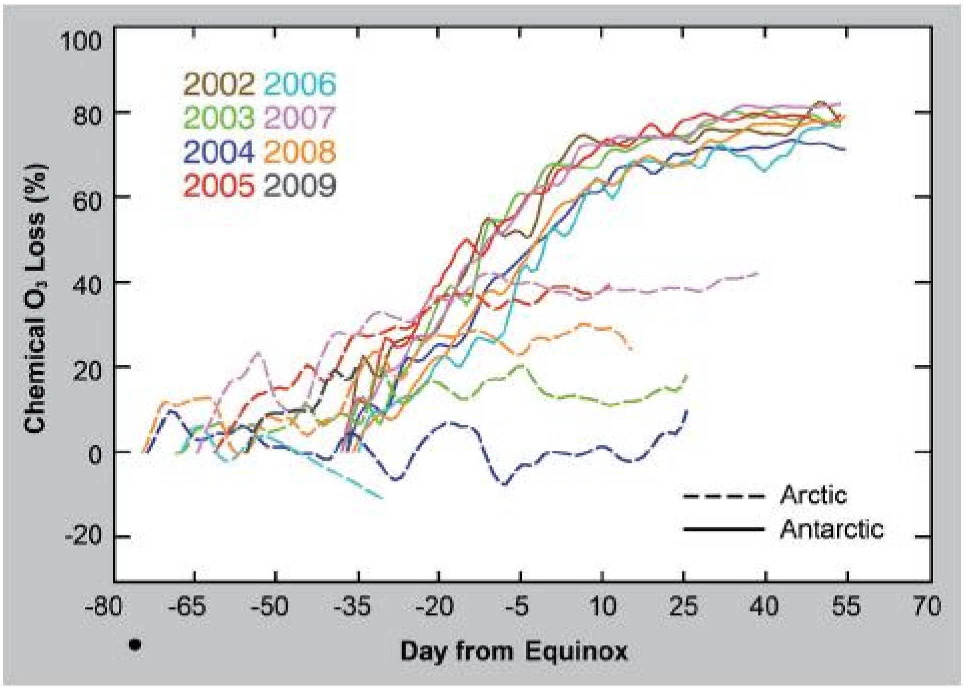

Relative chemical ozone losses at the 475 K isentropic level (around 18 km) for the period 2002-2009 in the Arctic (dotted lines) and Antarctic (solid lines) polar vortices. (Graphics: IUP-IFE, University of Bremen)

Fig. 3-16 depicts the relative chemical ozone losses at the 475 K isentropic level – corresponding to an altitude of about 18 km – for the period 2002-2009 in the Arctic and Antarctic polar vortices. Several obvious differences exist between the two hemispheres. The chemical ozone losses in the Antarctic polar vortex do not vary much from year to year. Even in the anomalous year 2002 (see above), the relative ozone loss inside the vortex is similar to all other years. In the northern hemisphere, however, significant inter-annual variability exists, with some years, e.g. 2005 and 2007, exhibiting relatively strong chemical ozone losses and other years (2004, 2006) showing little or no ozone loss. (fig. 3-16)

Ozone depletion occurring during winter and spring in each hemisphere inside the polar vortices is a more localised phenomenon when compared to the global and continuous effects of anthropogenic halogen emissions on the stratospheric ozone layer. Again, O_3 limb profiles have proven a valuable tool for investigating long-term trends in stratospheric ozone. Steinbrecht et al. (*2009*) determined upper stratospheric ozone trends for several latitude bands from 1979 to 2008 using ground-based LIDAR and microwave as well as satellite observations with SAGE II, HALOE, SBUV, GOMOS and SCIAMACHY. As demonstrated by Steinbrecht et al. (*2009*), 'witnessing' the recovery of stratospheric ozone requires long-term datasets. These are usually not provided by a single instrument but by a series of preferably similar sensors. Since SCIAMACHY is GOME heritage, combining GOME, GOME-2 and SCIAMACHY total columns from nadir measurements generates a unique repository. Loyola et al. (2009) formed a homogeneous dataset by merging O_3 columns from June 1995 to August 2009. Measurements from over 70 globally distributed Dobson and Brewer ground stations served as validation reference. Since the GOME data record is very stable, it was used as a transfer standard and SCIAMACHY and GOME-2 data in periods of instrument overlap were adjusted accordingly. Global ozone trends were then derived by applying statistical methods, including the entire 60°N-60°S average serving as a near global mean. Fig. 3-17 illustrates how well the merged GOME/GOME-2/SCIAMACHY dataset of total ozone columns compares with results from the chemistry-climate model (CCM) E39C-A. This figure again displays the so-called 'O_3 anomaly' which is the residual when subtracting the mean annual cycle from the satellite measurements. Apparently, the phase of minimum stratospheric ozone is just occurring and a recovery can be expected in the next decades.

The current good match between the CCM and the observations in fig. 3-17 is a hint that the models' predications are trustworthy.

fig. 3.17

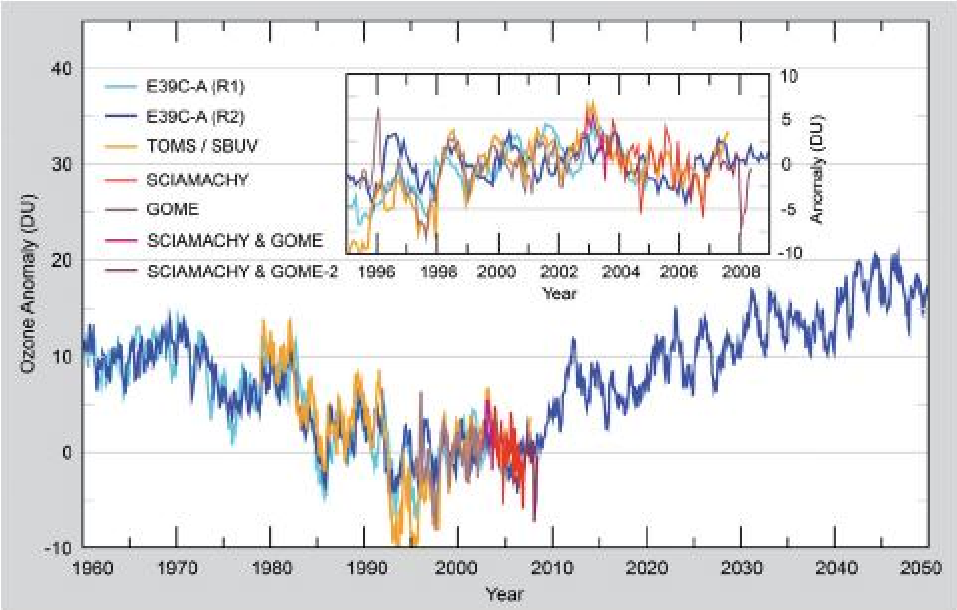

Total ozone anomaly from 60?N to 60?S from the merged GOME/SCIAMACHY/GOME-2 dataset. For comparison, the results from the merged TOMS/SBUV/OMI are given, together with predictions from climate-chemistry model runs. (Graphics: Loyola et al. 2009, reproduced/modified by permission of American Geophysical Union)

Chlorine Dioxide – OClO

One key question related to the expected recovery of stratospheric ozone is the degree of chlorine activation observed in polar winter and spring in both hemispheres. This effect depends not only on the total available inorganic chlorine amount but also on the presence of PSC for the activation of the chlorine reservoirs. The latter is a function of temperature and polar vortex stability and therefore is impacted by changes of the stratospheric dynamics and temperatures in response to increased concentrations of greenhouse gases. One good indicator for chlorine activation is the presence of OClO which is formed by reaction of BrO and ClO.

While SCIAMACHY observations in nadir (*Kühl et al. 2006*) continue the global measurements of total columns of OClO started with GOME (*Wagner et al. 2001, Kühl et al. 2004, Richter et al. 2005b*), vertical profiles of OClO can also be derived from the limb observations (Kühl et al. 2008). By applying a tomographic 2D approach (*Pu??te et al. 2008*), the retrieval can take into account horizontal gradients in the distribution of OClO, which is particularly important at the edge of the polar vortex. Fig. 3-18 shows the OClO number density at 19 km altitude above the northern hemisphere derived from the SCIAMACHY limb observations (top), and the corresponding total column derived from nadir view (bottom) for mid of February in the Arctic winters 2002/03 to 2008/09. The data displays strong stratospheric chlorine activation only inside the polar vortex for cold winters, reflecting the strong dependence of the degree of chlorine activation on the meteorological conditions of the respective winter, such as temperature and potential vorticity. While almost no OClO is found for the warm winters 2003, 2004, 2006 and 2009, much stronger activation of chlorine is observed for the cold winters 2005, 2007 and 2008.

fig. 3-18

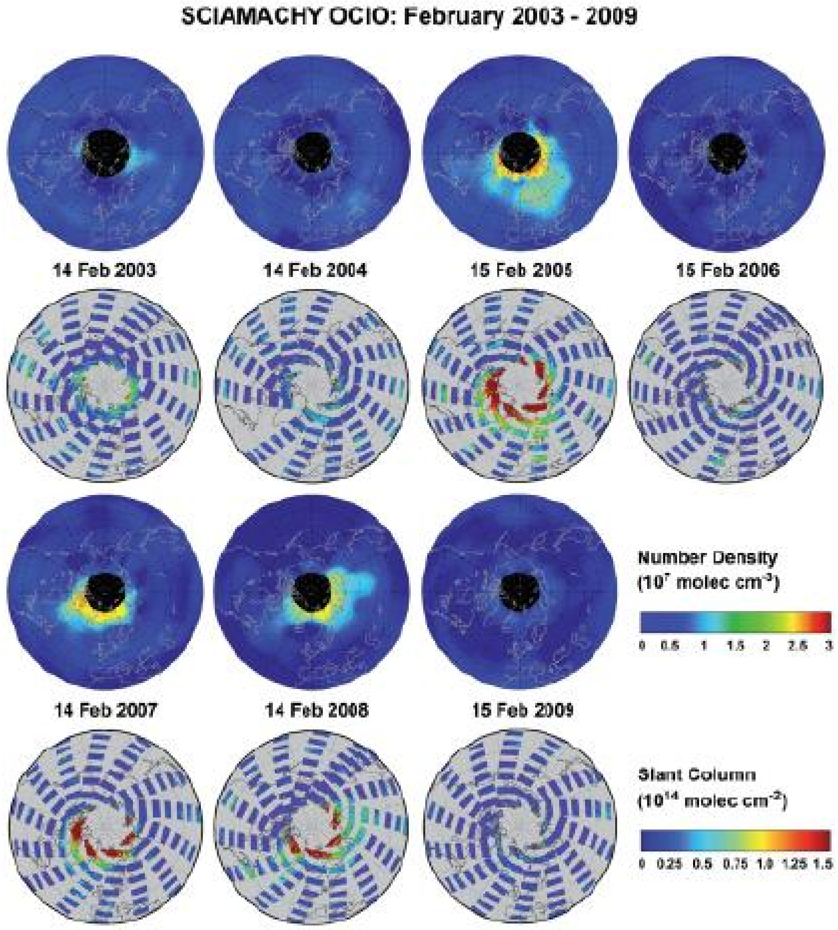

OClO number density at 19 km altitude above the northern hemisphere derived from SCIAMACHY limb observations (rows 1 and 3), and the corresponding total OClO slant column derived from nadir views (rows 2 and 4) for mid of February in the Arctic winters 2002/03 to 2008/09. (Graphics: S. Kühl; MPI for Chemistry, Mainz)

These findings are in good agreement with observations of the main active ozone depleting chlorine species ClO, the determining meteorological parameters, results from atmospheric chemistry models, and the related chemical ozone loss (compare Figs. in the section on ozone). The strong inter-annual variability in the degree of chlorine activation reveals that despite the decrease of the stratospheric inorganic chlorine loading, large enhancements of OClO are still observed in the Arctic stratosphere during cold winters. Therefore, monitoring of stratospheric chlorine activation and detailed investigation of the relation to meteorological parameters is necessary to broaden the understanding of the related processes.

Bromine Oxide – BrO

Bromine compounds play an important role in the catalytic destruction of stratospheric ozone. Despite their importance, however, there are only few measurements of bromine compounds in the stratosphere. For the first time, SCIAMACHY provided global observations of stratospheric BrO profiles down to the lower stratosphere (*Rozanov et al. 2005, Sioris et al. 2006, Kühl et al. 2008*). The long-term changes of BrO as observed from SCIAMACHY agree well with ground-based observations at mid-latitudes (*Hendrick et al. 2009*). The seasonal cycle, including the activation during winter and long-term changes, are consistently seen by both instruments. When comparing zonal mean BrO at selected stratospheric altitudes obtained from limb observations and from model simulations, an additional source of stratospheric bromine from very short-lived substances (VSLS) is required (fig. 3-19) to explain the difference. This component amounts to about 3 to 6 parts per trillion by volume (pptv), or about 20% (*WMO 2007, Sinnhuber et al. 2005*). In an opposite analysis approach, Theys et al. (2009) used the SCIAMACHY limb stratospheric BrO observations to demonstrate the validity of a new stratospheric BrO profile climatology.

fig. 3-19

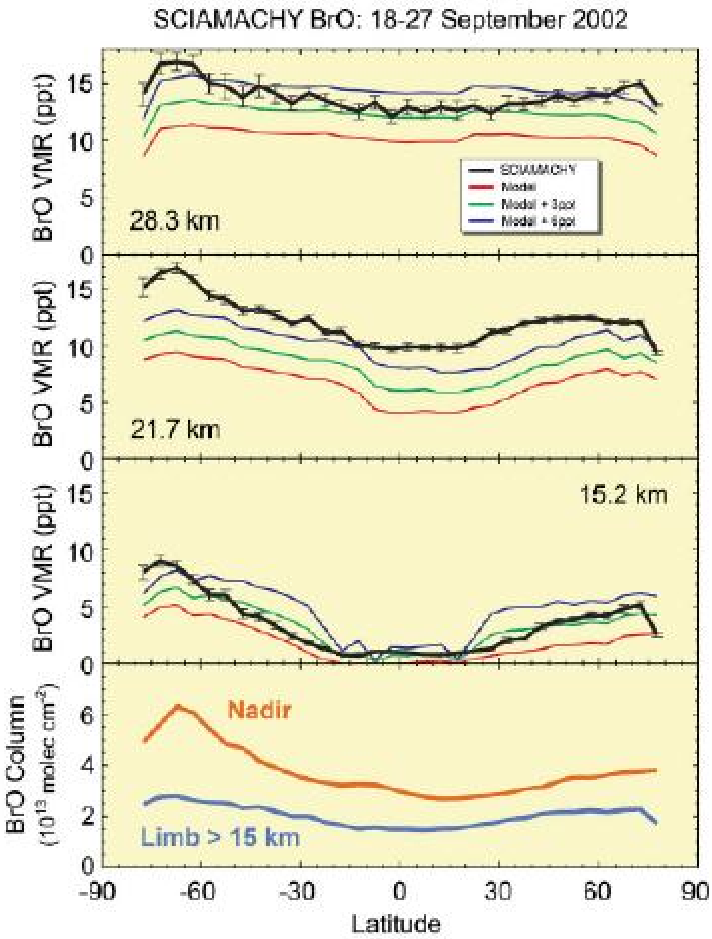

Zonal mean BrO at selected altitudes obtained from SCIAMACHY limb observations and from model calculations. Additional bromine of 0, 3, and 6 pptv, respectively, has been added to the model calculations to account for the contribution from very short-lived substances (VSLS). (Graphics: adapted from WMO 2007 - based on Sinnhuber et al. 2005)

Polar Stratospheric Clouds – PSC

Polar Stratospheric Clouds play a key role in the chemical processes which lead to severe ozone depletion in the polar stratosphere. These clouds are necessary for transferring inactive chlorine compound reservoirs such as HCl and ClONO2 to active Cl that participates in different catalytic O3 destruction cycles. PSC form at altitudes of about 15-25 km and exist as different types. Type Ia consists of crystalline NAT (nitric acid tri-hydrate) particles, the liquid type Ib PSC consist of ternary solutions of nitric acid, sulphuric acid and water. Type II PSCs are made of water ice. A common feature of all types is that they only form at very low temperatures of less than about -78°C (195 K). PSC scatter solar radiation and thus affect the measured limb radiance spectra. Since PSC are rather Mie-scatterers than Rayleigh-scatterers in the UV-SWIR spectral range, the spectral dependence – although highly variable – of their scattering cross section differs from the l-4 spectral dependence of the molecular Rayleigh scatterering. This spectral difference can be exploited in a colour-index approach to detect PSC (*von Savigny et al. 2005b*).

Fig. 3-20 shows the occurrence rate of PSC in the southern hemisphere for September in the years 2002 to 2008. With the exception of 2002, the PSC occurrence rate at high southern latitudes is typically quite large. It is obvious that PSC are not symmetrically distributed around the South Pole, but the distribution is characterised by a wave-1 structure with a maximum in the South Atlantic sector and a minimum in the Australian sector. The low PSC occurrence rates in September 2002 are due to the anomalous mid-winter major stratospheric warming after 22 September, which caused PSC to disappear. In most cases there is a good correspondence between the detected PSC and their formation threshold of -78° C.

fig. 3-20

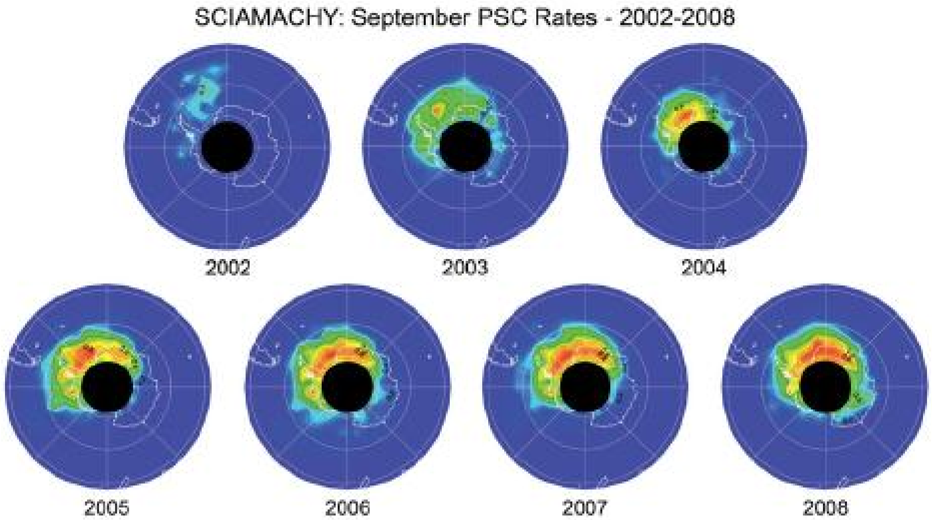

Maps of PSC occurrence rates for September of the years 2002-2008. Contours levels correspond to 0.2, 0.4, 0.6, and 0.8. Red areas indicate occurrence rates exceeding 0.8. (Graphics: C. von Savigny, IUP-IFE, University of Bremen)

3.4 The Upper Atmosphere and Solar Activity

The upper atmosphere, i.e. the mesosphere and lower part of the thermosphere (MLT region), is still a relatively poorly explored region. The MLT region forms a transition between interplanetary space and the terrestrial atmosphere, both influenced by extraterrestrial impacts – e.g. solar radiation, solar wind, meteors or cosmic dust – as well as by impacts from the lower atmosphere. Thus, there are indications that effects of global climate change in the upper atmosphere can be detected rather early. Solar-terrestrial interactions can be studied, and at the same time, the impact of anthropogenic emissions on our atmosphere at remote altitudes can be investigated.

Noctilucent Clouds – NLC

Noctilucent Clouds, also referred to as *Polar Mesospheric Clouds*, are a high latitude summertime mesospheric phenomenon, even observable from ground. They occur at altitudes of about 83-85 km near the polar summer mesopause and consist of H_2O ice particles with radii ranging from a few nm up to about 80-100 nm. NLC received a significant amount of scientific interest in recent years, since they may be early indicators of global change. This is because they react very sensitively to small changes in ambient conditions, particularly to changes in temperature and H_2O abundance. The scattering properties of the NLC particles allow mapping of these high altitude clouds. Since they scatter solar radiation efficiently, they affect the measured limb radiance profiles significantly, especially in the northern hemisphere where scattering angles at polar latitudes are particularly small for SCIAMACHY limb observations.

SCIAMACHY observations of NLC have contributed in different ways to the current research on the polar summer mesopause. The main focus of these investigations was to improve the scientific understanding of the natural variability in NLC in order to better understand the role of NLC as indicators of global change. The natural variability is partially driven by the solar input and by dynamical processes such as planetary waves.
SCIAMACHY NLC observations were used to observe a depletion of NLC for the first time during a solar proton event (SPE, *von Savigny et al. 2007a*). Associated with such an event in January 2005, highly energetic solar protons precipitated into the Earth's polar cap areas. The January 2005 SPE is included in the period covered by fig. 3-21.

fig. 3-21

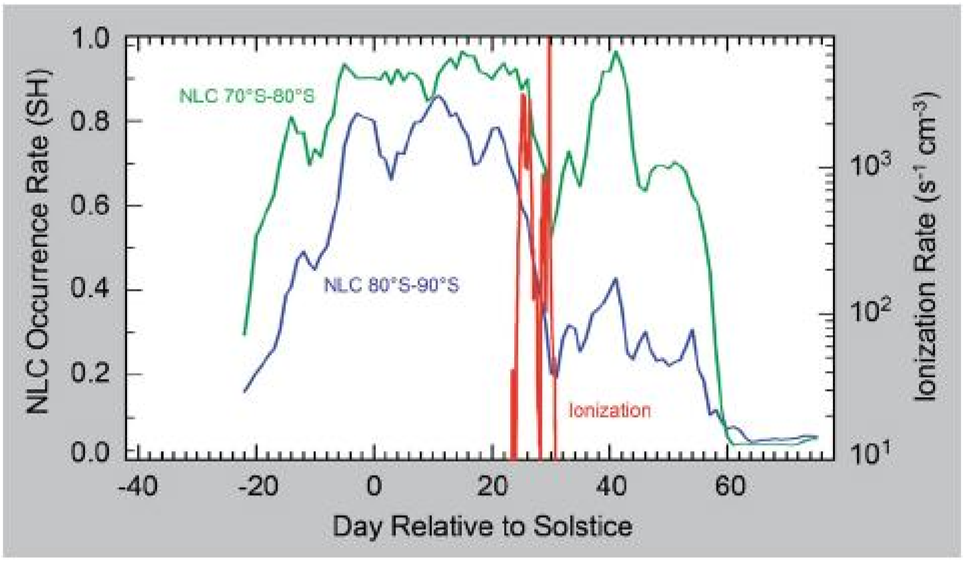

Smoothed zonally averaged NLC occurrence rates in the southern hemisphere NLC season 2004/2005 (left abscissa) and ionisation rates at 82 km (right abscissa). At the time of the solar proton event, the ionisation rate increases and causes a drop in the NLC rate. (Graphics: C. von Savigny, IUP-IFE, University of Bremen)

This graph shows SCIAMACHY NLC occurrence rates at different latitudes in the southern hemisphere during the 2004/2005 NLC season, together with the ionisation caused by the precipitating solar protons. At the time of the SPE, the NLC occurrence rate in both southern latitude bands decreased rapidly. A mechanism for SPE-induced NLC depletion is proposed by Becker and von Savigny (*2010*) using model simulations with a General Circulation Model (GCM). It suggests that a polar mesopause warming is caused by the SPE-driven catalytic ozone loss in the middle mesosphere, followed by different stages of dynamic processes, and finally leading to a reduced upwelling above the pole, i.e. reduced adiabatic cooling. The January 2005 event is not the only event where NLC depletion has been detected. Rahpoe et al. (*2010*) demonstrated that a depletion of NLC also occurred during some of the other strong SPE in the last three decades.

Solar proton events are rather intermittent and irregular events mainly occurring during solar maximum. They are not the only cause for NLC variability linked to solar impacts seen in SCIAMACHY observations. A 27-day solar cycle signature in NLC was identified for the first by Robert et al. (*2010*). Maxima in solar activity associated with the 27-day solar cycle – quantified for example using the MgII index described below (*Skupin et al. 2004*) – coincide with minima in the NLC occurrence frequency. Using MLS (Microwave Limb Sounder) observations of middle atmospheric temperatures, a 27-day solar cycle signature in the polar mesopause temperature was identified as the immediate cause of the apparent 27-day signature in NLC.

Another important driver for variability in NLC are planetary wave signatures. The most important of these signatures are the quasi-2-day-wave and the quasi-5-day-wave. Both of them are caused by instabilities of the summer mesosphere jet and occur intermittently during the NLC seasons in both hemispheres. SCIAMACHY NLC observations, again in combination with MLS temperature observations, showed for the first time, that the quasi 5-day-wave signatures in NLC are caused by similar wave signatures in mesopause temperatures (*von Savigny et al. 2007b*).

Apart from the detection and mapping of NLC, SCIAMACHY observations also permit the estimation of the NLC particle size. For wavelengths below about 310 nm, the multiple scattering and surface reflection components to the limb signal are negligible. In single scattering approximation, the spectral exponent of the NLC scattering spectrum can be related to the NLC particle size assuming for example Mie theory and the refractive index of H2O ice (*von Savigny et al. 2004a*). NLC particle sizes of 40-50 nm were determined from a distance of about 3300 km. The SCIAMACHY NLC size dataset currently presents the most comprehensive satellite dataset of NLC particle sizes. The derived particle sizes are in good agreement with independent observations (*von Savigny and Burrows 2007, von Savigny et al. 2009*).

Mesospheric Ozone and the October/November 2003 Solar Storm

Highly energetic protons ejected from the Sun during phases of high coronal activity, such as solar flares or solar coronal mass ejections, reach the Earth with the solar wind, ionise the atmosphere and lead to the formation of HOx and NOx in the mesosphere and upper stratosphere. Both families participate in catalytic O3 destruction cycles, with HOx being more efficient above about 50 km and NOx below about 50 km. Consequently, enhanced O3 destruction is expected after strong solar proton events.

Mesopause Temperatures

A good opportunity to study the impact of solar activity on mesospheric ozone fields was a period in October/November 2003 – also known as the 'Halloween Storm' – when the Sun exhibited extremely large coronal SPE. Fig. 3-22 presents an analysis of the impact of the solar proton event at the end of October 2003 on the upper atmospheric O3 (*Rohen et al. 2005*). A strong ozone depletion of more than 50% even deep in the stratosphere is observed at high geomagnetic latitudes in the northern hemisphere, whereas the observed ozone depletion in the more sunlit southern hemisphere is much weaker. SCIAMACHY measurements of the O3 loss due to SPE agree well with model simulations, indicating that the main processes leading to the O3 loss are fairly well understood. (fig. 3-22)

fig. 3-22

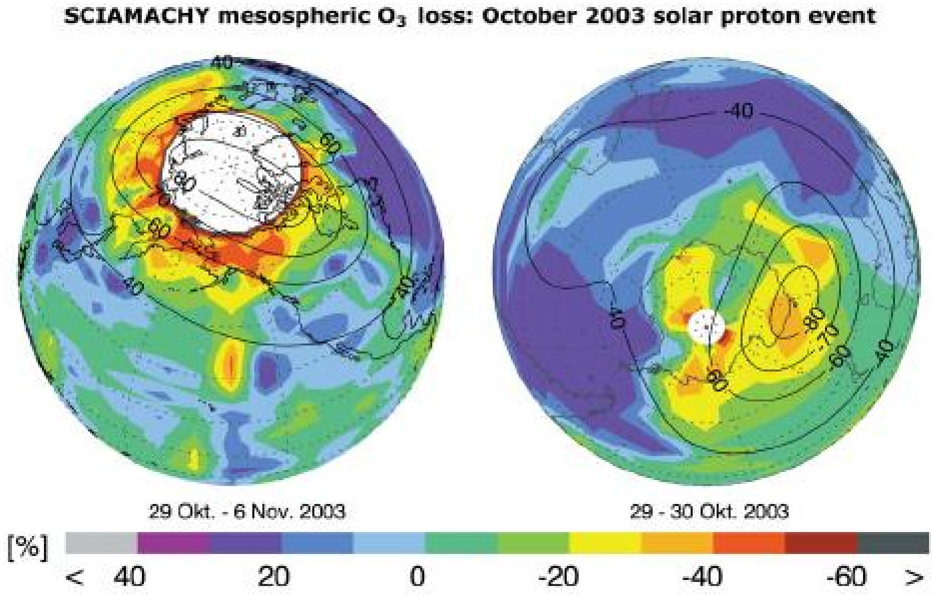

Measured change of ozone concentration at 49 km altitude due to the strong solar proton events end of October 2003 in the northern and southern hemisphere relative to the reference period of 20-24 October 2003. White areas depict regions with no observations. The black solid lines are the Earth's magnetic latitudes at 60 km altitude for 2003. (Graphics: Rohen et al. 2005)

Mesopause Temperatures

A number of atomic and molecular emission signals from the mesosphere and lower thermosphere (MLT) can be detected throughout the SCIAMACHY spectral range, e.g. neutral and ionised magnesium (Mg) lines as well as NO gamma bands in the UV, OH Meinel band emissions in the SWIR, several transitions from excited-state O2 or sodium lines and atomic oxygen in the VIS range. These emission signals can be used to characterise the distribution of the atoms, ions and molecules in the upper atmosphere.

SCIAMACHY measurements of molecular emissions in the upper atmosphere provided for the first time the retrieval of OH* rotational temperatures at the mesopause from satellite measurements during night. OH* is vibrationally excited at the mesopause through the reaction of H and O3. This produces an OH* emission layer centred at about 87 km with a width of 8-10 km. Several of the OH* Meinel emission bands are observable in the SCIAMACHY spectral range, e.g. the OH* (3-1) band at around 1500 nm. This emission band is used for the retrieval of OH* rotational temperatures because it is one of the most intense emission bands. From the relative intensity of two or more rotational lines, the effective temperature of the emitting layer can be retrieved from SCIAMACHY data. For several decades, this method has been applied to retrieve mesopause OH* rotational temperatures from ground measurements (e.g. *Bittner et al. 2002*). Therefore, coincident ground-based OH* rotational temperature measurements over Germany in Wuppertal and Hohenpeissenberg, as well as over Hawaii, had originally been used to validate the novel SCIAMACHY space-based approach (*von Savigny et al. 2004b*). A comparison of both methods yielded very good agreement. Fig. 3-23 shows the monthly averaged mesopause temperatures retrieved from SCIAMACHY OH* (3-1) emission measurements for January, April, July and October 2009 as an example. As the observations used for the retrievals are made on the Earth's nightside, the OH rotational temperatures are only available at higher latitudes during wintertime. (fig. 3-23)

fig. 3-23

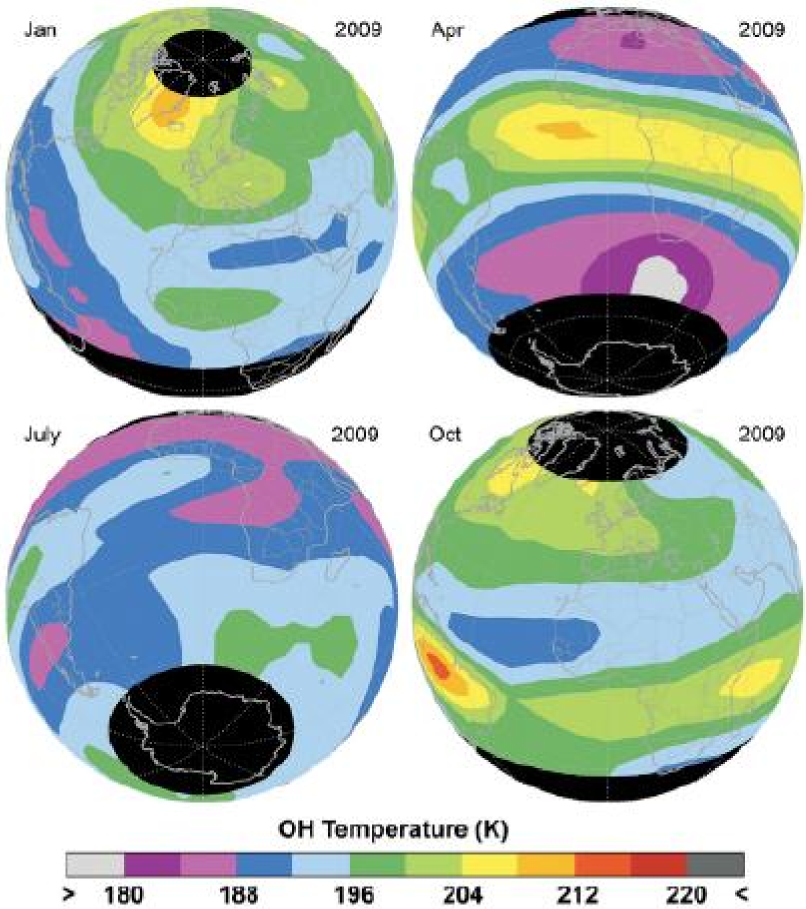

Monthly averaged SCIAMACHY retrievals of OH rotational temperatures at about 87 km for January, April, July and October 2009. (Graphics: K.-U. Eichmann, IUP-IFE, University of Bremen)

Retrieval of OH* rotational temperatures is not the only scientific application of SCIAMACHY's OH Meinel-band emission observations. The data can also be used to study atmospheric wave signatures (*Ern et al. 2009*) or to determine chemical heating rates associated with the exothermic chemical reaction H + O3 ® OH* + O2, which forms the vibrationally excited OH molecules as mentioned above (*Kaufmann et al. 2007*).

Observing the Active Sun - The Mg II Index

SCIAMACHY's scientific objective to explore atmospheric trace constituents is achieved by analysing solar radiation, both in terms of scattered and reflected sunlight, and also by direct viewing for calibration purposes. Due to its high sensitivity and spectral stability, SCIAMACHY is also feasible for retrieving information about those aspects of solar activity which manifests themselves in the emitted radiation. Therefore, solar observations are analysed on a regular time grid offering the possibility to monitor solar variations and their impact on the atmosphere. The solar activity shows some well-known periodic variations such as the 27-day cycle caused by solar rotation. Another is the 11-year solar cycle, coupled with the 22-year magnetic cycle which correlates with changes in sunspots and Fraunhofer lines. During phases of high solar activity, an increase in the number of sunspots in the photosphere and large chromospheric plage areas are observed. The plage areas are hotter than the surrounding areas and cause the enhancement of the emission core within the absorption features of many solar Fraunhofer lines. Thus, solar proxy indicators can be given by the core-to-wing ratio of selected Fraunhofer lines. The Mg II index is defined as the core-to-wing ratio of the Mg II Fraunhofer line centered at 279.9 nm. It can be used as a proxy for spectral variations in the solar extreme UV (EUV, *Viereck et al. 2001*) and correlates with atmospheric ozone variations and other relevant atmospheric quantities.

For the understanding of the solar-terrestrial climate interaction, the establishment of long time series covering several solar cycles is important. Due to the limited lifetime of spaceborne missions, this has to be constructed from different satellite experiments. Figure 3-26 combines the Mg-II indices for the solar cycles 21 to 23, using data from NOAA missions (*Viereck et al. 2004*), GOME (*Weber 1999*) and SCIAMACHY (*Skupin et al. 2004*). Both the 27-day periodicity and the declining phase of solar cycle 23 are clearly visible. Differences between SCIAMACHY and GOME are mostly below ±0.5%, between SCIAMACHY and NOAA below ±0.25 %. The derived MgII index was used to identify a correlation of stratospheric ozone with the 27-day solar cycle (*Dikty et al. 2010*). SCIAMACHY is the first spaceborne instrument that observes daily solar spectral irradiance (SSI) continuously between 230 nm and 1750 nm. In order to address how much the irradiance changes in the UV-VIS-NIR and SWIR range on 27-day and 11-year timescales, short-term SSI variations were parameterised in terms of the proxies faculae brightening, i.e. MgII index, and sunspot darkening, i.e. photometric sunspot index (*Pagaran et al. 2009*). (fig. 3-26)

fig. 3-26

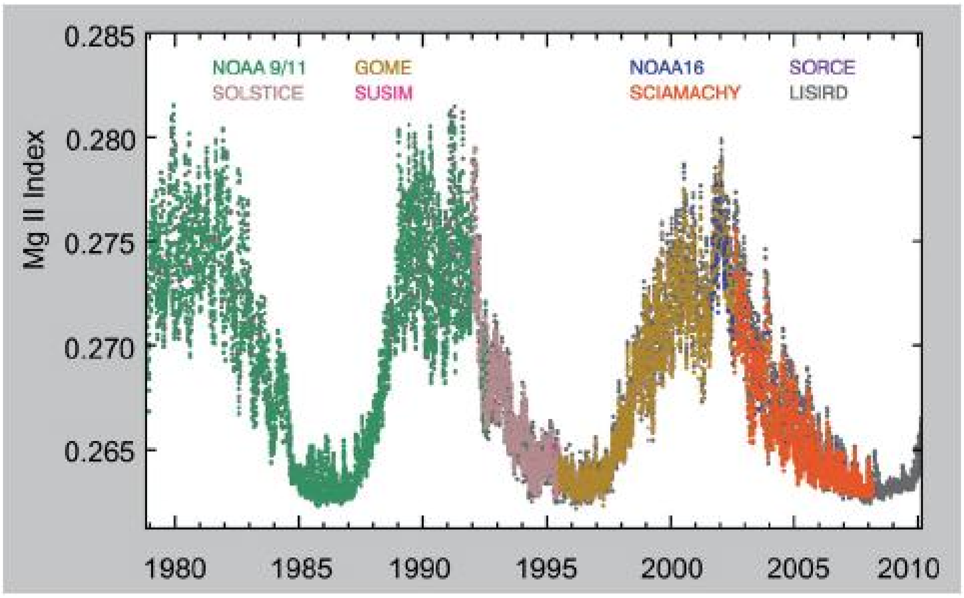

Solar activity measured via the Mg II index by several satellite instruments, including GOME and SCIAMACHY. By combining various satellite instruments, the composite Mg II index covers more than three complete 11-year solar cycles. (Graphics: M. Weber, IUP-IFE, University of Bremen)

3.5 The Earth Surface and Beneath

SCIAMACHY's realm is the Earth's atmosphere. However, the measured earthshine spectra are also affected by surface reflection and absorption, i.e. by the broadband ground albedo, and by narrowband spectral structures of different origins. These features went unnoticed in trace gas retrieval algorithms for a long time. The initial approach is certainly to take them into account for improving the tropospheric trace gas information. However, these features can also be used to derive various surface parameters over land or even phytoplankton properties of the oceans.

Land Vegetation Characteristics

Vegetation is a unique property of the Earth. Understanding how it changes contributes to many applications, ranging from global climate change to predicting crop yield. Usually, vegetation indices exploit spectrally broadband differences in reflectivity between the red and NIR wavelength range. Atmospheric sensors like SCIAMACHY provide a higher spectral resolution, i.e. such differences can be analysed on a much finer spectral scale. While optimising DOAS trace gas retrievals, Wagner et al. (*2007*) noticed that the resulting residuals displayed distinct structures, particularly over vegetated land. These structures could be reduced in amplitude when vegetation data such as spectral reflectances of conifers, deciduous trees or grass were included in the spectral fitting. Fig. 3-27 shows the fit results for deciduous vegetation for summer 2003-2004. A correspondence to deciduous vegetation is obvious, but interference with other vegetation types and coastal waters is still present. Since retrieving vegetation information from remotely sensed atmospheric data is a rather novel approach, current results are still preliminary and require further investigations. There is a clear need to collect more spectral reference data at spectral resolutions similar to SCIAMACHY.

fig. 3-27

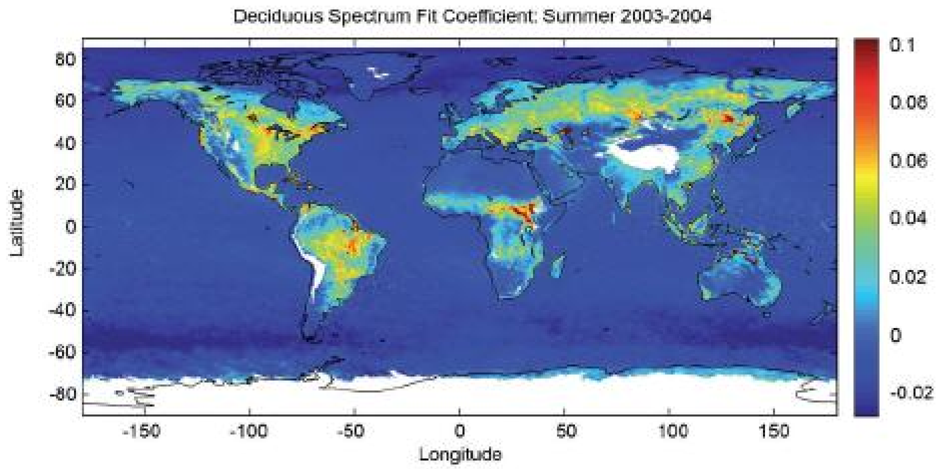

Global mean deciduous vegetation signature - DOAS fitting coefficient of the logarithm of the deciduous vegetation spectrum- for summer 2003-2004 for cloud-free scenes. (Graphics: T. Wagner, MPI for Chemistry, Mainz)

Oligotrophic Oceanic Regions

Oligotrophic Oceanic Regions

Certain regions of the world’s oceans are oligotrophic, i.e. they contain very low levels of nutrients and are thus almost free of biogenic activity. As a consequence, solar irradiation partly penetrates into the uppermost water layers. This has two effects on the spectra of the backscattered light: first, the ocean water causes rather broadband absorptions according to its cross section. In addition, vibrational Raman scattering occurs causing high-frequent spectral structures (*Vasilkov et al. 2002; Vountas et al. 2003*) similar to the atmospheric *Ring* effect. Global maps of fit results for vibrational Raman scattering show consistent global patterns with high values for the oligotrophic oceanic regions and have been obtained from SCIAMACHY data by applying differential optical absorption spectroscopy in the UV-A region (*Vountas et al. 2007*).

Oceanic Phytoplankton Characteristics

In open water, marine phytoplankton is the basis of the marine food web. They contribute 50% to the global primary production via photosynthesis. Microscopic algae also play an important role in the global carbon cycle. For photosynthesis, sunlight is absorbed by certain pigments, such as chlorophyll. The absorption spectrum is typical for particular groups of algae due to their characteristic pigment composition. The absorption signatures can be identified in SCIAMACHY data, allowing the quantitative evaluation of the global distribution of phytoplankton. By including a phytoplankton absorption spectrum in the DOAS retrieval, Vountas et al. (*2007*) was able to retrieve global maps of marine chlorophyll concentrations from SCIAMACHY data successfully. Furthermore, Bracher et al. (*2009*) could even distinguish different types of phytoplankton, namely diatoms from cyanobacteria (fig. 3-28). The resulting global maps are in good agreement with biochemical models and with independent *in situ* measurements obtained during cruises with the German research vessels *Polarstern*, *Maria S. Merian* and *Sonne* in the Atlantic and Pacific Oceans. These comparisons again proved the validity of the phytoplankton concentrations retrieved from SCIAMACHY measurements.

fig. 3-28

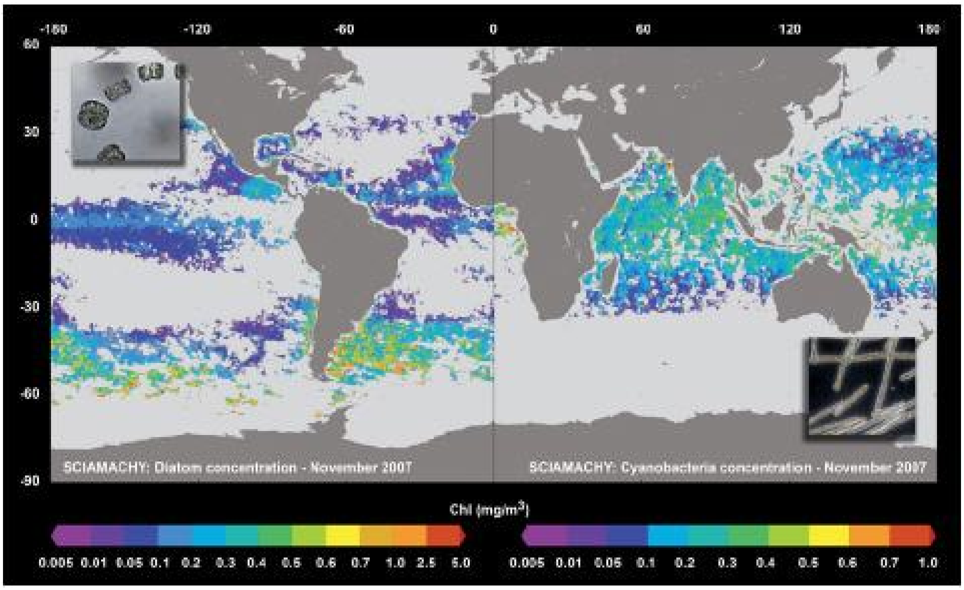

Global biomass distributions of diatoms (left hemisphere) and cyanobacteria (right hemisphere) in November 2007 as derived from SCIAMACHY data using the PhytoDOAS method. The insets show members of the two algae groups. (Graphics: A. Bracher IUP-IFE, University of Bremen and Alfred Wegener Institutefor Polar and Marine Research, adapted from Bracher et al. 2009; photo diatoms: E. Allhusen, cyanobacteria: S. Kranz; both Alfred Wegener Institutefor Polar and Marine Research)

CHAPTER 4

4. Calibration & Monitoring

Spaceborne spectral measurements over long time periods require to translate the measured signals into physical quantities and to maintain this process with high precision. Therefore calibration and monitoring of the instrument is a crucial prerequisite for any successful retrieval of atmospheric geophysical parameters. Calibration of the instrument should be valid during any point in the mission. For calibration measurements which can not be performed in flight it is necessary to perform these before launch. Once in orbit the instrument can be expected to change, and needs to be calibrated in flight where possible, and monitored where in-flight calibration is not feasible.

4.1 Calibration

4.1.1 The General Calibration Equation

The goal of the calibration is to convert electronic signals of detectors (Binary Units – BU) into physical units (e.g. W/m2/nm). This is achieved by applying a complex sequence of individual calibration steps to measurement data. For a detailed description of each step see *Slijkhuis (2000a)* and *Lichtenberg et al (2005*). Following the light from the earth through the telescope, slit, spectrometer, detector, and on-board processing we arrive at the following equations for a scanning instrument which measures only the spatially integrated light of one ground pixel at a time:

$$\vec{I}(\lambda,\alpha,\beta)=\vec{\vec{P}}_t * \vec{I}(\lambda,lat,lon)$$

where *I* is the polarised intensity at wavelength *λ* and geographic position *lat* and *lon*, polarisation is represented in Stokes notation with a vector, and *Pt* is the point spread function of the telescope which may affect the polarisation state of the light and is represented here as a matrix. Optical distortion due to the telescope is implicitly included in *Pt* which thus may depend on *α* and *β*. The coordinates *α* and *β* are defined in the focal plane of the telescope at the entrance slit to the spectrometer part of the instrument. Convolution is denoted with *.
After having passed through the telescope with optical properties represented by the point spread function with possible polarisation sensitivity, the light passes through the entrance slit where the intensity masked out by the slit is removed:

$$\vec{I}_{slit}(\lambda,\alpha,\beta)=\vec{I}(\lambda,\alpha,\beta)\cdot F(\alpha,\beta)$$

where *F* is a function of the focal plane coordinates *α* and *β* and is zero where the light is blocked and unity where the light passes unhindered through the slit.
The optics after the slit project the image of the slit on the detector and add wavelength dispersion in order to obtain a spectrum. For instruments with an integrated instantaneous field of view, like SCIAMACHY, the detector can be 1-dimensional. For instruments with a spatially resolved slit, the detector must be 2-dimensional. We consider only the 1-dimensional case here:

$$I(x)=\iint_{detector}\vec{\vec{P}}_0 * \vec{I}_{slit}(\lambda,\alpha,\beta)+B$$

where *Po* is the wavelength and polarisation dependent point spread function of the optics, including the dispersion introduced by the spectrometer. The coordinate *x* is the index for the detector pixels, and integration is performed over each pixel individually. Possible self-emission of the instrument (thermal background radiation) is covered by *B* which may be position dependent. Note that polarisation information is lost once the signal has been projected on the detector.
Once integrated over the detector pixels, the signal can be treated electronically. Up to this point the signal has been considered purely linear in *I*, but the detector material and electronics may introduce non-linearity and hysteresis:

$$S_{det} = E\left(I, t_{exp}, I(t)\right)$$

where *E* is the function describing the transfer of *I* into the digitally sampled detector signal *Sdet*, taking into account the exposure time *texp*. The function *E* may depend on the history of *I*, represented here as *I(t)*.
On-board processing may modify the digitally sampled signal *Sdet*, in the case of SCIAMACHY only in the form of co-adding multiple read-outs of the detector. The electronic sampling function *E* can be simplified into a linear term in *I*, a constant offset in *I*, a constant offset in *Sdet*, and additive terms describing remaining effects.
Combining all of the equations above, considering a dedicated correction for polarisation sensitivity (see below), describing the effects of the point spread function of the optics *Po* on the recorded spectrum as an additive component, and introducing explicit temperature dependence of the detector quantum efficiency, the equations can be simplified to (equ. 4-1b):

$$S_{\mathrm{det}} = I\ (\lambda) \cdot \Gamma_{inst}\ (\lambda) \cdot QE\ (T_{\mathrm{det}}, \lambda) + S_{stray} + DC + S_{elec}$$

where *Γinst* is the total transmission of the instrument, *QE* the detector temperature dependent quantum efficiency, *Sstray* the stray light, *DC* the total dark signal and *Selec* electronic effects such as non-linearity. This equation must be solved for every detector pixel. In order to obtain the spectrum as a function of wavelength *λ* for each pixel, the wavelength has to be determined and the equation has to be inverted to calculate the intensity *I*. Generally, the transmission of the instrument is dependent on the polarisation of the incoming light.

The experience gained from GOME flying on-board the ERS-2 satellite, where various air-vacuum effects led to calibration problems, showed that spectrometers should ideally be calibrated under thermal vacuum conditions. In the case of SCIAMACHY a range of incidence angles on the mirror(s) and mirror-diffuser combinations had to be covered in the calibration, requiring a rotation of the instrument. The available vacuum chamber hardware did not allow rotation of the instrument itself, and only provided views in a limited angular range centred on nadir and limb in the flight direction. Therefore, a combination of thermal vacuum (TV) and ambient measurements was used.

The radiometric sensitivity and the polarisation sensitivity of the instrument were measured under TV conditions for *one* reference angle α0 and all necessary instrument modes (limb, nadir and irradiance). In order to be able to calibrate all incidence angles on the mirrors (or diffusers), component level measurements of all possible mirror combinations and the mirror/ESM diffuser combination were made under ambient conditions. The detectors used in the ambient calibration were different from the detectors used on-board SCIAMACHY. These ambient measurements occurred for a set of angles – including the reference angle measured under TV conditions – and a set of selected wavelengths. From such ambient measurements the so-called *scan-angle correction* is calculated.

The reference angle measurement is used to transfer the results from the ambient measurement to the TV conditions. Measurements included both unpolarised and linearly polarised light. Combining TV measurements with the ambient measurements gives ideally the correct instrument response for all incidence angles at Begin-of-Life (BOL) of the instrument. The implicit assumptions for the combination of the TV and ambient measurements are that the polarisation dependence of the mirrors and diffusers are the same in air and in vacuum and that there is no temperature dependence. Both assumptions are reasonable for SCIAMACHY, since uncoated mirrors are used.

Critical points in the transfer of ambient and TV measurements are the geometry (incidence angles on the mirrors or diffusers), the illumination conditions and the detector used for the component measurements. Obviously, errors in the geometry lead to an incorrect angle dependence for the calibration quantity to be measured. Light levels during instrument measurements and during component measurements will always be different. While the footprint of the light source on the component can be matched to the footprint during the instrument measurements, it is impossible to recreate the exact illumination conditions. This may introduce systematic errors into the calibration. Finally, care has to be taken that the detector from the measurements under ambient conditions does not introduce artefacts.

In order to minimise potential errors from the measurements performed under ambient conditions, only ratios of measurements were used for the calibration where possible. The individual calibration parameters derived from the on-ground measurements are combined into a set of data files, the so-called *Key Data* files. These Key Data are applied by the data processor to derive calibrated spectra. (fig. 4-1)

fig. 4-1:

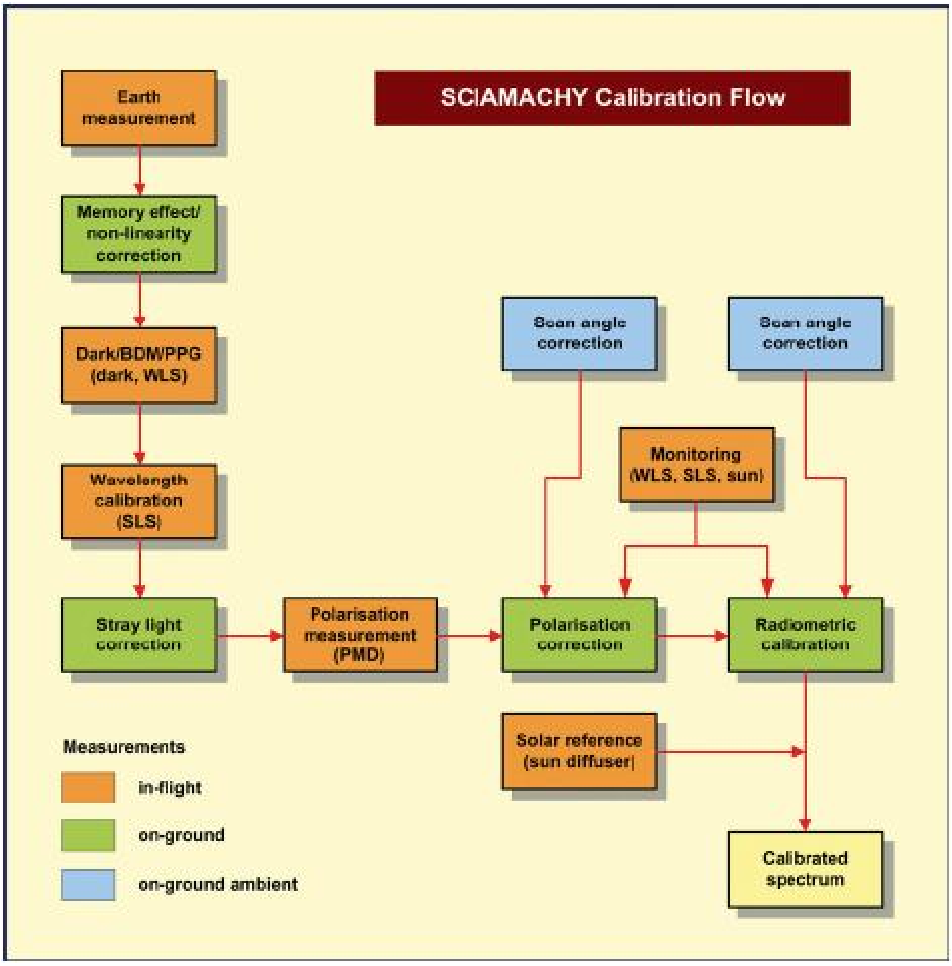

Calibration concept for SCIAMACHY. The final calibrated Earth radiance spectra are obtained by applying several calibration steps to the measured Earthshine signals. They include in-flight calibration measurements (red), on-ground measurements performed under thermal vacuum conditions (green) and component measurements from on-ground ambient tests (blue). The optical performance monitoring (red) provides additional corrections. (Graphics: SRON)

The TV on-ground calibration was performed during several campaigns using the OPTEC facility. SCIAMACHY had been placed inside the vacuum chamber with the thermal hardware being replaced by a system based on liquid nitrogen and heaters to reach and maintain the correct temperature. Optical windows in the tank allowed the light from external optical stimuli to enter. In the Key Data the effect of the optical window has been compensated for. The OPTEC facility was first used for requirement verification tests, i.e. a check to see if the instrument met its requirements. Later, calibration measurements were performed in OPTEC. Mainly due to major hardware changes in the instrument, several OPTEC campaigns had to be scheduled and executed.

After the OPTEC-1 campaign it was discovered that the mounting of the optics was unreliable at low temperatures. The refurbishment implied a re-testing, and thus an OPTEC-2 campaign. Here it was found that the SWIR channels 7 & 8 were out of focus so that the OPTEC-3 campaign, executed after repositioning of channels 7 & 8, verified the required performance. In the OPTEC-4 campaign the instrument was relocated inside the facility to get representative illumination for the on-board diffuser. This configuration yielded improved measurements quantifying the instrument's radiometric properties. Finally, the stray light in the UV channels was reduced by some hardware changes which required the OPTEC-5 campaign. In all, the various OPTEC campaigns ran from summer 1997 till spring 2000.
The ambient calibration was executed between December 1997 and April 1998 in a dedicated set-up, the so-called ARCF (Absolute Radiometric Calibration Facility). In order to allow a rotation of the mirror(s) or the mirror/diffuser combination to any required position, they were placed on a special optical bench. Having two mirrors or a mirror plus a diffuser on the optical bench permitted direct measurement of the combined response of both optical elements and calibration of all SCIAMACHY instrument modes at the appropriate angles. A monochromator and polarisers were used to obtain the response for different wavelengths and polarisations. All measurements took place in a class 100 cleanroom with a controlled temperature of 20° C and 50% air humidity.

4.2 Detector Corrections

Several corrections related to the electronics of the detectors and the detectors themselves, i.e. the terms *Selec* and *DC* in equ. 4-1 have to be applied (see fig. 4-1). The UV-VIS-NIR channels 1-5 and the SWIR channels 6-8 must be treated separately during the calibration due to their different detector material and readout electronics. Signals are described in terms of Binary Units. The Analogue-to-Digital Converter (ADC) of SCIAMACHY digitises the signal of the detector with 16 bit resolution, meaning that detector signals (also referred to as 'fillings') range from 0 BU to 65535 BU.

Channels 1-5 (UV-VIS-NIR)

The first correction to the data is the so-called *Memory* effect. The Memory effect was discovered in 1996 during an investigation of the linearity of channels 1-5. In a number of measurements covering the range from low detector fillings to saturation it was found that the signal deviated from a linear response which is defined by a linear fit for all points of up to 90% of the maximum detector fillings (see fig. 5-2). The deviation was independent of the actual signal level, but dependent on the signal level of the *previous* readout (hence the name *Memory* effect). Note that the effect depends on the signal level *including* the analogue offset (see below) and dark current. Thus it has to be applied before any other correction. In order to characterise the Memory effect, WLS measurements followed by several dark measurements were performed on-ground and in-flight. The difference between the first dark measurement after the WLS measurement and subsequent dark measurements gives a correction value as a function of detector filling. This value needs to be subtracted from the data to correct for the Memory effect which is the same for all pixels. The total correction for a single readout amounts from -0.61% to 0.21% of the detector filling of the previous readout with a maximum effect at fillings around 19000-21000 BU, depending on the channel. More information can be found in *Lichtenberg (2003).* (fig. 4-2)

fig. 4-2:

Memory effect for channel 3. Yellow crosses mark the in-flight measurement of the Mem-ory effect. The blue solid line is a spline fit through the measurements that is used for the correction. (Graphics: SRON)

The second detector correction to be applied is the dark signal correction. The dark signal is measured in every orbit during eclipse using 5 different states. In channels 1-5 the dark signal consists of two components: the analogue offset (AO) and the leakage current (LC). The analogue offset is independent of time, it is just a fixed signal added to the measured signal to avoid negative signals. The leakage current is caused by thermally created electron-hole pairs. The total dark signal for channels 1-5 is (equ. 4-2)

$$DC_{ch15} = f_{coadd} \cdot AO + f_{coadd} \cdot t_{PET} \cdot LC$$

where *fcoadd* and *tPET* are the co-adding factor of the cluster and the pixel exposure time, respectively. Note that the analogue offset is only multiplied with the co-adding factor since it is not dependent on the integration time and is added to the signal for every detector readout. Linear fitting to dark measurements with different integration times yields the in-flight dark signal correction. The dark signal in the UV-VIS-NIR channels is dominated by the analogue offset while the leakage current amounts to only 0.04-0.5 BU/sec and has roughly doubled since launch.

Channels 6-8 (SWIR)

The SWIR channels do not suffer from the Memory effect. However, these channels display a significant non-linearity, i.e. a deviation in the detector response from a (chosen) linear curve. The non-linearity has been measured during the on-ground calibration campaign and a correction algorithm was defined. The maximum value of the non-linearity is around 250 BU which can be significant for weak absorbers such as CO. A separate **non-linearity correction** for the channels 6, 6+, 7 and 8 has been derived. Within these channels the non-linearity differs for odd and even pixels (starting pixel numbering with 0) because of the different multiplexers used for odd and even pixels. Additionally, there is a clear difference in the non-linearity between pixel numbers higher and lower than pixel number 511. This leads to 14 correction curves, four per channel with the exception of channel 6+, which covers only pixels 794 to 1024. Fig. 5-3 shows the non-linearity curves derived for channel 8. The accuracy of the non-linearity correction corresponds to 5-21 BU for detector fillings from 10000-40000 BU, depending on the channel. As for the Memory effect correction, the non-linearity has to be corrected before any other correction is applied. More details about the non-linearity can be found in *(Kleipool 2003).*

In addition to the non-linearity, Channels 6+, 7 and 8 contain a significant number of unusable pixels due to the lattice mismatch between the light detecting InGaAs layer and the InP substrate. These channels are doted with a higher amount of Indium (see chapter 3). It changes the lattice constant of the light detecting layer so that it no longer matches the lattice constant of the substrate on which the detecting layer is grown. The resulting degraded pixels are called ‘bad’ or ‘dead’ pixels. There are various effects making these pixels unusable:

- disconnected pixels preventing any signal readout
- so-called Random Telegraph (RT) pixels which spontaneously and unpredictably jump between two levels of dark current leading to different detected signals for the same intensity
- other effects including excessive noise or too high leakage current that saturates the detector

All these effects were measured on-ground and a **Bad and Dead Pixel Mask (BDM)** was created. Pixels of the BDM have to be ignored in any retrieval. As a result of radiation damage to the detectors in orbit, previously sound pixels may become flagged as bad or dead. A dynamic BDM is determined in-flight based on monitoring and calibration measurements, and updated as pixels change their status as defined by the quality criteria listed above. In order to be less affected by noise on the measurements, the dynamic BDM is smoothed in time.

After the application of the non-linearity and the BDM, the **dark signal** has to be corrected. The dark signal correction in channels 7 and 8 is complicated by the presence of a large thermal background *BGth* and the unforeseen growth of an ice layer on the detector (see chapter 6.3). The ice layer slowly changes the detector temperature and attenuates the signal on the detector, including the thermal background. The dark signal in these channels becomes (equ. 4-3)

$$DC_{ch68} = f_{coadd} \cdot (AO + t_{PET} \cdot LC + t_{PET} \cdot \Gamma_{ice} \cdot QE(T_D, \lambda) \cdot BG_{th}(\varphi))$$

where *Γice* is the transmission coefficient that changes due to the ice layer and *QE* is the quantum efficiency for the detector. (fig. 4-3)

fig. 4-3:

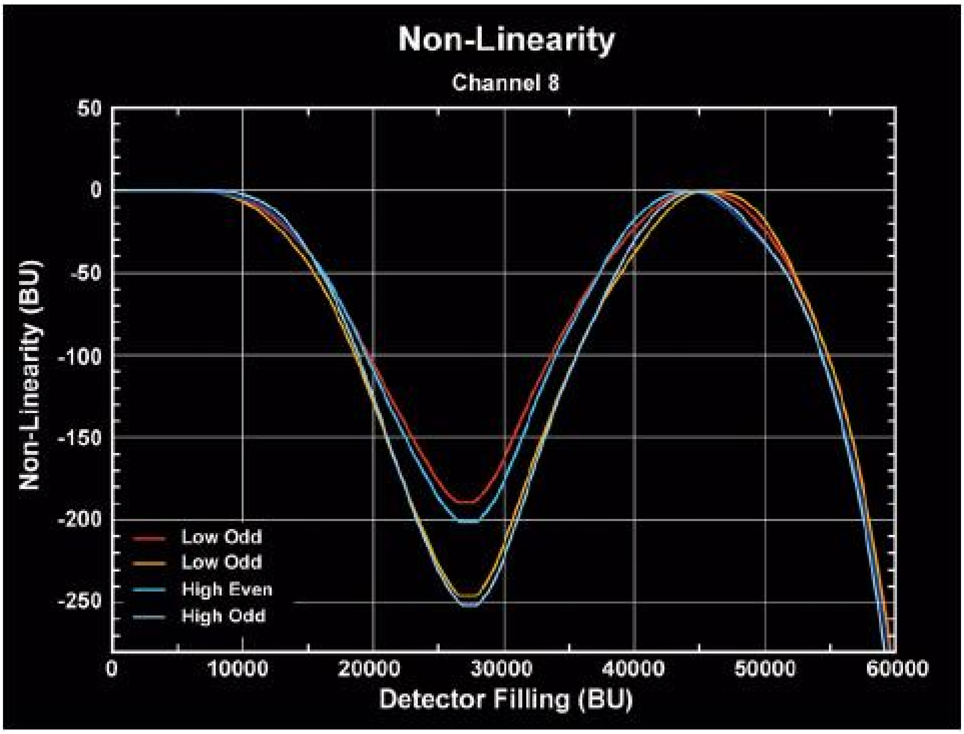

Non-Linearity in channel 8 for different pixel regions (indicated by colours). 'Low' pixels are those with pixel numbers below 512. The pixel numbering starts at 0. (Graphics: SRON)

For channels 6+ and 8 the quantum efficiency changes with the detector temperature *Tdet*, whereas the first part of channel 6 and channel 7 shows no significant temperature dependence. The thermal background is caused by the thermal radiation of the instrument and is the dominant part of the dark signal (about 4000 BU/sec) in channel 8. It depends on the orbit phase *φ* because the temperature gradients in the instrument are not completely stable but vary over one orbit due to the changing angle of solar irradiation. The variation of the dark signal over the orbit can reach up to 60 BU/sec which has significant impact on the retrievals of trace gases. In-flight the orbital variation is measured once a month during a special calibration orbit in which only dark signal measurements are performed by looking to deep space at a tangent height of 250 km in limb mode. The variation of the transmission makes the dark signal correction time dependent meaning that for channels 7 and 8 a dark signal correction, calculated from measurements in the same orbit, must be used.

The final detector related correction is the **Pixel-to-Pixel Gain (PPG)** correction. The pixels in the SWIR channels do not show the same response to incoming light. Variations of a few percent can be observed. The PPG is derived by first smoothing a WLS measurement, assuming the spectrum is flat. Then the original spectrum is divided by the smoothed measurement, leaving only the high frequent variations that are caused by the different pixel gains in the result. The PPG is strictly an effect caused by the electronics and the detector and is thus associated to the individual pixels but not to the wavelength.

4.3 Wavelength Calibration

In-flight spectral calibration of SCIAMACHY data uses the internal SLS measurements with the exception of channels 7 and 8 (see below). For selected lines the Falk algorithm determines the pixel positions *(Falk 1984)*. These are then fitted to theoretical line positions provided with the calibration data. From the polynomial coefficients of the fit the wavelength for each pixel can be calculated. Measurements of solar Fraunhofer lines serve as a quality check. In channels 7 and 8 a calibration with the internal SLS lamp is impossible because in these channels not enough useful lines are available to calculate the wavelength calibration with sufficient accuracy. In channel 8 this is caused by bad pixels interfering with the determination of the line position. Channel 7 only contains two strong doublet lines preventing an accurate determination of line positions over the whole channel. In both channels data from on-ground gas cell absorption measurements establish the wavelength calibration.
An additional effect discovered during the on-ground calibration is the so-called *Blocking Shift*: During the spectral calibration on-ground, the internal SLS and an external SLS were used. A comparison of the measurements done with the two lamps revealed a wavelength shift of up to 0.07 nm. The reason is a partial blocking of the light path during internal SLS measurements. The blocking shift was characterised and is part of the calibration data. Verification of the spectral calibration in-flight has proven that SCIAMACHY is spectrally very stable.

4.4 Stray Light

There are two types of stray light (*Sstray* in equ. 5-1), the spectral stray light and the spatial stray light. Stray light is characterised as a fraction of the total measured intensity for a given pixel. Spectral stray light is light of a certain wavelength which is scattered to a detector pixel 'belonging' to a different wavelength. It can lead to distortions in the shape of the spectrum. This type of stray light may be caused by a reflection in the instrument after the dispersion of the light beam, or by periodic errors in the spacing of the ruled grooves in a diffraction grating. The source of spectral stray light can be within the same channel, referred to as *intra-channel* stray light, or it can scale with the intensity in a different channel, referred to as *inter-channel* stray light.
Spatial stray light is light entering the telescope from outside the instantaneous field of view. It is dispersed just like light from the observation target. Depending on the source of the stray light, the spatial stray light component can add an additional offset to the spectrum and/or distort the spectrum, if the primary source of the stray light has spectral characteristics that differ significantly from the observed target.

Spectral Stray Light

In a full matrix approach, the spectral stray light determination would measure the stray light contribution from each individual pixel to all other pixels separately. In practice, however, this is not always possible. In the case of SCIAMACHY an 8192 x 8192 matrix would be needed making the calculation of stray light too slow. Initially the spectral stray light for SCIAMACHY was separated into three types: uniform stray light, ghost stray light and channel 1 stray light. As it turned out, the split into uniform and ghost stray light did not provide a sufficient correction of the stray light, so the uniform stray light correction was expanded to include a reduced matrix correction.
Stray light was characterised on-ground using measurements employing a monochromator. A monochromator produces light in a narrow, pre-defined spectral band. The centre wavelength of the spectral band can be adjusted. In the derivation of the stray light fractions from monochromator measurements it is assumed that any signal in detector pixels outside this spectral band is caused by stray light. During the on-ground calibration the spectral stray light was measured by changing the central wavelength of the monochromator spectral band, thus covering the whole wavelength range of SCIAMACHY. Dividing the integrated light of the monochromator peak(s) by the light detected outside the peak yielded the stray light fraction. The resulting data is part of the calibration data set and is used to correct the spectral stray light in-flight.

Ghost stray light is caused by a more or less focused reflection of one part of a spectrum to another part of the spectrum. It can distort the shape of the 'true' spectrum, because it does not add signal to all pixels. During the on-ground measurements many tens of ghost signals were detected in channels 3-8, of which the 20 strongest ones were characterised. The total sum of ghost stray light in a channel is at maximum 1% of the incoming intensity.

The reduced stray light matrix describes any of the remaining stray light as a matrix multiplication of an input spectrum and a stray light matrix. A measured spectrum is resampled to lower resolution (1022 pixels instead of 8192), and yields a stray light spectrum of 2048 pixels after matrix multiplication. This stray light spectrum is interpolated to the full 8192 pixel grid and subtracted from the input spectrum. As of 0-1 processor version 7 that became operational in February 2010 the reduced matrix multiplication is implemented for channel 2. The complete reduced matrix multiplication for all channels will allow for inter-channel stray light correction and will be implemented in the version 8 processor.

For channel 1 the situation is less favourable with respect to stray light levels. The on-ground measurements revealed that the spectral stray light in channel 1 can reach levels of up to 10% of the incoming signal for a typical input spectrum. It is also highly wavelength dependent. The main reason for the larger stray light fraction in channel 1 is the high dynamic range of the spectra in this channel, with the lowest signal 3 orders of magnitude smaller than the highest signal. The initial coarse, artificial separation in uniform and ghost stray light turned out to be insufficient for a correction in channel 1 and an alternative method was formulated already before launch, i.e. before the stray light matrix was implemented for channel 2. The chosen approach combines the correction of uniform and ghost stray light in a modified matrix approach. In addition to the matrix approach discussed above, the approach in channel 1 also considers the polarisation of the incoming light.

Spatial Stray Light

In order to avoid signal-to-noise problems during the spectral stray light measurements, ten wavelength bands were defined separately for s- and p-polarised light leading to a total of 20 bands. For both polarisation directions 9 bands were located in channel 1 to characterise intra-channel stray light and one band covered the signal from channels 2-5 to characterise inter-channel stray light. The channel 1 detector material is not sensitive for light with wavelengths longer than 1000 nm so the SWIR channels did not need to be considered. For each band the stray light contribution to all detector pixels was calculated leading to a 10 x 1024 matrix for both, s- and p-polarised light. The stray light fraction in channel 1 ranges from less than 1% to as much as 10%. The correction has an accuracy of around 25% and reduces the stray light by an order of magnitude leaving at most 1% stray light in the spectrum after correction.

Spatial Stray Light

Shortly after ENVISAT emerges from eclipse and passes the North Pole, the sun shines directly into the limb port. In this orbit region spatial stray light cannot be avoided, i.e. the particular effect was foreseen and the data are flagged accordingly. In order to minimise spatial stray light, the ASM is rotated such that the edge of the mirror/diffuser plate points into flight direction, with the diffuser looking to the instrument side during all measurements using the ESM only.
Both on-ground performance measurements and in-flight limb measurements indicated that there was a small fraction of spatial stray light present. Dedicated in-flight measurements confirmed the performance measurements and indicate periodic structures in the optics before the slit, resulting in a small fraction of the light being dispersed as by a grating. This has no significant impact for nadir measurements, but limb measurements with a dynamic range of several orders of magnitude over a few degrees suffer from the spatial stray light. At the moment there are no corrections for spatial stray light.

4.5 Polarisation

SCIAMACHY is – as all grating spectrometers without a polarisation scrambler – sensitive to the polarisation of the incoming light, i.e. the response will not only depend on the intensity but also on the polarisation of the light. Thus polarisation correction is required. It uses the Mueller matrix approach (see e.g. *Azzam and Bashara 1977*, *Coulson 1988*). Measurements of polarised light can be expressed by a so-called *Mueller matrix* **M** and the Stokes vector ***S***. Since the detectors only yield a single measurement value per pixel, they can be regarded as polarisation insensitive detectors, and any polarisation sensitivity can be included in the Mueller matrix of the optical components between the incoming light and the detector. Thus, only the top row of the end-to-end Mueller matrix of the instrument is relevant, and can be regarded as a polarisation sensitivity vector (equ. 4-4):

$$S_{\text{det}} = \vec{M} \cdot \vec{I}$$

SCIAMACHY has multiple viewing geometries, selected by appropriate configuration of the scanner unit containing mirrors and diffusers. After the scanner, the OBM is identical for Limb and Nadir measurements. The end-to-end Mueller matrix of the instrument can be split up in a Mueller matrix for the scanner, which is configuration dependent, and a fixed polarisation sensitivity vector of the OBM. This yields (equ. 4-5):

$$S_{det} = \begin{pmatrix} M_1^{OBM} & M_2^{OBM} & M_3^{OBM} & M_4^{OBM} \end{pmatrix} \cdot \begin{pmatrix} M_{11}^{sc} & M_{12}^{sc} & M_{13}^{sc} & M_{14}^{sc} \\ M_{21}^{sc} & M_{22}^{sc} & M_{23}^{sc} & M_{24}^{sc} \\ M_{31}^{sc} & M_{32}^{sc} & M_{33}^{sc} & M_{34}^{sc} \\ M_{41}^{sc} & M_{42}^{sc} & M_{43}^{sc} & M_{44}^{sc} \end{pmatrix} \cdot \begin{pmatrix} I \\ Q \\ U \\ V \end{pmatrix}$$

where on the left hand side of the equation a scalar describes the light as detected by the instrument, and on the right hand side we have the polarisation sensitivity vector $\vec{M}^{OBM}$ of the OBM, and the Mueller matrix $\vec{\vec{M}}^{sc}$ defining the response of the scanner to the incoming light represented by another Stokes vector. The first element of this Stokes vector, *I*, denotes the total intensity of the light. *Q* is a measure for the polarisation along the x- or y-axis of a chosen reference frame and can be described as $Q = I_x - I_y$. *U* is a measure for the polarisation along the 45¿ direction and is defined as

$U = I_{45} - I_{-45}$, and V is the circular polarisation component of the incoming light, which is negligibly small for atmospheric light. Note that the total intensity can be written as $I = I_x + I_y$ or $I = I_{45} + I_{-45}$. Often *Q* and *U* are normalised to the total intensity *I*. We will denote normalised fractions with *q* and *u*.The polarisation reference frame used in the calibration is defined w.r.t. the direction of the slit, at the plane of the slit: looking in the direction of the light entering the instrument after the scan mirrors, the +45¿ polarisation (*u=1)* direction is obtained by a 45¿ clockwise rotation from the long side of the entrance slit of SCIAMACHY (*q=1)*. All calibration data use this reference frame.

All $\vec{\vec{M}}^{sc}$ Mueller matrix elements are dependent on wavelength and on the incidence angle of the light on the scan mirror(s) or diffuser(s). In the calibration, ambient measurements on component level and instrument TV measurements have to be combined meaning that the actual instrument matrix has to be calculated by a multiplication of the matrix for the scanner (combination) and the OBM. Note that though the end-to-end circular polarisation sensitivity of the instrument is irrelevant when V is zero, the scanner may through its Mueller matrix introduce a circular polarisation component to the light, which requires the circular polarisation sensitivity of the OBM to be known. Though originally not foreseen for on-ground calibration, an update of the calibration concept introduced the circular polarisation sensitivity into the calibration equations. Defining the relative polarisation sensitivity vector of the OBM as:

$$\vec{\mu}^{OBM} = \begin{pmatrix} 1 & \mu_2^{OBM} & \mu_3^{OBM} & \mu_4^{OBM} \end{pmatrix} = \begin{pmatrix} 1 & \dfrac{M_2^{OBM}}{M_1^{OBM}} & \dfrac{M_3^{OBM}}{M_1^{OBM}} & \dfrac{M_4^{OBM}}{M_1^{OBM}} \end{pmatrix}$$

the response of the instrument to polarised light becomes:

$$S_{\det} = M_1^{OBM} \cdot \vec{\mu}^{OBM} \cdot \vec{\vec{M}}^{sc} \cdot \vec{I}$$

Combination of the polarisation response of the scanner and the OBM using

$$M_1^{instr} \cdot \vec{\mu}^{instr} = M_1^{OBM} \cdot \vec{\mu}^{OBM} \cdot \vec{\vec{M}}^{sc}$$

and making sure to normalise $\vec{\mu}^{instr}$ so that the first element μ_1^{instr} remains unity, gives the equation describing the instrument response as expressed in total intensity and fractional linear polarisation (equ. 4-6)

$$S_{\det} = M_1^{instr} \cdot I \cdot \left(1 + \mu_2^{instr} \cdot q + \mu_3^{instr} \cdot u\right)$$

where M_1^{instr} is the radiometric sensitivity of the instrument (with implicit dependence on wavelength for the main science channels, and determined as well for all 7 PMDs). The term in brackets is the inverse of the polarisation correction factor, *c pol*. It depends on the polarisation sensitivity of the instrument and the polarisation of the incoming light *q* and *u*.The instrument polarisation correction factor is thus with the definitions given above (equ. 4-7)

$$c_{pol} = \left(1 + \mu_2^{instr} \cdot q + \mu_3^{instr} \cdot u\right)^{-1}$$

The problem of correcting the response of the instrument for polarisation can thus be divided into two parts: (1) determining the polarisation sensitivity of the instrument and (2) determining the polarisation of the incoming light during the science measurements in-flight.

The instrument response was measured on instrument level under TV conditions while the mirror and the mirror/diffuser combination were measured under ambient conditions. The Fresnel equations for reflection off a dielectric medium are used to describe the scanner withthe index of refraction determined from the ambient measurements, and hence used to calculate the

Mueller matrix elements of the scanner $\vec{\vec{M}}^{sc}$ for arbitrary angles used during TV measurements or in flight. While the OBM polarisation sensitivities $\vec{\mu}^{OBM}$ (fig. 4-4) were derived during the on-ground calibration under thermal vacuum, from measurements with fully linearly polarised light at a range of polarisation angles.

fig. 4-4:

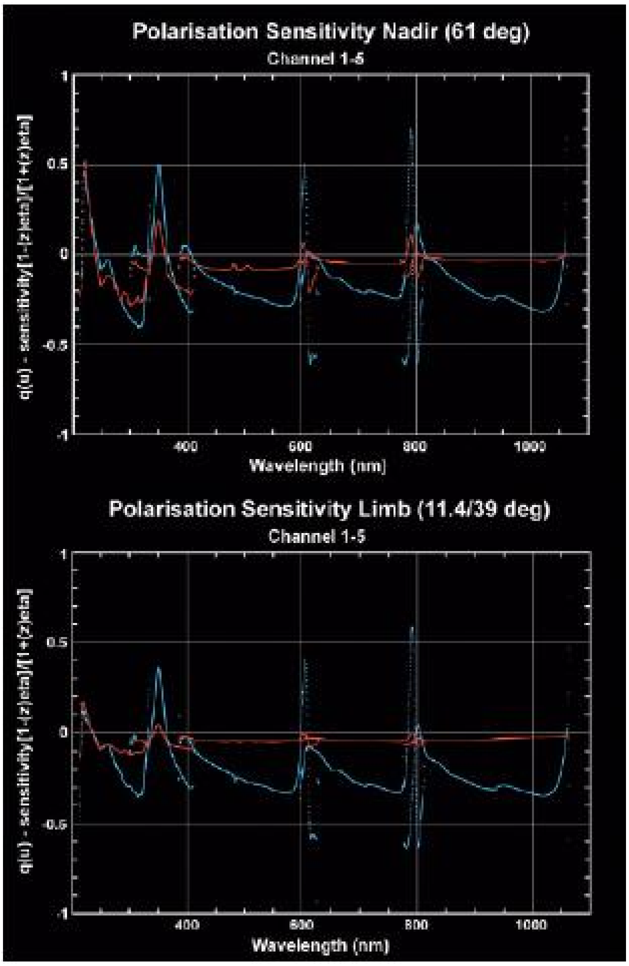

q (blue) and u (red) sensitivity from equ. 4-6 for nadir (elevation angle of 61° top) and for limb (elevation angle of 11.4° and azimuth angle of 39°, bottom) for channels 1-5. Note that these sen-sitivities are multiplied with the polarisation fractions to get cpol and the correction will thus be smaller than displayed for lower polarisation. (Graphics: SRON)

The second step, the determination of the polarisation of the incoming light is done by determining the ratio of the signal in the PMD channels – which is fully polarised due to the Brewster reflection at the pre-disperser prism (see chapter 3.2) – and the corresponding signal in the science channel for each individual measurement. During calibration this ratio was determined for different combinations of u- and q-polarised light. The comparison of the in-flight ratio with the calibration data gives 7 polarisation values for the whole spectrum, one for each PMD channel.

Polarisation values *q* are calculated from PMD A-F needing the corresponding value of *u*. The ratio *u*/*q*, which depends only on the polarisation angle, is assumed to be constant, such that (equ. 4-8)

$$u_{measured} = q_{measured} \cdot (u/q)_{const}$$

In the original calibration concept, for UV-VIS wavelengths below 600 nm the polarisation angle from single scattering theory was planned to be used (see below), whereas for higher wavelengths the ratio *u*/*q* from PMD D and PMD 45°, both centred around 850 nm, had to be taken. The values of *q* and *u* here are derived by iteration, until the *u* needed to calculate *q* from PMD D and the *q* needed to calculate *u* from PMD 45°, match. In-flight it was noted that PMD 45° delivers systematically signals which are 10-15%

higher than expected, even for unpolarised sources such as the sun. As there are indications that this PMD suffers from stray light, it remains currently unused. Instead, *u*/*q* is taken from single scattering theory for the complete wavelength range. From POLDER satellite measurements of *u/q* this appears to be a sufficiently accurate assumption *(Schutgens et al. 2004)*. Note, that for small values of *q*, this ratio becomes very large, thereby amplifying small measurement errors on *qmeasured* into large measurement errors on *umeasured*. However, since the instrument is much more sensitive to *q* than to *u*, this has little impact on the radiometric calibration, even though *u* is notably unreliable. In limb, the calculated polarisation displayed an unexpected drift with increasing tangent height, which is probably due to increasing significance of the spatial stray light contribution as the limb intensity decreases. Therefore the PMD measurements are only used up to 30 km. Radiative transfer calculations show that above this height the depolarisation remains constant *(Mc Linden et al. 2002)*, such that for higher limb tangent heights we are able to scale the measured polarisation at 30 km with a value obtained from single scattering theory.

The PMD channels cover only the instrument channels 2-8. For channel 1 the backscattered radiation is dominated by single scattering as can be inferred from radiative transfer calculations. Similarly to the GOME instrument, a theoretical value based on single scattering geometry is used here *(Slijkhuis 2000b, Tanzi 1999, Tilstra et al. 2003)*. The transition region from single scattering to multiple scattering and/or ground reflection in the region between approximately 300-325 nm requires special attention. For GOME, a parameterisation of the degree of polarisation as a function of wavelength was derived by R. Spurr *(Balzer et al. 1996)*, known as the ‘general distribution function’ (GDF) for polarisation. The GDF is characterised by the single scattering value plus three parameters. These parameters are currently obtained using a simplified version of the algorithm from *Schutgens and Stammes (2002)* where the dependence on scene albedo and ozone content is neglected. More polarisation information may be derived from the channel overlaps of channels 1-6 (five polarisation points) where the different polarisation sensitivities of each channel leads to two independent measurements for the two variables *q* and *u*. However, due to calibration inconsistencies, these polarisation points are currently not reliable.

The polarisation values *q* and *u* on the level 1b products are specified in an ‘atmospheric’ coordinate frame which is different from the coordinate frame used for the on-ground calibration and Key Data specification. The ‘atmospheric’ coordinate frame is related to the geometry of the scattering of light in the atmosphere. The choice has been to define *q* as parallel to the local meridian plane – the plane through satellite, zenith, and centre-of-FoV (where its Z axis points in the travel direction of light, i.e. towards the instrument). This plane is depicted in Figure 5-5 for nadir viewing geometry. For limb viewing geometry, the polarisation plane in the figure is rotated 90° as the line-of-sight is approximately in the flight direction. (fig. 4-5)

fig. 4-5:

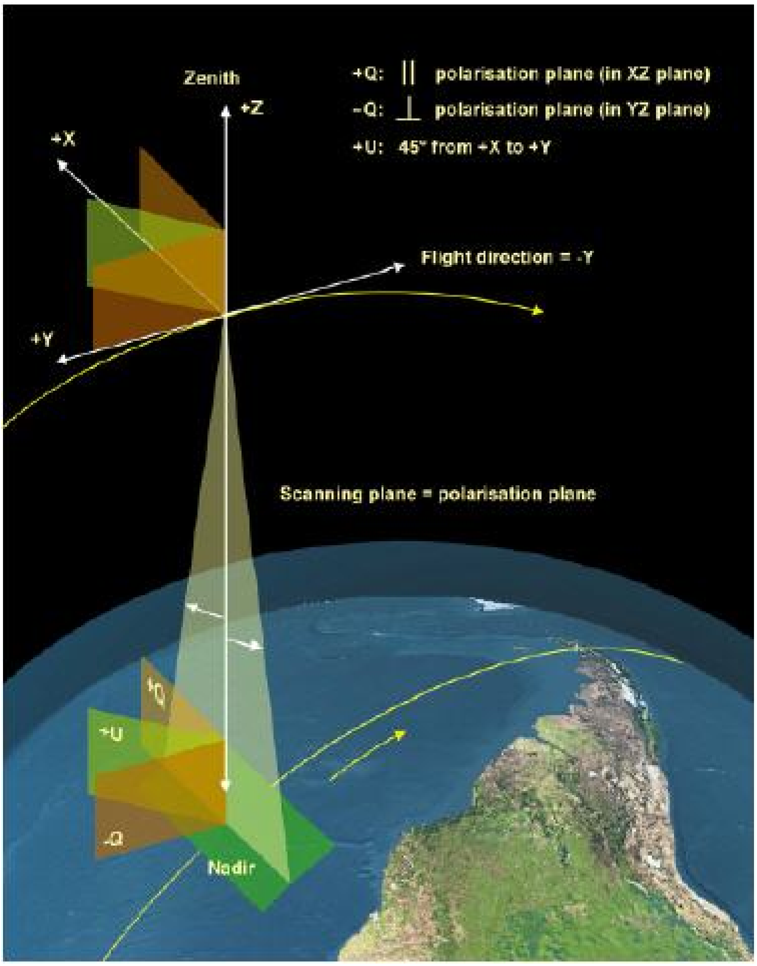

Definition of the coordinate frame used in the data processor for polarisation values q = Q/I, u = U/I. (graphics: DLR-IMF)

4.6 Radiometric Calibration

4.6 Radiometric Calibration

The final step in the calibration of the data is the radiometric calibration. The retrieval of trace gases usually uses the reflectance, the ratio of Earth radiance and solar irradiance. The solar irradiance is measured with on-board diffusers in-flight. The reflectance can be written as (equ. 4-9)

$$R = \frac{\pi}{\mu_0} \cdot \frac{I_{Earth}}{I_{Sun}} = \frac{\pi}{\mu_0} \cdot \frac{M_1^{sun}}{M_1^{N,L}} \cdot \frac{S_{\det}^{Earth} \cdot c_{pol}}{S_{\det}^{sun}}$$

with $I_{Earth,Sun}$ and $S_{\det}^{Earth}$ as the Earth and sun intensity and measured signal, μ_0 as the cosine of the solar zenith angle, $M_1^{N,L}$ as the instrument radiometric response for limb (*L*) and nadir (*N*) and M_1^{sun} as the instrument radiometric responses for sun diffuser measurements, as calculated from the Mueller matrix for the scanner and the polarisation sensitivity of the OBM. Because all matrix elements in equ. 4-9 relate to the detectors, we left the superscript ?*D*? out for better legibility. For a proper calibration the instrument responses have to be determined as a function of wavelength λ and incidence angle α. All polarisation properties are calculated relative to the element of the polarisation sensitivity vectors, so the only remaining term needed for radiometric calibration is the M_1^{instr} term which depends on M_1^{OBM}, $\vec{\mu}^{OBM}$ and $\vec{\vec{M}}^{sc}$ for any limb, nadir or solar viewing geometry summarised here as:

$$M_1^{instr} = \left| M_1^{OBM} \vec{\mu}^{OBM} \cdot \vec{\vec{M}}^{sc} \right|_1$$

where $\left|\vec{x}\right|_1$ identifies the first element in vector $\vec{x}$. M_1^{OBM} and $\vec{\mu}^{OBM}$ are provided in the calibration key data as determined from on-ground TV measurements, and $\vec{\vec{M}}^{sc}$ is calculated with the scanner model using as input the actual viewing geometry of the instrument, the complex index of refraction of the mirror material as determined during on-ground ambient calibration, and optionally any contamination built-up on the scan mirrors since launch.

The OBM contains a neutral density filter (NDF) for which needs to be corrected for those solar measurements where the NDF is in the beam. This is done by dividing the recorded signal with the throughput of the NDF.

4.7 Optical Throughput Monitoring

Contrary to system monitoring, optical performance monitoring aims at assuring an as complete as possible description of the optical performance in order to correct for degradation effects throughout the instrument's lifetime. Therefore, monitoring serves as a general prerequisite for continuous high data product quality. Monitoring related to the optical performance of SCIAMACHY is to a large degree linked to the instrument calibration & characterisation status. It establishes in-flight information which permits proper application of on-ground calibrations and modelling of the in-orbit environment.
Optical component degradation monitoring is one of the main long-term monitoring activities to be performed over the mission's lifetime (*Noël et al. 2003*). It applies regular trend analyses to measurement data obtained with the internal WLS and of observations of the unobscured sun above the atmosphere. In order to monitor the different SCIAMACHY light paths, solar measurements are taken in various viewing geometries: in limb/occultation geometry (via ASM and ESM mirrors), in nadir geometry (via the ESM mirror through the sub-solar port), and via the so-called 'calibration light path' involving the ASM mirror and the ESM diffuser. Particularly the WLS produces a rather stable output over time – except for some degradation in channel 1 – which makes it well suited for throughput monitoring. (fig. 4-6)

fig. 4-6:

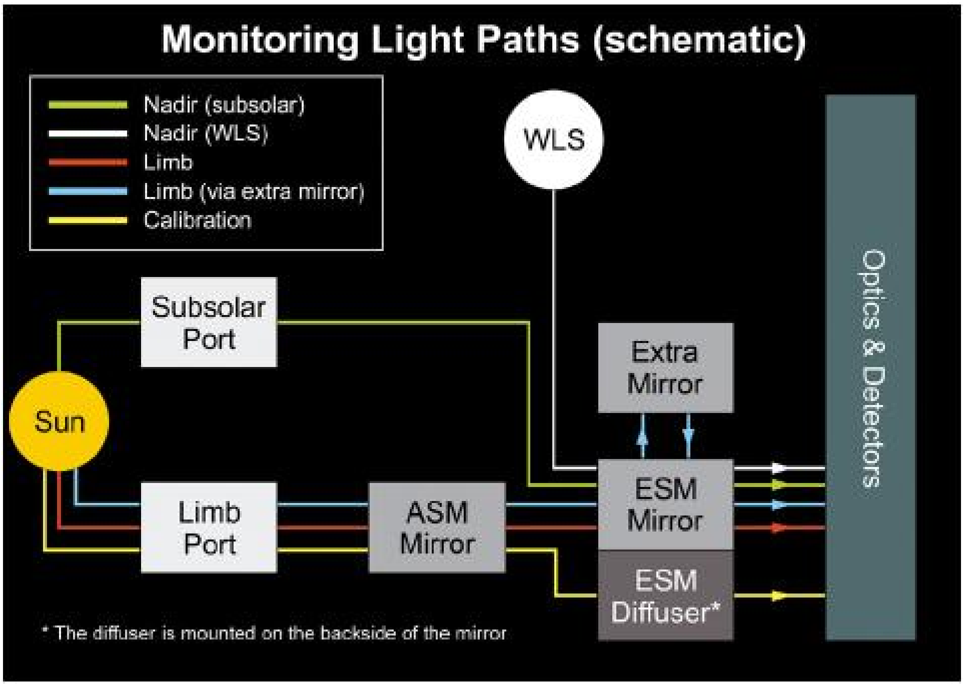

Schematic view of SCIAMACHY light paths used in performance monitoring. (Graphics: IUP-IFE, University of Bremen)

Because of the status of the operational data processing in the initial part of the mission, the monitoring of the optical performance of the SCIAMACHY instrument had to be based on the analysis of Level 0 data – which had been corrected for dead/bad pixels, dark current (fixed value from August 2002), scan angle dependencies, quantum efficiency changes and the seasonally varying distance to the sun – and not the fully calibrated level 1b spectra as originally envisaged. Due to this approach additional calibration corrections, e.g. stray light correction, were not applied. Therefore, optical throughput variations smaller than about 1% require careful investigation. However, once the light path monitoring can be based on fully calibrated data, it will yield so called *m-factors* to describe how the individual light paths degrade. These m-factors will be fed into operational data processing to ensure that the measured signals are fully matched to the performance of SCIAMACHY.

Moreover, from the combination of the results for the different light paths it will be possible to derive information about the degradation of individual optical components (mirrors and diffusers, see fig. 4-6). The degradation of the ASM mirror, for example, may be determined from the ratio of the limb to the nadir light path degradation. To determine the ESM mirror degradation it is necessary to combine the limb light path results with dedicated measurements involving the extra mirror which is located inside the instrument, only rarely used and thus assumed not to degrade. Finally, the degradation of the ESM diffuser can be computed from the combination of the nadir, limb, and calibration light path. A comparison of the limb and nadir light path monitoring results indicates that the major degrading element in the SCIAMACHY optical train seems to be the ESM mirror which shows around 50% degradation over 7 years in the UV (channel average).

An example for the wavelength dependence of the instrument degradation is depicted in fig. 4-7. It displays for channel 2 the relative variation of the nadir throughput – light enters the spectrometer via the ESM mirror only – as a function of time and wavelength, based on internal WLS measurements. The available measurement data have been interpolated to a daily grid. Times of reduced instrument performance (like switch-offs or decontamination periods) as well as dead/bad pixels have been masked out (gray bars). All measured signals are referenced to August 2nd, 2002 at about orbit 2200. The degradation is clearly wavelength dependent: In channel 2 (fig. 4-7) degradation can be identified which peaks at spectral regions of high polarisation sensitivity and in the overlap regions between the channels. However, the channel 4 monitoring data presented in Fig. 4-8 show the excellent absolute radiometric stability of SCIAMACHY. The degradation in this channel stays mostly within 2%, except for the channel overlaps. A similar trend can be observed in the other channels in the visible range. Spectrally dependent throughput monitoring may become an additional operational task once the operational availability of the required input products is ensured. (fig. 4-7, fig. 4-8)

fig. 4-7:

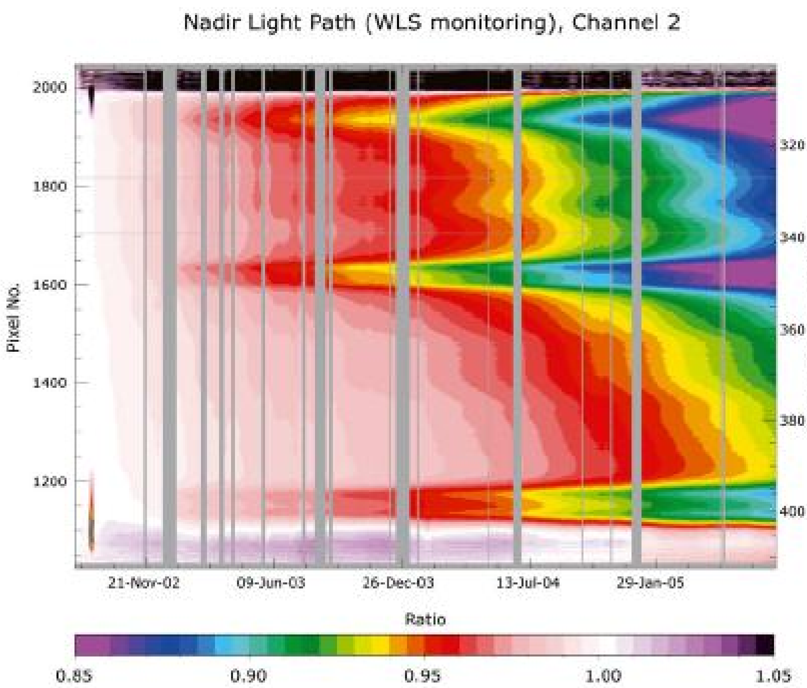

Monitoring results for the nadir light path using measurements with the internal WLS in channel 2. All available data have been interpolated to a daily grid. (Graphics: IUP-IFE, University of Bremen)

fig. 4-8:

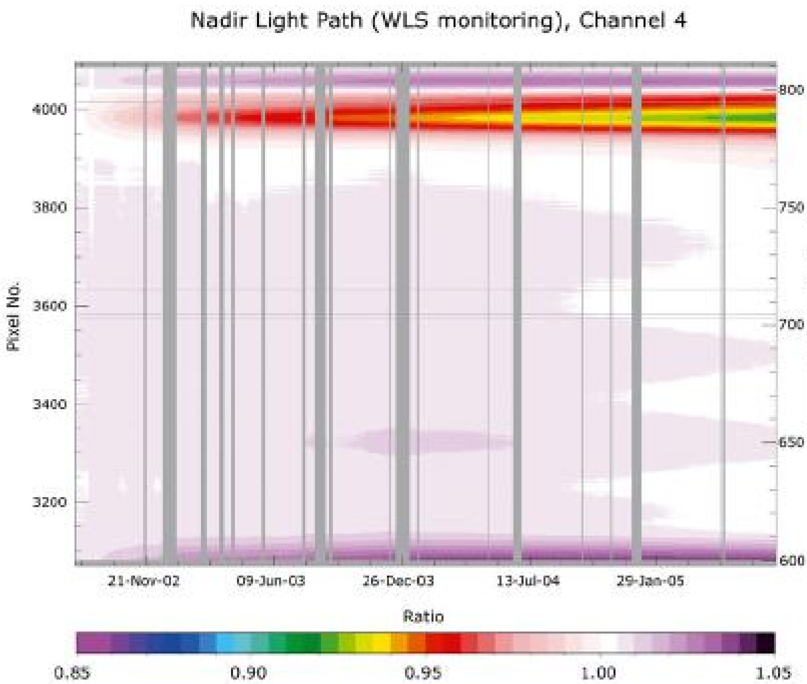

As fig. 4-7, but results for channel 4. (Graphics: IUP-IFE, University of Bremen)

CHAPTER 5

5: From Radiation Fields to Atmospheric Concentrations – Introduction into the Retrieval of Geophysical Parameters

The challenging task in spaceborne remote sensing of the atmospheric composition is the quantitative derivation of the constituent distributions – trace gases, aerosols, clouds – from the measured top-of-the-atmosphere spectral radiance or Earth spectral reflectance data. The main source of radiation for passive remote sounding of the atmosphere by SCIAMACHY in the UV-SWIR regions is the sun. The absorption, emission and scattering characteristics of the Earth's atmosphere can be determined by comparing the radiance reflected from and scattered by the atmosphere to the sensor with the extraterrestrial solar irradiance. The ratio of the radiance to irradiance, the Earth reflectance spectrum, contains the information relevant for determining the atmospheric composition. A quantitative analysis requires:

- spectra of high spectral and radiometric quality,
- an accurate modelling of the radiative transfer of the solar photons through the atmosphere to the sensor,
- techniques to relate the measured top-of-the-atmosphere spectra to the constituent properties (usually referred to as *Inversion Methods*).

The retrieval of information on atmospheric trace gases relies on the knowledge of the absorption, emission and scattering of electromagnetic radiation in the atmosphere. In the UV, VIS, NIR and SWIR spectral ranges, the radiative transfer through the atmosphere is affected by (see fig. 5-1):

- scattering by air molecules (Rayleigh-, Raman scattering),
- scattering and absorption by aerosol and cloud particles (Mie-scattering),
- absorption and emission by trace gases,
- refraction due to the density gradient in the atmosphere,
- and surface reflection.

These are the processes which must be quantitatively taken into account when retrieving atmospheric geophysical parameters from SCIAMACHY measurements. (fig. 5-1)

fig. 5-1:

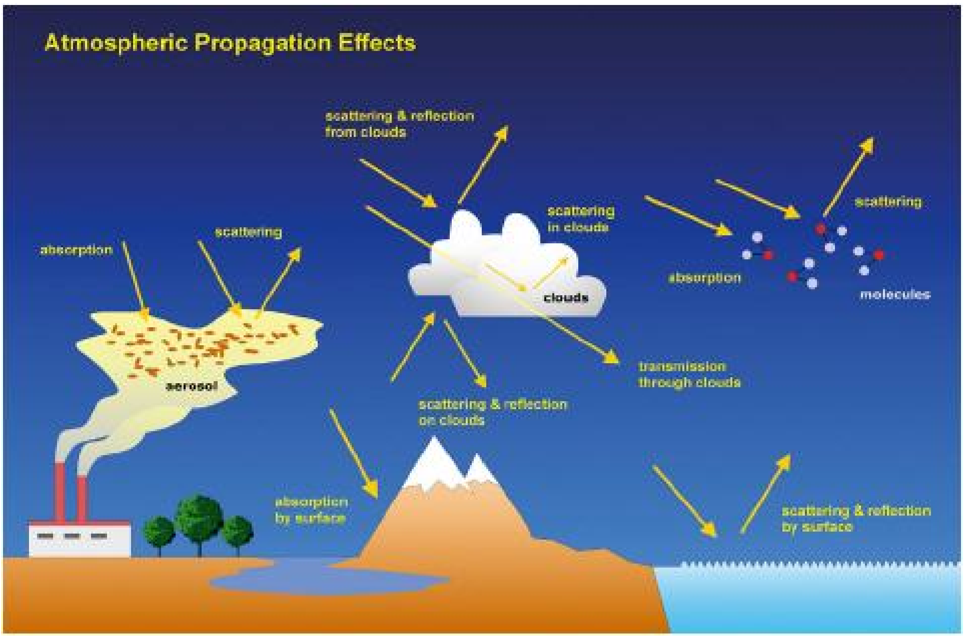

Scheme of the relevant interactions of solar light with the Earth's atmosphere and surface. (Graphics: DLR-IMF)

Trace gases usually exhibit characteristic fingerprint spectra in emission or absorption, originating from:

- rotational transitions: primarily observed in the far infrared and microwave spectral regions,
- vibrational-rotational transitions: can be measured in the infrared,
- electronic transitions: mainly detected in the UV, VIS and NIR spectral regions.

SCIAMACHY with its wide spectral coverage from the UV to the SWIR is detecting trace gases mainly via their electronic transition spectra.

Radiative Transfer in the Earths Atmosphere

5.1 Radiative Transfer in the Earth's Atmosphere

An important tool to simulate changes in the solar radiation due to atmospheric scattering and absorption processes are radiative transfer models, also referred to as *Forward Models*. They provide the synthetic radiances, as they would be measured by the sensor, for a specified state of the atmosphere. These models are an important part of any retrieval process. Considering the entire atmosphere, one usually talks about the radiation field, which describes the angular and spatial distribution of the radiation in the atmosphere.

The radiation field in the atmosphere is commonly characterized by its intensity which is defined as the flux of energy in a given direction per second per unit wavelength range per unit solid angle per unit area perpendicular to the given direction *(Liou 2002)*. All interactions between the radiation and the atmosphere are classified either as extinction or as emission. The two processes are distinguished by the sign of the change of the radiation intensity as a result of the interaction. *Extinction* refers to any process which reduces the intensity in the direction under consideration and therefore includes absorption as well as scattering processes from the original direction into other directions. *Emission* refers to any process which increases the intensity in the direction under consideration and thus includes scattering into the beam from other directions, as well as thermal or other emission processes within the volume. In the description of radiative transfer presented here we neglect the polarization state of light for reasons of simplicity. However, we note that polarization is important for SCIAMACHY for two reasons, namely in order to

- accurately simulate radiances in the UV and VIS
- account for the polarization sensitivity of the instrument when determining the true radiance

The general form of the radiative transfer equation describes all the processes which the radiance undergoes as a result of its interaction with a medium, taking energy conservation into account. It has the form (equ. 5-1)

$$\frac{dI}{ds} = -\alpha\,(I - J)$$

where *I* is the intensity of the radiation in a given direction, *a* is the extinction coefficient describing the fraction of the energy which is removed from the original beam and *J* is the source function which describes the energy emitted by the volume element, i.e., the increase of the intensity, *I*, in the original direction.

If the energy of the radiance travelling in a certain direction through the atmosphere can only be increased due to the scattering processes – as is the case for the spectral range covered by SCIAMACHY – the source function depends on the intensity falling on the elementary volume from all directions (equ. 5-2)

$$J = \frac{\omega}{4\pi} \int p(\gamma)\, I\, d\Omega$$

with γ being the scattering angle, i.e. the angle between the directions of the incident and scattered radiation, and ω is the single scattering albedo representing the probability that a photon which interacts with a volume element will be scattered rather than absorbed. The term $p(\gamma)\, d\Omega / 4\pi$ denotes the probability that the radiation is scattered into a solid angle $d\Omega$ about a direction forming an angle γ with the direction of the incident radiation and the quantity $p(\gamma)$ is called the phase function. The total radiation field can be split into two components: the direct radiation, I_{dir}, which is never scattered in the atmosphere or reflected from the Earth's surface and the diffuse radiation, I_{dif}, which is scattered or reflected at least once. Since there is no relevant process in the atmosphere which increases the intensity of the direct solar radiation, the radiative transfer equation for the direct radiation leads to the homogeneous differential equation (equ. 5-3)

$$\frac{dI_{dir}}{ds} = -\alpha\, I_{dir}$$

with a solution described by the Lambert-Beer's Law (equ. 5-4)

$$I_{dir} = I_{irr}\, exp\left(-\int \alpha(s)\,ds\right)$$

with I_{irr} being the solar irradiance and the integral $\int \alpha(s)ds$ along the photon path defining the optical depth τ. Integration is performed along the direct solar beam from the surface to the top of the atmosphere. This equation describes the attenuation of the direct solar or lunar light travelling through the atmosphere. Thus the direct component (equ. 5-4) simulates the radiative transfer when for example directly viewing the sun or the moon. Therefore, it describes SCIAMACHY measurements in occultation geometry. If the scattering processes in the atmosphere are non-negligible ? as for SCIAMACHY nadir and limb measurements ? the diffuse component has to be considered in addition to the direct one. This leads to the standard radiative transfer equation for the diffuse component for a plane-parallel atmosphere (equ. 5-5)

$$\frac{dI_{dif}}{ds} = -\alpha\left(I_{dif} - \frac{\omega}{4\pi}\int p(\gamma)\, I_{dif}\, d\Omega - \frac{\omega}{4\pi}\, p(\gamma_0) I_{irr}\, \exp\left(-\int \alpha(s)ds\right)\right)$$

where γ_o denotes the scattering angle between the direct solar beam and the direction of observation.
Scattering occurs by molecules and various types of aerosols and clouds. Molecular scattering cross-sections are characterised by the Rayleigh (λ^{-4}) law, with aerosol scattering typically showing a much less pronounced dependence on wavelength (about λ^{-1}). Molecular scattering dominates in the UV with aerosols replacing molecules as the major source of scattered light in the VIS and NIR range (see fig. 5-3). The molecular scattering consists of two parts: the elastic Rayleigh component which accounts for 96% of scattering events and the 4% inelastic rotational Raman component, which is considered responsible for the so called *Ring* effect (?filling in? of solar Fraunhofer lines in the Earthshine spectra). Further details on atmospheric radiative transfer can be found in e.g. *Liou (2002)*.(fig. 5-2)

fig. 5-2:

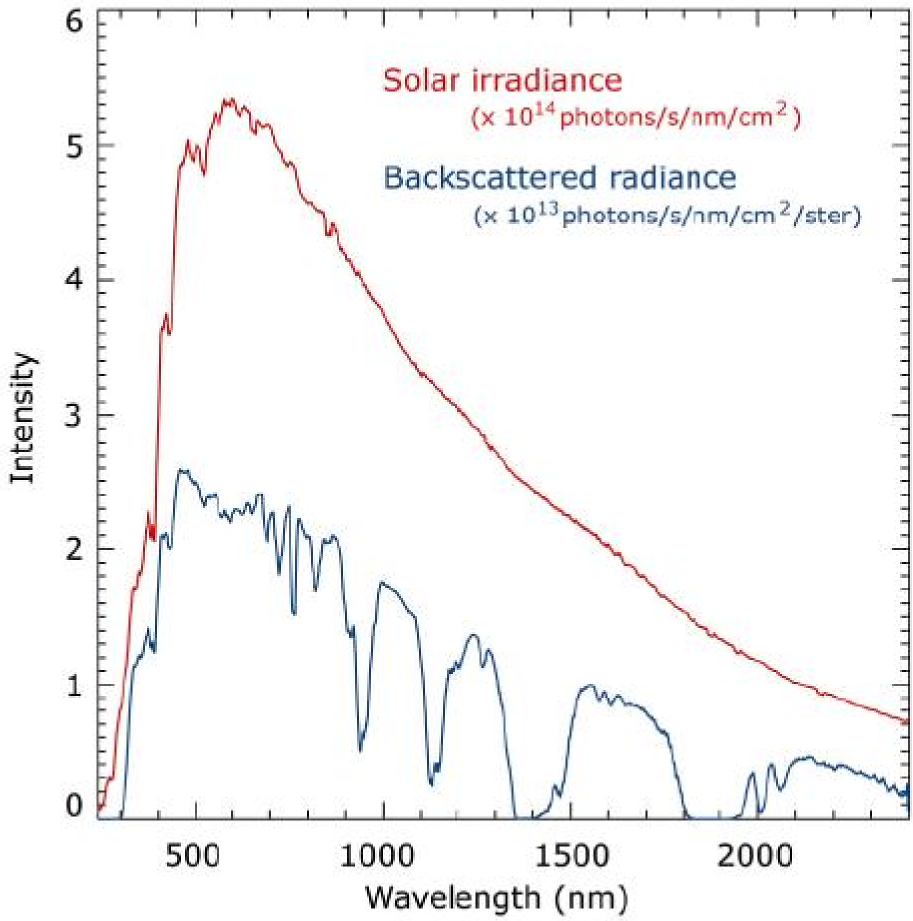

The solar irradiance spectrum (red) and Earth radiance spectrum (blue) with a shape modified by absorption of trace gases and scattering in the atmosphere. (graphics: IUP-IFE, University of Bremen)

Direct and diffuse radiations are attributed to different light paths. Equations 5-4 and 5-5 need to be solved employing standard methods *(Lenoble 1985)*. *Idir* and *Idif* must be added to describe the radiative transfer for the SCIAMACHY nadir geometry for not too large solar zenith angles (SZA). As an example, figure 5-2 shows the solar irradiance spectrum and the backscattered radiance at the top of the atmosphere. When SCIAMACHY nadir radiances at high SZA > 75° are simulated, the sphericity of the atmosphere must be taken into account in a pseudo-spherical approximation for the direct solar beam. For simulating SCIAMACHY limb radiances both the direct and the diffuse solar beam have to be treated in a spherical atmosphere, including refraction. The numerical solution of the radiative transfer equation is then accomplished by an iterative approach *(Rozanov et al. 2001)*. Depending on the scientific application, several radiative transfer models are used in the SCIAMACHY data analysis. They include GOMETRAN *(Rozanov et al. 1998)*, LIDORT *(Spurr et al. 2001)*, DAK *(Stammes 2001)*, SCIARAYS *(Kaiser and Burrows 2003)* and SCIATRAN 2.0 *(Rozanov et al. 2005a)*.

These radiative transfer models are not only able simulating the radiance measured by SCIAMACHY, but they are also optimised to deliver additional parameters to quantify the geophysical parameters of interest. One of these parameters is the *Weighting Function*. This function is the derivative of the modelled radiance with respect to the model parameter, and describes how sensitive the radiance changes are when the parameters are modified. Another important quantity to be delivered by radiative transfer models is the Airmass Factor (AMF, see chapter 5.2) which is a measure for the photon path in the atmosphere.

fig. 5-3:

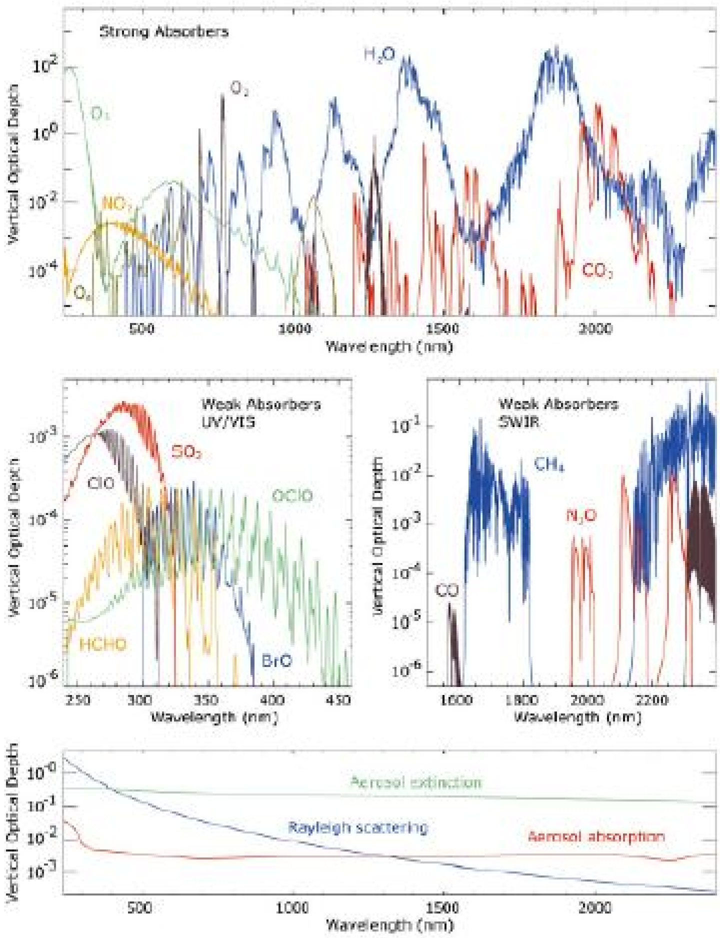

Simulated vertical optical depth of the targeted constituents to be observed at 55? N around 10 a.m. The strong absorbers are plotted in the upper part and the relevant weak absorbers in the middle part. In the lower part the vertical optical depth due to Rayleigh scattering, aerosol extinction and absorption is given. Note the large dynamic range of the differential absorption structures used for retrieval of the constituents. (Graphics: IUP-IFE, University of Bremen)

5.2 Total Column: Nadir Retrieval Schemes of DOAS-type

Many molecules of atmospheric relevance have structured absorption spectra in the UV-VIS spectral range (fig. 5-3). These can be used to determine the total atmospheric amount of the species from remote sensing measurements of scattered sunlight using the DOAS method. This powerful retrieval technique was originally developed for ground-based measurements using artificial light sources or scattered sunlight *(Solomon et al. 1987*, *Platt 1994)* but has successfully been adapted to nadir measurements from GOME (*Burrows et al. 1999* and references therein). Two main ideas form the basis of the DOAS approach (see also fig. 5-4).

- the isolation of the high frequency structures of molecular absorbers from broad band scattering features (Rayleigh, Mie) by a high pass filter,
- the separation of spectroscopic retrievals and radiative transfer calculations.

The first step of the data analysis consists of determining the total amount of absorption and scattering by dividing the Earthshine radiance by the direct solar irradiance. The latter provides the absorption free background. The molecular absorption cross section together with a polynomial is then fitted to the logarithm of this ratio, yielding the trace gas concentration along the light path (*slant column concentration*). Fig. 5-5 depicts a typical fit for NO2.

Finally, the average light path through the atmosphere is calculated using a radiative transfer model. The light path is often expressed as airmass factor which is the light path enhancement factor relative to a vertical transection of the atmosphere. Based on the AMF the vertical column concentration of the absorber may finally be calculated. Obviously clouds drastically modify the light path through the atmosphere and need to be properly taken into account when calculating the AMF (see chapter 5.3). The most important cloud parameter is the cloud fraction, as fractional cloudiness blocks the light path to atmospheric layers below the cloud. Using the DOAS algorithm, atmospheric columns of a number of species can be determined, including O3, NO2, SO2, HCHO, BrO, and OClO *(Burrows et al. 1999, Borell et al. 2003)*.

fig. 5-4:

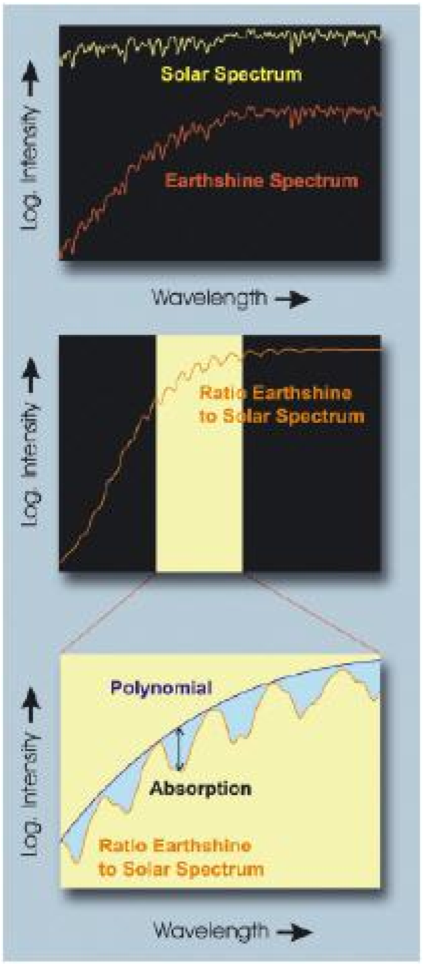

The main steps of the DOAS retrieval. For further details see the text. (graphics: IUP-IFE, University of Bremen)

fig. 5-5:

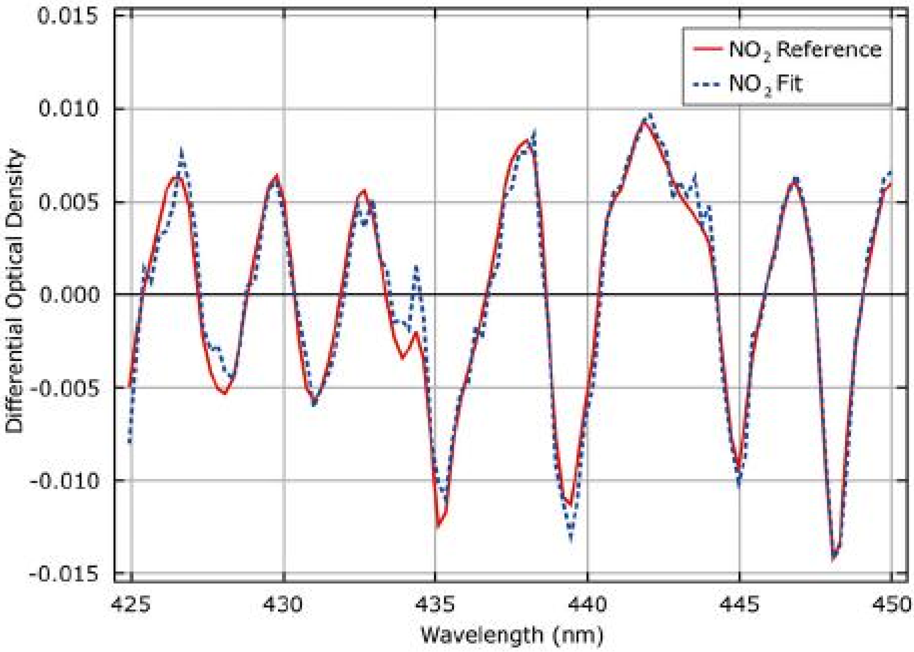

Typical SCIAMACHY NO2 fit results from a measurement over a polluted area in China on January 15th, 2006. The red line is the scaled NO2 laboratory cross-section, the dashed blue line the result of the fit after subtraction of all contributions with the exception of NO2. (graphics: IUP-IFE, University of Bremen)

One limitation of the classical DOAS technique is the assumption that the atmosphere is optically thin in the wavelength region of interest. In addition, 'line-absorbers' such as H2O, O2, CO, CO2 and CH4 usually cannot be retrieved precisely by standard DOAS algorithms because their strong absorption also depends on pressure, temperature and wavelength and in addition their spectra are often not fully spectrally resolved by SCIAMACHY. To overcome these drawbacks several DOAS-type techniques were developed to account for such effects and to permit successful retrievals of the trace gas species. They are for example the WFM-DOAS *(Buchwitz et al. 2000*, *de Beek et al. 2006)*, AMC-DOAS *(Noël et al. 2004)*, TOSOMI *(Eskes et al. 2005)*, SDOAS *(Van Roozendael et al. 2006)*, IMAP *(Frankenberg et al. 2005a, 2005b)* and IMLM *(Houweling et al. 2005)*. Figure 5-6 illustrates an example of one day of ozone columns derived from nadir observations with one of these schemes, the TOSOMI algorithm. Table 5-1 summarises the DOAS-type retrieval algorithms as applied to SCIAMACHY data and references to it. (fig. 5-6), (table 5-1)

fig. 5-6:

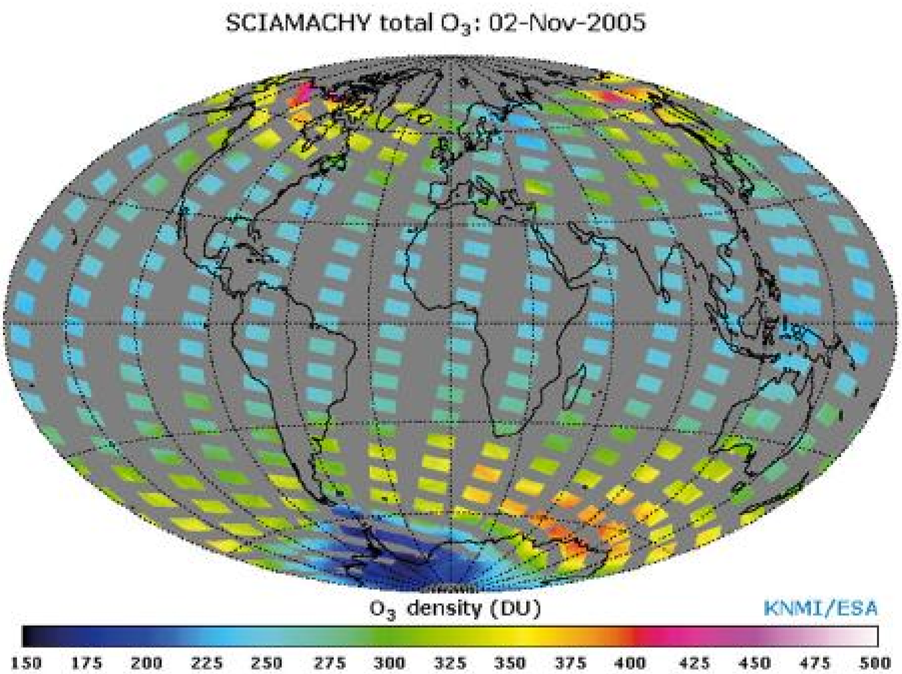

One day of total ozone densities obtained with the TOSOMI algorithm. (image: KNMI/ESA)

Parameter	*Spectral Window*	*Layer*	*Quantity*	*Retrieval Algorithm*	*Retrieval Algorithm Reference*

	(nm)		*(column)*		
O3	325 335	troposphere, stratosphere	total	operationalWFM-DOASTOSOMISDOAS	*Spurr 2000 Weber et al. 2005 Eskes et al. 2005 Van Roozendael et al. 2006*
NO2	425-450	troposphere, stratosphere	total, tropospheric	operational DOAS SDOAS	*Spurr 2000 Richter et al. 2005 Van Roozendael et al. 2006*
BrO	335-347(55)	troposphere, stratosphere	total	DOAS	
SO2	315-327	troposphere	total	DOAS	
HCHO	335-347(55)	troposphere	total	DOAS	
OClO	365-389	stratosphere	total	DOAS	
H2O	688-700	troposphere	total	AMC-DOAS	*Noel et al. 2004*
CO	2321(24)-2335	troposphere	total	WFM-DOAS IMLMIMAP	*de Beek et al. 2006 de Laat et al. 2006 Frankenberg et al. 2005b*
CH4	1627(30)-1671	troposphere	total	WFM-DOAS IMLMIMAP	*de Beek et al. 2006 Gloudemans et al. 2005 Frankenberg et al. 2005a*
CO2	1558(63)-1594(85)	troposphere	total	WFM-DOAS IMLMIMAP	*de Beek et al. 2006 Houweling et al. 2005 Frankenberg et al. 2005a*

Table 5-1: Atmospheric geophysical parameters and retrieval algorithms – nadir trace gases.

Parameter	*Spectral Window (nm)*	*Layer*	*Quantity (column)*	*Retrieval Algorithm*	*Retrieval Algorithm Reference*
O3	325 335	troposphere, stratosphere	total	operationalWFM-DOASTOSOMISDOAS	*Spurr 2000 Weber et al. 2005 Eskes et al. 2005 Van Roozendael et al. 2006*
NO2	425-450	troposphere, stratosphere	total, tropospheric	operational DOAS SDOAS	*Spurr 2000 Richter et al. 2005 Van Roozendael et al. 2006*
BrO	335-347(55)	troposphere, stratosphere	total	DOAS	
SO2	315-327	troposphere	total	DOAS	
HCHO	335-347(55)	troposphere	total	DOAS	
OClO	365-389	stratosphere	total	DOAS	
H2O	688-700	troposphere	total	AMC-DOAS	*No l et al. 2004*
CO	2321(24)-2335	troposphere	total	WFM-DOAS IMLMIMAP	*de Beek et al. 2006 de Laat et al. 2006 Frankenberg et al. 2005b*
CH4	1627(30)-1671	troposphere	total	WFM-DOAS IMLMIMAP	*de Beek et al. 2006 Gloudemans et al. 2005 Frankenberg et al. 2005a*
CO2	1558(63)-1594(85)	troposphere	total	WFM-DOAS IMLMIMAP	*de Beek et al. 2006 Houweling et al. 2005 Frankenberg et al. 2005a*

Table 5-1: Atmospheric geophysical parameters and retrieval algorithms – nadir trace gases.

5.3 Cloud and Aerosol Parameter Retrieval

The primary scientific objective of SCIAMACHY is the measurement of atmospheric trace gases in both the troposphere and stratosphere. However, clouds residing in the troposphere do interfere with the retrievals from SCIAMACHY measurements mainly by the shielding and albedo effects. Similarly, tropospheric and/or stratospheric aerosol interferes with the trace gas retrieval, as it alters the light path. Therefore, there is a clear need for cloud and aerosol information. In addition, cloud information from SCIAMACHY will also provide relevant data for cloud research.

In the UV, VIS and NIR spectral regions the solar radiation is strongly scattered by clouds and aerosol, thereby modifying the Earth reflectance spectrum. The presence of clouds and aerosol and their properties can therefore be determined by analysing the top-of-atmosphere reflection function R. It is defined as (equ. 5-6)

$$R = \pi \frac{I_{dif}}{\mu_0 I_{irr}}$$

where μ_0 is the cosine of the solar zenith angle, I_{irr} is the solar irradiance and I_{dif} is the scattered and reflected light in the direction towards the satellite sensor.

Prerequisites for high quality information about aerosol and clouds are high spatial resolution and high calibration accuracy of the reflectance measurements. Typical reflectance spectra for various cloud and surface conditions are shown in fig. 5-7. Various algorithms are required to determine cloud and aerosol properties from SCIAMACHY data. For a summary the reader is referred to table 5-2.

fig. 5-7:

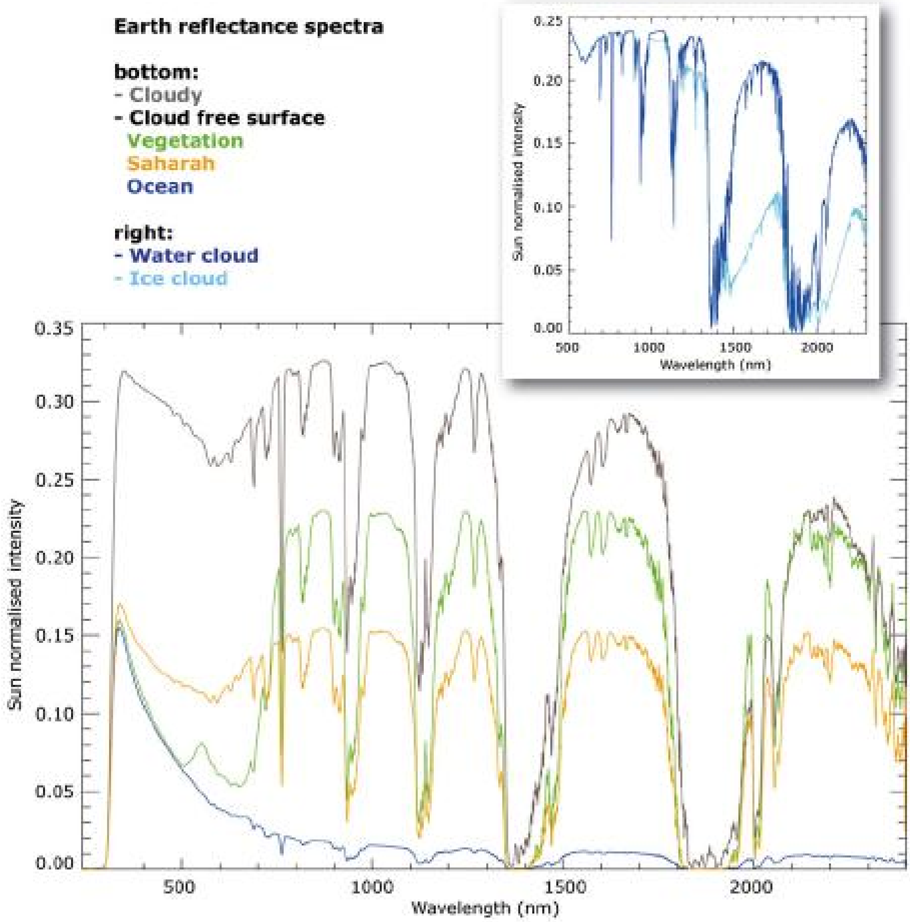

Earth reflectance spectra (sun normalised intensity) for various cloud and surface conditions. The inset shows the variation in the reflectance spectrum due to changes in the thermodynamic state of water from liquid water to ice. The large difference in the reflectance spectrum around 1600 nm is used to derive information on the thermodynamical state of water in clouds. (Graphics: IUP-IFE, University of Bremen)

Parameter	*Spectral Window (nm)*	*Retrieval Algorithm*	*Retrieval Algorithm Reference*
CF	PMD (RGB)	OCRA HICRUSPCASPICI	*Loyola 1998 Grzegorski et al. 2004 Yan 2005 Krijger et al. 2005*
	reflectance near O2 A-band	FRESCO SACURA	*Fournier et al. 2006 Kokhanovsky et al. 2005*
CTH	O2 A-band	FRESCOSACURA	*Fournier et al. 2006 Kokhanovsky et al. 2005, 2006*
COT	reflectance VIS-NIR	SACURA	*Kokhanovsky et al. 2005, 2006*
CGT	O2 A-band	SACURA	*Kokhanovsky and Rozanov 2005*
Reff,cld	reflectance VIS-NIR	SACURA	*Kokhanovsky et al. 2005, 2006*
CTP	reflectance NIR-SWIR	SACURA	*Kokhanovsky et al. 2005, 2006 Acarreta et al. 2004b*
AAI	340 and 380		*de Graaf and Stammes 2005*
AOT	several wavelengths in the VIS	SCIA-BAER	*von Hoyningen-Huene et al. 2003, 2006*
Aerosol type	several wavelengths, combination with AATSR	SYNAER	*Holzer-Popp et al. 2002a*

Table 5-2: Atmospheric geophysical parameters and retrieval algorithms – nadir cloud and aerosol parameters.

Cloud Parameters

5.3.1 Cloud Parameters

For SCIAMACHY information on cloud parameters are of twofold importance. Firstly, cloud parameters such as cloud fraction, top pressure (or height), and optical thickness (albedo) are required to correct the cloud impact on the trace gas concentrations. Secondly, due to its wide spectral range and despite its relatively low spatial resolution, SCIAMACHY data enables determination of important parameters for climate research like thermodynamic phase or geometrical thickness.

Cloud Fraction (CF): In order to correct for the effect of clouds, a fast and reliable cloud fraction algorithm is required for SCIAMACHY. Nearly all cloud fraction algorithms for SCIAMACHY use the PMD measurements, as their higher temporal readout frequency translates into a higher spatial resolution as compared to data from channel 1 to 8. The basic principle of the algorithms is that cloud albedo is much higher than the Earth’s surface albedo (see fig. 5-8). Therefore, a pixel that is contaminated by clouds will have a higher detector signal than one that is cloud free. Cloud fractions can therefore be determined through comparison of PMD intensities. Several derivates of cloud fraction algorithms using PMD data are currently applied to SCIAMACHY data, such as the Optical Cloud Recognition Algorithm (OCRA, *Loyola et al. 1998*) used in the operational processing, the SCIAMACHY PMD Cloud Algorithm (SPCA, *Yan 2005*), the Heidelberg Iterative Cloud Retrieval Utilities (HICRU, *Grzegorski et al. 2004*) or the SCIAMACHY PMD Identification of Clouds and Ice/snow (SPICI, *Krijger et al. 2005*). (fig. 5-8)

fig. 5-8:

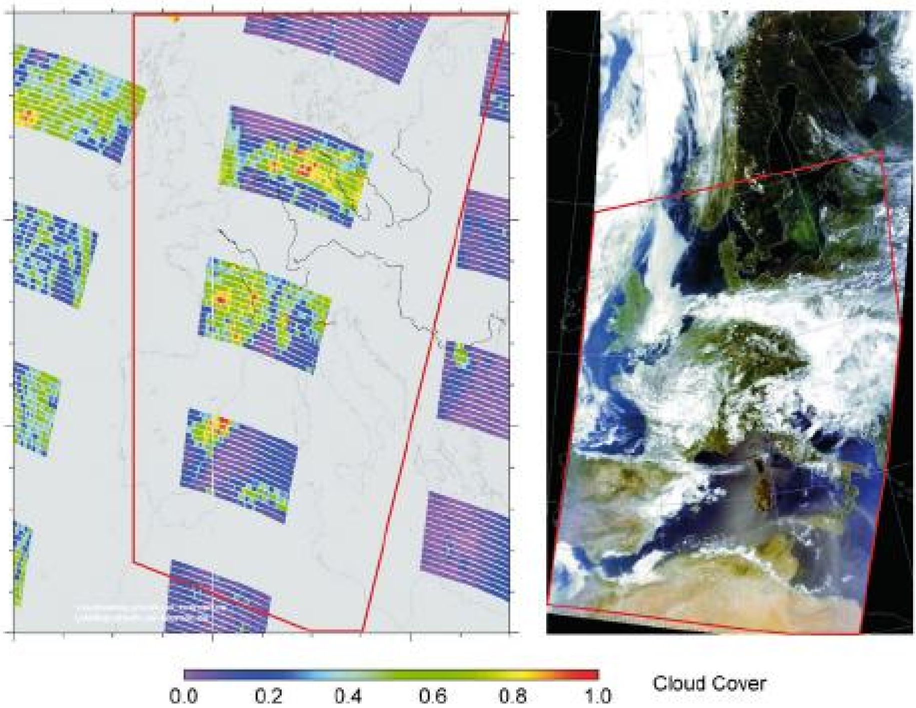

Clouds over Europe on July 9th, 2005. Cloud coverage as seen in a RGB composite (right) from MODIS on-board TERRA and cloud fraction (left) determined with OCRA using SCIAMACHY PMD data (images: IUP-IFE, University of Bremen and Dundee Satellite. Receiving Station)

Cloud Top Height (CTH): CTH can be estimated from measurements in the solar backscatter spectral ranges by using the changes in the penetration depth of solar photons due to strong changes in the absorption of trace gases with known vertical distributions such as O2 (see fig. 5-9). The idea for the CTH retrieval from O2 A-band absorption was originally proposed by *Yamomoto and Wark (1961)*.

For SCIAMACHY two algorithms are currently implemented to derive cloud top height from O2 A-band measurements. These are the Fast Retrieval Scheme for Clouds from the Oxygen A-band *(*FRESCO, *Koelemeijer et al. 2001*, *Fournier et al. 2006)* and the Semi-Analytical Cloud Retrieval Algorithm *(*SACURA, *Rozanov and Kokhanovsky 2004)*. It is worth mentioning that in addition to the O2 A-band, there is also the option to derive CTH information from the O2-O2 absorption *(Acarreta et al. 2004a)* or the Ring effect *(Joiner et al. 1995, de Beek et al. 2001)*. (fig. 5-9)

fig. 5-9:

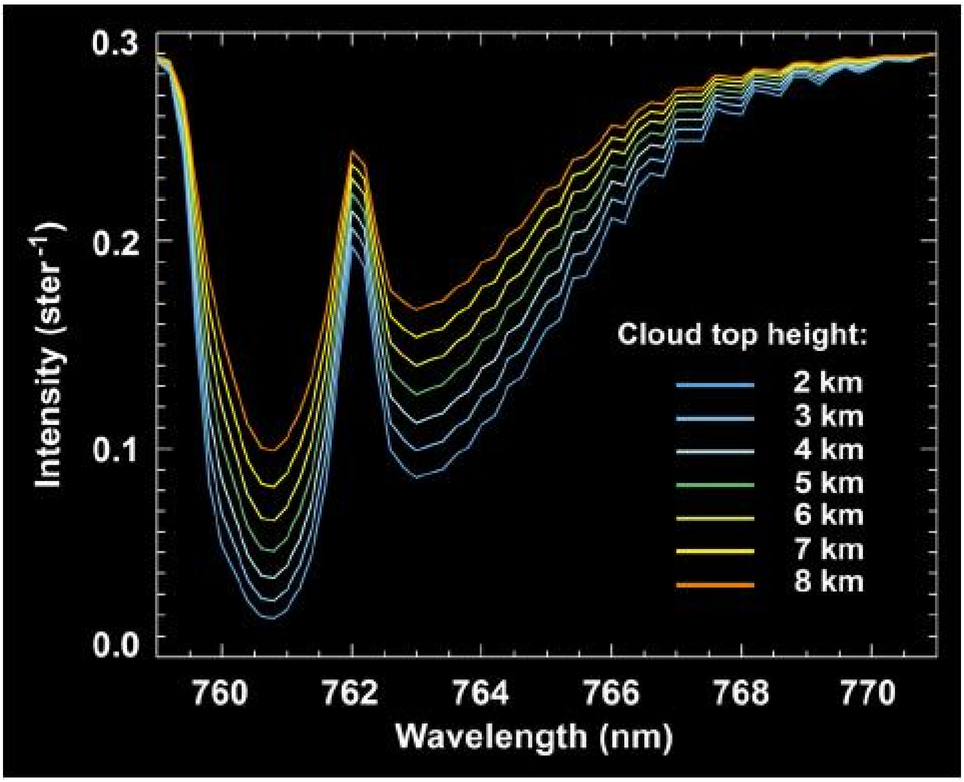

The top-of-atmosphere reflectance in the O2 A-band as a function of cloud top height. (Graphics: IUP-IFE, University of Bremen)

Cloud Geometrical Thickness (CGT): O2 A-band absorption can also be used to obtain an estimate of the CGT *(Asano et al. 1995)*. The CGT values represent an estimate of the light absorption inside a cloud and are therefore suited reducing uncertainties in the cloud top altitude measurements. This method was applied to SCIAMACHY data by *Kokhanovsky and Rozanov (2005)*.

Cloud Optical Thickness (COT) and Effective Radius (Reff,cld): Measurements of the Earth reflectance spectrum in the VIS or NIR range outside strong gaseous absorption bands permit derivation of the COT and Effective Radius *(Nakajima and King 1990, Platnick et al. 2003*). *Kokhanovsky et al. (2005, 2006)* applied the method to SCIAMACHY data. In the case COT and Reff,cld are known for a liquid water cloud, the liquid water path can be estimated.

Cloud Phase Index(CPI): SWIR reflectance measurements are also suitable for obtaining the cloud phase index CPI *(Knap et al. 2002, Acarreta et al. 2004b, Kokhanovsky et al. 2005, 2006)*, as the dependence of the single scattering albedo on the particle size is different for liquid water and ice.

In the GOME/SCIAMACHY data processing environment mainly two cloud retrieval algorithms are exploited. One is FRESCO, which uses measurements inside and outside the O2 A-band (758-778 nm). FRESCO is developed for cloud correction of trace gas retrievals, like O3 and NO2. It simultaneously retrieves an effective Cloud Fraction (CFeff) and an effective Cloud Top Height (CTHeff) assuming that the cloud can be represented as a bright Lambertian surface with a fixed albedo value of 0.8. The second cloud algorithm employed in the operational processing is the combination of OCRA with SACURA. OCRA delivers cloud fraction as input for SACURA to determine CTH and COT. In addition to that, an improved version of SACURA delivers cloud geometrical thickness, effective radius and the cloud thermodynamical state *(Kokhanovsky et al. 2005, 2006)*.

5.3.2 Tropospheric Aerosol Parameters

Aerosols are characterised by high spatial or temporal variability and a mixture of chemically and physically different particles, dependent on their origin *(Pöschl 2005)*. Detection of aerosol by spaceborne instruments utilise their effect on the reflected solar radiation observed at the top of the atmosphere. Contributions from Earth's surface reflections (see fig. 5-7) and atmospheric gases (see fig. 5-3) need to be separated using available information on the surface properties and the effects of gases. Thus the signatures of aerosols can be derived and can be used to retrieve aerosol properties.

Most of currently existing aerosol retrieval algorithms are aimed to determine the Aerosol Optical Thickness (AOT), i.e. columnar extinction by aerosol particles and their spectral behaviour. All higher level aerosol parameters (aerosol concentration, effective radius and others) can be derived from the magnitude and the spectral behaviour of the AOT. Thus, the spectral AOT may be regarded as the key parameter concerning retrieval of other aerosol properties. It is extracted by fitting modelled reflectance spectra to the measured reflectance spectra. This approach needs careful constraints based on the knowledge on molecular scattering, absorption and the surface reflectance *(von Hoyningen-Huene et al. 2003)*. The first application to SCIAMACHY data is found in von *Hoyningen-Huene et al. (2006)*.

From UV wavelengths below 400 nm the Absorbing Aerosol Index (AAI) can be derived. The AAI indicates the presence of absorbing aerosol, mainly caused by strong events like Sahara dust outflows or biomass burning (see fig. 5-10). Initially developed as an error indicator for ozone retrieved from TOMS data *(Herman et al. 1997)*, the AAI is the aerosol quantity with the longest data record. The AAI is derived as the residual between the measured reflectance from an atmosphere enriched with aerosols and the simulated reflectance of an atmosphere with only Rayleigh scattering, absorption by molecules, plus surface reflection and absorption *(de Graaf and Stammes 2005)*. Such an algorithm using SCIAMACHY data at 340 nm and 380 nm delivers meaningful AAI values, in case properly calibrated spectra are used *(de Graaf and Stammes 2005)*.

fig. 5-10:

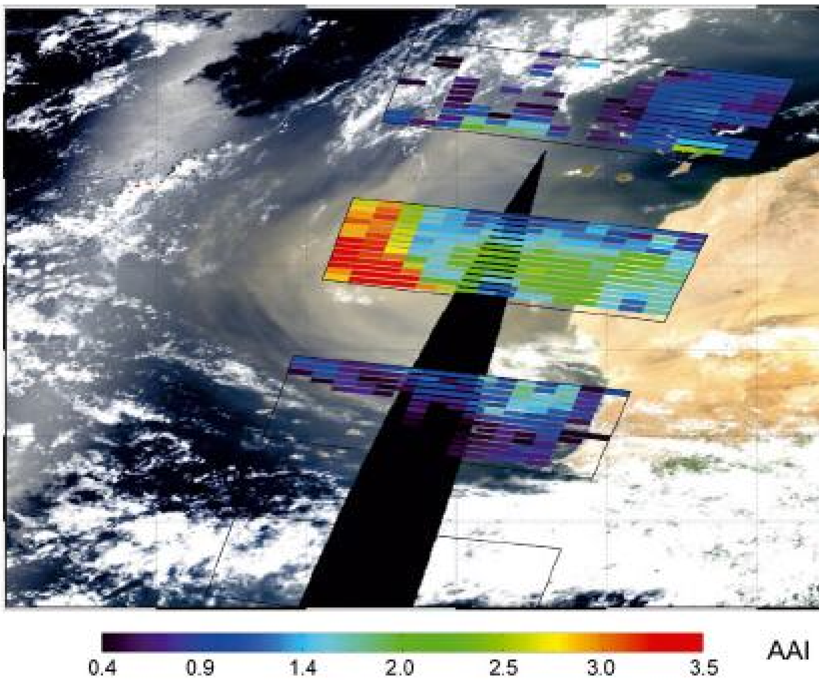

Saharan desert dust outbreak to the Atlantic on July 25th, 2004. Shown are the SCIAMACHY AAI at 9:15 UTC of that day overlaid on a MODIS RGB picture, acquired around 11:10 UTC (right side of the plot) and 12:50 UTC (left side of the plot). High SCIAMACHY AAI values coincide with the dust plume, visible as a yellow haze on the MODIS image. (Image: M. de Graaf, KNMI)

The combination of SCIAMACHY spectral information with data from high resolution images from AATSR on ENVISAT will enable the derivation of the aerosol type information, beside the AOT. The synergistic method SYNAER *(Holzer-Popp et al. 2002a, 2002b)* can be applied toexploit SCIAMACHY together with AATSR to derive aerosol type information.

5.4 Profile Retrieval

5.4.1 Inversion Theory

The forward modelling described earlier in chapter 5.1 is commonly employed to simulate a measured quantity, e.g., intensity of the radiation, for a predefined state of the atmosphere. Contrary to this, the objective of inversion problems is to retrieve certain characteristics of the atmospheric state – for example trace gas concentration profiles – based on the measured quantities. These can be for example the solar radiance transmitted through the Earth’s atmosphere in the occultation geometry or the radiance scattered by the Earth’s atmosphere or reflected by the surface in the limb or nadir geometry.

The parameters to be retrieved from the measurements are represented by a *model state vector x*. For example, for trace gas vertical profile retrieval, the model state vector contains the number densities of atmospheric constituents defined at discrete altitude levels.

Each state vector can be mapped to the measurement space by means of the forward model operator *F* to obtain the corresponding measurement vector *y*, i.e., for each atmospheric state described by vector *x* an appropriate measured quantity *y* can be simulated using a radiative transfer model as the forward model (see fig. 5-11).

fig. 5-11:

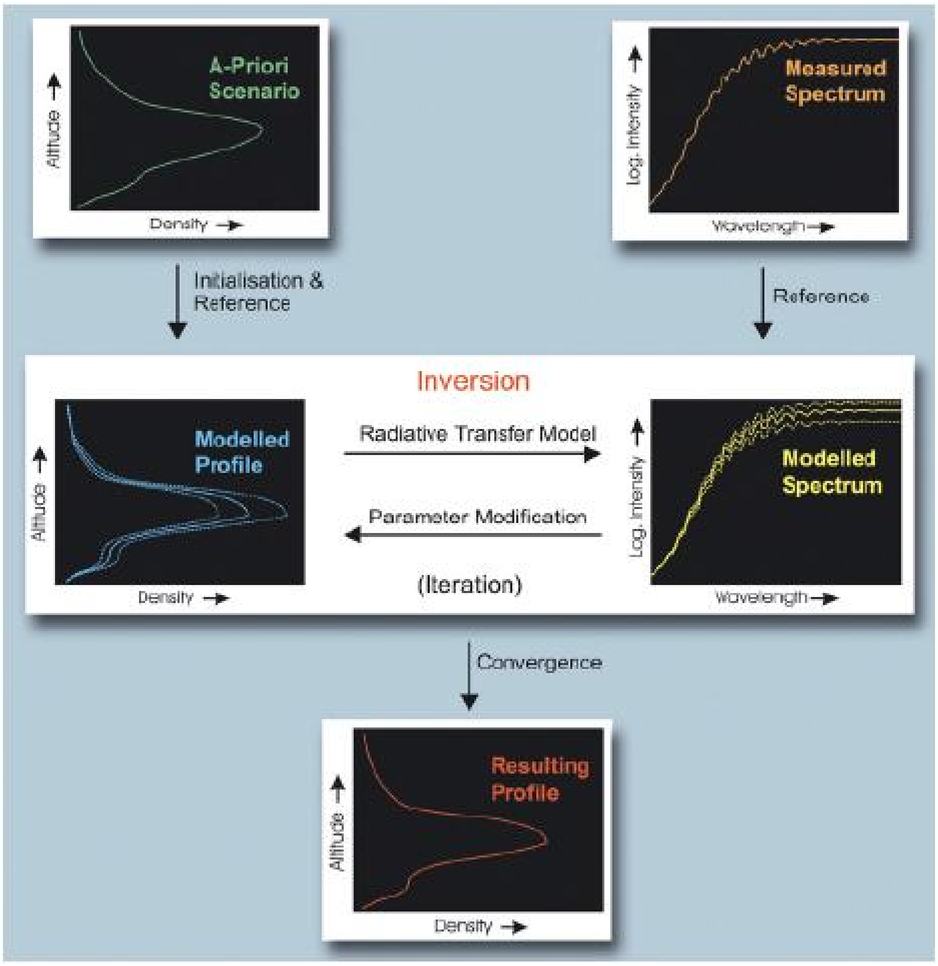

The principle of inversion for the retrieval of geophysical parameters. For further details see the text. (Graphics: IUP-IFE, University of Bremen)

In the case of SCIAMACHY occultation or limb measurements, the measured quantities are represented by a set of intensities measured at different tangent heights in selected spectral windows. Taking into account that measurements are made to a finite accuracy, a measurement error*e* has to be considered which is commonly assumed to be normally distributed with mean zero and known error covariance matrix *Sy*. Thus, the relationship between the model state vector and the measurement vector can be written as (equ. 5-7)

$$y = F(x) + \varepsilon$$

In order to solve the inverse problem, this non-linear relationship in equ. 5-7 has to be linearised expanding the forward model operator, *F,* as a Taylor series about a guessed value *x0* of the solution. Ignoring the higher-order terms one obtains (equ. 5-8)

$$F(\boldsymbol{x}) \approx F(\boldsymbol{x}_0) + \frac{\partial F}{\partial \boldsymbol{x}}\bigg|_{x_0} (\boldsymbol{x} - \boldsymbol{x}_0) = \boldsymbol{y}_0 + \boldsymbol{K}_0 (\boldsymbol{x} - \boldsymbol{x}_0)$$

Here, *K0* is the linearised forward model operator. In the discrete representation the linearised forward model operator is given by the weighting function matrix describing the sensitivity of the measured quantities to the variation of the atmospheric parameters at different altitude levels. This weighting function matrix is calculated with the radiative transfer model.
Atmospheric inversion problems are commonly ‘ill-posed’. Thus, additional constraints need to be introduced to determine a geophysical solution from the set of mathematically allowed solutions. Most commonly, the methods of statistical regularisation, as described e.g. by *Rodgers (2000)* are applied, i.e., the maximum likelihood condition, a priori value of the solution, *x0*, and its covariance matrix, *Sa*, are employed to solve the inversion problem. In this case the solution is found by minimising the following quadratic form (equ. 5-9)

$$\left\| (\boldsymbol{y} - \boldsymbol{y}_0) - \boldsymbol{K}_0 (\boldsymbol{x} - \boldsymbol{x}_0) \right\|^2_{S_y^{-1}} + \left\| \boldsymbol{x} - \boldsymbol{x}_0 \right\|^2_{S_a^{-1}} \rightarrow \boldsymbol{min}$$

This results in (equ. 5-10)

$$x_{n+1} = x_0 + \left(S_a^{-1} + K_n^T S_y^{-1} K_n\right)^{-1} K_n^T S_y^{-1} \left[(y - y_n) - K_n(x_0 - x_n)\right]$$

where subscripts *n* and *n+1* denote the number of the iteration. The measurement error covariance matrix, *Sy*, is usually assumed to be diagonal, i.e. no correlation between measurement errors at different wavelengths or different tangent heights is considered. In the retrieval of the vertical distributions of the atmospheric species the *a priori* covariance matrix, *Sa*, is commonly chosen as a block diagonal matrix, i.e. vertical distributions of different atmospheric trace gases are assumed to be uncorrelated. The diagonal elements of *Sa* represent the variances of the vertical distribution of atmospheric trace gases, *s*, which e.g. can be derived from a climatology.
The quality of the obtained solution is characterised by the *a posteriori* covariance matrix (equ. 5-11)

$$S = \left(K^T S_y^{-1} K + S_a^{-1}\right)^{-1}$$

and by the averaging kernels (equ. 5-12)

$$A = \frac{\partial x}{\partial x_{true}} = \left(K^T S_y^{-1} K + S_a^{-1}\right)^{-1} K^T S_y^{-1} K$$

characterising the response of the retrieved solution to the variation of the true atmospheric state. The root squares of the diagonal elements of the *a posteriori* covariance matrix are referenced to as the theoretical precisions.
Employing the averaging kernels, the retrieved solution, *x*, can be related to the true solution, *xtrue* as (equ. 5-13)

$$x = x_0 + A\left(x_{true} - x_0\right)$$

i.e., if the model state vector represents a vertical profile of an atmospheric trace gas, the retrieved values at each altitude are expressed as the sum of the *a priori* value at this altitude and of the deviation of the true profile from an a priori profile smoothed with the associated row of the averaging kernel matrix. For an ideal observing system, *A* is a unit matrix. In reality, the rows of the averaging kernel matrix are peaked with a finite width, which can be regarded as a measure of the vertical resolution of the retrieved profile.

5.4.2 Application of Inversion Theory to Limb Retrieval

For the retrieval of the vertical distributions of atmospheric species from the measurements performed by SCIAMACHY the so called *Global Fit* technique is an effective way of implementing the inversion. The measurement vector contains the logarithms of the radiances in all selected spectral points and at all line-of-sights, both for limb and occultation geometry, referenced to an appropriate irradiance spectrum.

In the limb viewing geometry, the irradiance spectrum can be replaced by a limb measurement at an upper tangent height. Due to this normalisation the retrieval is relatively robust with respect to the radiometric calibration. In addition, the normalisation significantly reduces the sensitivity of the retrievals with respect to ground albedo and cloud cover. Commonly, before the main inversion step, a pre-processing is performed intended to correct for possible misalignment in the wavelength calibration and account for known atmospheric corrections such as the Ring effect. If required, a polynomial can be subtracted from all relevant spectra involved, accounting for both missing or inappropriate instrument calibration and unknown scattering properties of the atmosphere.

To illustrate the limb inversion in practice, fig. 5-12 shows an example of averaging kernels, weighting functions at 338.6 nm, and theoretical precision typical for BrO vertical profile retrieval from SCIAMACHY limb measurements. These results were obtained using the limb measurement at a tangent height of 38.5 km as a reference spectrum. As can be seen in the figure, the peak values of the averaging kernels are close to 1.0 only at tangent heights above 15 km. The peak value of about 0.55 at 12 km altitude indicates an increased dependence of the retrieved BrO amount at this altitude on BrO amount at neighbouring altitude levels and *a priori* information. Looking at the width of the averaging kernels, the height resolution of the measurements can be estimated to about 3 km, close to the geometrical resolution of the instrument. The weighting functions in the middle panel exhibit relatively sharp peaks near the tangent height down to 18 km tangent height, whereas at all lower tangent heights the weighting functions peak at about 18 km altitude. Nevertheless, the BrO amounts down to 12 km can be retrieved due to different shapes of the corresponding weighting functions. In accordance with the averaging kernels, the theoretical precision of the BrO vertical profile retrieval shown in the left panel has reasonable values of 10-40% only above 14 km altitude and rapidly decreases below indicating the low information content in the measurements below 14 km. (fig. 5-12)

fig. 5-12:

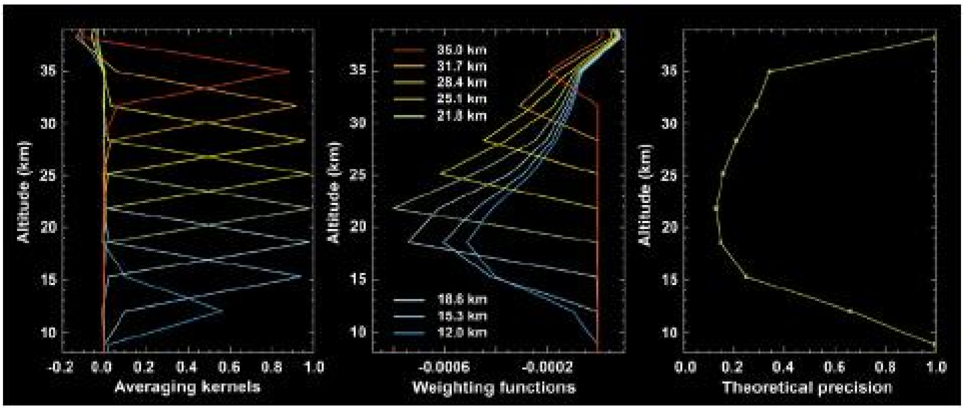

Averaging kernels (left), weighting functions at 338.6 nm (middle), and theoretical precision (right) for BrO vertical profile retrievals from SCIAMACHY limb measurements. (graphics: IUP-IFE, University of Bremen)

To date, such type of retrieval algorithm and associated derivates has been used to obtain stratospheric profiles of O_3, NO_2 *(Bracher et al. 2005*, *Sioris et al. 2004)* and BrO *(Rozanov et al. 2005b)* from SCIAMACHY limb scattering profiles. This type of inversion algorithm was also applied and used to derive trace gas concentrations from lunar *(Amekudzi et al. 2005a, 2005b)* and solar occultation *(Meyer et al. 2005)* measurements. It is interesting to note that a similar approach as described above can also be applied to retrieve trace gas information from nadir measurements, as for example demonstrated for the Ozone profile retrieval from GOME nadir measurements *(Munro et al. 1998*, *Hoogen et al. 1999)*.

All the applications listed above use a continuous spectral range to derive the trace gas information. Another group of limb inversion algorithms employs discrete spectral points in and outside strong trace gas absorption bands for the retrieval of vertical profiles. Retrieval algorithms utilising the difference in absorption between the centre and wings of the ozone Chappuis and Huggins bands were devised by *Flittner et al. (2000).* In a first step the limb radiance profiles are normalised with respect to a reference tangent height between 40 and 45 km. For the SCIAMACHY O_3 Chappuis band retrieval *(von Savigny et al. 2005a)*, the normalised limb radiance profiles are divided by the limb radiance profile at a non-absorbing wavelength and then analysed in an optimal estimation scheme to retrieve the stratospheric O_3 profiles. Retrievals in the O_3 Chappuis band allow extraction of stratospheric O_3 profiles for altitudes between about 12-14 and 40 km.

The retrieval range is limited at lower altitudes because the atmosphere becomes optically thick with respect to Rayleigh scattering and/or O3 absorption. Above about 40 km the O3 absorption signatures become too weak to be observed. However, normalised limb radiance profiles in the O3 Hartley and Huggins bands can also be used without further wavelength pairing for the derivation of ozone profiles in the upper stratosphere and lower mesosphere *(Rohen et al. 2006)*. The O3 retrievals may be extended up to at least 65 km since the absorption cross sections in the Hartley and Huggins bands are significantly larger than in the Chappuis band.
The wide variety of retrieval algorithms currently applied to SCIAMACHY limb and occultation data are summarised in table 5-3, together with their corresponding references.

Parameter	***Spectral Window (nm)***	***Layer***	***Quantity***	***Retrieval Algorithm Reference***
O3	525, 600, 675525-590	stratosphere	profile	*von Savigny et al. 2005 a Doicu et al. 2002, Doicu 2005*
	240-310 (selected wavelengths)	mesosphere	profile	*Rohen et al. 2006*
	520-595	stratosphere	profile sun occultation	*Meyer et al. 2005*
	510-560	stratosphere	profile moon occultation	*Amekudzi et al. 2005a*
NO2	425-450(70)	stratosphere	profile limb	*Rozanov et al. 2005 b Sioris et al. 2004 Doicu et al. 2002, Doicu 2005*
	420-460	stratosphere	profile sun occultation	*Meyer et al. 2005*
	430-460	stratosphere	profile moon occultation	*Amekudzi et al. 2005a*
NO3	610-680	stratosphere	profile moon occultation	*Amekudzi et al. 2005b*
BrO	335-360	stratosphere	profile	*Rozanov et al. 2005 b Dorf et al. 2005*
OClO	365-389	stratosphere	profile	
NLC	265-300	mesosphere	indicator, particle radius	*von Savigny et al. 2004a*
PSC	750, 1090	stratosphere	indicator	*von Savigny et al. 2005b*
Tmesopause	1515-1550	mesosphere	nighttime temperature at mesopause	*von Savigny et al. 2004b*

Table 5-3: Atmospheric geophysical parameters and retrieval algorithms – limb and occultation.

5.5 Derivation of Tropospheric Information

Of major scientific – and public – interest are distributions of trace gases in the troposphere. Two cases need to be distinguished:

- Constituents with the majority of the atmospheric amount residing in the lower troposphere (e.g. CO, CH4, CO2, HCHO, SO2, H2O): The total column derived from UV-VIS and SWIR solar backscatter measurements with the techniques derived in chapter 5.2 directly represents the tropospheric column amount including the boundary layer under cloud free conditions.
- Trace gases with comparable column amounts in the troposphere and stratosphere (e.g. BrO, NO2) or with the stratospheric amount dominating the total column (e.g. O3): Additional techniques have to be applied to separate tropospheric and stratospheric concentrations.

For the latter case dedicated techniques are required to separate the tropospheric and the stratospheric concentrations. One approach is to use measurements over a clean air region as a background, the so-called *Reference Sector Method* (see below). In addition, SCIAMACHY's unique limb/nadir matching capabilities provide a nearly simultaneous stratospheric profile measurement for each nadir measurement. In that respect, SCIAMACHY is clearly superior to its predecessor GOME which obtained measurements of the same species in the UV-VIS range but only in nadir geometry.

5.5.1 Reference Sector Method

The Reference Sector Method, also referred to as *Tropospheric Residual Method (Velders et al. 2001*, *Richter and Burrows 2002*, *Martin et al. 2002)* allows the separation of tropospheric and stratospheric contributions to the total NO2 content under the assumption of a stable – both spatial and temporal – NO2 distribution over the clean, free Pacific Ocean. It is assumed that the stratospheric NO2 distribution is homogeneous with longitude. Then the tropospheric NO2 is primarily the difference between the total column measured over a polluted area and the total column measured over the clean Pacific Ocean. This technique needs no stratospheric profile information and can therefore be applied to generate a consistent GOME – SCIAMACHY tropospheric NO2 data set.

5.5.2 Limb/Nadir Matching

One important area of uncertainty in the determination of the tropospheric column concentration from solar backscatter nadir measurements is the error introduced by estimating the stratospheric column concentration *(Boersma et al. 2004)*. To improve on this topic, it is required to use the measured stratospheric column above the ground scene of interest. SCIAMACHY with its limb/nadir matching measurement mode provides radiances from the same volume of air in limb and nadir geometry since 2002. This allows inference of vertical stratospheric concentration profiles directly over the region of the nadir measurement. Integrating these profiles from the tropopause upwards yields the measured stratospheric column above the target area while the collocated nadir measurement provides the total column amount. The tropospheric column is then – very briefly speaking – determined as the difference between the total and the stratospheric column. An initial application of this approach to derive tropospheric NO2 was presented in *Sierk et al. (2006)*. The method described here is unique in the sense that the information on the stratospheric content is taken directly from the collocated limb measurement and no other assumptions (longitudinal homogeneity) or an estimate of the stratospheric column from a model or from data assimilation are necessary.

5.6 Data Assimilation and Value Added Products

Data assimilation generates synoptic trace gas fields from asynoptic spaceborne measurements. This enables the derivation of interpolated concentration fields, e.g. to separate tropospheric and stratospheric contributions, as well as information about transport mechanisms. Several assimilation schemes are applied to SCIAMACHY measurements to combine stratospheric modelling and nadir column data. They produce results usually referred to as *Value Added* products.

5.6.1 Tropospheric Trace Gases – the NO2 Example

NO2 permanently resides in the stratosphere and shows significant amounts in the troposphere near source areas. First, the stratospheric and tropospheric parts of the column need to be separated and subsequently, a tropospheric airmass factor needs to be applied to the tropospheric slant column. At KNMI, in collaboration with BIRA/IASB, a data assimilation system was applied to NO2 to derive the stratospheric part of the slant column by assimilation of observed slant columns in a chemistry-transport model *(Eskes et al. 2003)*. This results in a stratospheric analysis consistent with the observations as well as with variations observed in the stratosphere that are due to the atmospheric dynamics and chemical reactions. The tropospheric NO2 slant column is then extracted by subtracting the assimilated stratospheric slant column from the retrieved total slant column.

In a similar way the stratospheric NO2 slant column density, exactly for the SCIAMACHY overpass time, is derived from the stratospheric chemistry transport model ROSE at DLR-DFD. To avoid a bias, the modelled analyses are scaled to ‘clean conditions’ over the Pacific Ocean. The tropospheric NO2 slant column is then extracted by subtracting the modelled stratospheric slant column from the retrieved total slant column. Fig. 5-13 shows the resulting tropospheric NO2 distribution over Europe. The tropospheric NO2 distributions can be further improved by using NO2 profile shapes estimated by air quality models like EURAD. In this case also properties of clouds, aerosols and the surface have to be taken into account.

fig. 5-13:

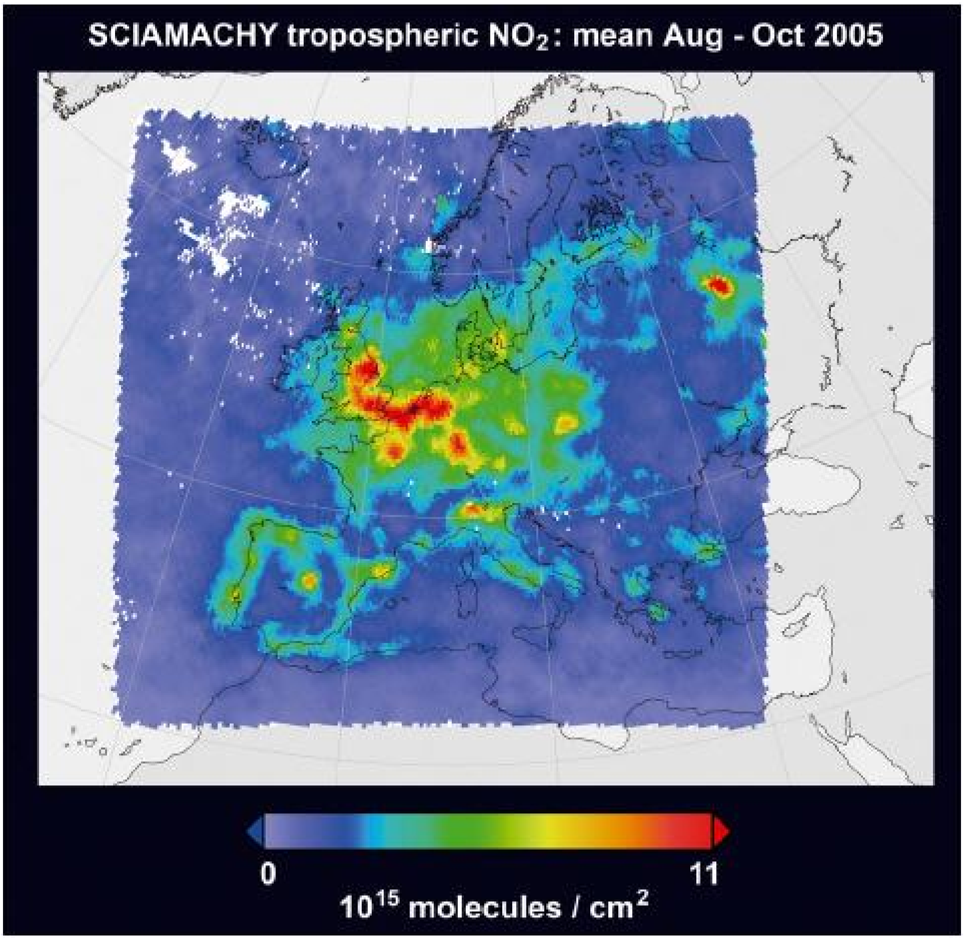

Mean tropospheric NO2 vertical column densities over Europe as derived from SCIAMACHY for August to October 2005 with the DLR-DFD assimilation approach. (Image: T. Erbertseder, DLR-DFD)

5.6.2 Stratospheric O3

Assimilated total column and stratospheric profile fields are ideally suited for applications such as scientific studies of the evolution of the ozone layer and of special events (e.g. ozone hole or low ozone episodes) or inter-comparisons with models (e.g. study of dynamical and chemical processes). Since assimilated fields are globally available, comparison with independent observations can be performed without space/time mismatches.

Stratospheric O3 is also of particular interest as it can be assimilated into operational weather forecasts and improves the model representation of stratospheric wind fields and thereby the quality of the forecast. Since forecast services are provided on short timescales, the availability of near-realtime O3 data is essential. Total columns of ozone can be derived from SCIAMACHY measured backscatter reflectivities in near-realtime (*Eskes et al. 2005*). These ozone columns serve as an input for the assimilation analysis and a subsequent forecast of how the stratospheric ozone layer will develop in the upcoming 9 days. The assimilation yields a complete picture of the global ozone distribution (see fig. 5-14). Within the error margins of both model and observations it is consistent with observations and our knowledge of atmospheric transport and chemistry *(Eskes et al. 2002, Eskes et al. 2003)*. SCIAMACHY ozone columns are currently also assimilated operationally in the numerical weather prediction model of the ECMWF. Several centres use the ozone forecasts for UV radiation predictions.

To further analyse and quantify atmospheric processes such as ozone depletion or ozone loss rates, an optimal combination of models and asynoptic or heterogeneously distributed observations is essential. By using for example the ROSE transport model, SCIAMACHY observations of O3, NO2, OClO and BrO can be assimilated in order to derive a consistent global chemical analysis of the stratosphere.

fig. 5-14:

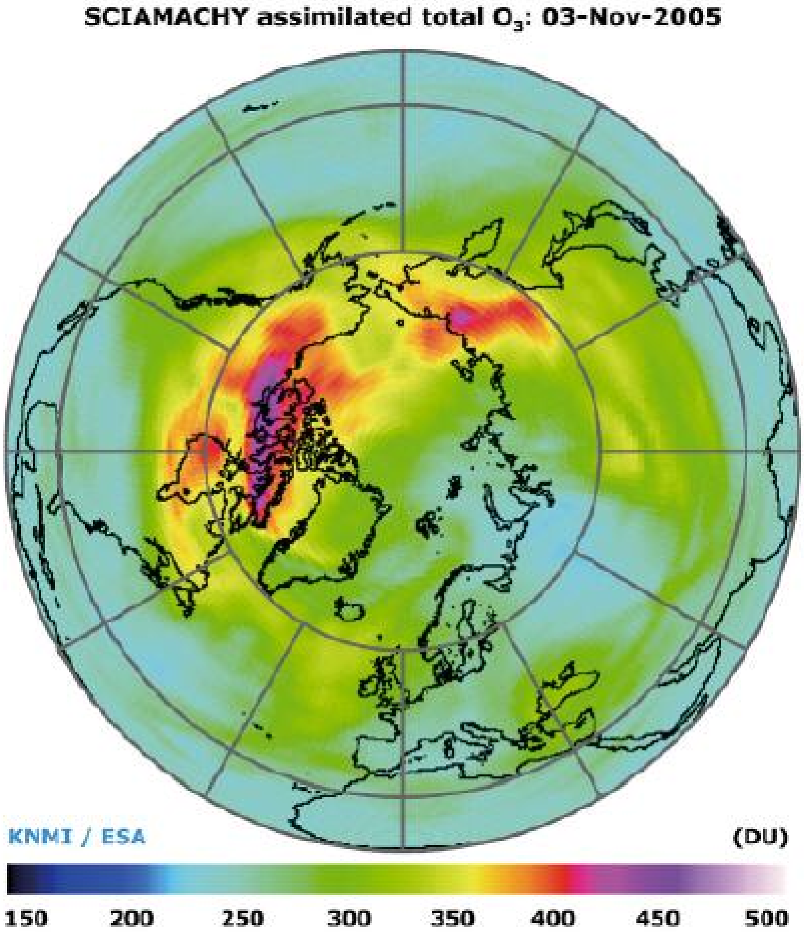

A forecasted North Pole view of the assimilated total ozone column field for November 3rd, 2005 at 12:00 UTC based on SCIAMACHY data. (Image: KNMI/ESA)

CHAPTER 6

6: SCIAMACHY Operational Data Products and Algorithms

The operational data processing follows the specific guidelines and rules of the ENVISAT Payload Data Segment (PDS) architecture and organisation. Scientific product generation is based on science groups' algorithms which have not been developed in the framework of the PDS.

The baseline for each higher level product is the level 1b product containing orbit wise geo-referenced measurements including their calibration and instrument monitoring data. Level 2 products are specifically dedicated to geophysical parameters including column densities, stratospheric profiles of atmospheric constituents and information about clouds and aerosols. Each day of SCIAMACHY operations generates 14 or 15 level 1b and level 2 products. With level 2, ENVISAT's responsibility for data generation, dissemination and archiving ends. This does not however, as outlined above, exclude experienced science users from processing their own scientific products of the same levels. It is up to the individual user how to specify and process value added (VA) products. In the VA environment, geophysical parameters are often gridded on a global scale, i.e. these products are well suited to provide the interested public with SCIAMACHY's view of the Earth atmosphere.

Basic processing related information is provided via the file names of the products, e.g.
SCI_NL__1PRDPA20061029_012353_000060442052_00275_24377_0673.N1
File names include the sequence

- product ID: SCI_NL__0P, SCI_NL__1P or SCI_OL__2P for level 0, 1b or 2 data (SCI_NL__1P)
- processing status flag: N for NRT (Near-realtime) products (this flag is no longer used, since we are in Phase F), letters between N and W for consolidated products (R, currently used Y)
- originator ID: PDK, PDE, LRA, D-P for PDHS-K, PDHS-E, LRAC or D-PAC (DPA)
- start date: year, month and day of measurement start (20061029)
- start time: hours, minutes and seconds of measurement start in UTC (012353)
- duration of product coverage in seconds (00006044)
- ENVISAT mission phase (2)
- ENVISAT cycle number (052)
- relative orbit number within cycle (00275)
- absolute orbit number at product start (24377)
- processing file counter (0673)
- file extension: N1 corresponds to ENVISAT

That permits an unambiguous allocation of the file to a particular measurement. All operational data products are subject to quality monitoring. The Payload Data Control Center (PDCC) does a processing control, while the main quality control is performed within ESA SPPA-IDEAS. Its goal is to screen all products at the time of generation in order to identify anomalies or deviations from expected results. Quality monitoring includes content and consistency checks, e.g. formal correctness of the product or parameter limits. In case of detected anomalies, data shall be flagged to initiate further actions. The SPPA executes quality monitoring activities on various timescales ranging from daily to multi-monthly.

6.1 Level 0 Products

A level 0 product contains all measurement data for one complete orbit in the case of consolidated products. The difference to the raw data as sent down to the ground station is that level 0 data are time ordered and already have data headers which describe the data. Usually users do not need level 0 products, since level 1b data contain the same data with the addition of the geolocation and calibration data. Level 0 data are *not* distributed operationally.

6.2 Operational Level 1b Products and Algorithms

6.2.1 Level 1b Processor

SCIAMACHY level 1 data products comprise geolocated and calibrated radiances of the scientific measurements, as well as measurements for calibration and instrument monitoring.

The algorithms used in operational level 0 to 1 processing are primarily driven by the scientific needs to convert measured signals into calibrated radiances (see following section). However, constraints imposed by the instrument operation, and in particular constraints imposed by the operational data processing environment, may force one to take different strategies as one would employ for a ground-based instrument. The wish to obtain a level 1 data product which is not excessively large and complicated imposes an additional constraint. The principle processing cycle starting with instrument level 0 data and ending with the level 2 product is outlined in figure 6-1. A major constraint from the ENVISAT PDS architecture rules is that there may be only one output product per processing chain, in this case the level 1b product. As a consequence, the level 1b product must not only hold processed science data, but also calibration measurements and instrument monitoring data, as well as newly calculated calibration parameters. The latter are collected in the Annotation Data Set (ADS) in contrast to the measurement data which can be found in the Measurement Data Sets (MDS). In order to keep the size of the product as small as possible, the individual dark signal calibration measurements are discarded after calculation of the dark signal calibration parameters. For each dark state only the average signal of all measurements together with the deviation derived from the averaging is kept. All other calibration and monitoring measurements are retained, albeit in unprocessed form.

fig 6-1:

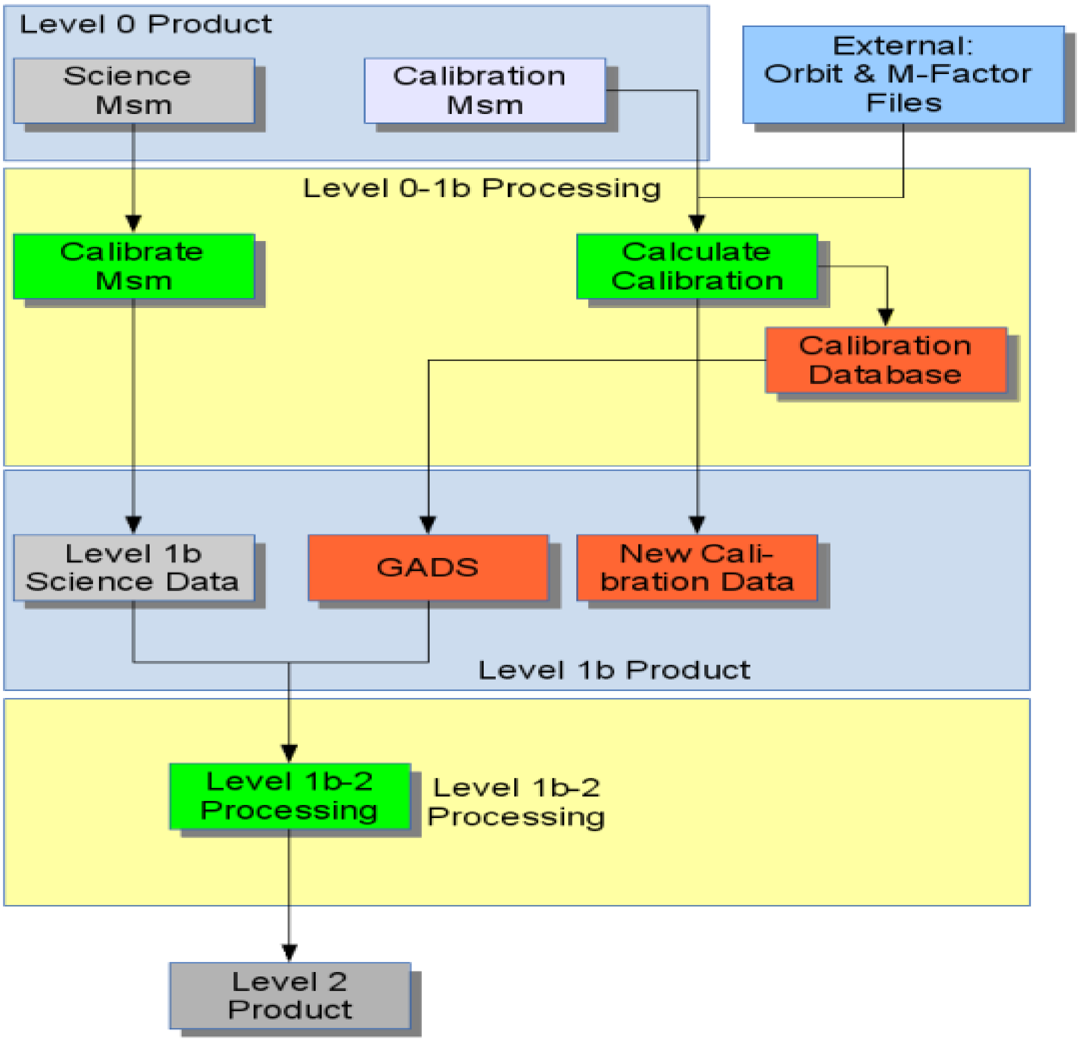

Overview of processing flow.

In the operational processing from level 0 to 1b, all necessary calibration constants for each science measurement are processed from the input calibration data, ground-based and in-flight as well. The level 1b data product contains the raw detector signals of the science measurements plus these calibration constants, mainly coded in 1-byte integers. In addition to measurement-specific calibration constants, e.g. stray-light or atmospheric polarization determination for each measurement, lookup-tables are generated for globally applicable calibration constants, e.g. instrument polarization sensitivity as function of scan angle. The calibration data files themselves are generated by the Level 0-1 processor using Level 0 data and key data as an input. The calibration data are saved into a database and written to the Level 1b product during processing. A calibration application tool (*SciaL1c*) is provided to the users supplementing the operational level 1b product such that the users can inflate level 1b products to level 1c containing fully calibrated data. For the user's convenience certain calibrations can be optionally omitted at extraction or a sub-set of data can be filtered out. However, operational level 1c products are not generated by the PDS, they need to be generated by the users. Fig. 6-2 provides an overview of the processing steps for level 0 to 1b and level 1b to 1c calibration of scientific measurements (nadir, limb and solar occultation), as well as the corresponding output on the level 1b and level 1c data products in a flow diagram. The individual calibration related steps are reflecting the calibration characteristics as described in the following sectionand specified in (Slijkhuis 2004). (fig. 6-2)

Relevant calibration parameters

fig 6-2:

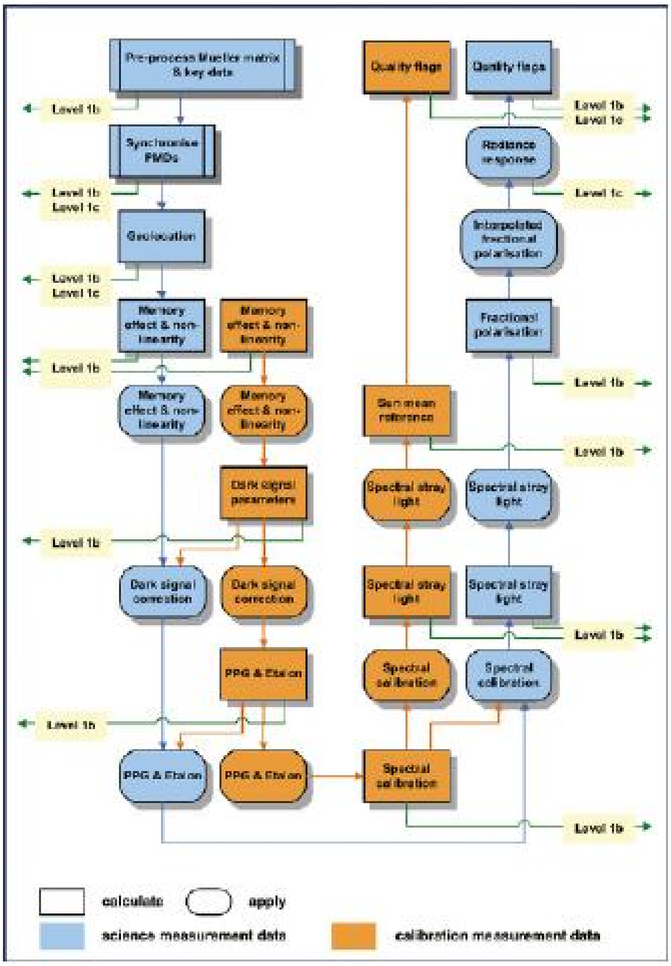

Overview of Level 0-1c processing.

6.2.2 Relevant calibration parameters

Only a very short overview for the calibration is given here. For details the reader is directed to the Level 0-1c Algorithm Technical Basis Document (ATBD). All corrections can be applied by using the SciaL1c *tool (see Annex 1)*.

6.2.2.1 Memory Effect and Non-Linearity correction

The UV/VIS and the SWIR detectors require different detector corrections. The UV/VIS channels have a memory effect, i.e. they “remember” the previous illumination and a small signal is left in the next readout, depending on the signal level. The SWIR detectors 6-8 show a non-linearity depending on the signal level of the incoming signal. Both corrections are parameterized as a function of the electronic signal on the detector and were measured in-flight and on-ground. The memory effect correction can be described as one function per channel for all pixels. The non-linearity can be described with four functions per channel for odd pixels, even pixels and pixels with a number higher and lower than 512 (the middle pixel). The functions are part of the key data. In the Level 1b product the correction value for each pixel is contained within one byte as a compressed value.

6.2.2.2 Dead and Bad Pixel Mask

The SWIR channels 6-8 suffer from a rising number of bad pixels that are not (or only to a small degree) usable for retrieval. The reason was a lattice constant mismatch between the substrate material and the light detecting material of the detectors. The bad pixels are detected using dark, WLS and sun measurements. Several thresholds for the three were determined to separate bad from good pixels. The number of bad pixels rised with the life time of the instrument due to proton impact. The mask is calculated for each orbit and stored in the Pixel-to-Pixel Gain *(PPG) ETALON* ADS.

6.2.2.3 Dark correction

Dark Signal values are measured in every orbit on the night side and once a month around the whole orbit. Operationally the dark signal is divided into the following parts:

- The analogue offset or fixed pattern noise. This is a signal added by the electronics to each pixel to avoid negative or near zero signals. This value is independent from external changes to the observation condition and also independent from exposure time. However, for each readout, the analogue offset is added meaning that a measurement with coadding factor *n* contains *n x analogue offset.* (???)
- The leakage current. This is the time dependent part of the dark signal mainly caused by thermally created electron-hole pairs. It is conceptually divided in two parts:
- One that is independent form orbit phase. This part is derived from the orbital measurements on the dark side of the Earth
- One that depends on orbit phase because of the different illumination of the instrument and resulting small temperature changes. This part is derived as a function of twelve orbit segments from the monthly dark measurements that are done for a complete orbit. The variable leakage is only relevant for the SWIR channels.
- The stray light. Near sun rise, the limb port of the instrument is directly illuminated by the sun leading to a large amount of spatial stray light. This stray light is characterised during the monthly dark orbits. It is only relevant for orbit phases around sun rise, i.e. over the Northern pole.

All orbit phase independent dark parameters are part of the *LEAKAGE CONSTANT* ADS. The *LEAKAGE VARIABLE* ADS contains the orbit phase dependent components of the dark signal. Both ADS's are used for the dark correction. The *LEAKGE NEW* ADS contains the newly calculated parameters that were obtained on that orbit for each block of dark measurements. For the UV/VIS channels 1-5 the dark signal is calculated from the fixed pattern noise, the orbit independent leakage current and the stray light component. The SWIR channels are treated differently, because more variations can be expected due to the thermal background of the instrument and the ice layers on the detectors of channel 7 and 8. For these channels the dark parameters are calculated from the measurements of the same orbit, i.e. from the *LEAKAGE NEW* ADS. Additionally the variable leakage signal from the *LEAKAGE VARIABLE* ADS is used to take into account the thermal background. The individual dark measurements are no longer part of the level 1b product, but state wise averages are stored in the *DARK AVERAGE* ADS.

6.2.2.4 Stray Light Correction

The stray light correction uses the key data to obtain a correction value for each pixel in each measurement. The correction values are stored directly in each MDS of the level 1 product in one byte (i.e. 255 values).

6.2.2.5 Wavelength Calibration

The wavelength calibration uses on-ground and in-flight data for channels 1-6. From weekly and monthly in-flight measurements of the spectral line source, the difference to the on-ground calibration is determined. The line positions are determined using the Falk algorithm. Subsequently a wavelength for each pixel is stored in the product. Since the spectral line source does not have enough lines in the infrared and bad pixels interfere with the line position determination, for channels 7 and 8 the on-ground wavelength calibration is taken without any changes for these channels.

6.2.2.6 PPG/Etalon Correction

The PPG correction aims to correct relative gain changes with time in the pixels of the SWIR channels. It is determined in-flight using the White Light Source (WLS) measurements. However, observations show that the PPG does not change significantly in-flight and the correction is currently not applied.
In the measured spectra interference structures can be seen as a result of multiple reflections on the boundaries of the protective layer of SiO on the light detecting silicon. This so-called etalon effect can change if material is deposited on top of the protective layer. The correction for this change is derived from the weekly WLS measurements and is only relevant for channels 1-5. Both corrections are stored in the *PPG ETALON* ADS.

6.2.2.7 Polarization Correction

The polarization correction is necessary because SCIAMACHY does not employ a polarization scrambler and the detected signal is thus dependent on the polarization of the incoming light. The polarization response was determined on-ground using the Polarization Measurement Devices (PMDs). The key data contain the ratio of the PMD signal to the science channel signal for several instrument configurations and polarization directions. The polarization is also measured in-flight and from the calculated polarization and the key data a linear polarization correction factor is calculated for all wavelengths. All data necessary to calculate the polarization correction factors are stored in the Level 1b product: The polarization sensitivities from on-ground measurement are stored in the *POLARIZATION SENSITIVITY* ADS for nadir, limb and occultation. The polarization fractions and the integrated PMD values for each observation are directly stored in the MDS.

6.2.2.8 Radiometric Correction

Finally, the data have to be radiometrically calibrated. This is done by using on-ground key data. The radiometric sensitivity for each observation is stored directly in the MDS of the level 1b product.

6.2.2.9 Sun Mean Reference

The sun mean reference (SMR) is used to calculate the reflectance. It is derived from daily diffuser measurements of the Elevation Scan Mechanism (ESM) diffuser and the Azimuth Scan Mechanism (ASM) diffuser. For both diffusers a fully calibrated SMR and a SMR with all calibrations applied except the radiometric calibration are available. The latter is provided, because tests showed that some retrieval have better quality when the radiometric calibration was switched off. All SMRs are stored in the *SUN MEAN REFERENCE* ADS. This ADS also contains sun occultation measurements and ESM diffuser measurements that are not used to calculate the reflectance. The identifiers are as follows:

- **E0 : Not radiometrically calibrated ESM sun spectrum,** Neutral Density Filter **(NDF) in**
- E1 : Not radiometrically **calibrated** ESM sun spectrum, NDF out
- **A0 : Not radiometrically calibrated ASM sun spectrum**
- A1 : Fixed ASM spectrum (manually provided at begin of mission)
- **D0 : Fully calibrated ESM sun spectrum, NDF in**
- D1 : Fully calibrated ESM sun spectrum, NDF out
- D2 : Scaled ASM sun spectrum, using ESM calibration data, i.e. these data are only scaled and *not* calibrated
- O*x* : Occultation data (calibrated and scaled using limb radiometric response)
- S : Subsolar data (calibrated and scaled using nadir radiometric response)
- U : Occultation data (calibrated excluding limb radiometric response)
- V : Subsolar data (calibrated excluding nadir radiometric response)

Note that only the spectra in **bold type** are useful for sun normalization of the Earthshine data! The ESM diffuser data without the NDF in are made for monitoring purposes and partly saturate. The scaled diffuser ASM spectrum (A1) does not give the absolute radiometric response but only corrects roughly instrument characteristics in the spectrum. The occultation and subsolar measurements have the general problem that they are measured with the small aperture that was not thoroughly characterized on-ground. Thus they are mainly useful for monitoring purposes. All sun spectra are averaged over the number of available and suitable measurements in a state (see the level 0-1c ATBD for details).

6.2.2.10 Degradation Correction

The degradation correction with the monitoring factors (m-factors) is implemented in the Level 0-1b processing, but at the moment not operationally used. The radiometric degradation correction is applied in the level 1b-2 processing (see section xxx). However, the user has the possibility to apply the radiometric degradation correction with the *SciaL1c* tool and thus produce corrected Level1c data.

6.2.3 Relevant Auxiliary Data

The auxiliary files contain data that are external input to the processing either because they were measured independently (e.g. during on-ground calibration) or because they are measured less frequently (e.g. daily sun measurements). Auxiliary data files (ADF) are calculated by the *SciCal* tool and stored in the IECF data base. The IPF then copies them to the level 1b files into the Global Annotation Data Set (GADS). All auxiliary data necessary to generate a calibrated level 1c product are stored in the level 1b product itself with the exception of the m-factor file. The m-factor files for the mission can be obtained at this address: SCIAMACHY m-factors (http://www.iup.uni-bremen.de/sciamachy/mfactors/downloads.html)

Once the m-factor files are locally stored, the *SciaL1c* user tool can be used to apply the m-factors. If only the location of the m-factor files is given, the file is chosen in the same way as in the operational processing. Additionally the user has the option to specify the file that should be used to read in the correction factors.

6.2.4 Degradation Correction: m-factors

M–factors are used in the 0-1b processor to compensate for the radiometric degradation of SCIAMACHY. In general, an m-factor is defined as the ratio between a measured spectrum of a constant light source (typically the sun) at a certain time to a spectrum obtained for the same optical path at a reference time. M-factors therefore provide an end-to-end degradation correction for each individual light path. (fig. 6-3)

fig. 6-3:

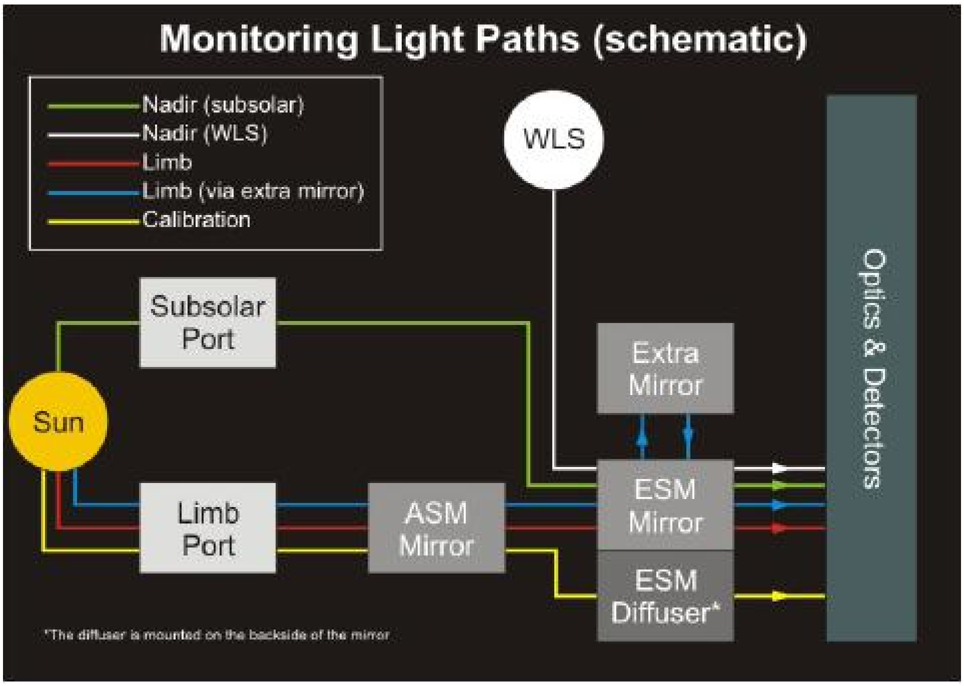

Schematic view of the different SCIAMACHY monitoring light paths

M–factors have an impact on the polarization correction and on the absolute radiometric calibration.
The m–factors for the science detectors are multiplicative factors to the absolute radiometric calibration of SCIAMACHY. The m–factors for the PMDs influence in a non-linear way the polarization correction of SCIAMACHY.
Regarding the m–factors for the polarization requires re-processing of the full mission, as the calculation of the polarization correction has to be done by the Level 0-1b processor. The concept for calculation and provision of m-factors foresees two steps:

- A short-term solution where only science detector readouts are corrected.
- A long-term solution where all light paths are corrected.

Details about the generation of m-factors are given in a corresponding Technical Note (Bramstedt, 2008).
SCIAMACHY long-term monitoring results based on partly calibrated Level 0 data are also available.

6.2.4.1 Short-Term Concept

The m-factor impact on polarization correction is neglected within the short–term solution.
The m–factors are provided by an external database, which than can be applied by a modified Level 1b-1c applicator. Advantages of this approach are:

- The application of m-factors can be switched on and off by the Level 1 data users.
- M-factors are decoupled from the operational 0-1b processing; therefore a fast implementation is possible.
- Updates of the m-factor data base are possible independent from a Level 1 re-processing.

Only the m-factors describing the degradation of the science channels are needed here; the PMD m-factors are set to 1.

6.2.4.2 Long-Term Concept

On long-term, a full set of m-factors including PMDs can be set up. For this concept, changes of the Level 0-1b processor are necessary. The m-factors are included in the Level 1 product and cannot be switched off, if polarization correction or absolute radiometric calibration is needed. Advantage of this approach is full consistency for reprocessed products.

6.2.5 Algorithm Baseline Documentation

The algorithm baseline documentation consists of a collection of documents that together give a complete specification of the data processor. The most relevant for the user are:

- **ATBD L0-1c:** Algorithm theoretical baseline description for Level 0-1c processing.
  This document describes in detail all calibration algorithms that are used in the operational processing.
  The same algorithms are used by the *SciaL1c* tool.
- **IODD:** Input/output data definition for Level 0 and 1b.
  This document contains a description of the level 1b format.
- ***SciaL1c* SUM:** Software user manual of the *SciaL1c* tool.
  This document explains all user options and also contains a description of the level 1b and the level 1c product format.

The documents are available at the DLR web page.

6.2.6 Data Format Description

SCIAMACHY Level 1b products follow the generalized ENVISAT product structure consisting of ASCII and binary structures. A Level 1b product includes headers (MPH, SPH), calibration data sets which are constant for the entire product, the so-called Global Annotation Data Sets (GADS), Annotation Data Sets varying over time (ADS) and several Measurement Data Sets (MDS) for the different viewing modes.
The Main Product Header (MPH) and the Specific Product Header (SPH) are ASCII structures of a fixed number of bytes. The Main Product Header (MPH) identifies the product and its main characteristics: product identification, data acquisition, processing details, etc. The Specific Product Header (SPH) contains information specific to the whole product such as start and stop times and location, summary of the number of states, also with Data Set Descriptors (DSDs) which describe individual Data Sets (DSs) within the product.

The Data Sets (DSs) contain the actual data of interest and may be Measurement Data Sets (MDS), Annotation Data Sets (ADS) or Global Annotation Data Sets (GADS). Data Sets are in mixed-binary format and consist of one or more Data Set Records (DSRs) each.
The measurement data sets (MDSs) include the raw signal values of the array detectors and geolocation information for nadir, limb and occultation measurements.
The different global annotation data sets (GADS) include leakage current and noise characteristics,pixel-to-pixel gain and Etalon parameters, spectral and radiometric calibration parameters, sun reference spectra and the polarization sensitivity parameters and errors on the Key Data.

The time dependent annotation data sets (ADS) include information about the sequence ofstates, the PMD and auxiliary data packets of the level 0 data and optionally a set of newly calculatedin-flight calibration parameters if the corresponding measurements are present in the level 0 data. More details regarding the product structure are given in the SCIAMACHY Product Specification document (Volume 15) and in the SCIAMACHY Level 0 to 1b Processing IODD.

The format description is also available on the web-page of the Basic Envisat Atmospheric Toolbox (BEAT), developed by S&T and available here. The BEAT Software provides a set of tools for ingesting, processing, and analyzing SCIAMACHY products.

6.2.7 Product Quality Information

A Readme file describing data quality and known instrument and processing issues as well as major improvements with respect to previous IPF versions is regularly maintained by the SCIAMACHY Quality Working Group and provided to the users. The document applying to the SCIAMACHY Level 1b products (SCI_NL__1P) is available here.

6.3 Operational Level 2 Products and Algorithms

The goal of the level 1b-2 data processing is to provide geophysical parameters as column densities, profiles from atmospheric constituents and cloud and aerosol parameters. Those data are given in the MDS of the level 2 product in combination with geolocation and additional auxiliary information (state geolocation, quality flagging, etc.) in the appropriate ADSs.

As outlined above, the operational level 1b-2 data processing occurs in Offline (OL) mode using two different types of processors, SCIAMACHY Ground Processor (SGP) L12 NRT and SGP L12 OL until 2006. In 2010 the fast delivery chain has been activated, using the same OL L2 processor, but NRT level 1 inputs. The level 1b-2 OL product includes retrievals from limb and nadir observation geometry. Algorithms and processors permanently evolve such that the product suite will be subject to changes. (see table 6-1)

Spectral Range	***Nadir***		***Limb***
UV-VIS-NIR	O3 (vertical column)	HCHO (slant column)	O3 (profile)
	NO2 (vertical column)	cloud cover	NO2 (profile)
	BrO (vertical column)	cloud optical thickness	BrO (profile)
	SO2 (vertical column)	cloud top height	
	OClO (slant column)	AAI	
	H2O (vertical column)		
SWIR	CO (vertical column)		

Table 6-1: Operational SCIAMACHY level 2 product. The SWIR products are strongly affected by the icing in channels 7 and 8, and operational processing within the PDS needs major revisions to cope with the icing.

The general processing chain for the level 1b-2 data processors is outlined in fig. 6-4 (nadir) and 6-5 (limb). It presents the functional flow, but does not display software implementation. The SGP L12 OL is implemented as a multi-processor Linux cluster system. Particularly experience gained from scientific product generation will be reflected in the operational chain stepwise. Assuming that scientific algorithms are usually more evolved than the operational ones due to development timescales determined by the rules for PDS processor s/w updates, it is a valid scientific requirement to re-generate operational level 2 products whenever significant algorithm knowhow can be transferred from the scientific to the operational environment. Even beyond the in-orbit mission lifetime, an ambitious atmospheric science project like SCIAMACHY asks for requires continuing retrieval algorithm research and reprocessing. In the following subsections a rough overview of the used retrieval algorithms is given. Details can be found in the ATBD. (fig. 6-4, fig. 6-5)

fig. 6-4:

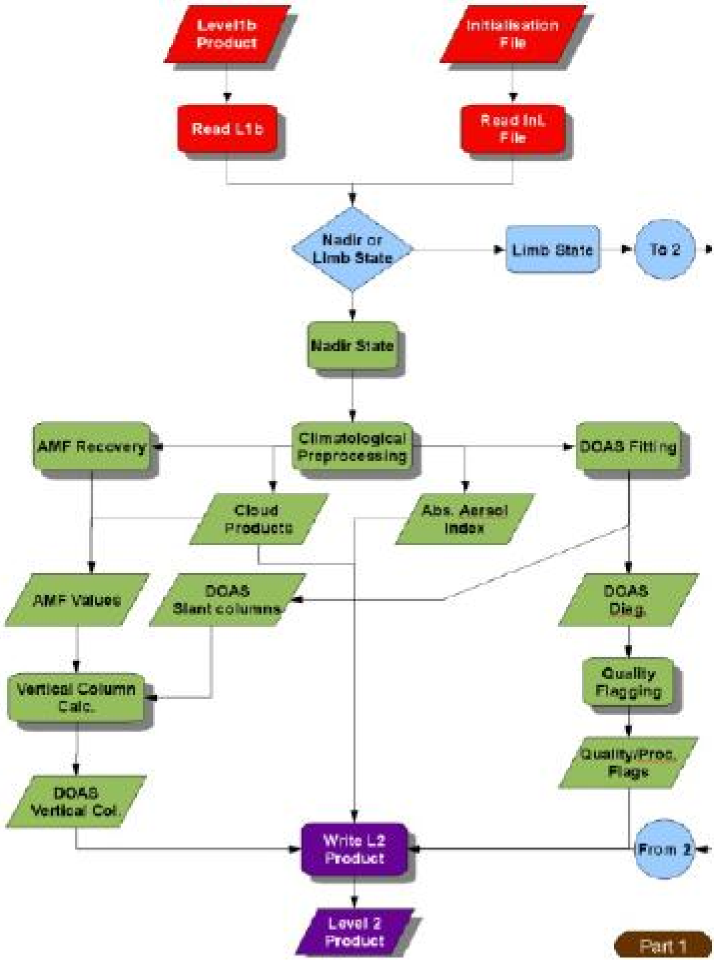

Offline level 2 processing part 1: Nadir and reading/writing of products. Continued in figure 6-5.

Cloud and Aerosol Parameters

fig 6-5:

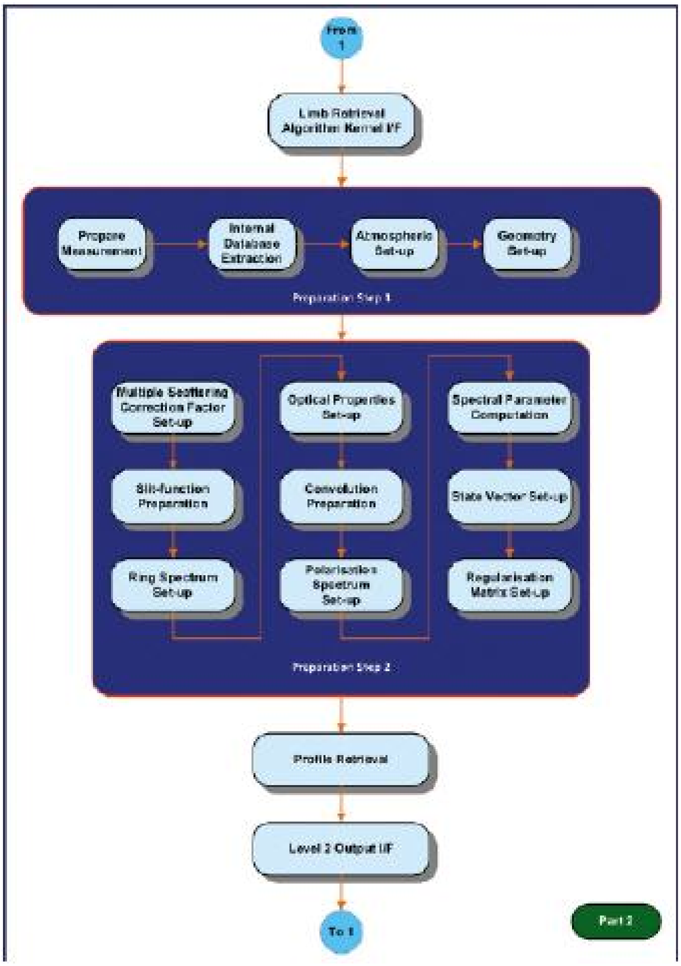

Offline Level 2 processing continued from figure 6-4 for Limb products.

6.3.1 Cloud and Aerosol Parameters

The cloud parameter cloud fraction is determined by the threshold algorithm Optical Cloud Recognition Algorithm OCRA (Loyola 1998). Polarization Measurement Device (PMD) measurements identified to be free of clouds from the red, green, and blue PMD are stored as RGB composite. The distance between the white point in the RGB reflectance space, which is dedicated to the fully cloudy case, and the actually determined PMD reflectance is taken to determine the cloud fraction. Heuristically derived scaling factors allow the appropriate representation of cloud fraction between zero (cloud-free) and one (fully cloudy). In the initial processor versions cloud top height or cloud top pressure was extracted from the ISCCP (International Satellite Cloud Climatology Project) database but it is replace from version 3.0 onwards by an algorithm based on evaluation of the O_2 A-band in the visible spectral region (SACURA, Rozanov and Kokhanovsky 2004). This yields improved cloud top height and cloud optical thickness parameters since in the former implementation only one value for optical thickness serves as fixed input.
The absorbing aerosol index AAI relies on the ratio of the reflectances between spectral bands around 340 nm and 380 nm. From the logarithmic difference to a model calculation (DAK) that does not contain aerosols the AAI is then computed. It indicates the presence of absorbing aerosols and depends strongly on an accurate calibration of the reflectance including degradation correction.

6.3.2 Nadir Trace Gas Retrievals

OL data processing uses the Differential Optical Absorption Spectroscopy (DOAS) approach for the retrieval of slant column densities from launch onwards. The DOAS concept together with the derivation of vertical column densities is described in chapter 5. Vertical column densities are deduced for the species O_3, NO_2, BrO,H_2O, CO, and SO_2, while only slant columns are provided for OClO. The current operational DOAS algorithm is based on the approach originally implemented for GOME data processor (GDP, Thomas and Spurr 1999). Since DOAS algorithm development undergoes permanent improvements – currently GDP 4.0 is operational (Spurr et al. 2004, Van Roozendael et al. 2006) – also SCIAMACHY's processor SGP L12 OL follows these changes (Lerot et al. 2009). For O_3 the GDP 4.0 implementation yields vertical columns which are derived in an iterative way by taking into account radiative transfer calculations for the AMF and the DOAS slant column density determination for each iteration step. For other species, the usual approach based on the distinction between AMF extraction, slant column density derivation, and the vertical column density calculation is used.

6.3.2.1 Ozone Total Column

Retrieval settings summary:

L0-1c settings	
Calibration	All calibrations applied
SMR	D0
DOAS settings	
Fitting Interval	325 - 335 nm
Wavelength Shift	Wavelength calibration of sun reference optimised over fitting interval by NLLS adjustment on pre-convolved NEWKPNO atlas
Polynomial Degree	3rd order
Absorption Cross Sections / Fitted Curves	
NO_2	Bogumil et al, Temperature = 243 K
O_3	Bogumil et al. 243 K, shifted + 0.02 nm, scaled by 1.03
O_3 Difference spectrum	T = 223 K, Difference $\sigma_{O3}^{243K} - \sigma_{O3}^{223K}$, shifted + 0.02, scaled by 1.03
Ring Spectrum	Calculated by convolution of the Chance and Spurr (1997) solar atlas with RRS cross-sections of molecular N_2 and O_2
Total Column Calculation: Profiles / AMF	
AMF ref. wavelength	325.5 nm
O_3 Profile	TOMS V.8 Climatology using iterative method with profiles parametrised by total column
Radiative Transfer Model	LIDORT
CTH, COT, CTA	SACURA
Cloud Fractions	OCRA

6.3.2.2 NO2 Total Column

Retrieval settings summary:

L0-1c settings	
Calibration	All calibrations applied except applied radiometric calibration and m-factors
SMR	A0
DOAS settings	
Fitting Interval	426.5 - 451.5 nm
Wavelength Shift	Wavelength calibration of sun reference optimised over fitting interval by NLLS adjustment on pre-convolved NEWKPNO atlas
Polynomial Degree	2nd order
Absorption Cross Sections / Fitted Curves	
NO_2	Bogumil et al, Temperature = 243 K
O_3	Bogumil et al. 243 K, shifted + 0.025 nm
O_3 Difference spectrum	T = 223 K, Difference $\sigma_{O3}^{243K} - \sigma_{O3}^{223K}$, shifted + 0.025 nm
	Greenblatt et al. (1990); Wavelength axis corrected by Burkholder

O_2 - O_2	
H_2O	Generated from HITRAN database
Ring Spectrum	Calculated by convolution of the Chance and Spurr (1997) solar atlas with RRS cross-sections of molecular N_2 and O_2
Offset and slope correction	Inverse Earthshine
Total Column Calculation: Profiles / AMF	
AMF ref. wavelength	439.0 nm
O_3 Profile	HALOE (Lambert et al, 2000)
Radiative Transfer Model	LIDORT
CTH, COT, CTA	SACURA
Cloud Fractions	OCRA

BrO Total Comumn

6.3.2.3 BrO Total Column

Retrieval settings summary:

LO-1c settings	
Calibration	All calibrations applied except radiometric calibration and m-factors
SMR	A0
DOAS settings	
Fitting Interval	336 - 351 nm
Wavelength Shift	Cross correlation according to Chance and Spurr solar line atlas
Polynomial Degree	3^{rd} order
Absorption Cross Sections / Fitted Curves	
NO_2	Bogumil et al, Temperature = 243 K
O_3	Bogumil et al. 243 k, shifted
O_3 Difference spectrum	T = 223 K, Difference $\sigma_{O3}^{243K} - \sigma_{O3}^{223K}$, shifted
O_2 - O_2	Greenblatt et al. (1990); Wavelength axis corrected by Burkholder
BrO	Fleischmann et al. (2004), T=223K
Ring Spectrum	Vountas at al. (1998)
Empirical Functions	Eta Nadir Key Data
Offset and slope correction	Inverse Earthshine
Total Column Calculation: Profiles / AMF	
AMF ref. wavelength	343.5 nm
BrO Profile	Stratospheric profiles from Theys et al. (2009)
Radiative Transfer Model	LIDORT
CTH, COT, CTA	SACURA
Cloud Fractions	OCRA

6.3.2.4 SO2 Total Column

Retrieval settings summary:

LO-1c settings	
Calibration	All calibrations applied except applied radiometric calibration and m-factors
SMR	A0
DOAS settings	
Fitting Interval	315 - 327 nm
Polynomial Degree	3^{rd} order
Absorption Cross Sections / Fitted Curves	
SO_2	Vandaele et al. (1994)
Background Database	Initially empty
O_3	Bogumil et al. 243 K
O_3 Difference spectrum	T = 223 K, Difference $\sigma_{O3}^{243K} - \sigma_{O3}^{223K}$, shift allowed

Undersampling	Constant Undersampling Spectrum calculated by IUP-Bremen
Ring Spectrum	Vountas et al. (1998)
Background Ref. Sector	180 - 200 deg (Pacific)
Empirical Functions	Eta NAdir (angle =)
Offset and slope correction	Inverse Spectrum of Earthshine radiance
Total Column Calculation: Profiles / AMF	
AMF ref. wavelength	315 nm
SO_2 Profile Anthropogenic	Pollution scenario: 1 DU present from surface to 1 km height
SO_2 Profile Volcannic	Eruption scenario: 10 DU present in layer between 10 and 11 km
Radiative Transfer Model	LIDORT
CTH, Cloud Top	Not applied, ghost column set to 0
Cloud Fraction	Not applied

SO2 slant columns retrieved with DOAS are known to have an offset to the correct values that is dependent from latitude and time. This error can be corrected by subtracting the offset values from the retrieved slant columns. For determination of the offset it is assumed that no SO2 is present over the Pacific, in the so called reference sector. The values from the reference sector (i.e. the assumed offsets) are stored in SO2DB as background values. For details see (Richter 2006).

6.3.2.8 OClO Slant Column Retrieval

Retrieval Setting Summary

Level 1b-1c Settings	
Calibration	All calibrations except radiometric
SMR	A0 (Sun over ASM diffuser without radiometric calibration)
DOAS Main Settings	
Fitting Interval	365 - 389 nm
Polynomial Degree	4th order
Absorption Cross Sections/Fitted Curves	
NO2	Bogumil et al (2003) @223 K
O4	Hermans et al (1999)
OClO	Kromminga et al (2003)
Ring Spectrum	Vountas et al (1998)
Undersampling	Constant Undersamping Spectrum caclulated by IUP
Empirical Functions	
Offset and Slope Correction	Inverse Earthshine spectrum (radiance)
Polaristion Feature Correction	*h* Nadir included in the fit
Intensity Correction Ratio	Ratio of cloudy and cloud-free measurements calculated by IUP

6.3.2.9 HCHO Total Column Retrieval

Retrieval Settings Summary

Level 1b-1c Settings	
Calibration	All calibrations except radiometric
SMR	A0 (Sun over ASM diffuser without radiometric calibration)
DOAS Main Settings	
Fitting Interval	328.5 - 346 nm
Polynomial Degree	5th order
Absorption Cross Sections/Fitted Curves	
NO2	Vandaele et al. (1998) @ 220 K
O3	Brion et al. (1998) @ 228 K & 243 K, I0-corrected
HCHO	Meller and Moortgat (2000) @ 298 K
BrO	Fleischmann et al. (2004) @ 223 K
OClO	Bogumil et al. (2003) @ 293 K
Ring Spectrum	SCIAMACHY irradiance of 20030329, KPNO solar spectrum, Gaussian slit function
Undersampling	Constant Undersamping Spectrum calculated by BIRA
Empirical Functions	
Offset and Slope Correction	Inverse Earthshine spectrum (radiance)
Polaristion Feature Correction	Eta and Zeta Nadir included in the fit

Background Correction	SCD from reference sector over the Pacific (180 - 220 deg)
Total Column Calculation: Profiles/AMF	
AMF ref. Wavelength	340 nm
HCHO Profile	IMAGES (Mueller and Brasseur, 1995)
Radiative Transfer Model	LIDORT
Cloud Top Height	SACURA
Cloud Fraction	OCRA

6.3.2.10 CHOCHO Total Column Retrieval

Retrieval Settings Summary

Level 1b-1c Settings	
Calibration	Dark Current, Memory Effect and etalon correction
SMR	A0 (Sun over ASM diffuser without radiometric calibration)
DOAS Main Settings	
Fitting Interval	435 - 457 nm
Polynomial Degree	4th order
Absorption Cross Sections/Fitted Curves	
NO2	Bogumil et al (2003) @223 K
O4	Greenblatt et al. (1990)
CHOCHO	Volkamer et al (2005)
O3	Bogumil et al (2003) @273 K
H2O Liquid	Pope and Fry (1997)
Ring Spectrum	Vountas et al (1998)
Empirical Functions	
Offset and Slope Correction	Inverse Earthshine spectrum (radiance)
Background correction	SCD from reference sector over the Pacific (180 - 200 deg)
Total Column Calculation: Profiles/AMF	
AMF ref. Wavelength	446 nm
CHOCHO Profile	IMAGES (Müller and Brasseur, 1995)
Radiative Transfer Model	LIDORT
Cloud Top Height	SACURA
Cloud Fraction	OCRA

H2O Total Column

6.3.2.8 H2O Total Column

Water vapour is calcualted with the AMC DOAS Method (Noël et al., 1999). The AMC-DOAS algorithm is based on the well-known Differential Optical Absorption Spectroscopy (DOAS) approach (Platt, 1994) which has been modified to handle effects arising from the strong differential absorption structures of water vapour. The general features of this modified DOAS method are that

1. saturation effects arising from highly structured differential spectral features which are not resolved by the measuring instrument are accounted for, and

2. O2 absorption features are fitted in combination with H2O to determine a so-called air mass factor (AMF) correction which compensates to some degree for insufficient knowledge of the background atmospheric and topographic characteristics, like surface elevation and clouds.

The main equation of the Air Mass Corrected DOAS method is given by:

equ 6-1

$$\ln\left(\frac{I}{I_0}\right) = P - a\left(\tau_{O_2} + c \cdot C_V^b\right)$$

with

*I,I*0 Earthshine radiance and solar irradiance
P Polynomial to correct for broadband contributions (resulting e.g. from Rayleigh and Mie scattering or surface albedo)
*tO*2 Optical depth of O2
CV Vertical column amount of water vapour
b,c Spectral quantites describing saturation effect and absorption

c contains the effective reference absorption cross section and the air mass factor. The scalar parameter *a* is the above mentioned AMF correction factor. The quantities *tO*2, *b*, and *c* are determined from radiative transfer calculations performed for different atmospheric conditions and solar zenith angles. *CV* and *a* are then derived from a non-linear fit. The error of the vertical column is calculated from the covariance matrix also resulting from the fit.

6.3.2.9 CO Total Column

Carbon monoxide retrieval from SCIAMACHY nadir observations is rather challenging: Only channel 8 from 2259 to 2386 nm features CO absorption signatures, albeit very weak and superposed by stronger absorption lines of concurrent gases, i.e. H2O and CH4. Additionally, an ice layer on the detector modifies the measured signal. Even worse, degradation of the detector increasingly reduces the number of reliable pixels, i.e. only about 50 of 1024 pixels in channels 8 are useful for CO retrieval.

The forward model is based on the MIRART (Modular InfraRed Atmospheric Radiative Transfer) line-by-line code, developed for arbitrary observation geometry, instrumental field-of-view and spectral response functions *(Schreier and Schimpf, 2001)*. Molecular absorption cross sections are calculated using spectroscopic line parameters from the Hitran, Geisa and other databases, together with optional continuum corrections (continuum corrections to the absorption coefficient are supported). Derivatives of transmission and/or radiance spectra are obtained by means of automatic differentiation. MIRART has been extensively verified by intercomparisons with other codes, e.g. in the framework of the EU study AMIL2DA.

The relation between forward model *F* and measured signal *I* is

$$F(x) = I(\nu) = \mathrm{r}\, I_{sun}(\nu) \exp\left(-\sum x_m \tau_m(\nu)\right) \otimes S(\nu,\gamma) + b$$

where τ_m is the optical depth along the entire line-of-sight (Sun-ground-satellite) for the reference atmosphere, ν is the wavenumber and $S(\nu,\gamma)$ is the spectral response function. The state vector x to be retrieved comprises the column density scaling factors x_m, the slit function half width γ, the surface reflectivity (albedo) r and the baseline correction b. Note that the reflectivity r and the baseline b enter the forward model linearly and the least squares problem can be reduced to a separable nonlinear least squares problem. For the solution of the least squares problem, BIRRA uses solvers provided in the PORT Optimization Library based on a scaled trust region strategy. BIRRA provides the option to use a least squares with simple bounds (e.g., non-negativity) to avoid unphysical results.

Retrieval Setting Summary

Level 1b-c Settings	
Calibration	All calibrations except polarisation and radiometric
SMR	A0 (Sun over ASM diffuser without radiometric calibration)
Main Settings	
Fitting Interval	2324.4 - 2335.0 nm
Absorbers Fitted	CO, CH4 , H2O
Polynomial Degree Albedo	2
Slit function	Gaussian
Proxy for xCO	CH4

6.3.2.10 CH4 Total Column

The CH4 retrieval uses two spectral windows in channel 6. As a proxy correction to take into account the effect of clouds and transmission changes CO2 is used, since its variations are small compared to methane. As for CO two columns can be found in the product, the total column and the total column corrected by the CO2 proxy.

Retrieval Setting Summary

Level 1b-1c Settings	
Calibration	All calibrations except polarisation and radiometric
SMR	A0 (Sun over ASM diffuser without radiometric calibration)
Main Settings	
Fitting Interval	1557.18 - 1594.13 nm & 1628.93 - 1670.56 nm
Absorbers Fitted	CO2, CH4 , H2O
Polynomial Degree Albedo	2
Slit function	Gaussian
Proxy for xCO	CO2

6.3.3 Limb

The limb retrieval can be summarized into the following steps:

- 1) Forward Model Calculation
- Calculation of the line-of-sight through the atmosphere
- Calculation of single and multiple scattering terms for each layer
- First approximation of the radiation field with pseudo-spherical approximation (also called independent pixel approximation).
- Calculation of the radiation field with Picard iteration with open boundaries (fully spherical) using the radiation field calculated in the previous step as the initial field.
- 2) Inversion: Thikonov regularisation with a-priori parameter choice method.

The profiles are calculated fromthe first cloud free height (taken from the Limb cloud product, see below) above a predefined minimum height up to 100 km. Before the inversion the spectra are divided by the measured spectrum at a configurable reference height. For each state a maximum of 4 profiles in East-West direction are calculated (depending on the integration time of the state. Fig. 6-5 depicts the s/w architecture of both limb retrieval algorithms with two preparational steps and the retrieval of the profile information.

6.3.3.1 Ozone Profile

Input spectra	
Calibration	All calibrations applied
Retrieval Height Range	13.5 (or lowest cloud free height) - 46 km
Fit Settings	
Fitting Interval	520 - 590 nm
Polynomial Degree	4^{th} order
Number of Layers	33
Absorption Cross Sections/Fitted Curves	
O_3	Bogumil et al (2003) @243 K
NO_2	Bogumil et al (2003) @243 K
Profiles	
O_3	McLinden (2000)
NO_2	McLinden (2000)

6.3.3.2 NO2 Profile

Input spectra	
Calibration	All calibrations applied
Retrieval Height Range	13.5 (or lowest cloud free height) - 43 km
Reference Height	43 km
Fit Settings	
Fitting Interval	420 - 470 nm
Polynomial Degree	3rd order
Number of Layers	33
Absorption Cross Sections/Fitted Curves	
NO_2	Bogumil et al. (2003), @243 K
O_3	Bogumil et al. (2003), @243 K
Profiles	
NO_2	McLinden (2000)
O_3	McLinden (2000)

6.3.3.3 BrO Profile

Input spectra	
Calibration	All calibrations applied
Retrieval Height Range	10.5 (or lowest cloud free height) - 43 km
Reference Height	35 km
Fit Settings	
Fitting Interval	337 - 357 nm
Polynomial Degree	4th order
Number of Layers	33
Absorption Cross Sections/Fitted Curves	
BrO	Bogumil et al. (2003), @243 K
O_3	Bogumil et al. (2003), @243 K
Profiles	
BrO	McLinden (2000)
O_3	McLinden (2000)

6.3.3.4 Cloud flagging and top height

Input spectra	
Calibration	All calibrations applied
Retrieval Height Range	0 - 18 km
Reference Height	35 km
Algorithm Settings	
Used Wavelengths	337 - 357 nm
Algorithm	Based on threshold by ratioing two wavelengths
Number of Layers	33 (?)

6.3.4 Algorithm Baseline Documentation

The algorithm baseline documentation consist of a collection of documents that together give a complete specification of the data processor. The most relevant for the user are:

- **ATBD L1b-2:** Algorithm theoretical baseline description for Level 1b-2 processing <addlink?>. This document describes in detail all retrieval algorithms that are used in the operational processing.
- **IODD:** Input/output data definition for Level 2. This document contains a description of the level 2 format.

Both documents are available at the DLR SCIAMACHY web page.

6.3.5 Data Format Description

SCIAMACHY Level 2 products follow the generalized ENVISAT product structure consisting of ASCII and binary structures.
A Level 2 product includes headers (MPH, SPH), annotation data sets (ADSs) and several measurement data sets (MDSs) depending on the number of fitting window applications.
The main product header (MPH) has a fixed format (as described in ENVISAT Product Specification Document), and includes information about product identification and data acquisition and processing details.The specific product header (SPH) includes a reference to climatological data base and look-up table versions,the adopted fitting window and retrieved molecule also with the data set description records (DSD).
The annotation data sets (ADS) include condensed quality information, geolocation of the states and three ADSs with information about the states of the product and the detailed geolocation for nadir and limb.
The first measurement data set (MDS) of the Level 2 product includes cloud and aerosol information for each nadir ground pixel.
This data set is followed by the MDSs with geophysical parameters of several fitting windows for Nadir and Limb measurements, associated errors, and diagnostics from the level 1b to 2 algorithms.
The MDSs are labeled according to the type of measurement (nadir, limb or occultation); there are two types of MDSs - one for nadir and the other for limb and occultation, with different record structure.
The number of trace gas constituents retrieved is related to the algorithm baseline version. The Level 2 product is prepared to include results from further fitting window applications that will be introduced with future processor version.
More details regarding the product structure are given in the SCIAMACHY Product Specification document (Volume 15 issue 3L version 1.1) and in the SCIAMACHY Level 1b to 2 Processing IODD.
The format description is also available on the web-page of the Basic Envisat Atmospheric Toolbox (BEAT), developed by S&T and available at http://www.stcorp.nl/beat/documentation/codadef
The BEAT Software provides a set of tools for ingesting, processing, and analyzing SCIAMACHY products.

6.3.6 Product Quality Information

A Readme file describing data quality and known instrument and processing issues as well as major improvements with respect to previous processor versions is regularly maintained by the SCIAMACHY Quality Working Group and provided to the users. The document applying to the SCIAMACHY Level 2 products is available here.

6.3.7 Software Tools

ESA provides a set of software tools to the remote sensing user community, in order to exploit atmospheric data for scientific analysis. These tools allow the data users to read, process, and visualize SCIAMACHY data. All software listed below can be freely downloaded starting from the ESA Software tools page.

Basic ERS & Envisat Atmospheric Toolbox (BEAT)

The Basic ERS & Envisat Atmospheric Toolbox (BEAT) is a collection of executable tools and an application programming interface (API) which has been developed to facilitate the utilization, viewing and processing of ESA GOMOS, MIPAS, SCIAMACHY, and GOME data. The current release is BEAT version 6.8.0.

CFI Software

The CFI software is a collection of multiplatform precompiled C libraries for timing, coordinate conversions, orbit propagation, satellite pointing calculations, and target visibility calculations. This software is made available by the Envisat project to any user involved in the Envisat mission preparation/exploitation. Access to the user is provided after filling in and sending a formal registration form.

SciaL1C Tool

The SciaL1C tool is an application provided to the users of SCIAMACHY Level 1b products. This application allows selecting specific calibrations to apply to SCIAMACHY Level 1b data and generate Level 1c products suitable for the user's particular applications. Level 1b products contain not fully calibrated Level 0 spectral information in combination with calculated calibration data. Details on the calibration concept for SCIAMACHY measurements are available here.

References Chapter 1

ANNEX 1: References

(Arrhenius 1896)
Arrhenius, S.,"On the influence of carbonic acid in the air upon the temperature of the ground", **Philosophical Magazine and Journal of Science**, 41, 237, 1896

(Burrows et al. 1988a)
Burrows J.P., K.V. Chance, P.J. Crutzen, H. van Dop, J.C. Geary, T.J. Johnson, G.W. Harris, I.S. A. Isaksen, G.K. Moortgat, C. Muller, D. Perner, U. Platt, J.-P. Pommereau, H. Rodhe, E. Roeckner, W. Schneider, P. Simon, H. Sundqvist, J. Vercheval, "SCIAMACHY – A European proposal for atmospheric remote sensing from the ESA Polar Platform", published by Max-Planck-Institut für Chemie, Mainz, Germany, 1988

(Burrows et al. 1988b)
Burrows, J.P., P.J. Crutzen, K.V. Chance, J.C. Geary, F. Goutail, G.W. Harris, G.K. Moortgat, C. Muller, D. Perner, U. Platt, J.-P. Pommereau, W. Schneider, P. Simon, "SCIAmini", published by May-Planck-Institut für Chemie, Mainz, Germany, 1988

(Burrows et al. 1999)
Burrows, J.P., M. Weber, M. Buchwitz, V.V. Rozanov, A. Ladstädter-Weissenmayer, A. Richter, R. de Beek, R. Hoogen, K. Bramstedt, K.-U. Eichmann, M. Eisinger, D. Perner, "The Global Ozone Monitoring Experiment (GOME): Mission Concept and First Scientific Results", **J. Atmos. Sci.**, 56, 151-175, 1999

(Chandra et al. 1997)
Chandra, S., C.H. Jackman, E.L. Fleming, J.M. Russell III, "The Seasonal and Long-Term Changes in Mesospheric Water Vapor," **Geophys. Res. Lett.**, 24, 639-642, 1997

(Crutzen et al. 1995)
Crutzen, P.J., J.-U. Grooß, C. Brühl, R. Müller, J.M. Russell III, "A reevaluation of the ozone budget with HALOE UARS data: No evidence for the ozone deficit", **Science**, 268, 705, 1995

(Crutzen and Stoermer 2000)
Crutzen, P.J., E.F. Stoermer, "The anthropocene", **IGBP Newsletter**, 41, 17-18, 2000

*(Gottwald et al. 2006)*M. Gottwald, H. Bovensmann, G. Lichtenberg, S. Noel, A. von Bargen, S. Slijkhuis, A. Piters, R. Hoogeveen, C. von Savigny, M. Buchwitz, A. Kokhanovsky, A. Richter, A. Rozanov, T. Holzer-Popp, K. Bramstedt, J.-C. Lambert, J. Skupin, F. Wittrock, H. Schrijver, J.P. Burrows: « SCIAMACHY, Monitoring the Changing Earth's Atmosphere »; Published by DLR, 2006

(Holton et al. 1995)
Holton, J.R., P.H. Haynes, M.E. McIntyre, A.R. Douglass, R.B. Hood, L. Pfister, "Stratosphere-troposphere exchange", **Rev. Geophys.**,33, 403-439, 1995

(IPCC 2001)
IPCC, "Climate change 2001 – The scientific basis", IPCC, Cambridge University Press, Cambridge, UK, 2001

(IPCC 2007)
Climate Change 2007: Synthesis Report. Contribution of Working Groups I, II and III to the Fourth Assessment Report of the Intergovernmental Panel on Climate Change [Core Writing Team, Pachauri, R.K and Reisinger, A. (eds.)]. IPCC, Geneva, Switzerland, 104 pp.
(Lovelock, 1979)
Lovelock, J.E., "Gaia:A new look at life on earth", Oxford University Press, Oxford, 1979

(Munro et al. 1998)
Munro, R., R. Siddans, W.J. Reburn, B.J. Kerridge, "Direct measurement of tropospheric ozone distributions from space", **Nature**, 392, 168-171, 1998

(Shindell et al. 1998)
Shindell, D.T., D. Rind, P. Logan, "Increased polar stratospheric ozone losses and delayed eventual recovery owing to increasing greenhouse-gas concentrations", **Nature**, 392, 589-592, 1998

(Summers et al. 1997)
Summers, M.E., R.R. Conway, D.E. Siskind, M.H. Stevens, D. Offermann, M. Riese, P. Preusse, D.F. Strobel, J.M. Russell III, "Implications of satellite OH observations for middle atmospheric H2O and ozone", **Science**, 277, 1967-1970, 1997

(Wayne 1992)
Wayne, R.P., "Chemistry of Atmospheres", Oxford University Press, Clarendon Press, Oxford, 1992

(Wild et al. 2005)
Wild, M., H. Gilgen, A. Roesch, A. Ohmura, C.N. Long, E.G. Dutton, B. Forgan, A. Kallis, V. Russak, A. Tsvetkov, "From Dimming to Brightening: Decadal Changes in Solar Radiation at Earth's Surface", **Science**, 308, 847-850, 2005

(WMO 1995)
WMO 1995, "Scientific Assessment of Ozone Depletion 1994", Global Ozone Research andMonitoring Project Report No. 37, 1995

(WMO 2003) WMO 2003, "Scientific Assessment of Ozone Depletion:2002", Global Ozone Research andMonitoring Project Report No. 47, Geneva, 2003

(WMO-IGACO 2004)
WMO, "The Changing Atmosphere – An Integrated Global Atmospheric Chemistry Observation, Theme for the IGOS Partnership, Report of the Integrated Global Atmospheric Chemistry Observation, Theme Team", WMO Report GAW No. 159, WMO TD No. 1235, 2004

References Chapter 2

(Bovensmann et al. 1999)
Bovensmann, H., J.P. Burrows, M. Buchwitz, J. Frerick, S. Noël, V.V. Rozanov, K.V. Chance, A.P.H. Goede, “SCIAMACHY: Mission Objectives and Measurement Modes”, **J. Atmos. Sci.**, 56, 127-150, 1999

(Burrows and Chance 1991)
Burrows, J.P., K.V. Chance, “Scanning imaging absorption spectrometer for atmospheric chartography”, **Proceedings of SPIE,**1490, 146-155, 1991

(DARA 1998)
DARA, “SCIAMACHY Instrument Requirements Document”, PO-RS-DAR-EP-0001, **Technical Document**, 1998

(Goede et al. 1991)
Goede, A.P.H., H.J.M. Aarts, C. van Baren, J.P. Burrows, K.V. Chance, R. Hoekstra, E. Hölzle, W. Pitz, W. Schneider, C. Smorenburg, H. Visser, J. de Vries “SCIAMACHY Instrument Design”, **Adv. Space Res.**, 11, 243-246, 1991

(Hoogeveen et al. 2001)
Hoogeveen, R.W.M., R. van der A, A.P.H. Goede, ‘Extended wavelength InGaAs infrared (1.0-2.4 μm) detector arrays on SCIAMACHY for space-based spectrometry of the earth atmosphere”, **Infrar. Phys. Techn.**, 42, 1-16, 2001

References Chapter 3

(Barkley et al. 2007)
Barkley, M.P., Monks, P.S., Hewitt, A.J., Machida, T., Desai, A., Vinnichenko, N., Nakazawa, T., Yu Arshinov, M., Fedoseev, N. and Watai, T. ‘Assessing the near surface sensitivity of SCIAMACHY atmospheric CO2 retrieved using (FSI) WFM-DOAS’, **Atmos. Chem. Phys**., 7, 3597-3619,2007.

(Barkley et al. 2009)
Barkley, M.P., Palmer, P.I., De Smedt, I., Karl, T., Guenther, A. and Van Roozendael, M. “Regulated large-scale annual shutdown of Amazonian isoprene emissions?”, **Geophys. Res. Lett**., 36, L04803, doi:10.1029/2008GL036843,2009.

(Barrie et al. 1988)
Barrie, L.A., Bottenheim, J.W., Schnell, R.C., Crutzen, P.J. and Rasmussen, R.A. “Ozone destruction and photochemical reactions at polar sunrise in the lower Arctic atmosphere”, **Nature,** 334, 138-141, 1988.

(Becker et al. 2010)
Becker, E. and von Savigny, C. “Dynamical heating of the polar summer mesopause induced by solar proton events”, **J. Geophys. Res***.* 115, doi:10.1029/2009JD012561,2010.

(Begoin et al. 2010)
Begoin, M., Richter, A., Kaleschke, L., Tian-Kunze, X., Stohl, A. and Burrows, J.P. “Satellite observations of long range transport of a large BrO cloud in the Arctic”. **Atmos. Chem. Phys.,**10, 6515-6526,2010.

(Beirle et al. 2004)
Beirle, S., Platt, U. and Wagner, T.,“Monitoring nitrogen oxides with satellite instruments: High resolution maps from GOME narrow swath mode and SCIAMACHY”, **Proc. ENVISAT & ERS Symposium 2004**, Salzburg, Austria, ESA SP-572, 2004.

(Bergamaschi et al. 2009)
Bergamaschi, P., Frankenberg, C., Meirink, J.F., Krol, M., Villani, M.G., Houweling, S., Dentener, F., Dlugokencky, E.J., Miller, K.B., Gatti, L.V., Engel, A. and Levin, I“Inverse modeling of global and regional CH4 emissions using SCIAMACHY satellite retrievals”, **J. Geophys. Res.**, 114, D22301, doi:10.1029/2009JD012287, 2009.

(Bittner et al. 2002)
Bittner, M., Offermann, D., Graef, H.H., Donner, M. and Hamilton, K.”An 18 year time series of OH rotational temperatures and middle atmosphere decadal variations”, **J. Atmos. Sol.-Terr. Phys.**, 64, 1147-1166, 2002.

(Bösch et al. 2006)
Bösch, H., Toon, G.C., Sen, B., Washenfelder, R.A., Wennberg, P.O., Buchwitz, M., de Beek, R., Burrows, J.P., Crisp, D., Christi, M., Connor, B.J., Natraj, V. and Yung, Y.L.,“Space-based near-infrared CO2 measurements: Testing the Orbiting Carbon Observatory retrieval algorithm and validation concept using SCIAMACHY observations over Park Falls, Wisconsin”, **J. Geophys. Res.**, 111, D23302, doi:10.1029/2006JD007080, 2006.

(Boersma et al. 2008)
Boersma, K.F., Jacob, D.J., Eskes, H.J., Pinder, R.W., Wang, J. and van der A, R.J.,“ Intercomparison of SCIAMACHY and OMI tropospheric NO2 columns: Observing the diurnal evolution of chemistry and emissions from space”, **J. Geophys. Res.,**113, D16S26, doi:10.1029/2007JD008816, 2008.

(Bracher et al. 2005)
Bracher, A., Eichmann, K.-U., von Savigny, C., Sinnhuber, B.-M., Weber, M., Bramstedt, K. and Burrows, J.P„Polar ozone distributions in the arctic winter/spring 2004/05 as measured by the Envisat instruments GOMOS and SCIAMACHY”, **Geophys. Res. Abstr.,**7, 08693, 2005.

(Bracher et al. 2009)
Bracher, A., Vountas, M., Dinter, T., Burrows, J.P., Röttgers, R. and Peeken, I,“Quantitative Observation of cyanobacteria and diatoms from space using PhytoDOAS on SCIAMACHY data”, **Biogeosciences,**6, 751-764, 2009.

(Buchwitz et al. 2005a)
Buchwitz, M., de Beek, R., Noël, S., Burrows, J.P., Bovensmann, H., Bremer, H., Bergamaschi, P., Körner, S. and Heimann, M. „Carbon monoxide, methane and carbon dioxide columns retrieved from SCIAMACHY by WFM-DOAS: Year 2003 initial data set”, **Atmos. Chem. Phys.,**5, 3313-3329, 2005a.

(Buchwitz et al. 2005b)
Buchwitz, M., de Beek, R., Burrows, J.P., Bovensmann, H., Warneke, T., Notholt, J., Meirink, J.F., Goede, A.P.H., Bergamaschi, P.,Körner, S., Heimann, M. and Schulz, A.,“Atmospheric methane and carbon dioxide from SCIAMACHY satellite data: Initial comparison with chemistry and transport models”, **Atmos. Chem. Phys.**, 5, 941-962, 2005b.

(Buchwitz et al. 2007a)

Buchwitz, M., Schneising, O., Burrows, J.P., Bovensmann, H., Reuter, M. and Notholt, J. 2007a. Corrigendum to 'First direct observation of the atmospheric CO2 year-to-year increase from space' published in Atmos. Chem. Phys., 7, 4249-4256, **Atmos. Chem. Phys.,**7, 5341-5342, 2007a.

(Buchwitz et al. 2007b)
Buchwitz, M., Khlystova, I., Bovensmann, H. and Burrows, J.P. “Three years of global carbon monoxide from SCIAMACHY: Comparison with MOPITT and first results related to the detection of enhanced CO over cities”, **Atmos. Chem. Phys.,**7, 2399-2411, 2007b.

Correira et al. 2008)

Correira, J., Aikin, A.C., Grebowsky, J.M., Pesnell, W.D. and Burrows, J.P. “Seasonal variation of magnesium atoms in the mesosphere-thermosphere”, **Geophys.Res. Lett.,**35, doi:10.1029/2007GL033047, 2008.

(de Graaf et al. 2010)
de Graaf, M., Tilstra, L.G., Aben, I., Stammes, P.,„Satellite observations of the seasonal cycle of absorbing aerosols in Africa related to the monsoon rainfall”, **Atmos. Env**., 44, 1274-1283, doi:10.1016/j.atmosenv.2009.12.038, 2010.

(deLaat et al. 2006)
de Laat, A.T.J., Gloudemans, A.M.S., Schrijver, H., van den Broek, M.M.P., Meirink, J.F., Aben, I. and Krol,, M. “Quantitative analysis of SCIAMACHY total carbon monoxide column measurements”, **Geophys. Res. Lett.,** 33, L07807, doi:10.1029/2005GL025530, 2006.

(de Smedt et al. 2008)
De Smedt, I., Müller, J.-F., Stavrakou, T., van der A, R., Eskes, H. and Van Roozendael, M.,“Twelve years of global observations of formaldehyde in the troposphere using GOME and SCIAMACHY sensors”, **Atmos. Chem. Phys.**, 8, 4947-4963, 2008.

(de Smedt et al. 2010)
De Smedt, I., Stavrakou, T., Müller, J.F., van der A, R.J., and Van Roozendael, M.,“Trend detection in satellite observations of formaldehyde tropospheric columns”, **Geophys. Res. Lett.,**37, L18808, doi:10.1029/2010GL044245, 2010.

(Dikty et al. 2010)
Dikty, S., Weber, M., von Savigny, C., Sonkaew, T., Rozanov, A. and Burrows, J.P.,“Modulations of the 27-day solar cycle signal in stratospheric ozone from SCIAMACHY”, **J. Geophys. Res.**, 115, D00I15, doi:10.1029/2009JD012379, 2010.

(Dufour et al. 2009)
Dufour, G., Wittrock, F., Camredon, M., Beekmann, M., Richter, A., Burrows, J.P.,“SCIAMACHY formaldehyde observations: Constraint for isoprene emissions over Europe?”, **Atmos. Chem. Phys**.,9, 1647-1664, 2009.

(Ern et al. 2009)
Ern, M., Lehmann, C., Kaufmann, M. and Riese, M.,“Spectral wave analysis at the mesopause from SCIAMACHY airglow data compared to SABER temperature spectra”, **Annales Geophysicale**, 27, 1, 407-416, 2009.

(Eskes et al. 2005)
Eskes, H., Segers, A. and van Velthoven, P.F.J.,“Ozone Forecasts of the Stratospheric Polar Vortex-Splitting Event in September 2002”, **J. Atmos. Sci.,**62, 812-821, 2005.

(Franke et al. 2009)
Franke, K., Richter, A., Bovensmann, H., Eyring, V., Jöckel, P. and Burrows, J.P.,“Ship emitted NO2 in the Indian Ocean: Comparison of model results with satellite data”, **Atmos. Chem. Phys.,**9, 7289-7301, 2009.

(Frankenberg et al. 2005)
Frankenberg, C., Meirink, J.F., van Weele, M., Platt, U. and Wagner, T.,„Assessing methane emissions from global space-borne observations”,**Science**, 308, 1010-1014, 2005.

(Frankenberg et al. 2008)
Frankenberg, C., Bergamaschi, P., Butz, A., Houweling, S., Meirink, J.F., Notholt, J., Petersen, A.K., Schrijver, H., Warneke, T. and Aben, I.,„Tropical methane emissions: A revised view from SCIAMACHY onboardENVISAT”, **Geophys. Res. Lett**., 35, L15811, doi:10.1029/ 2008GL034300, 2008.

(Frankenberg et al. 2009)
Frankenberg, C., Yoshimura, K., Warneke, T., Aben, I., Butz, A., Deutscher, N., Griffith, D., Hase, F., Notholt, J., Schneider, M., Schrijver, H. and Röckmann, T.,„Dynamic Processes Governing Lower-Tropospheric HDO/H2O Ratios asObserved from Space and Ground”, **Science**, 325, 1374, DOI: 10.1126/science.1173791, 2009.

(Fu et al. 2008)
Fu, T.-M., Jacob, D.J., Wittrock, F., Burrows, J.P., Vrekoussis, M. and Henze, D.K.,„Global budgets of atmospheric glyoxal and methylglyoxal, and implications for formation of secondary organic aerosols”, **J. Geophys. Res.**, 113, D15303, doi:10.1029/2007JD009505, 2008.

(Gloudemans et al. 2005)
Gloudemans, A.M.S., Schrijver, H., Kleipool, Q., van den Broek, M.M.P., Straume, A.G., Lichtenberg, G., van Hees, R.M., Aben, I. and Meirink, J.F., “The impact of SCIAMACHY instrument calibration on CH4 and CO total columns” **Atmos. Chem. Phys**., 5, 2369-2383, 2005.

(Gloudemans et al. 2009)
Gloudemans, A.M.S., de Laat, A.T.J., Schrijver, H., Aben, I., Meirink, J.F., and van der Werf, G.R.,"SCIAMACHY CO over land and oceans: 2003-2007 inter-annual variability", **Atmos. Chem. Phys**., 9, 3799-3813, 2009.

(Gottwald et al. 2009)
Gottwald, M., Slijkhuis, S., Krieg, E., Schreier, F., Lichtenberg, G., Vasquez, M., Snel, R., Stam, D. and de Kok, R. „Venus Observations with SCIAMACHY", **Proc Atmospheric Science Conference**, Barcelona, Spain, ESA SP-676, 2009.

(Hendrick et al. 2009)
Hendrick, F., Rozanov, A., Johnston, P.V., Bovensmann, H., De Maziere, M., Fayt, C., Hermans, C., Kreher, K., Lotz, W., Sinnhuber, B.-M., Theys, N., Thomas, A., Burrows, J.P. and Van Roozendael, M.,« Multi-year comparison of stratospheric BrO vertical profiles retrieved from SCIAMACHY limb and ground-based UV-visible measurements", **Atmos. Meas. Tech**., 2, 273-285, 2009.

(Kaleschke et al. 2004)
Kaleschke, L., Richter, A., Burrows, J.P., Afe, O., Heygster, G., Notholt, J., Rankin, A.M., Roscoe, H.K., Hollwedel, J., Wagner, T. and Jacobi, H.-W.,"Frost flowers on sea ice as a source of sea salt and their influence on tropospheric halogen chemistry", **Geophys. Res. Lett.**, 31,doi:10.1029/2004GL020655, 2004.

(Kaufmann et al. 2007)
Kaufmann, M., Lehmann, C., Hoffmann, L., Riese, M., Lopez-Puertas, M., Funke, B. and von Savigny, C. „Chemical heating rates derived from SCIAMACHY vibrationally excited OH limb emission spectra", **Adv. Space Res**., 41(11), 1914-1920, 2007.

*(Kim et al. 2006)*Kim, S.-W., Heckel, A., McKeen, S.A., Frost, G.J., Hsie, E.-Y., Trainer, M.K., Richter, A., Burrows, J.P.,Peckham, S.E. and Grell, G.A.,"Satellite observed U.S. power plant NOx emission reductions and their impact on air quality", **Geophys. Res. Lett**., 33, L22812, doi:10.1029/2006GL027749, 2006.

(Kim et al. 2009)
Kim, S.-W., Heckel, A., Frost, G.J., Richter, A., Gleason, J., Burrows, J.P., McKeen, S., Hsie, E.-Y., Granier, C. and Trainer, M."NO2 columns in the western United States observed from space and simulated by a regional chemistry model and their implications for NOx emissions", **J. Geophys. Res**., 114, D11301, doi:10.1029/2008JD011343, 2009.

(Konovalov et al. 2008)
Konovalov, I., Beekmann, M., Burrows, J.P. and Richter, A.,"Satellite measurement based estimates of decadal changes in European nitrogen oxides emissions", **Atmos. Chem. Phys**., 8, 2623-2641, 2008.

(Konovalov et al. 2010)
Konovalov, I.B., Beekmann, M., Richter, A., Burrows, J.P., Hilboll, A.,"Multi-annual changes of NOx emissions in megacity regions: Nonlinear trend analysis of satellite measurement based estimates", **Atmos. Chem. Phys**., 10, 8481-8498, 2010.

(Kühl et al. 2004)
Kühl, S., Dörnbrack, A., Wilms-Grabe, W., Sinnhuber, B.-M., Platt, U. and Wagner, T.,„Observational evidence of rapid chlorine activation by mountain waves above northern Scandinavia",**J. Geophys. Res**.,109, D22309, doi:10.1029/2004JD004797.

(Kühl et al. 2006)

Kühl, S., Wilms-Grabe, W., Frankenberg, C., Grzegorski, M., Platt, U. and Wagner, T.,„Comparison of OClO Nadir Measurements from SCIAMACHY and GOME", **Adv. Space Res.**, 37, 2247-2253, 2006.

(Kühl et al. 2008)
Kühl, S., Puķīte, J., Deutschmann, T., Platt, U. and Wagner, T.,"SCIAMACHY limb measurements of NO2, BrO and OClO. Retrieval of vertical profiles: Algorithm, first results, sensitivity and comparison studies", **Advances in Space Research**, 42, 1747-1764, 2008.

(Loyola et al. 2009)
Loyola, D., Coldewey-Egbers, M., Dameris, M., Garny, H., Stenke, A., Van Roozendael, M., Lerot, C., Balis, D. and Koukouli, M.,"Global long-term monitoring of the ozone layer - a prerequisite for predictions", **Int. J. Rem. Sens**., 30(15), 4295-4318, 2009.

(Marbach et al. 2009)
Marbach, T., Beirle, S., Platt, U., Hoor, P., Wittrock, F., Richter, A., Vrekoussis, M., Grzegorski, M., Burrows, J.P. and Wagner, T.,"Satellite measurements of formaldehyde from shipping emissions", **Atmos. Chem. Phys**., 9, 8223-8234, 2009.

(Meirink et al. 2008)
Meirink, J.F., Bergamaschi, P., Frankenberg, C., d'Amelio, M T.S., Dlugokencky, E.J., Gatti, L.V., Houweling, S., Miller, J.B., Röckmann, T., Villani, M.G. and Krol,M.,"Four-dimensional variational data assimilationfor inverse modelling of atmospheric methane emissions: Analysis ofSCIAMACHY observations", **J. Geophys. Res**., 113, D17301,doi:10.1029/2007JD009740, 2008.

(Mieruch et al. 2008)
Mieruch, S., Noël, S., Bovensmann, H. and Burrows, J.P., "Analysis of global water vapour trends from satellite measurements in the visible spectral range", **Atmos. Chem. Phys**.,8, 491-504, 2008.

(Myriokefalitakis et al. 2008)
Myriokefalitakis, S., Vrekoussis, M., Tsigaridis, K., Wittrock, F., Richter, A., Brühl, C., Volkamer, R., Burrows, J.P. and Kanakidou, M.,"The influence of natural and anthropogenic secondary sources on the glyoxal global distribution", **Atmos. Chem. Phys**.,8, 4965-4981, 2008.

(Newman et al. 2007)
Newman, P.A., Daniel, J.S., Waugh, D.W. and Nash, E.R., “A new formulation of equivalent effective stratospheric chlorine (EESC)”, **Atmos. Chem. Phys**.,7,4537-4552, 2007.

*(*Noël *et al. 2004)*
Noël, S., Buchwitz, M., Bovensmann, H. and Burrows, J.P.,“First retrieval of global water vapour column amounts from SCIAMACHY measurements”, **Atmos. Chem. Phys**.,4,111-125, 2004.

(O’Dowd et al. 2002)
O’Dowd, C.D., Jimenez, J.L., Bahreini, R., Flagan, R.C., Seinfeld, J.H., Hameri, K., Pirjola, L., Kulmala, M., Jennings, S.G. and Hoffmann, T.,“Marine aerosol formation from biogenic iodine emissions”, **Nature**, 417, 632-636, 2002.

(Pagaran et al. 2009)
Pagaran, J.,Weber, M., Burrows, J.P.,“Solar variability from 240 to 1750 nm in terms of faculae brightening and sunspot darkening from SCIAMACHY”, **Astrophys. J**.*,*700, 1884-1895, 2009.

(Piot et al. 2008)
Piot, M. and von Glasow, R.,“The potential importance of frost flowers, recycling on snow, and open leads for ozone depletion events”, **Atmos. Chem. Phys**.,8,2437-2467.

(Pukite et al. 2008)
Puķīte, J., Kühl, S., Deutschmann, T., Platt, U. and Wagner, T.,“Accounting for the effect of horizontal gradients in limb measurements of scattered sunlight”, **Atmos. Chem. Phys**.,8,3045-3060, 2008.

(Rahpoe et al. 2010)
Rahpoe, N., von Savigny, C., Robert, C.E., DeLand, M.T. and Burrows, J.P. “Impact of Solar Proton Events on Noctilucent Clouds”, **J. Atmosph. Sol.-Terr. Phys.,** doi:10.1016/j.jastp.201007017 (in press), 2010.

(Reuter et al. 2010)
Reuter, M., Buchwitz, M., Schneising, O., Heymann, J., Bovensmann, H. and Burrows, J.P., “A method for improved SCIAMACHY CO2 retrieval in the presence of optically thin clouds”, **Atmos. Meas. Tech**., 3, 209-232, 2010.

(Rex et al. 2006)
Rex, M., Salawitch, R.J., Deckelmann, H., von der Gathen, P., Harris, N.R.P., Chipperfield, M.P., Naujokat, B., Reimer, E., Allaart, M., Andersen, S.B., Bevilacqua, R., Braathen, G.O., Claude, H., Davies, J., De Backer, H., Dier, H., Dorokhov, V., Fast, H., Gerding, M., Godin-Beekmann, S., Hoppel, K., Johnson, B., Kyrö, E., Litynska, Z., Moore, D., Nakane, H., Parrondo, M.C., Risley, A.D., Skrivankova, P., Stübi, R., Viatte, P., Yushkov, V., Zerefos, C., “Arctic winter 2005: Implications for stratospheric ozone loss and climate change, **Geophys. Res. Lett**., 33, L23808, doi:10.1029/2006GL026731, 2006.

(Richter et al. 2004)
Richter, A., Eyring, V., Burrows, J.P., Bovensmann, H., Lauer, A., Sierk, B. and Crutzen, P.J., « Satellite Measurements of NO2 from International Shipping Emissions”, **Geophys. Res. Lett**., 31, L23110, doi:10.1029/2004GL020822, 2004.

(Richter et al. 2005a)
Richter, A., Burrows, J.P., Nüß, H., Granier, C. and Niemeier, U.,“Increase in nitrogen dioxide over China observed from space”, **Nature,**437, 129-132, 2005a.

(Richter et al. 2005b)
Richter, A.,Wittrock, F., Weber, M., Beirle, S., Kühl, S., Platt, U., Wagner, T., Wilms-Grabe, W. and Burrows, J.P.,“GOME observations of stratospheric trace gas distributions during the splitting vortex event in the Antarctic winter 2002 Part I: Measurements”, **J. Atm. Sci**.,62, 778-785, 2005b.

(Robert et al. 2010)
Robert, C.E., von Savigny, C., Rahpoe, N., Burrows, J.P., DeLand, M.T. and Schwartz, M.J.,“First evidence of a 27-day signature in noctilucent cloud occurrence frequency”, **J. Geophys. Res**., 115,D00I12, doi:10.1029/2009JD012359, 2010.

(Rohen et al. 2005)
Rohen, G.J., von Savigny, C., Sinnhuber, M., Eichmann, K.-U., Kaiser, J.W., Llewellyn, E.J., Rozanov, A., Bovensmann, H. and Burrows, J.P.,“Impact of the October/November 2003 Solar Proton Events on Mesospheric Ozone: SCIAMACHY Measurement and Model Results”, **J. Geophys. Res**., 110,A09S39, doi:10.1029/2004JA010984, 2005.

(Rozanov et al. 2005)
Rozanov, A., Bovensmann, H., Bracher, A., Hrechanyy, S., Rozanov, V., Sinnhuber, M., Stroh, F., and Burrows, J.P., “NO2 and BrO vertical profiles retrieval from SCIAMACHY limb measurements: Sensitivity studies”, **Adv. Space Res.**, 36, 846-854, doi:10.1016/j.asr.2005.03.013, 2005.

(Saiz-Lopez et al. 2007)
Saiz-Lopez, A., Chance, K., Liu, X., Kurosu, T.P. and Sander, S.P.,“First observations of iodine oxide from space”, **Geophys. Res. Lett**., 34, L12812, doi:10.1029/2007GL030111, 2007.

(von Savigny et al. 2004a)
von Savigny, C., Kokhanovsky, A., Bovensmann, H., Eichmann, K.-U., Kaiser, J.W., Noël, S., Rozanov, A.V., Skupin, J. and Burrows, J.P.,“NLC Detection and Particle Size Determination: First Results from SCIAMACHY on ENVISAT”, **Adv. Space Res.**,

34, 851-856, 2004a.

(von Savigny et al. 2004b)
von Savigny, C., Eichmann, K.-U., Llewellyn, E.J., Bovensmann, H., Burrows, J.P., Bittner, M., Höppner, K., Offermann, D., Steinbrecht, W., Winkler, P., Taylor, M.J. and Cheng, Y."First near-global retrieval of OH rotational temperatures from satellite-based Meinel band emission measurement", **Geophys. Res. Lett**., 31, L15111, doi:10.1029/2004GL020410,2004b.

(von Savigny et al. 2005a)
von Savigny, C., Rozanov, A., Bovensmann, H., Eichmann, K.-U., Noël, S., Rozanov, V.V., Sinnhuber, B.-M., Weber, M. and Burrows, J.P.,« The ozone hole break-up in September 2002 as seen by SCIAMACHY on ENVISAT",*J. Atmosph. Sci.*, 62, 721-734,2005a.

(von Savigny et al. 2005b)
von Savigny, C., Ulasi, E.P., Eichmann, K.-U., Bovensmann, H. and Burrows, J.P.,"Detection and Mapping of Polar Stratospheric Clouds using Limb Scattering Observations", **Atmos. Chem. Phys**.,5,3071-3079,2005b.

(von Savigny et al. 2007a)
von Savigny, C., Sinnhuber, M., Bovensmann, H., Burrows, J.P., Kallenrode, M.-B. and Schwartz, M.J.,"On the Disappearance of Noctilucent Clouds during the January 2005 Solar Proton Events", **Geophys. Res. Lett**., 34, L02805, doi:10.1029/2006GL128106,2007a.

(von Savigny et al. 2007b)
von Savigny, C., Robert, C., Bovensmann, H., Burrows, J.P. and Schwartz, M. "Satellite observations of the quasi 5-day wave in noctilucent clouds and mesopause temperatures", **Geophys. Res. Lett**., 34, L24808, doi:10.1029/2007GL030987,2007b.

(von Savigny et al. 2007)
von Savigny, C. and Burrows, J.P. "Latitudinal variation of NLC particle radii derived from northern hemisphere SCIAMACHY/Envisat limb measurements", **Adv. Space Res.**, 40(6), 765-771, doi:10.1016/j.asr.2007.12.032,2007.

(von Savigny et al. 2009)
von Savigny, C., Robert, C.E., Baumgarten, G., Bovensmann, H. and Burrows, J.P.,"Comparison of NLC particle sizes derived from SCIAMACHY/Envisat observations with ground-based LIDARmeasurements at ALOMAR (69°N)", **Atmos. Meas. Tech**., 2, 523-531,2009.

(Scharringhausen, 2007)
Scharringhausen, M.,"Investigation of mesospheric and thermospheric magnesium species from space", **PhD thesis**, University of Bremen,2007.

(Scharringhausen et al., 2008)
Scharringhausen, M., Aikin, A.C., Burrows, J.P. and Sinnhuber, M.,"Space-borne measurements of mesospheric magnesium species - a retrieval algorithm and preliminary profiles", **Atmos. Chem. Phys**.,8,1963-1983.2008

(Schneising et al., 2008)
Schneising, O., Buchwitz, M., Burrows, J.P., Bovensmann, H., Reuter, M., Notholt, J., Macatangay, R. and Warneke, T.,"Three years of greenhouse gas column-averaged dry air mole fractions retrieved from satellite - Part 1: Carbon dioxide", **Atmos. Chem. Phys**.,8,3827-3853,2008.

(Schneising et al., 2009)
Schneising, O., Buchwitz, M., Burrows, J.P., Bovensmann, H., Bergamaschi, P. and Peters, W. "Three years of greenhouse gascolumn-averaged dry air mole fractions retrieved from satellite - Part 2:Methane", **Atmos. Chem. Phys**.,9,443-465,2009.

(Schönhardt et al., 2008)
Schönhardt, A., Richter, A., Wittrock, F., Kirk, H., Oetjen, H., Roscoe, H.K. and Burrows, J.P.,"Observations of iodine monoxide columns from satellite", **Atmos. Chem. Phys**., 8, 637-653, 2008.

(Schrijver et al., 2009)
Schrijver, H., Gloudemans, A.M.S., Frankenberg, C. and Aben, I. "Water vapour total columns from SCIAMACHY spectra in the 2.36μm window", **Atmos. Meas. Tech**., 2, 561-571,2009.

(Simpson et al., 2007)
Simpson, W.R., von Glasow, R., Riedel, K., Anderson, P., Ariya, P., Bottenheim, J., Burrows, J., Carpenter, L.J., Frieß, U., Goodsite, M.E., Heard, D., Hutterli, M., Jacobi, H.-W., Kaleschke, L., Neff, B., Plane, J., Platt, U., Richter, A., Roscoe, H., Sander, R., Shepson, P., Sodeau, J., Steffen, A., Wagner, T. and Wolff, E.,"Halogens and their role in polar boundary-layer ozone depletion », **Atmos. Chem. Phys**.,7,4375-4418,2007.

(Sinnhuber et al., 2005)
Sinnhuber, B.-M., Rozanov, A., Sheode, N., Afe, O.T., Richter, A., Sinnhuber, M., Wittrock, F., Burrows, J.P., Stiller, G.P., von Clarmann, T. and Linden, A.,"Global observations of stratospheric bromine monoxide from SCIAMACHY", **Geophys. Res. Lett**., 32, L20810, doi: 10.1029/2005GL023839,2005.

(Soris et al., 2006)
Sioris, C.E., Kovalenko, L.K., McLinden, C.A., Salawitch, R.J., Van Roozendael, M., Goutail, F., Dorf, M., Pfeilsticker, K., Chance, K., von Savigny, C., Liu, X., Kurosu, T.P., Pommereau, J.P., Bösch, H. and Frerick J.,« Latitudinal and vertical distribution of bromine monoxide in the lower stratosphere from Scanning Imaging Absorption Spectrometer for Atmospheric Chartography limb

scattering measurements", **J. Geophys. Res**., 111,D14301, doi:10.1029/2005JD006479,2006.

(Skupin et al., 2004)
Skupin, J., Weber, M., Bovensmann, H. and Burrows, J.P.,"The Mg II solar activity proxy indicator derived from GOME and SCIAMACHY", **Proc. ENVISAT and ERS Symposium**, Salzburg, Austria, ESA SP-572,2004.

(Sonkaew et al., 2010)
Sonkaew, T., von Savigny, C., Eichmann, K.-U., Rozanov, A., Weber, M., Bovensmann, H. and Burrows, J.P.. Chemical ozone loss in Arctic and Antarctic polar winter/spring derived from SCIAMACHY limb measurements 2002-2009. *in preparation,* 2010

(Stavrakou et al., 2008)
Stavrakou, T., Müller, J.-F., Boersma, K.F., De Smedt, I. and van der A, R.J.,"Assessing the distribution and growth rates of NOxemission sources by inverting a 10-year record of NO2 satellite columns", **Geophys. Res. Lett**., 35, L10801, doi:10.1029/2008GL033521,2008.

(Stavrakou et al., 2009)
Stavrakou, T., Müller, J.-F., De Smedt, I., Van Roozendael, M., van der Werf, G.R., Giglio, L. and Guenther, A.,„Evaluating the performance of pyrogenic and biogenic emission inventories against one decade of space-based formaldehyde columns", **Atmos. Chem. Phys**.,9,1037-1060, 2009.

(Steinbrecht et al., 2009)
Steinbrecht, W., Claude, H., Schönenborn, F., McDermid, I.S., Leblanc, T., Godin, S., Keckhut, P., van Gijsel, A., Swart, D.P.J., Bodeker, G., Parrish, A., Boyd, I., Kämpfer, N., Hocke, C., Stolarski, R.S. Frith, S.M., Thomason, L.W., Remsberg, E.E., von Savigny, C., Rozanov, A. and Burrows, J.P.,"Ozone and temperature trends in the upper stratosphere at five stations of the Network for the Detection of Atmospheric Composition Change", **Int. J. Rem. Sens**., 30(15-16), 3875-3886,2009.

(Tangborn et al., 2009)
Tangborn, A., Stajner, I., Buchwitz, M., Khlystova, I., Pawson, S., Burrows,.J, Hudman, R., Nedelec, P.,"Assimilation of SCIAMACHY total column CO observations: Global and regional analysis of data impact", **J. Geophys. Res**., 114, D07307.doi10.1029/2008JD010781, 2009.

(Theys et al., 2009)
Theys, N., Van Roozendael, M., Errera, Q., Hendrick, F., Daerden, F., Chabrillat, S., Dorf, M., Pfeilsticker, K., Rozanov, A., Lotz, W., Burrows, J.P., Lambert, J.-C., Goutail, F., Roscoe, H.K. and De Mazière, M.,« A global stratospheric bromine monoxide climatology based on theBASCOE chemical transport model", **Atmos. Chem. Phys**.,9,831-848,2009.

(van der A et al., 2008)
van der A, R.J., Eskes, H.J., Boersma, K.F., van Noije, T.P.C., Van Roozendael, M., De Smedt, I., Peters, D.H.M.U. and Meijer, E.W.,« Trends, seasonal variability and dominant NOx source derived from a ten year record of NO2measured fromspace", **J. Geophys. Res**., 113,D04302, doi:10.1029/2007JD009021,2008.

(Vasilkov et al., 2002)
Vasilkov, A.P., Joiner, J., Gleason, J. and Bhartia, P.K., "Ocean Raman scattering in satellite backscatter UV measurements", **Geophys. Res. Lett**., 29(17), 1837, doi:10.1029/2002GL014955, 2002.

(Viereck et al., 2001)
Viereck, R.A., Puga, L.C., McMullin, D., Judge, D., Weber, M. and Tobiska, W.K, "The Mg II Index: A Proxy for Solar EUV", **Geophys. Res. Lett**., 28, 1343-1346.2001.

(Viereck et al., 2004)
Viereck, R.A., Floyd, L.E., Crane, P.C., Woods, T.N., Knapp, B.G., Rottman, G., Weber, M., Puga, L.C. and DeLand, M.T., "A composite Mg II index spanning from 1978 to 2003", **Space Weather**, 2, S10005, doi:10.1029/2004SW000084, 2004.

(Vountas et al., 2003)
Vountas, M., Richter, A., Wittrock, F. and Burrows, J.P.,"Inelastic scattering in ocean water and its impact on trace gas retrievals from satellite data", **Atmos. Chem. Phys**.,3,1365-1375,2003.

(Vountas et al., 2007)
Vountas, M., Dinter, T., Bracher, A., Sierk, B. and Burrows, J.P., "Spectral studies of ocean water with space-borne sensor SCIAMACHY using Differential Optical Absorption Spectroscopy (DOAS)", **Ocean Sciences**, 3, 429-440, 2007

(Vrekoussis et al., 2009)
Vrekoussis, M., Wittrock, F., Richter, A. and Burrows, J.P.,"Temporal and spatial variability of glyoxal as observed from space", **Atmos. Chem. Phys**.,9,4485-4504,2009.

(Wagner et al., 2001)
Wagner, T., Leue, C., Pfeilsticker, K. and Platt, U.,"Monitoring of the stratospheric chlorine activation by Global Ozone Monitoring Experiment (GOME) OClO measurements in the austral and boreal winters 1995 through 1999", **J. Geophys. Res**., 106,4971-4986,2001.

(Wagner et al., 2007)
Wagner, T., Beirle, S., Deutschmann, T., Grzegorski, M. and Platt, U.,„Satellite monitoring of different vegetation types by differential optical absorption spectroscopy (DOAS) in the red spectral range", **Atmos. Chem. Phys**.,7,69-79, 2007.

(Weber, 1999)
Weber, M.,"Solar activity during solar cycle 23 monitored by GOME", **Proc. European Symposium Atmospheric Measurements from Space (ESAMS'99)**, 1999.

(Wittrock et al., 2006)
Wittrock, F., Richter, A., Oetjen, H., Burrows, J.P., Kanakidou, M., Myriokefalitakis, S., Volkamer, R., Beirle, S., Platt, U. and Wagner, T.,"Simultaneous global observations of glyoxal and formaldehyde from space", **Geophys. Res. Lett**., 33, L16804, doi:10.1029/2006GL026310,2006.

(WMO, 2007)
WMO (World Meteorological Organization). "Scientific Assessment of Ozone Depletion: 2006", **Global Ozone Research and Monitoring Project – Report** No. 50, 572pp., Geneva, Switzerland, 2007.

References Chapter 4

(Azzam and Bashara, 1977)
Azzam, R.M.A. and Bashara, N.M., “Ellipsometry and Polarized Light”, **Elsevier Science Publishers**, Amsterdam, 1997.

(Balzer et al. 1996)
Balzer, W., Aberle, B., Loyola, D. and Spurr, R., “GOME Level 0 to 1b Algorithm Description”, (ER-TN-DLR-GO-0022), **Technical Document**, DLR, 1996.

(Coulson, 1988)
Coulson, K.L., ”Polarisation and intensity of light in the atmosphere”, **A. Deepak Publishing**, Hampton, VA. USA, 1988.

Nuclear Instruments and Methods in Physics Research, 220, 473-478, 1984.

(Kleipool 2003)
Kleipool, Q., “SCIAMACHY: Recalculation of OPTEC 5 Non-Linearity”, (SRON-SCIA-PhE-RP-013), **Technical Document**, SRON, 2003.

(Lichtenberg, 2003)
Lichtenberg, G.,“SCIAMACHY channel 1-5 Memory Effect I: Key data implementation and inflight Measurements”, (SRON-PhE-RP-11), **Technical Document**, SRON, 2003.

(Lichtenberg et al, 2005)
Lichtenberg, G., Kleipool, Q., Krijger, J.M., van Soest, G., van Hees, R., Tilstra, L.G., Acarreta, J.R., Aben, I., Ahlers, B., Bovensmann, H., Chance, K., Gloudemans, A.M.S., Hoogeveen, R.W.M., Jongma, R., Noël, S., Piters, A., Schrijver, H., Schrijvers, C., Sioris, C.E., Skupin, J., Slijkhuis, S., Stammes, P. and Wuttke, M., “SCIAMACHY Level 1 data: Calibration concept and in-flight calibration”, **Atmos. Chem. Phys**., 6, 5347-5367, 2005.

(Mc Linden et al., 2002)
McLinden, C.A., McConnell, J.C., Griffioen, E. and McElroy, C.T.,“A vector radiative-transfer model for the Odin/OSIRIS project”, **Can. J. Phys**., 80, 375-393, 2002.

(*Noël et al. 2003*)
Noël, S., Bovensmann, H., Skupin, J., Wuttke, M.W., Burrows, J.P., Gottwald, M. and Krieg, E., ”The SCIAMACHY calibration/monitoring concept and first results”, **Adv. Space Res.**, 32, 2123-2128, 2003.

(Schutgens and Stammes, 2002)
Schutgens, N.A.J. and Stammes, P., "Parametrisation of Earth’s polarisation spectrum from 290 to 330 nm”, **J. Quant. Spectr. Rad. Transfer**, 75, 239-255, 2002.

(Schutgens et al., 2004)
Schutgens, N.A.J., Tilstra, L.G., Stammes, P. and Bréon, F.-M., "On the relationship between Stokes parameters Q and U of atmospheric ultraviolet/visible/near-infrared radiation”, **J. Geophys. Res.**,109, D09205, doi:10.1029/2003JD004081, 2004.

(Slijkhuis, 2000a)
Slijkhuis, S., “ENVISAT-1 SCIAMACHY Level 0 to 1c Processing: Algorithm Theoretical Basis Document”, **Technical Document**, DLR, 2000.

(Slijkhuis, 2000b)
Slijkhuis, S., “Calculation of Polarisation from Rayleigh Single Scattering”, (ENV-TN-DLRSCIA-0043), **Technical Document**, DLR, 2000.

(Tanzi,1999)
Tanzi, C.P., “Considerations on Stokes parameters derived from memo ‘The seventh point polarisation algorithm by P. Stammes’. **Internal Report**, SRON, 1999.

(Tilstra et al., 2003)
Tilstra, L.G., Schutgens, N.A.J. and Stammes, P., “Analytical calculation of Stokes parameters Q and U of atmospheric radiation”, (WR-2003-01), **Scientific Report**, KNMI, 2003.

References Chapter 5

(Acarreta et al. 2004a)
Acarreta, J.R, J.F. de Haan, P. Stammes, “Cloud pressure retrieval using O2 – O2 absorption band at 477 nm”, **J. Geophys. Res.**, 109, D05204, doi:10.1029/2003JD003915, 2004

(Acarreta et al. 2004b)
Acarreta, J.R., P. Stammes, W.H. Knap, “First retrieval of cloud phase from SCIAMACHY spectra around 1.6 micron”, **Atmos. Res.**, 72, 89-105, 2004

(Amekudzi et al. 2005a)
Amekudzi L.K., A. Bracher, J. Meyer, A. Rozanov, H. Bovensmann, J.P. Burrows, “Lunar occultation with SCIAMACHY: First retrieval results”, **Adv. Space Res.**, 36, 906-914, 2005

(Amekudzi et al. 2005b)
Amekudzi, L.K., B.-M. Sinnhuber, N.V. Sheode, J. Meyer, A. Rozanov, L. Lamsal, H. Bovensmann, J.P. Burrows, “Retrieval of stratospheric NO3 vertical profiles from SCIAMACHY lunar occultation measurement over the Antarctic”, **J. Geophys. Res.**,110, D20304, doi:10.1029/2004JD005748, 2005

(Asano et al. 1995)
Asano, S., M. Shiobara, A. Uchiyama, “Estimation of cloud physical parameters from airborne solar spectral reflectance measurements for stratocumulus clouds”, **J. Atmos. Sci.**, 52, 3556-3576, 1995

(Boersma et al., 2004)
Boersma, K.F., H.J. Eskes and E.J. Brinksma, “Error analysis for tropospheric NO2 retrieval from space”, **J. Geophys. Res.**, 109, D04311, doi:10.1029/2003JD003962, 2004

(Borell et al. 2003)
Borrell, P., J.P. Burrows, U. Platt, A. Richter, T. Wagner, “New Directions: New Developments in Satellite Capabilities for Probing the Chemistry of the Troposphere”, **Atmos. Environ.**, 37, 2567-2570, 2003

(Bracher et al., 2005)
Bracher, A., M. Sinnhuber, A. Rozanov, J. P. Burrows, “NO2 Modelling used for the comparison of NO2 Satellite Measurements at different Solar Zenigh Angles”, **Atmos. Chem. Phys.**, 4, 5515-5548, 2005

(Buchwitz et al. 2000)
Buchwitz, M., V.V. Rozanov, J.P. Burrows, “A near-infrared optimized DOAS method for the fast global retrieval of atmospheric CH4, CO, CO2, H2O, and N2O total column amounts from SCIAMACHY Envisat-1 nadir radiances”, **J. Geophys. Res.**, 105, 15231-15245, 2000

(Burrows et al. 1999)
Burrows, J.P., M. Weber, M. Buchwitz, V. Rozanov, A. Ladstätter-Weißenmayer, A. Richter, R. DeBeek, R. Hoogen, K. Bramstedt, K.-U. Eichmann, M. Eisinger, D. Perner, “The Global Ozone Monitoring Experiment (GOME): Mission Concept and First Scientific Results”, **J. Atmos. Sci.**,56, 151-175, 1999

(de Beek et al. 2001)
de Beek, R., M. Vountas, V.V. Rozanov, A. Richter, J.P. Burrows, “The Ring effect in the cloudy atmosphere”, **Geophys. Res. Lett.**, 28, 721-724, 2001

(de Beek et al. 2006)
de Beek, R., M. Buchwitz, S. Noël, J.P. Burrows, H. Bovensmann, M. Bruns, H. Bremer, P. Bergamaschi, S. Körner, M. Heimann, “Atmospheric carbon gases retrieved from SCIAMACHY by WFM-DOAS: improved global CO and CH4 and initial verification of CO2 over Park Falls (46° N, 90° W)”, **Atmos. Chem. Phys. Discuss.**, 6, 363-399, 2006

(de Graaf et al. 2005)
de Graaf, M., P. Stammes, R.B.A. Koelemeijer, O. Torres, “Absorbing Aerosol Index: sensitivity analysis, application to GOME and comparison with TOMS”, **J. Geophys. Res.**, 110, D01201, doi:10.1029/2004JD005178, 2005

(de Graaf and Stammes 2005)
de Graaf, M., P. Stammes, “SCIAMACHY Absorbing Aerosol Index – calibration issues and global results from 2002-2004”, **Atmos. Chem. Phys.**,5, 2385-2394, 2005

(de Laat et al. 2006)
de Laat, A.T.J., A.M.S. Gloudemans, H. Schrijver, M.M.P. van den Broek, J.F. Meirink, I. Aben, M. Krol, “Quantitative analysis of SCIAMACHY total carbon monoxide column measurements”, **Geophys. Res. Lett.**, 33, L07807, doi:10.1029/2005GL025530, 2006

(Doicu et al. 2002)
Doicu A., F. Schreier, M. Hess, "Iteratively regularized Gauss-Newton method for atmospheric remote sensing", **Comp. Phys. Comm.**, 148, 214-226, 2002

(Doicu 2005)
Doicu A., "SCIAMACHY Level 1b to 2 OFL Processing Algorithm Change Description Document Limb Profile Retrieval Algorithm", ENV-TN-DLR-SCIA-0062 Issue 1, **Technical Document**, DLR, 2005

(Dorf et al. 2005)
Dorf, M., H. Bösch, A. Butz, C. Camy-Peyret, M.P. Chipperfield, A. Engel, F. Goutail, K. Grunow, F. Hendrick, S. Hrechanyy, B. Naujokat, J.-P. Pommereau, M. Van Roozendael, C. Sioris, F. Stroh, F. Weidner, K. Pfeilsticker, "Balloon-borne stratospheric BrO measurements: comparison with Envisat/SCIAMACHY BrO limb profiles", **Atmos. Chem. Phys. Discuss.**, 5, 13011-13052, 2005

(Eskes et al. 2002)
Eskes, H.J., P.F.J. van Velthoven, H.M. Kelder, "Global ozone forecasting based on ERS-2 GOME observations", **Atmos. Chem. Phys**., 2, 271-278, 2002

(Eskes et al. 2003)
Eskes, H. J., P.F.J. van Velthoven, P.J.M. Valks, H.M. Kelder, "Assimilation of GOME total ozone satellite observations in a three-dimensional tracer transport model", **Quart. J. Roy. Meteorol. Soc.**, 129, 1663-1681, 2003

(Eskes et al. 2005)
Eskes, H.J., R.J. van der A, E.J. Brinksma, J.P. Veefkind, J.F. de Haan, P.J.M. Valks, "Retrieval and validation of ozone columns derived from measurements of SCIAMACHY on Envisat", **Atmos. Chem. Phys. Discuss**., 5, 4429-4475, 2005

(Flittner et al. 2000)
Flittner, D. E., P. K. Bhartia, B. M. Herman, "O3 profiles retrieved from limb scatter measurements: Theory", **Geophys. Res. Lett.**, 27, 2061-2064, 2000

(Fournier et al., 2006)
Fournier, N., P. Stammes, M. de Graaf, R. van der A, A. Piters, M. Grzegorski, A. Kokhanovsky, "Improving cloud information over deserts from SCIAMACHY Oxygen A-band measurements",**Atmos. Chem. Phys.**, 6, 163-172, 2006

(Frankenberg et al. 2005a)
Frankenberg, C., U. Platt, T. Wagner, "Iterative maximum a posteriori (IMAP)-DOAS for retrieval of strongly absorbing trace gases: Model studies for CH4 and CO2 retrieval from near infrared spectra of SCIAMACHY onboard ENVISAT", **Atmos. Chem. Phys.**, 5, 9–22, 2005

(Frankenberg et al. 2005b)
Frankenberg, C., U. Platt, T. Wagner, "Retrieval of CO from SCIAMACHY onboard ENVISAT: detection of strongly polluted areas and seasonal patterns in global CO abundances", **Atmos. Chem. Phys.**, 5, 1639–1644, 2005

(Gloudemans et al. 2005)
Gloudemans, A.M.S., H. Schrijver, Q. Kleipool, M.M.P. van den Broek, A.G. Straume, G. Lichtenberg, R.M. van Hees, I. Aben J.F. Meirink, "The impact of SCIAMACHY instrument calibration on CH4 and CO total columns", **Atmos. Chem. Phys.**, 5, 2369-2383, 2005

(Grzegorski et al. 2004).
Grzegorski, M., C. Frankenberg, U. Platt, M. Wenig, N. Fournier, P. Stammes, T. Wagner, "Determination of cloud parameters from SCIAMACHY data for the correction of tropospheric trace gases", **Proceedings of the ENVISAT & ERS Symposium**, Salzburg, Austria, ESA publication SP-572, 2004

(Herman et al. 1997)
Herman, J.R., P.K. Bhartia, O. Torres, C. Hsu, C. Seftor, E.A. Celarier, "Global distributions of UV-absorbing aerosols from NIMBUS 7/TOMS data", **J. Geophys. Res.**, 102, 16911-16922, 1997

(Holzer-Popp et al. 2002a)
Holzer-Popp, T., M. Schroedter, G. Gesell, "Retrieving aerosol optical depth and type in the boundary layer over land and ocean from simultaneous GOME spectrometer and ATSR-2 radiometer measurements, 1, Method description", **J. Geophys. Res.**, 107, doi:10.1029/2001JD002013, 2002

(Holzer-Popp et al. 2002b)
Holzer-Popp, T., M. Schroedter, G. Gesell, "Retrieving aerosol optical depth and type in the boundary layer over land and ocean from simultaneous GOME spectrometer and ATSR-2 radiometer measurements, 2, Case study application and validation", **J. Geophys. Res.**, 107, doi:10.1029/2002JD002777, 2002

(Hoogen et al. 1999)
Hoogen, R., V.V. Rozanov, J.P. Burrows, "Ozone profiles from GOME satellite data: algorithm description and first validation", **J. Geophys. Res.**, 104, 8263–8280, 1999

(Houweling et al. 2005)
Houweling, S., W. Hartmann, I. Aben, H. Schrijver, J. Skidmore, G.-J. Roelofs, F.-M. Breon, "Evidence of systematic errors in SCIAMACHY-observed CO2 due to aerosols", **Atmos. Chem. Phys.**, 5, 3003-3013, 2005

(Joiner et al. 1995)
Joiner, J., P.K. Bhartia, R.P. Cebula, E. Hilsenrath, R.D. McPeters, H. Park, “Rotational Raman scattering (ring effect) in satellite backscatter ultraviolet measurements”, **Appl. Opt.**, 34, 4513–4525, 1995

(Kaiser and Burrows 2003)
Kaiser, J.W., J.P. Burrows, “Fast weighting functions for retrievals from limb scattering measurements”, **J. Quant. Spectr. Rad. Transfer**, 77, 273-283, 2003

(Knap et al. 2002)
Knap, W.H, P. Stammes, R.B.A. Koelemeijer, “Cloud thermodynamic phase determination from near-infrared spectra of reflected sunlight”, **J. Atmos. Sci.**, 59, 83-96, 2002

(Koelemeijer et al. 2001)
Koelemeijer, R.B.A., P. Stammes, J.W. Hovenier, J.F. de Haan, “A fast method for retrieval of cloud parameters using oxygen A band measurements from the Global Ozone Monitoring Experiment”, **J. Geophys. Res.**, 106, 3475-3490, 2001

(Kokhanovsky and Rozanov 2005)
Kokhanovsky, A.A., V.V. Rozanov, “Cloud bottom altitude determination from a satellite”, **IEEE Transactions on Geoscience and Remote Sensing Letters**, 2, 280-283, 2005

(Kokhanovsky et al. 2005)
Kokhanovsky, A.A., V.V. Rozanov, T. Nauss, C. Reudenbach, J.S. Daniel, H.L. Miller, J.P. Burrows, 2005, “The semianalytical cloud retrieval algorithm for SCIAMACHY: I. Validation”, **Atmos. Chem. Phys. Discuss.**, 5, 1995-2015, 2005

(Kokhanovsky et al. 2006)
Kokhanovsky, A.A., W. von Hoyningen-Huene, V.V. Rozanov, S. Noël, K. Gerilowski, H. Bovensmann, K. Bramstedt, M. Buchwitz, J.P. Burrows, “The semianalytical cloud retrieval algorithm for SCIAMACHY II. The application to MERIS and SCIAMACHY data”, **Atmos. Chem. Phys. Discuss.**, 6, 1813–1840, 2006

(Krijger et al. 2005)
Krijger, J.M., I. Aben, H. Schrijver, “Distinction between clouds and ice/snow covered surfaces in the identification of cloud-free observations using SCIAMACHY PMDs”, **Atmos. Chem. Phys.,**5, 2729-2738, 2005

(Lenoble 1985)
Lenoble, J., “Radiative Transfer in Scattering and Absorbing Atmospheres”, pp. 34-82, A. DEEPAK Publishing, Hampton, Virginia, 1985

(Liou 2002)
Liou, K.N., “An Introduction to Atmospheric Radiation”, Academic Press, **International Geophysical Series**, Vol. 84, 2002

(Loyola 1998)
Loyola, D., “A New Cloud Recognition Algorithm for Optical Sensors”, **IEEE International Geoscience and Remote Sensing Symposium, IGARSS’98 Digest**, Volume II, 572–574, 1998

(Martin et al. 2002)
Martin, R.V., K. Chance, D.J. Jacob, T.P. Kurosu, R.J.D. Spurr, E. Bucsela, J.F. Gleason, P.I. Palmer, I. Bey, A.M. Fiore, Q. Li, R.M. Yantosca, R.B.A. Koelemeijer,“An improved retrieval of tropospheric nitrogen dioxide from GOME”, **J. Geophys. Res.**, 107, 4437-4456, doi:10.1029/2001JD001027, 2002

(Meyer et al. 2005)
Meyer J., A. Bracher, A. Rozanov, A.C. Schlesier, H. Bovensmann, J.P. Burrows, “Solar occultation with SCIAMACHY: algorithm description and first validation”, **Atmos. Chem. Phys.**, 5, 1589-1604, 2005

(Munro et al. 1998)
Munro, R., R. Siddans, W.J. Reburn, B. Kerridge, “Direct measurement of tropospheric ozone from space”, **Nature**, 392, 168-171, 1998

(Nakajima and King 1990)
Nakajima, T., M.D. King, “Determination of the optical thickness and effective particle radius of clouds from reflected solar radiation measurements. Part I: Theory”, **J. Atmos. Sci**., 47, 1878-1893, 1990

(Noël et al. 2004)
Noël, S., M. Buchwitz, H. Bovensmann, J.P. Burrows, “First retrieval of global water vapour column amounts from SCIAMACHY measurements”, **Atmos. Chem. Phys.**, 4, 111-125, 2004

(Platnick et al. 2003)
Platnick, S., M.D. King, S.A. Ackerman, W.P. Menzel, B.A. Baum, J.C. Riedi, R.A. Frey, “The MODIS cloud products: Algorithms and examples from Terra”, **IEEE Transactions on Geoscience and Remote Sensing**, 41, 459-473, 2003

(Platt 1994)
Platt, U., “Differential optical absorption spectroscopy (DOAS), in Air Monitoring by Spectroscopic Techniques”, **Chem. Anal. Ser.**, 127, edited by M. W. Sigrist, John Wiley, New York, 1994

(Pöschl 2005)

Pöschl, U., "Atmospheric Aerosols: Composition, Transformation, Climate and Health Effects", **Angew. Chem. Int. Ed.**, 44, 7520-7540, 2005

(Richter and Burrows 2002)
Richter, A., J.P. Burrows, "Retrieval of Tropospheric NO2 from GOME Measurements", **Adv. Space Res.**, 29,1673-1683, 2002

(Richter et al. 2005)
Richter, A., J.P. Burrows, H. Nüß, C. Granier, U. Niemeier, "Increase in nitrogen dioxide over China observed from space", **Nature**, 437, 129-132, 2005

(Rodgers 2000)
Rodgers, C.D., "Inverse Methods for Atmospheric Sounding: Theory and Practice", 1st ed., World Sci., River Edge, N.J., 2000

(Rohen et al. 2006)
Rohen, G., C. von Savigny, K.-U. Eichmann, E. J. Llewellyn, A. Bracher, J.P. Burrows, "Retrieval of mesospheric ozone profiles from SCIAMACHY limb scattering observations: Theory, first validation results and ozone depletion during the Oct./Nov. 2003 solar proton event", **Adv. Space Res**., in press, 2006

(Rozanov et al. 1998)
Rozanov, V.V., T. Kurosu, J.P. Burrows, "Retrieval of atmospheric constituents in the UV-visible: A new quasi-analytical approach for the calculation of weighting functions", **J. Quant. Spectr. Rad. Transfer**, 60, 277-299, 1998

(Rozanov et al. 2001)
Rozanov, A., V. Rozanov, J.P. Burrows, "A numerical radiative transfer model for a spherical planetary atmosphere: Combined differential-integral approach involving the Picard iterative approximation", **J. Quant. Spectr. Rad. Transfer**, 69, 491-512, 2001

(Rozanov and Kokhanovsky 2004)
Rozanov, V.V., A.A. Kokhanovsky, "Semi-analytical cloud retrieval algorithm as applied to the cloud top altitude and the cloud geometrical thickness determination from top-of-atmosphere reflectance measurements in the oxygen A-band", **J. Geophys. Res.**, 109, D05202, 10.1029/2003JD004104, 2004

(Rozanov et al. 2005a)
Rozanov, A., V. Rozanov, M. Buchwitz, A. Kokhanovsky, J.P. Burrows, "SCIATRAN 2.0 – A new radiative transfer model for geophysical applications in the 175 – 2400 nm spectral region", **Adv. Space Res.**, 36, 1015–1019, 2005

(Rozanov et al. 2005b)
Rozanov, A., H. Bovensmann, A. Bracher, S. Hrechany, V. Rozanov, M. Sinnhuber, F. Stroh, J.P. Burrows, "NO2 and BrO vertical profile retrieval from SCIAMACHY limb measurements: sensitivity studies", **Adv. Space Res.**, 36, 846–854, 2005

(Sierk et al. 2006)
Sierk, B., A. Richter, A. Rozanov, C. von Savigny, A.M. Schmoltner, M. Buchwitz, H. Bovensmann, J.P. Burrows, "Retrieval and Monitoring of atmospheric trace gas concentrations in nadir and limb geometry using the space-borne SCIAMACHY instrument", **Environ. Mon. Assess.**, in press, 2006

(Sioris et al. 2004)
Sioris, C.E., T.P. Kurosu, R.V. Martin, K. Chance, "Stratospheric and tropospheric NO2 observed by SCIAMACHY: First results", **Adv. Space Res.**, 34, 780-785, 2004

(Solomon et al. 1987)
Solomon, S., A.L. Schmeltekopf, R.W. Sanders, "On the interpretation of zenith sky absorption measurements", **J. Geophys. Res.**, 92, 8311–8319, 1987

(Spurr 2000)
Spurr, R.J.D., "ENVISAT-1 SCIAMACHY Level 1c to 2 Processing, Algorithm Technical Basis Document", ENV-ATB-SAO-SCIA-2200-0003, **Technical Document**, DLR, 2000
available at http://atmos.caf.dlr.de/

(Spurr et al. 2001)
Spurr, R.J.D., T.P. Kurosu, K.V. Chance, "A linearized discrete ordinate radiative transfer model for atmospheric remote-sensing retrieval," **J. Quant. Spect. Rad. Transfer**, 68, 689-735, 2001

(Stammes 2001)
Stammes, P., "Spectral radiance modelling in the UV-Visible range, in: *IRS 2000: Current problems in Atmospheric Radiation*", Eds. W.L. Smith and Y.M. Timofeyev, A. Deepak Publ., Hampton, VA, pp. 385-388, 2001

(Van Roozendael et al. 2006)
van Roozendael, M., R.S.P. Spurr, C. Lerot, D. Loyola, T. Schröder, A. von Bargen, "SCIAMACHY Level 1b-2 Off-line Data Processing: Algorithm Theoretical Baseline Document for Trace Gas Retreival from UV/VIS Nadir Spectra", ENV-ATB-BIR-SCIA-0074, **Technical Document**, 2006

(Velders et al. 2001)
Velders, G.J.M., C. Granier, R.W. Portmann, K. Pfeilsticker, M. Wenig, T. Wagner, U. Platt, A. Richter, J.P. Burrows,"Global tropospheric NO2 column distributions: Comparing 3-D model calculations with GOME measurements", **J. Geophys. Res.**, 106, 12643-12660, 2001

(von Hoyningen-Huene et al. 2003)
von Hoyningen-Huene, W., M. Freitag, J.P. Burrows, “Retrieval of aerosol optical thickness over land surfaces from top-of-atmosphere radiance”, **J. Geophys. Res.**, 108, doi:10.1029/2001JD002018, 2003

(von Hoyningen-Huene et al. 2006)
von Hoyningen-Huene, W., A.A. Kokhanovsky, M. Wuttke, M. Buchwitz, S. Noël, K. Gerilowski, J.P. Burrows, B. Latter, R. Siddans, B.J. Kerridge, “Validation of SCIAMACHY top-of-atmosphere reflectance for aerosol remote sensing using MERIS L1 data”, **Atmos. Chem. Phys. Discuss.**,6, 673-699, 2006

(von Savigny et al. 2004a)
von Savigny, C., A. Kokhanovsky, H. Bovensmann, K.-U. Eichmann, J.W. Kaiser, S. Noël, A.V. Rozanov, J. Skupin, J.P. Burrows, “NLC Detection and Particle Size Determination: First Results from SCIAMACHY on ENVISAT”, **Adv. Space Res.**, 34, 851-856, 2004

(von Savigny et al. 2004b)
von Savigny, C., K.-U. Eichmann, E.J. Llewellyn, H. Bovensmann, J.P. Burrows, M. Bittner, K. Höppner, D. Offermann, W. Steinbrecht, P. Winkler, M.J. Taylor, Y. Cheng, “First near-global retrieval of OH rotational temperatures from satellite-based Meinel band emission measurements”, **Geophys. Res. Lett**., 31, L15111, doi:10.1029/2004GL, 2004

(von Savigny et al. 2005a)
von Savigny, C., A. Rozanov, H. Bovensmann, K.-U. Eichmann, S. Noël, V.V. Rozanov, B.-M. Sinnhuber, M. Weber, J.P. Burrows, “The ozone hole break-up in September 2002 as seen by SCIAMACHY on ENVISAT”, **J. Atmos..Sci**., 62, 721 – 734, 2005

(von Savigny et al. 2005b)
von Savigny, C., E.P. Ulasi, K.-U. Eichmann, H. Bovensmann, J.P. Burrows, “Detection and Mapping of Polar Stratospheric Clouds using Limb Scattering Observations”, **Atmos. Chem. Phys.**, 5, 3071-3079, 2005

(Weber et al. 2005)
Weber, M., L.N. Lamsal, M. Coldewey-Egbers, K. Bramstedt, J.P. Burrows, “Pole-to-pole validation of GOME WFDOAS total ozone with groundbased data”, **Atmos. Chem. Phys.**, 5, 1341-1355, 2005

(Yamamoto and Wark 1961)
Yamamoto, G,A. D.Q. Wark, “Discussion of the letter by R.A. Hanel: *Determination of cloud altitude from satellite*”, **J. Geophys. Res.**, 66, 3596, 1961

(Yan 2005)
Yan, X., “A fast SCIAMACHY PMD Cloud Algorithm (SPCA)”, **Master Thesis**, University of Bremen, 2005

References Chapter 6

(Bogumil et al. 2003)
Bogumil, K., J. Orphal, T. Homann, S. Voigt, P. Spietz, O. C. Fleischmann, A. Vogel, M. Hartmann, H. Bovensmann, J. Frerik and J.P. Burrows, “Measurements of Molecular Absorption Spectra with the SCIAMACHY Pre-Flight Model: Instrument Characterization and Reference Data for Atmospheric Remote-Sensing in the 230-2380 nm Region”, **J. Photochem. Photobiol. A**., 157, 167-184, 2003.

(Bramstedt 2008)
K. Bramstedt, "Calculation of SCIAMACHY M-Factors“, Technical Note, IFE-SCIA-TN-2007-01-CalcMFactor, Issue: 1, 2008. (http://www.iup.uni-bremen.de/sciamachy/mfactors/mfactor-TN-1-0.pdf)

(Chance and Spurr 1997)
Chance, K. V. and Spurr, R. J. D., “Ring effect studies: Rayleigh scattering, including molecular parameters for rotational Raman scattering, and the Fraunhofer spectrum”, **App. Opt**., 5224-5230, 1997.

(Fleischmann et al. 2004)
Fleischmann, O.C., M. Hartmann, J.P. Burrows and J. Orphal, “New ultraviolet absorption cross-sections of BrO at atmospheric temperatures measured by time-windowing Fourier transform spectroscopy”, **J. Photochem. Photobiol. A**, 168, 117-132, 2004.

(Greenblatt et al. 1990)
Greenblatt, G. D. and Orlando, J. J. and Burkholder, J. B. and Ravishankara, A. R., “Absorption measurements of oxygen between 330 and 1140 nm”, **J. Geophys. Res.,** 18577-18582, 1990.

(Hermans 1999)
Hermans, C., Vandaele, A. C., Carleer, M., Fally, S., Colin, R., Jenouvrier, A., Coquart, B., and Mèrienne, M.-F.: Absorption cross-sections of atmospheric constituents: NO2, O2, and H2O, Environ. Sci. Pollut. R., 6, 151-158, 1999.

(Kromminga 2003)
Kromminga, H., Orphal, J., Spietz, P., Voigt, S., and Burrows, J. P.: The temperature dependence (213-293 K) of the absorption cross-sections of OClO in the 340-450 nm region measured by Fourier-transform spectroscopy, **J. Photochem. Photobiol. A**., 157, 149-160, 2003.

(Lambert et al. 2000)
Lambert, J.-C., J. Granville, M. Van Roozendael, J.-F.Müller, F. Goutail, J.-P. Pommereau, A. Sarkissian, P. V. Johnston, and J. M. Russell III, “Global Behaviour of Atmospheric NO2 as Derived from the Integrated Use of Satellite, Ground-based Network and Balloon Observations”, in Atmospheric Ozone - 19th Quad. Ozone Symp., Sapporo, Japan, 2000, Ed. by NASDA, 201-202, 2000.

(Lerot et al. 2009)
Lerot, C., M. Van Roozendael, J. van Geffen, J. van Gent, C. Fayt, R. Spurr, G. Lichtenberg, and A. von Bargen, “Six years of total ozone column measurements from SCIAMACHY nadir observations”, **Atmos. Meas. Tech.**, 2, 87-98, 2009.

(McLinden 2000)
McLinden CA., Routine for generating model atmospheres. Personal Communication, 2000.

(Noel 1999)
Noël, S., Buchwitz, M., Bovensmann, H., Hoogen, R., and Burrows, J. P.: Atmospheric water vapor amounts retrieved from GOME satellite data, **Geophys. Res. Lett.**, 26, 1841-1844, doi:10.1029/1999GL900437, 1999.

(Platt 1994)
Platt, U.: Differential optical absorption spectroscopy (DOAS): in Air Monitoring by Spectroscopic Techniques, John Willey, New York, 1994.

(Richter 2006)
A. Richter, Algorithm Description SCIAMACHY SO2 Vertical Columns, University of Bremen, available from: http://www.iup.uni-bremen.de/doas/manuals/ad_iup_bremen_so2_nadir.pdf, 2006.

(Schreier 2001)
Schreier, F., and B. Schimpf, A new efficient line-by-line code for high resolution atmospheric radiation computations incl. derivatives. In W.L. Smith and Y. Timofeyev, editors, IRS 2000: Current Problems in Atmospheric Radiation, p. 381-384. A. Deepak Publishing, 2001.

(Theys 2008)
Theys, N., van Roozendael, M., Errera, Q., Hendrick, F., Daerden, F., Chabrillat, S., Dorf, M., Pfeilsticker, K., Rozanov, A., Lotz, W., Burrows, J. P., Lambert, J.-C., Goutail, F., Roscoe, H. K., and de Mazière, M.: A global stratospheric bromine monoxide climatology based on the BASCOE chemical transport model, Atmospheric Chemistry & Physics Discussions, 8, 17 581—17 629, 2008.

(Vandaele et al. 1994)
Vandaele, A.C., P.C. Simon, J.M. Guilmot, M. Carleer, R. Colin SO2 absorption cross section measurement in the UV using a Fourier transform spectrometer, **J. Geophys. Res.**, 99(D12), 25599-25606, 1994.

(Van Roozendael et al. 2006)
Van Roozendael, M., Loyola, D., Spurr, R., Balis, D., Lambert, J.-C., Livschitz, Y., Valks, P., Ruppert, T., Kenter, P., Fayt, C., and Zehner, C, “Ten years of GOME/ERS-2 total ozone data – The new GOME data processor (GDP) version 4: 1. Algorithm description”, **J. Geophys. Res.**, 111, D14311, doi:10.1029/2005JD006375, 2006.

(Vountas et al. 1998)
Vountas, M., V.V. Rozanov and J.P. Burrows,“Ring effect: impact of rotational Raman scattering on radiative transfer in Earth's atmosphere”, **J. Quant. Spectrosc. Radiat.Transfer**,60, 943-961, 1998.

Atmospheric Gases

ANNEX 2: Atmospheric Gases

Atmospheric Gases

BrO	Bromine oxide
CFC	Chlorofluorocarbon
CFC11	Trichlorofluoromethane
CHOCHO	Glyoxal
CH4	Methane
CH3CN	Acetonitrile
ClO	Chlorine monoxide
CO2	Carbon dioxide
HCHO	Formaldehyde
HCl	Hydrogen chloride
HCN	Hydrogen cyanide
HF	Hydrofluor
HFC	Hydrofluorocarbon
HNO3	Nitric acid
H2O	Water vapour
IO	Iodine oxide
NAT	Nitric acid trihydrate
NO	Nitric oxide
NO2	Nitrogen dioxide
NO3	Nitrate radical
N2O	Nitrous oxide
OClO	Chlorine dioxide
OH	Hydroxyl radical
O3	Ozone
O2	Oxygen (molecular)
O2(1D)	Oxygen (singlet delta)
O4	Oxygen (dimer)
SO2	Sulphur dioxide

Abbreviations and Acronyms

ANNEX 3: Abbreviations and Acronyms

A	
AAI	Absorbing Aerosol Index
AATSR	Advanced Along Track Scanning Radiometer
ACE	Atmosphere Climate Experiment
ACVT	Atmospheric Chemistry Validation Team
ADC	Analogue-to-Digital Converter
ADEOS	Advanced Earth Observing System
ADS	Annotation Data Set
AMAX-DOAS	Airborne MAXDOAS
AMC-DOAS	Air Mass Corrected DOAS
AMF	Airmass Factor
AMON	Absorption par les Minoritaires Ozone et NOx
ANX	Ascending Node Crossing
AO	Announcement of Opportunity
AO	Analogue Offset
AOI	Announcement of Opportunity Instrument
AOP	AO Instrument Provider
AOT	Aerosol Optical Thickness
APSM	Aperture Stop Mechanism
ARCF	Absolute Radiometric Calibration Facility
ASAR	Advanced Synthetic Aperture Radar
ASI	Agenzia Spaziale Italiana
ASM	Azimuth Scan Mechanism
ASUR	Airborne Submillimeter Radiometer
ATBD	Algorithm Technical Basis Document
ATC	Active Thermal Control
ATSR	Along-Track Scanning Radiometer
AU	Astronomical Unit
AZACM	Azimuth Aperture Cover Mechanism

B	
BAER	Bremen Aerosol Retrieval
BCPS	Broadcast Pulse
BDM	Bad and Dead Pixel Mask
BIRA-IASB	Belgisch Instituut voor Ruimte-Aeronomie / Institut d'Aeronomie Spatiale de Belgique
BMFT	Bundesministerium fur Forschung und Technologie
BOL	Begin-of-Life
BONBON	balloon-borne cryogenic whole-air-sampler for the collection of air samples in the stratosphere

BU	Binary Unit
BUV	Backscattered Ultraviolet
C	
CA	Corrective Action
CARIBIC	Civil Aircraft for the Regular Investigation of the Atmosphere Based on an Instrument Container
C&C	Command & Control
CCA	Communication Area
CF	Cloud Fraction
CGT	Cloud Geometrical Thickness
CLRTAP	Convention on Long-Range Transboundary Air Pollution
CNES	Centre Nationale d'Etudes Spatiales
COT	Cloud Optical Thickness
CPI	Cloud Phase Index
CTH	Cloud Top Height
CTI	Configurable Transfer Item
CTP	Cloud Top Pressure
C1	Category 1
C2	Category 2
D	
DAK	Double-Adding code KNMI
DARA	Deutsche Agentur fur Raumfahrtangelegenheiten
DBU	Digital Bus Unit
DDS	Data Dissemination System
DFD	Deutsches Fernerkundungs-Datenzentrum
DHCM	Decontamination Heater Control Module
DIAL	Differential Absorption Lidar
DLR	Deutsches Zentrum fur Luft- und Raumfahrt
DLR-OP	DLR-Oberpfaffenhofen
DME	Detector Module Electronics
DNPM	Deutsch-Niederlundisches Projektmanagement
DNX	Descending Node Crossing
DOAS	Differential Optical Absorption Spectroscopy
DORIS	Doppler Orbitography and Radiopositioning by Satellite
D-PAC	German PAC
DU	Dobson Unit
E	
EA	Electronic Assembly
EADS	European Aeronautic Defense and Space Company
ECMWF	European Centre for Medium-Range Weather Forecasts
EDI	ESA Developed Instrument
EEPROM	Electrical Erasable Programmable Read Only Memory
ELACM	Elevation Aperture Cover Mechanism

ELHYSA	Etude l'Hygromerie Stratospherique
EMC	Electromagnetic Compatibility
ENVISAT	Environmental Satellite
ENVISOLAR	Environmental Information Services for Solar Energy Industries
EO	Earth Observation
EOL	End-of-Life
EOS	Earth Observing System
EPS	EUMETSAT Polar System
ERBS	Earth Radiation Budget Satellite
ERS	European Remote Sensing Satellite
ESA	European Space Agency
ESABC	ENVISAT Stratospheric Aircraft and Balloon Campaign
ESM	Elevation Scan Mechanism
ESOC	European Space Operation Centre
ESRIN	European Space Research Institute
EUMETSAT	European Organisation for the Exploitation of Meteorological Satellites
EURAD	European Air Pollution Dispersion
EURECA	European Retrievable Carrier
EUTELSAT	European Telecommunications Satellite
EUV	Extreme UV
EVDC	ENVISAT Validation Data Centre
F	
FMI	Finnish Meteorological Institute
Fin CoPAC	Finnish Co-PAC
FIRS	Far-Infrared Spectrometer
FISH	Fast In Situ Stratospheric Hygrometer
FOCC	Flight Operation Control Centre
FODP	Flight Operation and Data Plan
FOS	Flight Operation Segment
FoV	Field of View
FRESCO	Fast Retrieval Scheme for Clouds from the Oxygen A-band
FTIR	Fourier Transform Infrared
G	
GADS	Global Annotation Data Set
GAW	Global Atmospheric Watch
GBMCD	Ground-Based Measurement and Campaign Database
GDF	General Distribution Function
GDOAS	GODFIT DOAS
GDP	GOME Data Processor
GEO	Global Earth Observation
GeoFIS	Geostationary Fourier Transform Interferometer
GEOSS	Global Earth Observation System of Systems
GeoSCIA	Geostationary Scanning Imaging Absorption Spectrometer

GeoTROPE	Geostationary Tropospheric Explorer
GMES	Global Monitoring for Environment and Security
GODFIT	GOME Direct Fitting
GOME	Global Ozone Monitoring Experiment
GOMOS	Global Ozone Monitoring by Occultation of Stars
H	
HALOE	Halogen Occultation Experiment
HICRU	Heidelberg Iterative Cloud Retrieval Utilities
HK	Housekeeping
HSM	High Speed Multiplexer
I	
IABG	Industrieanlagen-Betriebsgesellschaft
IASI	Infrared Atmospheric Sounding Interferometer
ICU	Instrument Control Unit
IECF	Instrument Engineering and Calibration Facility
IFoV	Instantaneous Field of View
IGACO	Integrated Global Atmospheric Chemistry Observations Theme
ILoS	Instantaneous Line of Sight
IMAP	Iterative Maximum a Posteriori
IMAU	Institute of Marine and Atmospheric Research Utrecht
IMF	Institut fur Methodik der Fernerkundung
IMIA	Instrument Mission Implementation Agreement
IMLM	Iterative Maximum Likelihood Method
INTA	Instituto Nacional de Tecnica Aerospacial
IODD	Input/output data definition
IOM	Instrument Operation Manual
IPCC	Intergovernmental Panel of Climate Change
IPF	Instrument Processing Facility
IR	Infrared
ISCCP	International Satellite Cloud Climatology Project
IST	Integrated System Team
IT	Integration Time
IUP	Institut fur Umweltphysik (Heidelberg)
IUP-IFE	Institut fur Umweltphysik / Institut fir Fernerkundung (Bremen)
K	
KNMI	Koninklijk Nederlands Meteorologisch Instituut
L	
LC	Leakage Current
LEOP	Launch and Early Operation Phase
LIDORT	Linearized Discrete Ordinate Radiative Transfer
LLI	Life Limited Item

LoS	Line-of-Sight
LPMA	Laboratoire de Physique Moleculaire er Applications
LPMA-DOAS	Limb Profile Monitoring of the Atmosphere DOAS
LRAC	Low Rate Reference Archive Centre
LUT	Lookup Table
M	
MANTRA	Middle Atmosphere Nitrogen Trend Assessment
MAP	Measurement of Atmospheric Pollution
MASI	Models and data Assimilation, Satellite Intercomparison
MAX-DOAS	Multi-Axis DOAS
MCMD	Macrocommand
MDS	Measurement Data Set
MERIS	Medium Resolution Imaging Spectrometer
METEOSAT	Meteorological Satellite
METOP	Meteorological Operational Satellite
MIPAS	Michelson Interferometer for Passive Atmospheric Sounding
MIPAS-B	MIPAS for Balloons
MIR	Montgolfier Infra-Red
MLI	Multilayer Insulation
MLS	Microwave Limb Sounder
MO&C	Moon Occultation & Calibration
MODIS	Moderate Resolution Imaging Spectroradiometer
MOPITT	Measurements of Pollution in the Troposphere
MOZAIC	Measurement of Ozone and Water vapour by Airbus In-service aircraft
MPS	Mission Planning System
N	
NADIR	NILU Atmospheric Database for Interactive Retrieval
NASA	National Aeronautics and Space Administration
NASDA	National Space Development Agency of Japan
NCW	Nadir Calibration Window
NCWM	Nadir Calibration Window Mechanism
NDF	Neutral Density Filter
NDFM	Neutral Density Filter Mechanism
NDSC	Network for the Detection of Stratospheric Change
NH	Northern Hemisphere
NILU	Norsk Institutt for Luftforskning
NIR	Near Infrared
NIS	New Independent States
NIVR	Nederlands Instituut voor Vliegtuigontwikkeling en Ruimtevaart
NIWA	National Institute of Water and Atmospheric Research
NLC	Noctilucent Cloud
NNDEC	Non-nominal Decontamination
NOAA	National Oceanic and Atmospheric Administration

NOXAR	Measurements of Nitrogen Oxides and Ozone along Air Routes
NPP	NPOESS Preparatory Project
NPOESS	National Polar-orbiting Operational Environmental Satellite System
NRSC	National Remote Sensing Centre Ltd
NRT	Near-realtime
O	
OA	Optical Assembly
OBM	Optical Bench Module
OBT	On-Board Time
OCO	Orbiting Carbon Observatory
OCR	Operation Change Request
OCRA	Optical Cloud Recognition Algorithm
OE	Optimal Estimation
OIP	Optique et Instruments de Pr¿cision
OL	Offline
OLEX	Ozone Lidar Experiment
OMI	Ozone Monitoring Instrument
OMPS	Ozone Monitoring and Profiling Suite
OPTEC	Optical Test Facility
OSIRIS	Optical Spectrograph and Infrared Imager System
OU	Optical Unit
P	
PAC	Processing and Archiving Facility
PDAS	Payload Data Acquisition Station
PDCC	Payload Data Control Center
PDHS	Payload Data Handling Station
PDHS-E	Payload Data Handling Station - ESRIN
PDHS-K	Payload Data Handling Station - Kiruna
PDS	Payload Data Segment
PET	Pixel Exposure Time
PFM	Proto Flight Model
PI	Principle Investigator
PMC	Polar Mesospheric Cloud
PMC	Payload Management Computer
PMD	Polarization Measurement Device
PMTC	Power Mechanism & Thermal Control Unit
POAM	Polar Ozone and Aerosol Measurement
POEM	Polar Orbit Earth Observation Mission
PPF	Polar Platform
PPG	Pixel-to-Pixel Gain
PROMOTE	Protocol Monitoring for the GMES Service Element
PSC	Polar Stratospheric Cloud
PV	Potential Vorticity

PVU	Potential Vorticity Unit
R	
RADIBAL	Radiometre Balloon
RAM	Random Access Memory
RASA	Russian Aviation and Space Agency
RE	Radiated Emission
RGB	Red, Green, Blue
ROSE	Research on Ozone in the Stratosphere and its Evolution
RR	Reduced Resolution
RRU	Radiant Reflector Unit
RS	Radiated Susceptibility
RT	Random Telegraph
RTCS	Relative Time Command Sequence
S	
SAA	South Atlantic Anomaly
SABER	Sounding of the Atmosphere using Broadband Emission Radiometry
SACURA	Semi-Analytical Cloud Retrieval Algorithm
SAGE	Stratospheric Aerosol and Gas Experiment
SALOMON	UV-VIS Spectrometer
SAM	Stratospheric Aerosol Measurement
SAOZ	Syst¿me d'Analyse par Observations Z¿nithale
SBUV	Solar Backscatter Ultraviolet instrument
SCCVT	SCIAMACHY Calibration and Verification Team
SCIAMACHY	Scanning Imaging Absorption Spectrometer for Atmospheric Chartography
SCIARAYS	toolbox for radiative transfer modelling and atmospheric parameter retrieval in the UV-VIS
SCIATRAN	radiative transfer model for SCIAMACHY
SCIAVALIG	SCIAMACHY Validationand Interpretation Group
SCIA-VALUE	SCIAMACHY Validation and Utilization Experiment
SCOOP	SCIAMACHY On-board Operation Plan
SDLA-LAMA	Spectrometre Diode Laser Accordable Laser pour l'Analyse du Methane Atmospherique
SDPU	Science Data Processing Unit
SEM	Simplified Engineering Model
SEU	Single Event Upset
SF	Sun Follower
SFM	Spectrophotometer
SGP	SCIAMACHY Ground Processor
SH	Southern Hemisphere
SIRD	SCIAMACHY Instrument Requirements Document
SJT	SCIAMACHY Joint Team
SLS	Spectral Line Source
SME	Solar Mesospheric Explorer
SMR	Sun Mean Reference
SO&C	Sun Occultation & Calibration

SODAP	Switch-on and Data Acquisition Phase
SOLSTICE	Solar Stellar Irradiance Comparison Experiment
SOST	SCIAMACHY Operations Support Team
SPCA	SCIAMACHY PMD Cloud Algorithm
SPE	Solar Proton Event
SPICI	SCIAMACHY PMD Identification of Clouds and Ice/snow
SPIRALE	Spectroscopie Infra-Rouge par Absorption de Laser Embarqu¿
SRC	SCIAMACHY Radiant Cooler
SRON	SRON Netherlands Institute for Space Research
SSAG	SCIAMACHY Science Advisory Group
SSC	Swedish Space Corporation
STM	Structural Model
SME	Solar Mesospheric Explorer
SNSB	Swedish National Space Board
SUSIM	Solar Ultraviolet Spectral Irradiance Monitor
SWIR	Short-Wave Infrared
SYNEAR	Synergetic Aerosol Retrieval
SZA	Solar Zenith Angle
T	
TB	Thermal Balance
TC	Thermal Control
TCFoV	Total Clear Field of View
TEMIS	Tropospheric Emission Monitoring Internet Service
TES	Tropospheric Emission Spectrometer
TIMED	Thermosphere Mesosphere Ionosphere Energetics Dynamics
TOA	Top of Atmosphere
TOMS	Total Ozone Mapping Spectrometer
TOSOMI	Total Ozone retrieval algorithm for SCIAMACHY
TNO-TPD	Technisch-Naturwetenschappelijk Onderzoek - Technisch Physische Dienst
TRIPLE	Multi-instrument balloon payload
TRUE	Tangent Height Retrieval by UV-B
TV	Thermal Vacuum
U	
UARS	Upper Atmosphere Research Satellite
UK	United Kingdom
US	United States
UTC	Coordinated Universal Time
UV	Ultraviolet
V	
VA	Value added
VIS	Visible
VOC	Volatile Organic Compound

W	
WFM-DOAS	Weighting Function Modified DOAS
WGS84	World Geodetic System 1984
WLS	White Light Source
WMO	World Meteorological Organization

Frequently asked questions and typical EOHelp replies

SCIAMACHY Frequently asked questions (FAQs)

This section contains a collection of answers to frequently asked questions (FAQs) on SCIAMACHY, submitted to the ESA EO-Help support desk. These FAQs shall provide first line support to the SCIAMACHY user community, highlighting general aspects of the instrument, and pointing out documents or web resources where more technical details are addressed.

The FAQs are split into the following sections:

1 - Instrument and Mission;

2 - Data access, products' format and quality;

3 - Data handling

4 - Tools (e.g. SciaL1c, BEAT)

In case a question is not included here, please contact the EO Help team via TellUs.
Acronyms used throughout this section are defined here.

1. Instrument and Mission FAQs

1.1 What is SCIAMACHY?

SCIAMACHY - SCanning Imaging Absorption spectroMeter for Atmospheric CartograpHY - was a passive remote sensing spectrometer on board ESA Earth Observation satellite ENVISAT operated from March 2002 until April 2012, when the end of the mission was declared after the sudden loss of communication with the satellite.

The instrument observed the solar radiation backscattered, reflected, and transmitted from atmosphere and Earth's surface, in the wavelength range between 240 and 2380 nm. The high resolution and the wide wavelength range made possible to detect many different trace gases despite low concentrations, allowing global measurements in the troposphere and in the stratosphere.

SCIAMACHY had multi-viewing capabilities (nadir, limb, and sun/moon occultation geometries) which yield total column values as well as distribution profiles.

More details can be found here.

1.2 How can I start getting familiar with the SCIAMACHY instrument?

ESA provides an overview on the SCIAMACHY mission on the Earthnet Online web portal, introducing the SCIAMACHY instrument and its data products. Further internet resources are the SCIAMACHY Operations Support (SOST) web page and the SCIAMACHY web page providing technical details and operations concept. In addition, useful on-line documentation is available (see next FAQ).

1.3 What documentation exists for SCIAMACHY?

SCIAMACHY-related documents relevant for the user are listed below.
Check the Products Information page for the latest versions of the documents.

General

The book **SCIAMACHY - Exploring the Changing Earth's Atmosphere**, published in 2011 by Springer (ISBN 978-90-481-9895-5), explains all aspects of the SCIAMACHY mission, such as instrument concept, instrument operations, calibration and monitoring, retrieval of geophysical parameters, data processing and products format. The manuscript version is available on-line here.

Algorithms and Products Specifications

The **SCIAMACHY Product Specifications Volume 15** gives details on data product contents.

The algorithm baseline documentation consists of a collection of documents that together give a complete specification of the data processing.

The algorithm theoretical baseline documentation consists of a collection of documents that together gives the complete specification of the data processing.

The **Algorithm theoretical baseline description for Level 0-1c processing** describes in detail all calibration algorithms that are used in the operational processing of Level 1b products.

The **Algorithm theoretical baseline description for Level 1b-2 processing** describes in detail the operational processing of Level 2 products.

Data Quality

The **Product Quality Readme files** (previously indicated as Disclaimers) describe known artifacts and give up-to-date details on data quality for the Level 1b and the Level 2 datasets. A clear statement for each retrieved trace gases is provided there as well.

Tools

The **SciaL1c Software user manual** provides general instructions on the usage of the SciaL1c tool and explanations of all user options. It also contains a description of the Level 1c product format.

1.4 Which science groups are working on SCIAMACHY?

Many scientific groups at various institutes in Europe and abroad are involved in the scientific analysis and validation of SCIAMACHY data. A list of the teams and institutes involved in current and past SCIAMACHY-related projects is the following:

Information on Operational and Scientific Products, Validation and Science

- SCIAMACHY.org
- Tropospheric Emission Monitoring Internet Service (TEMIS)

SCIAMACHY Quality Working Group Teams

- Institut für Umweltphysik (IUP), University of Bremen, Germany
- Institut Netherlands Institute for Space Research (SRON)
- Belgian Institute for Space Aeronomy (BIRA-IASB)
- Institut für Methodik der Fernerkundung (IMF), DLR, Germany

SCIAMACHY Operations

- SCIAMACHY Operations Support, DLR-IMF/IUP-IFE

Further SCIAMACHY Teams

- Koninklijk Nederlands Meteorologisch Instituut (KNMI), The Netherlands
- Max-Planck-Institut für Chemie (MPIC), Germany
- Smithsonian Astrophysical Observatory (SAO), USA
- Institut für Umweltphysik, Universität Heidelberg, Germany

Space Agencies

- Netherlands Space Office
- German Space Agency

1.5 *How can I stay up-to-date with the latest news on SCIAMACHY?*

Due to the end of the mission, news on SCIAMACHY are rather unfrequent, and mainly related to the release of improved dataset from reprocessing campaigns.

ESA news are published on the Earthnet Online website and are circulated via the Earth Observation Newsletter sent by email every week. Subscription is free of charge and can be done here. Additionally, a RSS feed service allows users to automatically receive headlines from ESA as soon as they are published on the Earthnet Online website. Details are given here.

1.6 *How to get help with SCIAMACHY?*

If you do not find the answer to your specific question in these FAQs or in the documentation, the main user interface for queries related to ESA supported satellites and missions - including SCIAMACHY - is the web-based customer interface system "TellUs", replacing "EO-Support". The new interface is accessible at the following link: https://esatellus.service-now.com. Any customer, once authenticated via centralised Single Sign-On, will continue to have the ability to interface with the EO Help team by submitting a request, reporting an issue or opening a complaint through the new customised web forms.

1.7 How long the SCIAMACHY mission lasted?

The ENVISAT mission started in March 2002 with an expected nominal lifetime of 5-years. The careful management of the satellite orbital maneuvers allowed saving enough hydrazine for operating Envisat nominally for additional 3.5 years (i.e. until end 2010). At that time, following the excellent status of the platform and of the majority of its instruments, a further extension of the satellite operations was commenced with the modification of the satellite's orbit (October 2010). Extending SCIAMACHY operations beyond the specified five years mission lifetime required the reconfiguration of the instrument to compensate orbit dependent issues and subsystems degradation, ensuring the high quality of the data for the years to come. Expected duration of extended operations was until end 2014. Unfortunately, after ten years in orbit, communication with the ENVISAT satellite was suddenly lost on 8 April 2012. Any attempt to re-establish contact with ENVISAT was unsuccessful. The end of the mission was declared in May 2012.

1.8 *How was the orbit scenario after October 2010?*

At the end of October 2010, the sun-synchronous polar orbit of the ENVISAT satellite was lowered by 17.4 km to permit the extension of the mission. The extended mission orbit was characterized by a different repeat cycle: from 35-days/501-orbits to 30-days/431-orbits. In the new orbit, the orbital inclination control previously performed with orbit adjustments was interrupted in order to minimize fuel consumption and the satellite started to drift. The Mean Local Solar Time (MLST) for the Equator crossing was initially kept to a maximum deviation of +/- 1 km from ground track and +/- 5 minutes from 10:00 AM, after the lowering it was varying in the +/- 10 minutes range.

2. General data access and products format FAQs

2.1 How many product types are generated from SCIAMACHY observations?

SCIAMACHY products follow the general ENVISAT data structure: for each satellite's orbit one Level 0, Level 1b, and Level 2 files were generated. Level 2 products are the highest product level provided by ESA. Products were processed either in Near Real Time (NRT) at the acquisition facilities, or off-line, any time from a few hours following the acquisition, at the Processing and Archiving Centers (PACs). Off-line products had the same format and content of the NRT products, but benefitted from a-posteriori knowledge of calibration, auxiliary data and precise satellite orbit and attitude. Off-line products are also indicated as consolidated products. The Level 0 products are not distributed, while Level 1b and Level 2 data are accessible to users.

With the end of the mission only consolidated products are distributed.

Information on the datasets is summarized in the SCIAMACHY Products availability table.

2.2 What is the naming convention for the filenames?

ENVISAT product filenames contain themselves basic processing information and permit an unambiguous allocation of the file to a particular measurement type. The complete description of the ESA filename convention is available in the SCIAMACHY book (Figure 8.1) or here in the SCIAMACHY Product Handbook (Chapter 6).

2.3 How can I get access to SCIAMACHY data products?

A general description on how to access data provided by ESA can be found here.

Consolidated SCIAMACHY Level 1b (SCI_NL__1P) and Level 2 (SCI_OL__2P) datasets are available on-line. Products can be retrieved via FTP. Access information shall be requested via the web-based customer interface system "TellUs" (Single Sign-On authentication required), replacing "EO-Support". A request for registration to get data access can be submitted here.

2.4 What is the difference between consolidated and NRT products?

Consolidated and near-real-time (NRT) products are characterized by different time scale and were generated at different processing centers from different data processing chains and inputs.

The Near-Real-Time chain was conceived by ESA to provide during operations the EO user community with access to data products within a short time after sensing. NRT products (unconsolidated) were processed and disseminated within three hours from sensing, and were characterized by using NRT auxiliary information available at the time of product generation, e.g. predicted orbit state vectors and calibration data from about three days prior to acquisition. Additionally, NRT products had start/stop times defined by data receiving coverage times, not reflecting complete orbits and with possible overlaps. The NRT service was mainly intended for operational atmospheric and climate modeling applications.

Consolidated data products span one complete orbit between two consecutive ANX (Ascending Node Crossing). They benefit from an a-posteriori knowledge of information concerning calibration and auxiliary data, e.g. restituted attitude information and precise orbit. Usually a consolidated product was generated from two unconsolidated products and did not show overlaps or time gaps other than instrument unavailability. Since consolidated products represented the planned and executed measurements as precisely as possible, they are the products now distributed by ESA and suited for scientific studies.

2.5 Did SCIAMACHY Level 2 NRT products exist?

The generation of SCIAMACHY Level 2 near-real-time (NRT) products (SCI_NL__2P) was stopped in May 2006 and Level 2 NRT products were not distributed afterwards.

Starting from 2010, ESA implemented a Fast-Delivery processing service, providing SCIAMACHY Level 2 data (SCI_OL__2PN) within 24 hours from acquisition. These data were generated from Level 1b NRT products using predicted instead of consolidated auxiliary files and not using the restituted attitude information.

2.6 How can I distinguish between Fast Delivered and Off-line Level 2 products?

SCIAMACHY Level 2 operational products from the Fast Delivery and off-line processing chains shared the same processor version and processing center (D-PAC) but adopted different inputs. Fast Delivery products used as input Level 1b NRT data and auxiliary information available at the time of product generation. The off-line Level 2 data were based on consolidated Level 1b products and benefit from a posteriori knowledge of calibration information and satellite's attitude and state.
The only way to distinguish between the Fast Delivery and Off-line Level 2 products is checking the processing stage flag reported in the filename (and in the MPH ASCII header). Fast Delivery data present flag "N" (SCI_OL__2PN), while the off-line production adopted processing status flags P, R, U, W, Y (e.g. SCI_OL__2PW).

2.7 How can I read SCIAMACHY products?

SCIAMACHY products used ENVISAT specific data format. Each consolidated product is orbit based and contains several binary encoded geophysical quantities. The following tools support the reading of ENVISAT products format:

- The Basic ERS & ENVISAT Atmospheric Toolbox (BEAT) is a collection of executable tools and an application programming interface which has been developed by S&T to facilitate usage, viewing, and processing of GOMOS, MIPAS, SCIAMACHY, and GOME data. BEAT provides routines for data extraction from SCIAMACHY products.
- The Common Data Access toolbox (CODA) developed by S&T under ESA mandate provides a single interface for reading a very wide range of atmospheric data products. Supported instruments include GOMOS, MIPAS, SCIAMACHY, GOME, GOME-2, IASI, OMI, TES, and MLS. A set of command line applications (codacheck, codacmp, codadump, and codafind) permits direct access to earth observation data, while interfaces to programming languages allow to ingest products using e.g. Fortran, IDL, MATLAB, Java, and Python.
- VISAN is a visualization and analysis cross-platform application for Earth Observation data developed by S&T permitting the browsing of the SCIAMACHY products. VISAN provides some very powerful visualization functionality for 2D plots and world plots.
- HARP is a toolset developed and maintained by S&T for ingesting, processing, and inter-comparing satellite or model data against correlative data. The toolset is composed of a set of command line tools and a library of analysis functions. The current version of HARP handles SCIAMACHY Level 2 products.
- EnviView was a free application (developed in Java) that allowed ENVISAT data users to open data files and examine their content. The last release available is baseline version 2.8.1 dated 05 March 2010. The Enviview software remained frozen at March 2010.

With the next datasets (Level 1b version 9 and Level 2 version 7) the data format will be changed to netCDF.

2.8 How can I get information about SCIAMACHY data product quality?

During operations, information on data quality was provided on a daily basis by means of daily reports for every type of operational product generated from each processing chain. Expert reports, visualizing instrument key parameters for operational product (Levels from 0 to 2) are available here.

On a larger time scale, quality and operations information was made available through SCIAMACHY bimonthly reports, accessible here.

Specific Product Quality Readme files provide information about the quality status of the datasets.

A web-page reporting anomalies in the SCIAMACHY data production and indicating the corrective actions performed (e.g. data removal or re-processing) is regularly maintained.

2.9 Why are there missing products in the SCIAMACHY datasets?

SCIAMACHY was operated by ESA from March 2002 to April 2012, with quasi nominal operations starting on 02 August 2002. Along the mission, anomalies or events, such as satellite maneuvers, impacted SCIAMACHY's nominal measurements resulting in missing or corrupted measurements. A list of the SCIAMACHY evants and the instrumental availability interruptions is here. Also the SOST web page tracks the anomaly events, which caused a deviation from the planned measurements schedule. Moreover, processing failures happened during data generation. An overview of the complete SCIAMACHY Level 0, Level 1b, and Level 2 consolidated datasets is given here.

Please note that the Level 2 data set presents data gaps in correspondence of the monthly calibrations when Nadir or Limb measurements were not planned. These orbits were voted to calibration and were not processed up to Level 2 products.

2.10 What data version shall be used? (Data reprocessing campaigns)

The operational Level 1b and Level 2 ESA products are essential inputs to various atmospheric applications, such as weather forecasting, networks for volcanoes ashes detection, air quality monitoring.

Following algorithms and processor improvements, data reprocessing is carried out with the target of maintaining and improving the products quality both in terms of accuracy and number of available geophysical parameters.

The data re-processing campaigns are thus important in order to improve the quality of the existing dataset and generate long term series of geophysical parameters that are of vital interest for climate studies and trend analysis, especially considering the extension of the ENVISAT mission. Data reprocessing consists in gathering the consolidated Level 0 data from the full mission and generating the corresponding Level 1b and Level 2 products with the newest processor versions.

The latest SCIAMACHY Level 1b and Level 2 full-mission reprocessing were performed in 2016 with processor version 8 (8.01/8.02) and processor version 6.01 respectively. Data present processing status flag “Y”. The re-processed data are made available to the user community for direct download via the ESA centralised dissemination service (DissHarm). The overall status of the dataset also with availability statistics is given here.

An overview of the products currently distributed by ESA is available here.

Science users are strongly recommended to use for their particular applications consolidated Level 1b and Level 2 products processed with the latest processors.

Access to SCIAMACHY products can be provided through ESA Fast Registration.

2.11 What about validation?

Validation has to ensure that geophysical quantities derived from SCIAMACHY in-orbit radiometric measurements met quality requirements for scientific studies and applications. The goal of validation activities is to provide clear statements of the quality of all SCIAMACHY retrieved products. Given the evolution of the algorithms with the inclusion of new products this task has to be pursued continuously.

Results of the recent validation activities are detailed in reports available here.

- Keppens et al., “Multi-TASTE Phase F Validation report – Ground-based assessment of SCIAMACHY SGP 6.01 Level-2 Data Products O3, NO2, CO, CH4, BrO and H2O”, TN-BIRA-IASB-MultiTASTE-Phase-F-SCIA-SGP6-Iss1-RevB, Issue 1 / Rev. B, 52 pp., 21 December 2016.
- D. Hubert et al., “Multi-TASTE Phase F Report – Delta-validation of SCIAMACHY SGP upgrade from V5.02 to V6.00”, TN-BIRA-IASB-MultiTASTE-Phase-F-VR1-Iss2-RevA, 18 September 2015.
- D. Hubert et al., "Multi-TASTE Phase F Final Report / October 2013 - December 2015", TN-BIRA-IASB-MultiTASTE-Phase-F-FR, Issue 2 / Rev. A, 1 February 2016.

Previous results on the validation of operational and science data products can be found at http://www.sciamachy.org/products/.

2.12 What is an m-factor?

Monitoring factors (m-factors) are auxiliary files used to compensate for the radiometric degradation of SCIAMACHY, that were regularly calculated by SOST-IFE and provided to ESA for the operational data processing. The latest Level 0-1b processing (version 8) corrects for the optical degradation on the light paths affecting the SCIAMACHY instrument. In the previous processing baseline, degradation effects were corrected in the Level 1b to 2 processing stage. M-factors files are available from IUP University Bremen.

2.13 Are there known issues affecting SCIAMACHY products?

Known issues affecting SCIAMACHY products are usually indicated in the Product Quality Readme files, or on the web-page reporting processing anomalies.

3. Data handling

3.1 What spectral radiance units are used?

SCIAMACHY Level 1b products report the measured radiance as arbitrary Binary Units per second [BU/s] or [photons/cm2 nm s sr] respectively for un-calibrated and calibrated spectra. Details are in the Input/Output Data Description (IODD) document.

3.2 What is the definition for Limb viewing angles?

During limb measurements, SCIAMACHY sound the atmosphere in a sequence of vertical steps and horizontal scans. The scene of each limb observation is defined unambiguously through sets of angles specifying solar and viewing directions. In SCIAMACHY Level 1b products, for each limb scan, all relevant information is stored in the limb measurement data set (LIMB MDS). In particular, the solar azimuth angle (geo.sol_azi_ang) which stores 3 values (in degrees) for the angles at the start, the middle and the end of the integration time. Please note that Level 1b products also report the azimuth and elevation angles for the viewing direction, lines of sight (geo.los_azi_ang and geo.los_nad_ang). All these angles are given with respect to the height of 100 km above sea level, height considered as top of the atmosphere. A clear sketch of SCIAMACHY observation geometries and the coordinate system adopted is reported on the SCIAMACHY book (Figures 2.4 and 3.7).

3.3 Is it possible to use SCIAMACHY SWIR measurements?

There are some issues affecting SCIAMACHY SWIR channels, therefore warnings have to be raised for the usage of these spectral ranges.

In particular, detector channel 7 suffered from a light leak which is preventing successful Level 2 retrievals in that spectral range. Moreover, channels 7 and 8 were contaminated by an ice layer growing on top of the cylindrical lens covering the detectors. The ice layer produced a significant attenuation of the radiance response and modified the instrument slit function. It affected only channels 7 and 8 because these were the detectors operated at lowest temperatures. In order to remove the ice layer from the detector, several decontamination campaigns were done during the mission lifetime. Consequently, the impact of the ice layer is time-dependent.

All IR detectors (channels 6+ to 8) were degrading with time, in particular the number of pixels not responding or showing an abnormal behavior (with random intensity or negative values) was increasing along the mission lifetime. This aspect can be taken into account with the application of a dead and bad pixel mask (DBPM) indicating usable pixels. Bad Pixels have to be ignored for retrieval purposes.

Details also with decontamination intervals are reported in the Level 1b product quality Readme file.

3.4 How can I distinguish between forward and backward scans?

In almost all measurement types, the scanners executed oscillating movements (forward/backward scans) with specified scanner start positions and scan ranges defined by the orientation of the ASM and ESM devices. The current SCIAMACHY products do not give information on the pixel type (forward or backward scan) providing a clear flag. If users want to make this distinction, the corner coordinates of the ground pixels (latitudes and longitudes) have to be used in order to identify the sequence of pixel types.

3.5 Are Averaging Kernels included into the products?

Averaging Kernels are enclosed in the SCIAMACHY Level 2 products since SGP version 3.01. They are within the Limb MDS as Additional diagnostics (ADDDIAG). The arrangement of the information requires explanation that is provided in the Level 1b to 2 Off-line Processing - Input Output Data Definition (IODD) document (ENV-ID-DLR-SCI-2200-4), while instructions for the usage of the Level 2 products Limb MDS are in document SCIAMACHY 1b to 2 Off-line Processing Instructions (ENV-TN-DLR-SCIA-0077).

3.6 Which gas species are currently retrieved in ESA Level 2 processing?

The SCIAMACHY Level 2 data processing baseline is under continuous evolution and further trace gases are made available after the implementation of new algorithms. The list of retrieved geophysical parameters has been significant enhanced along the mission, also with improvements for data quality. The gas species currently enclosed in the Level 2 products (version 6.00) are indicated in the table below and in the Level 2 product quality Readme file.

Atmospheric trace constituents Level 2 version 6.00	Nadir	Limb
Absorbing Aerosol Index (AAI)	X	
O_3	X	X
NO_2	X	X
BrO	X	X
SO_2	X	
OClO	X	
HCHO	X	
CHO-CHO	X	
H_2O	X	
CO / xCO	X	
CH_4	X	
Clouds	Cover, Top Height, Optical Thickness	Classification

3.7 Is CO_2 enclosed in ESA Level 2 products?

CO_2 is an important gas species targeted for measurements by SCIAMACHY in the SWIR spectral region. However, CO_2 density columns are currently not retrieved as operational product so are not included into SCIAMACHY Level 2 products disseminated by ESA. Nevertheless, several studies covering atmospheric CO_2 distribution have been carried-out by research groups using SCIAMACHY observations. The products derived within studies implementing scientific algorithms are not distributed under ESA responsibility. We suggest the user to refer to scientific data products generated at IFE Bremen.

3.8 Are CO column densities within Level 2 products reliable?

Because of erroneous retrieval settings adopted in the operational Level 1b-2 processing with processor SGP version 5.01, users were recommended to not use the CO column densities enclosed in the Level 2 version 5.01 products. With the activation of processor SGP version 5.02, a spectral correction was implemented leading to a significant improvement in terms of quality of the CO product. The CO column densities are intended to be used as time-averaged products applying specific data filtering. Although single observations are provided, they have large errors and should not be used individually. More details are in the Level 2 product quality Readme file.

3.9 Why only OClO slant column densities have to be used?

The computation of vertical column densities (VCD) for OClO is difficult for its rapid photochemistry. VCDs included in the Level 2 products do not contain any correction for photochemical effects and should not be used. Slant column densities (SCD) are provided instead. Details are reported in the Level 2 product quality Readme file.

3.10 Are there limitations for BrO Vertical Column Densities?

Yes, users are recommended to not use BrO data for year 2002, due to low quality. For year 2002, the available version of Level 2 products (5.01) presents BrO column densities substantially too low with a lot of negative values. From 2003 onwards BrO data can be used without restrictions. Details are reported in the Level 2 product quality Readme file.

3.11 Why there are gaps in scan lines in both SCIAMACHY latitudinal and longitudinal directions?

SCIAMACHY measurements are set up in a nominal pattern where limb and nadir sequences are alternating on the dayside of the orbit. The sequence of nadir and limb states in a timeline is arranged so that limb and nadir ground pixels matches. At the beginning and end only limb or only nadir measurements are executed.

A clear sketch of the measurement sequence is provided on the SCIAMACHY book (Figure 4.2) http://atmos.caf.dlr.de/projects/scops/sciamachy_book/sciamachy_book_springer_editors_version.html.

3.12 Why there are two Nadir MDS for SO_2 column densities?

Within the Level 2 products, two types of SO_2 vertical column densities are reported; one representing an anthropogenic scenario (pollution dominated) and another one for a volcanic eruption. Since the vertical SO_2 distribution varies to a large degree between the two scenarios, the Air Mass Factor (AMF) used to convert the SO_2 slant columns to vertical columns cannot be derived from a single climatology. Two types of AMF are derived assuming a constant profile shape for two typical SO2 distributions:

- a profile with 1 DU of SO_2 in the boundary layer (from surface to 1 km height) simulating an anthropogenic pollution scenario;
- a profile with 10 DU of SO_2 between 10 and 11 km simulating a volcanic eruption.

Two different VCDs are thus computed and written into two different MDS: the anthropogenic SO_2 column (in UV5 limb MDS) and the volcanic SO_2 column (in UV7 limb MDS). Both retrievals use as input the same background-subtracted slant column, calculated from a reference sector over the Pacific Ocean as a pollution free correction. Details are reported in the Level 2 product quality Readme file.

3.13 I want to perform my own retrievals starting from spectra included in Level 1b products, and compare my results with ESA Level 2 products. Which calibrations and retrieval settings are operationally applied?

For details on the calibrations applied to the measured radiances, the user is directed to the **Algorithm theoretical baseline description for Level 0-1c processing** (ATBD L0-1c).

3.14 Are Limb Mesosphere-Thermosphere and Occultation measurements processed to Level 2?

From November 2008 onwards, SCIAMACHY performed regular limb measurements in the mesosphere and lower thermosphere. These measurements were carried out instead of "normal" limb states for 30 orbits every month split on two separate sequences of ~15 orbits each, with one sequence synchronized with the MIPAS Upper Atmosphere observations. SCIAMACHY Mesospheric Limb Measurements (state ID 55) were performed scanning altitudes between 60 and 150 km. Starting with the operational Level 1b data version 7.03, this new type of limb state was available in the Limb MDS of the Level 1b file. However, the Level 2 processing did not include these scientific measurements into the operational Level 2 products. Also occultation measurements were not operationally processed.

4. Tools FAQs

4.1 What is SciaL1c?

SciaL1c is a tool provided to the users of SCIAMACHY Level 1b products. This tool allows selecting specific calibrations to apply to SCIAMACHY Level 1b data that contain not fully calibrated spectral information in combination with calculated calibration data.

Once the user has identified within the Level 1b data the desired products to extract, it is recommended to run SciaL1c making use of all the filter options applicable. The generated Level 1c products are suitable for the user's particular applications. The output from the SciaL1c processing (Level 1c files) adopts ESA PDS format.

The SciaL1c tool is available here for download.

We recommend users to run SciaL1c making use of all the filter options applicable.
Few examples are: "-cat" to specify the type of measurements; "-cal" to specify the desired calibrations; "-topleft and -bottomright" to specify a geographical area of interest.

4.2 Are there known issues affecting SciaL1c?

An anomalous handling of the m-factor file during the calibration of SCIAMACHY Level 1b data was observed. The m-factor file (SCI_MF1_AX) is not correctly reported into the child product restituted from the SciaL1c processing. In particular, the MF1 filename does not fully appear in the DSD descriptor. The quality of the product is not impacted; this anomaly will be fixed with the next delivery of the SciaL1c tool.

4.3 What is the difference between Level 1b and Level 1c products?

Consolidated Level 1b products contain raw detector signals for all measurements for a complete orbit and have to be converted with the SciaL1c command line tool into Level 1c products containing fully calibrated measurements. Level 1c products are thus user specific products with the general ENVISAT data format. Such products are not operationally distributed as they are generated by the user specifying how data shall be calibrated. Level 1c products are suitable for the user's particular applications (e.g. spectral fitting and retrievals).

4.4 How to apply the m-factors when using SciaL1c?

Until data version 7.04, users of SCIAMACHY Level 1b products could compensate for the instrument degradation applying an end-to-end correction with the m-factor files (SCI_MF1_AXVIEC) while calibrating the Level 1b products with the SciaL1c applicator. A brief description of the syntax required for the application of the m-factor was indicated in the SciaL1c software user's manual.

With data version 8.0 of the Level 1b products, a new approach for the degradation correction of SCIAMACHY has been introduced as part of the radiometric calibration. SCIAMACHY calibrated spectra within version 8.0 products are always degradation corrected. Application of the m-factor to Level 1b products with SciaL1c is not possible anymore as correction has already been applied during level 0-1b processing step.

4.5 How to use BEAT?

The BEAT/CODA developers present a tutorial on the usage of BEAT on their web page. Below are reported few commands for the ingestion from SCIAMACHY Level 1b files in order to give a gist of the programs capabilities. Make sure you are using a version of the BEAT/CODA tool implementing the adequate data dictionary.

To open a Level 1b file:

p_id = coda_open('SCI_NL__1PUDPA20091113_111044_000060012084_00152_40286_8393.N1')

Ingesting a single specified field:

result = coda_fetch(p_id, 'MPH')

Retrieving the entire product:

result = coda_fetch(p_id)

Closing the Level 1b file:

result = coda_close(p_id)

4.6 Are there known issues affecting BEAT/CODA?

Issues affecting the BEAT/CODA software are promptly fixed by S&T with a new software delivery. However, new problems could be discovered affecting the current software release and are listed here .